



DISSERTATION

Investigations of quantum critical materials at low energies

Ausgeführt zum Zwecke der Erlangung des akademischen Grades einer Doktorin der
Naturwissenschaften unter der Leitung von

Univ. Prof. Dr.rer.nat. Silke Bühler-Paschen

E138

Institut für Festkörperphysik

eingereicht an der Technischen Universität Wien
Fakultät für Physik

von

Dipl. Phys. Diana Geiger

Matrikelnummer: 1127258
Favoritenstrasse 174, 1100 Wien

Wien, am 26.07.2016

Gutachter:

Univ. Prof. Dr.rer.nat. Silke Bühler-Paschen
Dr. rer. nat. habil. Steffen Wirth

Eingereicht am: 27.07.2016

Verteidigung am: 10.08.2016

Contents

Abstract	v
Kurzfassung	vii
1 Introduction	1
2 Theoretical background	5
2.1 Kondo physics	5
2.1.1 Kondo impurity	5
2.1.2 Kondo lattice and heavy fermion state	8
2.1.3 Fermi liquid theory	9
2.1.4 Magnetic interactions	12
2.2 Quantum criticality	13
2.2.1 Quantum phase transitions	13
2.2.2 T^* line and Kondo breakdown scenario	17
3 Experimental and technical background	21
3.1 Spectroscopy - ranges and techniques	21
3.2 Some microwave basics	22
3.2.1 A short glimpse into microwave transmission line theory	22
3.2.2 Coaxial lines	24
3.2.3 Coplanar waveguides	25
3.2.4 Vector network analyzer	26
3.3 Setups and techniques	29
3.3.1 Oxford Kelvinox 400 dilution refrigerator	30
3.3.2 Vienna nuclear demagnetization refrigerator	30
3.3.3 Garching microwave setup	34
3.3.4 Resistance, magnetoresistance, and Hall effect measurements	36
3.3.5 Specific heat measurements	38

3.3.6	Possible experimental approaches for microwave measurements . . .	39
3.3.7	Resonant measurement using a CPW resonator	44
3.3.8	Resistance measurements inside the CPW resonator box	49
4	Materials under investigation	53
4.1	YbRh ₂ Si ₂	53
4.2	CeNiAs _{1-x} P _x O	55
4.3	Ti _{1-x} Sc _x Au	57
4.4	CeB ₆	58
4.5	Ce ₃ Pd ₂₀ Si ₆	59
5	Results and discussion	61
5.1	Microwave simulations	61
5.1.1	Finite element simulations and Comsol	61
5.1.2	Creating a 3D simulation of a CPW resonator - realistic and sim- plified models	62
5.1.3	Results of the model system	69
5.2	YbRh ₂ Si ₂	74
5.2.1	Microwave measurements	74
5.2.2	Resistance measurements at ultra-low temperatures	104
5.3	CeNiAs _{1-x} P _x O	110
5.4	Ti _{1-x} Sc _x Au	126
5.5	CeB ₆	133
5.6	Ce ₃ Pd ₂₀ Si ₆	149
6	Summary and outlook	157
7	Bibliography	161

Abstract

Phase transitions at absolute zero in temperature are driven by quantum fluctuations and are therefore called quantum phase transitions. Their description requires a framework beyond that for finite temperature phase transitions. A second order quantum phase transition is a quantum critical point (QCP). At the QCP, quantum fluctuations are critical. This may have strong influence on the physical properties at finite temperatures, which are then called quantum critical. For metals, this becomes apparent through strong deviations from the predictions of Landau Fermi liquid (FL) theory, referred to as non-Fermi liquid (NFL) behaviour. Experimentally, quantum critical behaviour is best investigated by performing measurements at low energies (low temperatures and frequencies) because the signatures of quantum criticality are most pronounced near the QCP.

One particularly interesting group of materials in this context are heavy fermion compounds, where certain atoms with partially filled f -electron shells like Yb or Ce are constituents of the crystal structure. The f -electrons interact with the conduction electrons via the Kondo interaction, which induces a screening of the magnetic moments by the conduction electrons. They also interact with each other via the RKKY exchange interaction. External parameters like magnetic field, hydrostatic pressure, or doping can tune the relation between the two competing interactions to a critical value, where a QCP occurs.

In the course of this work, several compounds were investigated experimentally in the context of quantum criticality. Measurements were performed on the heavy fermion compounds YbRh_2Si_2 , $\text{Ce}_3\text{Pd}_{20}\text{Si}_6$, and CeB_6 , on the oxypnictide substitution series $\text{CeNiAs}_{1-x}\text{P}_x\text{O}$, and on the itinerant magnet doping series $\text{Ti}_{1-x}\text{Sc}_x\text{Au}$. All compounds order antiferromagnetically at ambient pressure, zero magnetic field, and $x = 0$. The ordering temperature was suppressed by the external parameters magnetic field (YbRh_2Si_2 , $\text{Ce}_3\text{Pd}_{20}\text{Si}_6$, CeB_6), pressure (CeNiAsO), and doping or isoelectronic substitution ($\text{CeNiAs}_{1-x}\text{P}_x\text{O}$, $\text{Ti}_{1-x}\text{Sc}_x\text{Au}$). The influence of magnetic field as an additional tuning parameter was investigated for different substitution levels of $\text{CeNiAs}_{1-x}\text{P}_x\text{O}$.

The temperature-dependent resistivity was measured down to dilution refrigerator temperatures for all compounds; furthermore, YbRh_2Si_2 samples were contacted and tested for measurements at ultra-low temperatures. Magnetoresistivity and Hall resistivity were measured with magnetic field applied along different crystallographic directions in cubic $\text{Ce}_3\text{Pd}_{20}\text{Si}_6$, which showed signatures of a direction-dependent second QCP (in addition to an isotropic one at lower fields). For CeB_6 , magnetic properties, specific heat, and resistivity were also measured with magnetic field applied along different crystallographic directions, and evaluated upon tuning the magnetic field towards the QCP. In $\text{Ti}_{1-x}\text{Sc}_x\text{Au}$, signatures of a QCP at $x = 13\%$ from previous resistivity measurements at higher temperatures could be confirmed at lower temperatures.

A central part of this thesis is devoted to a new microwave experiment to probe the dynamic response of quantum critical materials. In YbRh_2Si_2 , this is of particular interest for the investigation of its Kondo breakdown energy scale, which emerges from the QCP and strongly broadens with increasing temperature. To study its electronic excitations in the vicinity of the QCP and around this energy scale, YbRh_2Si_2 single crystals were coupled to the microwave field of a coplanar waveguide resonator, and the changes of the resonance properties were traced within the field-temperature phase diagram of YbRh_2Si_2 .

Kurzfassung

Phasenübergänge am absoluten Temperaturnullpunkt werden von Quantenfluktuationen verursacht und werden daher als Quantenphasenübergänge bezeichnet. Ihre physikalische Beschreibung erfordert einen Rahmen, der über die Beschreibung von Phasenübergängen bei endlichen Temperaturen hinausgeht. Ist ein solcher Quantenphasenübergang kontinuierlich und somit zweiter Ordnung, so ist er ein quantenkritischer Punkt. An diesem divergieren die Zeit- und Längenskalen der Quantenfluktuationen. Dies kann die Eigenschaften des Materials bei endlichen Temperaturen stark beeinflussen, ihr Verhalten wird dann quantenkritisch genannt. Bei Metallen äußert sich dies durch starke Abweichungen vom Landau Fermiflüssigkeitsverhalten, dem sogenannten Nicht-Fermiflüssigkeitsverhalten. Experimentell lässt sich quantenkritisches Verhalten am besten durch Messungen bei niedrigen Energien (niedrige Temperaturen und Frequenzen) untersuchen, da quantenkritische Eigenschaften in der Nähe des quantenkritischen Punktes am stärksten ausgeprägt sind.

In diesem Zusammenhang stellen Verbindungen mit schweren Fermionen eine besonders interessante Materialgruppe dar. In den Kristallstrukturen dieser Verbindungen sind Atome mit teilweise gefüllten f -Schalen wie Yb oder Ce eingebaut. Die f -Elektronen wechselwirken mit den Leitungselektronen über den Kondoeffekt, der eine Abschirmung der magnetischen Momente der f -Elektronen durch die Spins der Leitungselektronen bewirkt. Außerdem wechselwirken sie miteinander über die RKKY - Austauschwechselwirkung. Über externe Parameter wie Magnetfeld, Druck oder Dotierung kann das Gleichgewicht zwischen diesen einander entgegenwirkenden Effekten so verschoben werden, dass ein kritischer Parameterwert erreicht wird und ein quantenkritischer Punkt auftritt.

Im Rahmen dieser Arbeit wurden mehrere Verbindungen auf quantenkritisches Verhalten hin untersucht. Es wurden hierzu Messungen an den Schwere-Fermionen-Verbindungen YbRh_2Si_2 , $\text{Ce}_3\text{Pd}_{20}\text{Si}_6$ und CeB_6 durchgeführt, außerdem an der Sauerstoff-Pniktid-Substitutionsserie $\text{CeNiAs}_{1-x}\text{P}_x\text{O}$ und an der itinerant magnetischen Dotierungsserie $\text{Ti}_{1-x}\text{Sc}_x\text{Au}$. Alle erwähnten Verbindungen entwickeln bei Normaldruck, im Nullfeld und bei $x = 0$ antiferromagnetische Ordnung. Die entsprechende Ordnungstem-

peratur wurde mithilfe verschiedener externer Parameter unterdrückt: Magnetfeld für YbRh_2Si_2 , $\text{Ce}_3\text{Pd}_{20}\text{Si}_6$, CeB_6 , Druck für CeNiAsO und Dotierung für $\text{CeNiAs}_{1-x}\text{P}_x\text{O}$ und $\text{Ti}_{1-x}\text{Sc}_x\text{Au}$. Der Einfluss eines äußeren Magnetfeldes als zusätzlicher Parameter wurde für verschiedene Dotierstufen von $\text{CeNiAs}_{1-x}\text{P}_x\text{O}$ untersucht. Der temperaturabhängige Widerstand wurde für alle Verbindungen in einem $^3\text{He}/^4\text{He}$ -Mischungskryostaten gemessen; außerdem wurden mehrere YbRh_2Si_2 -Proben für Messungen bei ultratiefen Temperaturen kontaktiert und getestet. Der Magnetowiderstand und der Hall-Widerstand wurden im kubischen System $\text{Ce}_3\text{Pd}_{20}\text{Si}_6$ entlang verschiedener Kristallrichtungen gemessen, was weitere Hinweise auf einen richtungsabhängigen quantenkritischen Punkt lieferte (zusätzlich zu einem bereits bekannten isotropen quantenkritischen Punkt bei niedrigerem Magnetfeld). Im Fall von CeB_6 wurden Magnetisierung, spezifische Wärme und Widerstand entlang verschiedener Kristallrichtungen gemessen und bei Annäherung des angelegten Magnetfeldes an den kritischen Wert ausgewertet. Für $\text{Ti}_{1-x}\text{Sc}_x\text{Au}$ konnten typische Merkmale eines quantenkritischen Punktes, die aus vorhergehenden Widerstandsmessungen bei höheren Temperaturen hervorgegangen waren, bei niedrigeren Temperaturen bestätigt werden.

Im Material YbRh_2Si_2 sind dynamische Eigenschaften des elektronischen Systems von besonderem Interesse in Verbindung mit der Energieskala der Unterdrückung des Kondoeffektes. Ein Übergang zwischen zwei Zuständen der Fermifläche wird dieser Energieskala zugeordnet, welcher am quantenkritischen Punkt selbst abrupt ist, sich aber mit steigender Temperatur stark verbreitert. Um Informationen über die elektronischen Anregungen in der Nähe des quantenkritischen Punktes und der erwähnten Energieskala zu erhalten, wurden YbRh_2Si_2 -Einkristalle an das elektromagnetische Feld eines koplanaren Mikrowellenresonators gekoppelt, und die Änderungen der Resonatoreigenschaften beim Durchstimmen des Magnetfeld-Temperatur Phasendiagrammes von YbRh_2Si_2 beobachtet.

1 Introduction

In solid state compounds, the presence of a vast number of interacting atoms renders a large variety of collective effects possible, which determine the physical properties of a material. Overlapping electronic orbitals form bands, and in metals a small fraction of the electrons become delocalized conduction electrons. In simple metals and at high temperatures, the interactions between the electrons do not have to be considered explicitly to explain the materials' properties, and the electrons can be treated like independent particles in the periodic potential of screened nuclei. However, in some cases, and particularly at low temperatures, the correlations between electrons become relevant. In the class of strongly correlated electron materials, correlation effects between electrons play a crucial role in determining the properties of such systems. The field of strongly correlated electron systems has been intensively studied for several decades and comprises a number of fascinating phenomena, one example being unconventional superconductivity.

The interaction of conduction electrons with localized electrons carrying magnetic moments (e.g. from partially filled $4f$ -shells) provides the basis for the Kondo effect [1]. In the case of a lattice of localized magnetic moments, the Kondo interaction promotes the screening of the local moments and, in a band picture, the hybridization between the f -levels and the conduction band. This leads to the formation of flat hybridized bands around the Fermi energy and a peak in the electronic density of states. The Kondo interaction favours a nonmagnetic ground state, in which the local moments are fully screened by the conduction electrons and form heavy quasiparticles. The effective electron masses of the quasiparticles in heavy fermion compounds can be two or three orders of magnitude larger than the free electron mass [2].

The interaction between different localized electrons with magnetic moments, which is mediated by the conduction electrons, is the Ruderman-Kittel-Kasuya-Yosida (RKKY) exchange interaction [3, 4, 5]. It favours an ordered ground state, which in the case of heavy fermion compounds is usually antiferromagnetic.

Both RKKY and Kondo interactions are based on the exchange coupling of the

conduction electrons and the localized magnetic moments; this exchange coupling can be tuned to a critical ratio by external parameters like magnetic field, pressure, or doping. For instance, the antiferromagnetic ordering temperature of a material can be gradually suppressed by increasing an external magnetic field, until it becomes exactly zero at the critical field value. This point in the phase diagram, separating two phases at absolute zero in temperature, is a quantum critical point (QCP) if the phase transition is continuous. The competition between RKKY and Kondo interactions upon crossing the QCP can result in different types of QCPs. Most discussed are the spin-density-wave (SDW) type [6, 7, 8] and the Kondo destruction type [9]. Whereas the former is rather well understood, the latter type is the subject of current debates.

The quantum fluctuations at the QCP can strongly influence the physical properties of the material in the vicinity of the QCP, at finite temperatures. This quantum critical behaviour, or simply quantum criticality, exhibits anomalous temperature dependencies in various properties and cannot be explained within the framework of Landau Fermi liquid theory, which accounts for electronic correlations by renormalizing the properties of a Fermi gas [10].

In recent years, quantum critical behaviour has been found and studied in other strongly correlated material classes, including for instance iron-based [11] and cuprate [12] superconductors.

In the course of this thesis, several compounds (the heavy fermion materials YbRh_2Si_2 , $\text{Ce}_3\text{Pd}_{20}\text{Si}_6$, and CeB_6 , the nickel oxypnictide $\text{CeNiAs}_x\text{P}_{1-x}$, and the itinerant transition metal magnet $\text{TiSc}_{1-x}\text{Au}_x$) were investigated with respect to quantum criticality. Their electronic transport properties (electrical resistivity, Hall resistivity, and magnetoresistivity) were measured at low temperatures to reveal Fermi liquid (FL)/ non-Fermi liquid (NFL) behaviour and to collect information concerning the type of QCP. To study electronic low-energy excitations around the Kondo breakdown scale of YbRh_2Si_2 , a microwave measurement was set up, coupling YbRh_2Si_2 single crystals to coplanar waveguide (CPW) resonators.

Chapter 2, following this introduction (chapter 1), provides an overview on the relevant theoretical concepts: The Kondo impurity and lattice interactions are explained as a basis for the understanding of the formation of the heavy fermion state. FL theory is briefly discussed, being the framework for conventional correlated materials, followed by QCPs and quantum criticality and the NFL behaviour that occurs in quantum critical materials. A short introduction to the Kondo breakdown scenario for heavy fermion metals with antiferromagnetic QCPs will be given at the end of the chapter. In chapter

3, the used experimental setups and techniques are explained. Chapter 4 is a short summary on the investigated materials, containing their crystal structures and some basic information. Chapter 5 contains the obtained results. It starts with simulations of microwave measurements and is followed by the microwave results on YbRh_2Si_2 . The measurements on the other compounds are presented in consecutive sections of chapter 5. Chapter 6 provides a summary of the most important results, and an outlook on possible future investigations.

2 Theoretical background

2.1 Kondo physics

Already in the 1930s it was observed that metals with a small amount of magnetic impurities, for instance Cu doped with a few hundred ppm of Fe, exhibit a minimum in their temperature-dependent electrical resistivity at low temperatures [13]. At temperatures above the minimum there is no significant difference to the temperature dependence of the pure material. For several decades this phenomenon remained without theoretical explanation until Jun Kondo could solve the issue by taking the scattering of conduction electrons and magnetic impurities into account [1, 14], see also Sect. 2.1.1. Since then, many intriguing physical phenomena have been related to the complex interplay of conduction electrons and magnetic ions of partially filled d - or f -shells. Quantum criticality (see Sect. 2.2) represents one of the most relevant research topics in this field.

2.1.1 Kondo impurity

The single ion Kondo model was first proposed by Kondo in 1964 [1]. It yields a temperature-dependent scattering term for the conduction electrons for metals with diluted magnetic impurities. Dilute in this context means that interactions between the magnetic impurities can be neglected and the Kondo effect does not compete with magnetic ordering effects and Ruderman-Kittel-Kasuya-Yosida (RKKY) [4, 3, 5] interactions. The impurities are ions with partially-filled d - or f -orbitals, which are highly localized compared to the conduction electrons in the s - and p -bands (and sometimes d -bands). As an illustration of this fact, Fig. 2.1 (left) shows the radial electronic density in Ce orbitals. The details will be different in other magnetic ions, but the fact that $4f$ - (or $3d$ -) electrons are comparatively localized does not change. These impurity atoms with localized orbitals can, in a first approximation, be treated as defects that interact with the electrons in the conduction band via scattering and screening: This system of conduction electrons and dilute magnetic ions can be described by the Anderson model,

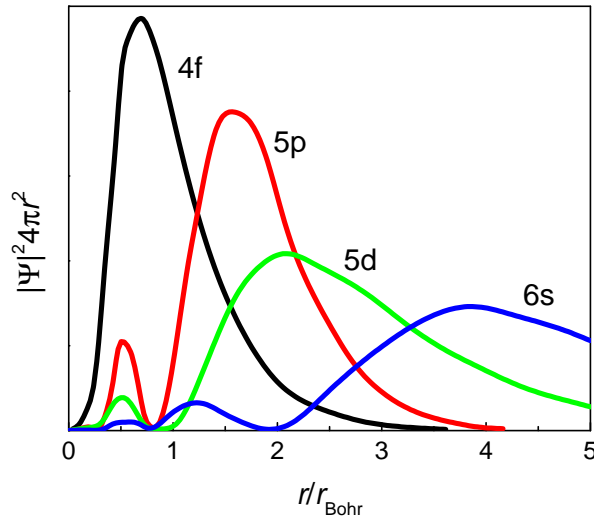


Figure 2.1: Schematic plot showing atomic 4f-, 5p-, 5d- and 6s-orbitals, calculated for Ce with the electronic structure [Xe] 4f¹ 5d¹ 6s² [15].

presented in 1961 [16]. It combines an electron sea picture with single-atom terms to express the different interactions. The Anderson Hamiltonian

$$H = \underbrace{\sum_{k,\sigma} \epsilon_k n_{k\sigma}}_1 + \underbrace{\sum_{\sigma} \epsilon_f n_{f\sigma}}_2 + \underbrace{U n_{f\uparrow} n_{f\downarrow}}_3 + \underbrace{\sum_{k\sigma} (V_{kf} c_{k\sigma}^\dagger c_{f\sigma} + V_{kf}^* c_{f\sigma}^\dagger c_{k\sigma})}_4 . \quad (2.1)$$

includes all important processes in systems with dilute magnetic impurities and has proven to be a good starting point for many calculations of physical properties. Conduction electrons are characterized by their wave vector \vec{k} and their spin σ . $c_{k\sigma}^\dagger$ and $c_{f\sigma}^\dagger$ are the creation operators of the conduction electrons and localized electrons, respectively ($c_{k\sigma}$ and $c_{f\sigma}$ the corresponding annihilation operators). $n_{k\sigma}$ and $n_{f\sigma}$ are number operators. The first term (1) represents the kinetic energy of the unperturbed conduction electrons. The second term (2) represents the bare impurity electron energies, ϵ_f being the electron energy without perturbation. The third term (3) is the Coulomb repulsion of two d - or f -electrons of the impurity in the same orbital (on-site interaction). This and the last term (4), namely the hybridization where electrons are created in the conduction band and annihilated at the impurity site or the other way around, are the essential parts for these materials. The Anderson model (and its refined variant, the Coqblin-Schrieffer model [17]) is one of the most versatile and successful impurity models. It can also be generalized to a lattice model. However, for illustrating the Kondo effect, Jun Kondo's way of explaining the resistivity minimum will be outlined.

It can be shown that the consequences of the Anderson model correspond to the ones of Kondo's approach [17]. Kondo's solution starts with the s - d model [14], established in 1951, which describes the interaction of an s -electron spin $\vec{\sigma}$ and a d -impurity spin \vec{S} via their exchange coupling $J(\vec{r})$ by

$$H = -J(\vec{r})\vec{\sigma} \cdot \vec{S} \quad . \quad (2.2)$$

By including second-order scattering processes (with spin-flips) of conduction electrons and magnetic impurities, Kondo obtained a temperature-dependent contribution to the resistivity [1]:

$$\rho_{\text{total}} = \rho_0 + AT^2 + BT^5 + C \ln \frac{D}{k_B T} \quad . \quad (2.3)$$

The first term is temperature-independent impurity scattering, the second term corresponds to the FL contribution from electron-electron scattering, the third term is associated with electron-phonon scattering and the last one is the Kondo impurity scattering term. A, B, C, and D are positive parameters, C is proportional to the density of magnetic impurities in the material and the antiferromagnetic exchange coupling constant (in case of ferromagnetic impurities C becomes negative).

The logarithmic term leads to an unphysical divergence of several physical quantities in the limit $T \rightarrow 0$; to overcome this unphysical behaviour, Abrikosov carried out a higher order perturbation calculation [18] including higher order logarithmic terms, and obtained a contribution

$$\rho_{\text{Abri}} \propto \frac{1}{(1 - 2JN(E_F) \ln(k_B T/D))^2} \quad . \quad (2.4)$$

$N(E_F)$ the density of states at the Fermi level. For antiferromagnetic exchange ($J = -|J|$), ρ_{Abri} diverges at the so-called Kondo temperature T_K ,

$$k_B T_K = D e^{-\frac{1}{2|J|N(E_F)}} \quad . \quad (2.5)$$

$k_B T_K$ is a characteristic energy scale for the electron-impurity interaction in a certain material, which only depends on the electronic properties of the material but not on the impurity concentration. Regimes of weak ($T > T_K$) and strong ($T \ll T_K$) coupling between electrons and magnetic impurities can be distinguished.

Further refinements to the theoretical description [19, 20] eliminated the divergence at T_K and showed that in the strong coupling regime, perturbation-type approaches are

insufficient because collective particle effects have to be considered, i.e. the moments are screened by the surrounding electron spins and a non-magnetic singlet ground state is obtained. An overview on the evolution of the Kondo problem from a theoretical point of view can be found in [21].

The energy $k_{\text{B}}T_{\text{K}}$ is the energy difference between the Kondo singlet and the magnetic triplet state and therefore the energy gain of a Kondo system when forming the singlet state. The Kondo temperature can vary over orders of magnitude for different materials, from approximately 1 mK (e.g. for $\underline{\text{CuMn}}$) to over 1000 K (e.g. for $\underline{\text{AlMn}}$) [22]. The physics of dilute Kondo systems attracted a lot of interest in the decades after its first discovery. Today, the single-ion Kondo effect in its original form is considered as solved and research focuses on Kondo lattices systems which are described below in Sect. 2.1.2.

2.1.2 Kondo lattice and heavy fermion state

In materials with high impurity concentrations and in Kondo lattice compounds (where the Kondo ions form a regular lattice), Kondo impurity models still explain the experimental findings at high temperatures ($T > T_{\text{K}}$). This is in particular true for $4f$ -ions where due to the strong localization of the $4f$ -wave function, ion-ion interactions only play a role at low temperatures. There, strong deviations from the predictions of the impurity models are found and the interactions of the magnetic ions with each other have to be accounted for: At a characteristic temperature, often referred to as coherence temperature T_{coh} , the logarithmic increase of the resistivity towards lower temperatures stops and turns into a strong decrease (Fig. 2.2). The periodicity of the Kondo lattice leads to a coherent state in which incoherent scattering is suppressed and the logarithmic resistivity term vanishes. In a band picture, the bands of the two electron types hybridize (Fig. 2.3 (left)) and a Kondo resonance forms in the electronic density of states, with a narrow gap within it (Fig. 2.3 (right)). Through the hybridization the bands in the proximity of the Fermi energy become extremely flat; this corresponds to a very high effective mass of the charge carriers, the so-called heavy fermions. In a single particle picture, the magnetic ions are completely screened by the conduction electron sea. As a result, heavy composite quasiparticles emerge and determine the electronic properties of the non-magnetic heavy fermion metal. Experimentally the renormalization of mass can, for instance, be observed from specific heat, electrical resistivity, or magnetic susceptibility measurements at low temperatures, where the heavy quasiparticles have completely formed. How the effective mass enters these quantities is described

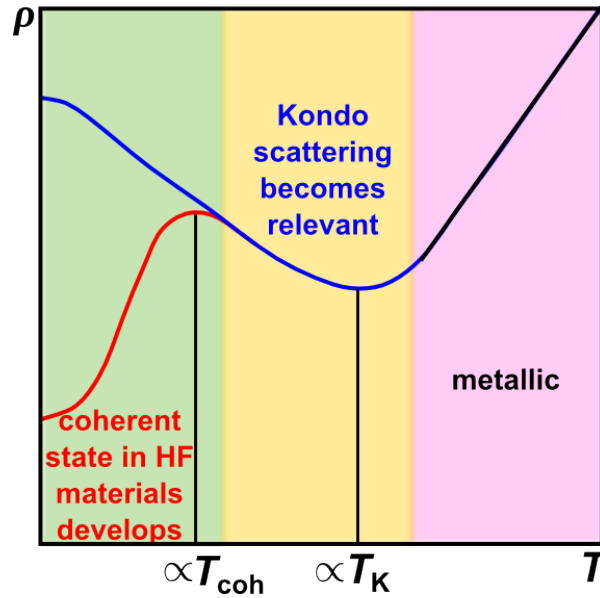


Figure 2.2: Schematic resistivity curves for single ion Kondo systems and Kondo lattice. The high-temperature region (red) has a metallic temperature dependence, in the yellow region the resistivity shows a logarithmic increase upon cooling. In this incoherent Kondo regime below the Kondo temperature T_K , the single-ion scattering term is the dominant temperature-dependent term. In the green region, lattice and single impurity systems differ significantly. Single impurity systems keep the logarithmic term until it saturates, Kondo lattice systems evolve into a coherent state and reenter a metallic temperature dependence.

by Fermi-liquid (FL) theory in Sect. 2.1.3.

2.1.3 Fermi liquid theory

FL theory, introduced by Landau in 1956, allows to treat interacting fermionic systems in a relatively simple manner [10]. Landau found that, at low energies and temperatures, there is a one-to-one correspondence between the low-energy excitations of a system consisting of non-interacting fermions (the Fermi gas) and those of a system of interacting fermions (the FL). These excitations are referred to as quasiparticles. The interaction leads to a renormalization of their characteristic properties, for instance their effective mass [24].

The validity of FL theory only at low energies and temperatures goes back to Landau's concept of adiabatically increasing the interaction strength while keeping track of each particle (one-to-one correspondence). This requires that during this process not collisions occur, which is possible only for low scattering rates. The Pauli exclusion principle is responsible for the strong suppression of scattering processes with temperature

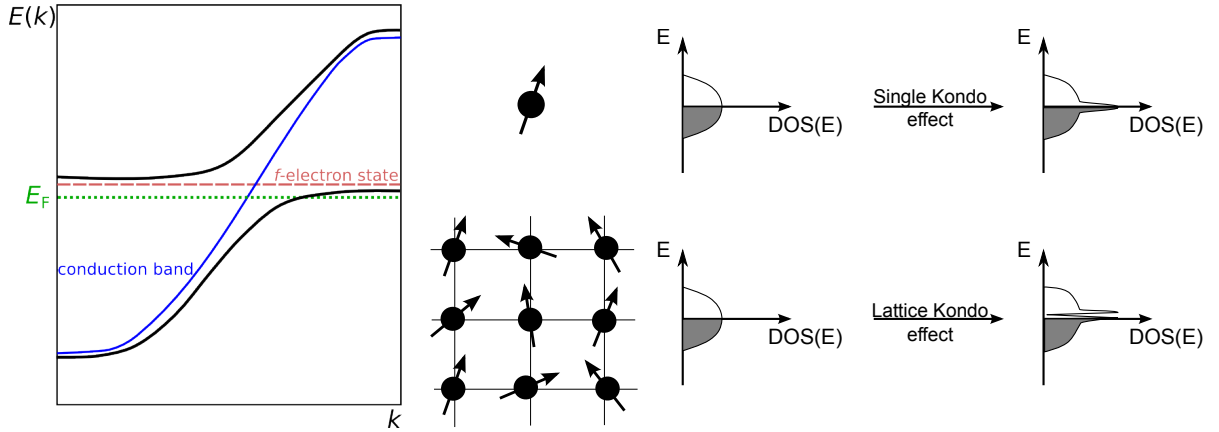


Figure 2.3: *Left:* Band picture of the hybridization of conduction electrons and localized f -electrons at low temperatures, leading to the formation of a flat band around E_F and a highly renormalized effective mass of the electrons (after [23]). *Right:* Changes in the electronic density of states induced by the single-ion Kondo effect and the Kondo lattice effect (Sects. 2.1.1 and 2.1.2, respectively). Isolated magnetic impurities lead to a resonance at the Fermi energy, the Kondo resonance; a Kondo lattice gives rise to a narrow energy gap within that resonance. Depending on band filling, the Fermi energy can be located in the band or the bandgap. The picture was adapted from [23].

and proximity of the particle's energy to the Fermi energy because it reduces the phase space available for scattering processes (no particle can scatter into an already occupied state). In a three-dimensional isotropic system FL theory yields for the specific heat capacity C , the magnetic susceptibility χ , and the electrical resistivity ρ :

$$C = \gamma_0 T \quad , \quad (2.6)$$

$$\chi = \chi_0 \quad , \text{ and} \quad (2.7)$$

$$\rho = \rho_0 + AT^2 \quad . \quad (2.8)$$

γ_0 is the Sommerfeld coefficient, ρ_0 the residual resistivity, and the prefactor of the T^2 term is referred to as A coefficient. The Kadowaki-Woods ratio (KWR), A/γ_0^2 , and the Sommerfeld-Wilson ratio (SWR), which is proportional to γ_0/χ_0 , are useful tools for the characterization of FL phases. In a FL state these ratios are universal because the mass renormalization cancels out [15, 25], see Fig. 2.4.

The expected temperature and energy dependence of the scattering rate of a FL is [27, 28]

$$\frac{1}{\tau} = a(k_B T)^2 + b(\hbar\omega)^2 \quad , \quad (2.9)$$

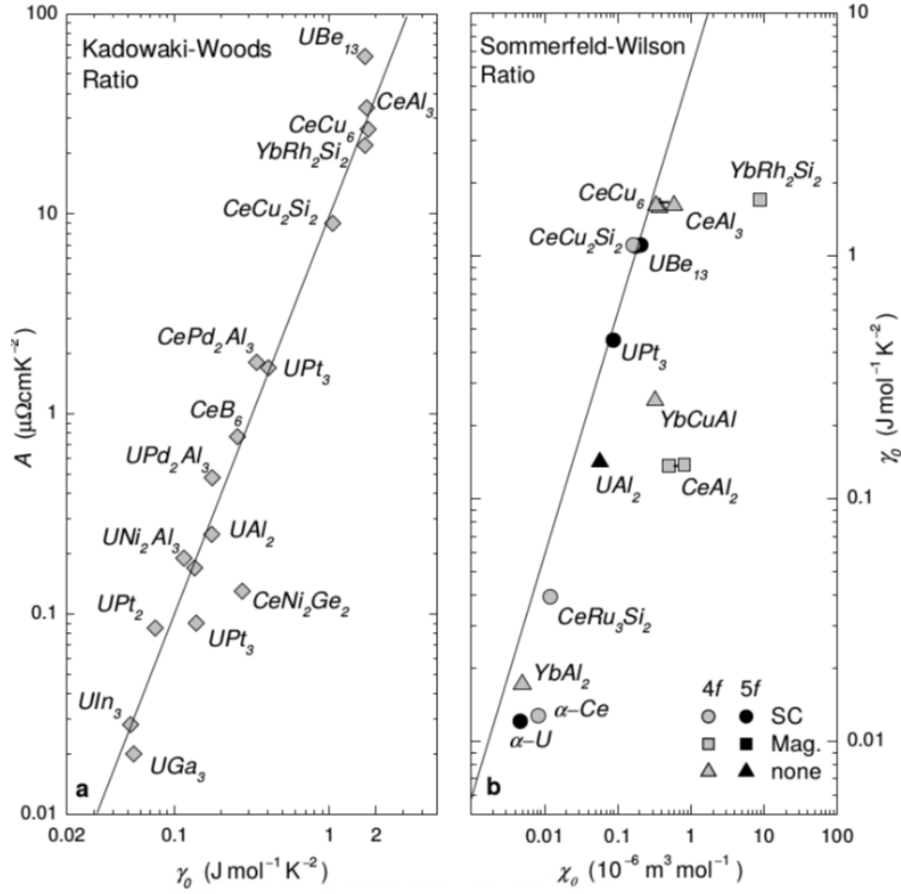


Figure 2.4: A vs γ_0 (left) and γ_0 vs χ_0 (right) of various compounds [26]. The solid lines represent the KWR (left) and the SWR (right).

where k_B is the Boltzmann constant, ω the angular frequency, and a and b are constant prefactors with the ratio $a/b = 4\pi^2$ [29, 30]. Equation 2.9 also expresses the symmetry between electromagnetic ($\hbar\omega$) and thermal ($k_B T$) energy forms. An important consequence of this equivalence is that both scales have to be sufficiently low to meet the requirements for the applicability of FL theory: High-energy excitations (for instance optical spectroscopy in the visible and UV spectral ranges) at lowest temperatures as well as low-energy excitations (for instance radio frequency, microwave or THz spectroscopy) at high temperatures should be discussed in a different framework.

Simple metals are expected to behave as FL at low energies. If a material shows strongly deviating characteristics (in a certain low-energy range), it is considered to be unconventional and effects beyond the FL approach have to be included. Experimentally observed (but frequently not fully understood) disagreement with FL theory is simply referred to as non-Fermi liquid (NFL) behaviour. However, it is important to keep in

mind that the term NFL only makes sense if the experiment is performed in a region where FL behaviour would actually be expected.

2.1.4 Magnetic interactions

As described above, the Kondo effect promotes full screening of the magnetic ions and a non-magnetic ground state. However, in Kondo lattices, a second interaction competes with the Kondo effect, the RKKY interaction. This is an indirect interaction between localized magnetic moments via the conduction electrons that favours magnetic order.

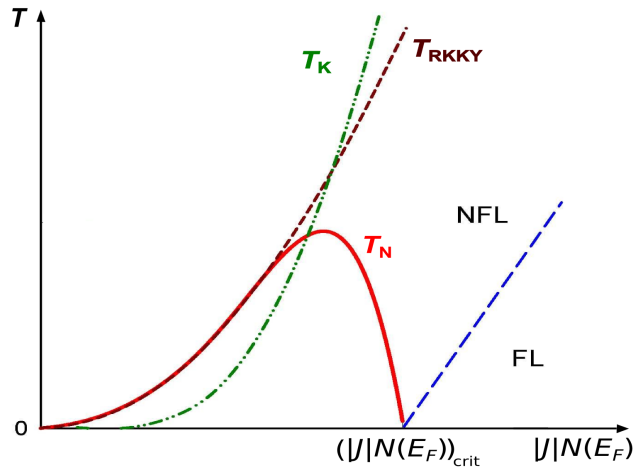


Figure 2.5: Doniach phase diagram of competing magnetic and Kondo energy scales, from [22], after the theoretical considerations of Doniach [31]. In experiments, the parameter $|J|N(E_F)$ can be tuned by pressure or magnetic field. The region below the red line is antiferromagnetically ordered.

In Sect. 2.1.1 it was shown that the relevant energy scale of the (single-ion) Kondo effect, the Kondo temperature $T_K \propto e^{-1/|J|N(E_F)}$, depends on the coupling between the d -/ f -electrons of the magnetic ions, J , and the electronic density of states at the Fermi level $N(E_F)$. The RKKY interaction is characterized by $T_{RKKY} \propto |J|^2 N(E_F)$. These competing scales were evaluated, starting from a periodic Anderson model, by Doniach in 1977 [31]. His model gave first insight into the competition between a magnetically ordered phase and a spin compensated phase, that coexist at a critical value $(|J|N(E_F))_{critical}$. Figure 2.5 illustrates the interplay of the two energy scales $k_B T_{RKKY}$ and $k_B T_K$. For $T_{RKKY} \gg T_K$ a magnetic ground state develops at the Néel temperature T_N . If $T_K \ll T_{RKKY}$, a metallic non-magnetic FL state (see also Sect. 2.1.3) is the ground state.

2.2 Quantum criticality

Quantum phase transitions, quantum critical points (QCP), and their influences on low-temperature phase diagrams of correlated electron materials have been studied extensively for the past few decades and are the subject of many ongoing theoretical and experimental investigations. Quantum critical phenomena have been reported to be relevant in a variety of materials, for instance high- T_C superconductors [12], iron pnictides [11], quantum Hall systems [32], and heavy fermion materials [33]. Numerous heavy fermion materials have been tuned to a QCP and the field has been largely driven by these materials.

Many heavy fermion systems order antiferromagnetically at low temperatures. The ordering temperature can frequently be reduced by applying an external parameter like magnetic field, pressure, or doping. If the transition remains continuous as it is fully suppressed to absolute zero, this point in the phase diagram is a QCP. Even though the actual QCP at 0 K cannot be accessed experimentally, the quantum fluctuations emerging from the QCP may strongly influence a certain finite-temperature region of the phase diagram. In this region, deviations from FL behaviour (Sect. 2.1.3) are frequently observed. The electronic system can show FL or NFL behaviour (see section 2.1.3) there.

In this section the concept of a Landau FL will be introduced, followed by information about QCPs and how they affect finite-temperature phase diagrams, with a few details on the so-called Kondo breakdown scenario. Some of the basic concepts on QCPs are valid independently of the specific material class, but the main focus will lie on QCPs in heavy fermion materials.

2.2.1 Quantum phase transitions

Quantum phase transitions happen at $T = 0$ K and are usually distinguished from classical phase transitions that occur at finite temperatures (for more details on the following section, see also [34, 35]). Classical phase transitions are thus driven by thermal fluctuations, quantum phase transitions by quantum fluctuations. Nevertheless, the terminology used to describe classical phase transitions can also be applied to quantum phase transitions.

The order of a phase transition is determined by the lowest order of the derivative of a thermodynamic potential that shows a discontinuity. The phase transition from water to ice, for example, involves latent heat (a discontinuity of the heat capacity

$\partial U/\partial T$) and is of first order. The phase transition in Fe from the ferromagnetic to the paramagnetic state is continuous and therefore of second order (the magnetization, the first derivative of the free energy with respect to magnetic, is continuous, whereas the magnetic susceptibility, the second derivative, changes discontinuously). We will focus on second-order phase transitions, that give rise to QCPs when occurring at $T = 0$ K.

Continuous transitions from an ordered to a disordered phase are commonly described by an order parameter, which is zero in the disordered and non-zero in the ordered phase. Taking the aforementioned ferromagnet to paramagnet transition, the order parameter is the total magnetization of the system.

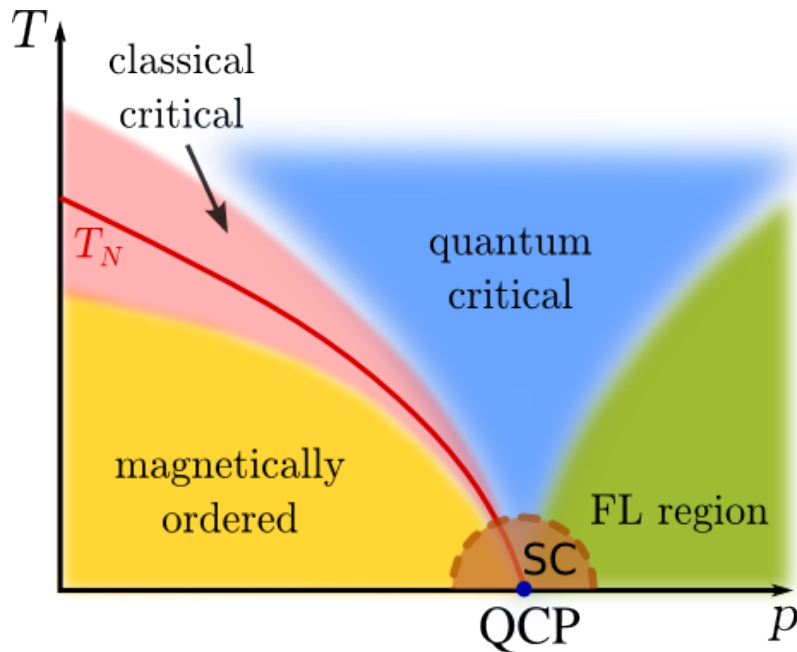


Figure 2.6: Phase diagram of a second order quantum phase transition, a QCP. In heavy fermion materials, the critical temperature is the Néel temperature and the QCP may or may not be surrounded by a superconducting phase, often called a superconducting dome (brown region, enclosed by the dashed line) [36]. The of this superconducting phase is a field of ongoing research, but in this work we focus on materials without (known) superconducting domes.

Although the thermodynamic average of the order parameter is zero in the disordered state, its fluctuations can be non-zero and become long-ranged in the vicinity of the critical point, where their typical length scale ξ (correlation length) and typical fluctuation

decay time scale τ_c (correlation time) diverge and become scale invariant:

$$\xi \propto t^{-\nu} = \left(\frac{|T - T_c|}{T_c} \right)^{-\nu}, \quad (2.10)$$

$$\tau_c \propto \xi^z \propto t^{-\nu z}. \quad (2.11)$$

The two exponents ν and z are the (correlation length) critical exponent and the dynamical critical exponent, respectively. The critical behaviour of finite temperature phase transitions is fully described by classical thermodynamics, even if the involved phases require a quantum mechanical description (e.g. superconductivity) [34]. This is due to the presence of a phase diagram region around the transition where classical fluctuations govern the physics of the system. In Fig. 2.6 this region is coloured in light red and is referred to as classical critical. It narrows down with decreasing temperature and vanishes at the QCP.

Experimentally, a QCP is induced by tuning a non-thermal parameter like pressure, chemical composition, or magnetic field to suppress a transition temperature to 0 K [37, 38]. It separates a magnetically ordered from a disordered ground state. Obviously, such a zero-temperature transition cannot be driven by thermal fluctuations; quantum fluctuations have to be the underlying source. As expressed in Eqns. 2.10 and 2.11, they diverge and become scale invariant at the QCP.

At finite temperatures, quantum fluctuations with an energy scale of $\hbar\omega_q$ and classical thermal fluctuations with an energy scale of $k_B T$ compete. ω_q is the characteristic frequency of a quantum fluctuation; it scales inversely with the correlation time τ_c . For $\hbar\omega_q > k_B T$, quantum fluctuations dominate the system's properties. As a consequence, it is possible to detect signatures of the QCP also at finite temperatures, in a quantum critical region above the QCP at sufficiently low temperatures. In Fig. 2.6, the quantum critical region is the blue tornado-shaped area. There, unconventional physical behaviour of NFL type occurs. The yellow region in Fig. 2.6 indicates the magnetically ordered phase. In the quantum critical region and the FL region (green), no magnetic order is present.

In the FL (and partially also in the ordered) region, enhancements of the FL parameters γ_0 , χ_0 , and A (Sect. 2.1.3) towards the QCP are frequently observed [39] and taken as first indication for quantum criticality. Also the KWR and SWR (Sect. 2.1.3) may change upon tuning towards a QCP.

There have been several theoretical approaches to describe NFL behaviour [41, 42], the most commonly applied being the approach by Hertz and Millis [6, 7, 8]. As men-

Table 2.1: Predictions of the temperature dependencies of the electrical resistivity ρ , the specific heat capacity C_p , and the magnetic susceptibility χ close to an antiferromagnetic SDW QCP [40]. Comparison to the FL expectations.

	2D	3D	FL
ρ	T	$T^{1.5}$	T^2
C_p/T	$-\ln(T)$	$-\sqrt{T}$	constant
χ	$-\ln(T)/T$	$T^{-1.5}$	constant

Table 2.2: Some examples of quantum critical heavy fermion materials with their critical doping levels, fields, or pressures and the typical temperature dependencies of specific heat and resistivity in the NFL region [23].

Compound	Critical Value	C_v/T	$\rho \propto T^\alpha$
CeCu _{6-x} Au _x	$x_c = 0.1$	$1/T_0 \ln(T_0/T)$	$T + c$
YbRh ₂ Si ₂	$B_{c\parallel} = 0.66 \text{ T}, B_{c\perp} = 0.07 \text{ T}$		T
YbRh ₂ Si _{2-x} Ge _x	$x_c = 0.1$	$1/T^{1/3} \leftrightarrow 1/T_0 \ln(T_0/T)$	T
YbAgGe	$B_{c\parallel} = 9 \text{ T}, B_{c\perp} = 5 \text{ T}$	$1/T_0 \ln(T_0/T)$	T
CeCoIn ₅	$B_c = 5 \text{ T}$	$1/T_0 \ln(T_0/T)$	$T^{1-1.5}$
CeNi ₂ Ge ₂	$p_c = 0$	$\gamma_0 - \gamma_1\sqrt{T}$	$T^{1.2-1.5}$

tioned above, the central point of quantum criticality is the divergence of temporal and spatial fluctuations at the QCP. These fluctuations can be discussed within Landau's framework of phase transitions in terms of a SDW order, focusing on the fluctuations of the order parameter and adjusting the dimensions to the quantum case. This scenario is commonly known as SDW QCP. Predictions for the temperature dependencies of the resistivity ρ and the specific heat capacity C_p of the SDW QCP model are given in Tab. 2.1. They depend on the dimensionality of the quantum fluctuations (2D or 3D). As all materials of this work order antiferromagnetically, predictions for ferromagnetic QCP's will not be discussed.

Heavy fermion systems are particularly well suited to study quantum critical phenomena. As explained in Sect. 2.1.2, there are two competing interactions: Magnetic order, promoted by the RKKY exchange interaction, and the Kondo interaction. The system can be tuned towards one or the other by changing the parameter $|J|N(E_F)$. Experimentally this is comparatively easy in many heavy fermion systems because it can be achieved by readily accessible magnetic fields, pressures, or small doping levels. Due to these competing interactions, quantum critical behaviour is a fundamental characteristic of these materials.

In the phase diagrams of heavy fermion systems, the ordered phase is usually an-

tiferromagnetic and the QCP occurs at the tuning parameter value where the Néel temperature is typically suppressed to 0 K. From this point, the finite temperature quantum critical region with NFL behaviour emerges.

In various heavy fermion compounds, a superconducting dome is found around the QCP (brown region in Fig. 2.6); including this feature, heavy fermion materials have phase diagrams that share similarities with another highly-studied group of correlated materials, the high- T_C cuprate superconductors. The energy scales in heavy fermion materials, however, are lower by orders of magnitude. The accessible energy scales and the lack of thermal excitations and other features (like phonons) at low energies makes heavy fermion materials suited model systems for strongly correlated and quantum critical materials [36].

The goal of this work was to access the unconventional properties of different materials in their quantum critical region experimentally. Table 2.2 lists some heavy fermion compounds with Yb and Ce magnetic ions and their properties in the NFL region.

2.2.2 T^* line and Kondo breakdown scenario

Whereas the predictions of the SDW QCP model seem to hold for some materials like CeCoIn₅ or CeNi₂Ge₂, strong deviations have been found in other materials [23]. One

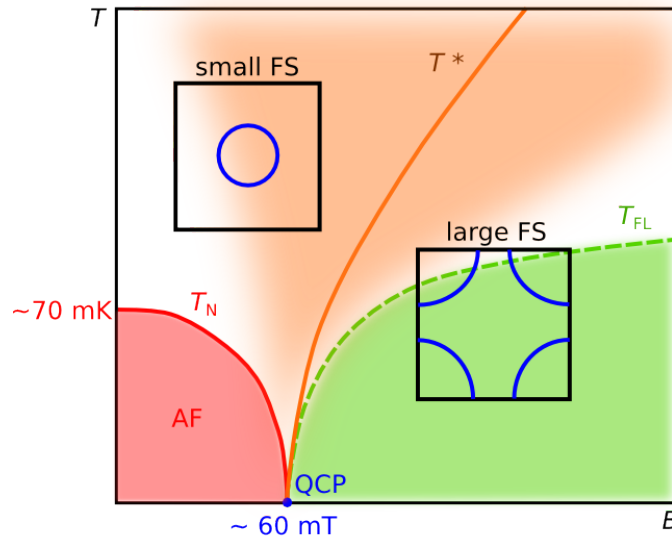


Figure 2.7: Phase diagram with regions of large and small Fermi surface volume of YbRh₂Si₂. The orange tornado-shaped region around the T^* line indicates the width of the crossover in the Hall effect. After data from [43].

particularly interesting example is YbRh₂Si₂, where an additional energy scale was found

in the quantum critical region of the phase diagram, which ends at the QCP. The phase diagram of YbRh_2Si_2 is schematically shown in Fig. 2.7. Across this energy scale, the Hall coefficient, which is a measure for the Fermi volume, shows a crossover with a decreasing width towards lower temperatures that extrapolates to zero at $T = 0\text{ K}$ [44, 43]. Often, the crossover energy is referred to as $k_{\text{B}}T^*$. The Fermi volume thus seems to change abruptly at the QCP. It changes from large in the paramagnetic phase to small (in the antiferromagnetic phase). This finding points to the existence of local discontinuities at the QCP and is referred to as Kondo breakdown scenario or local quantum criticality [9, 45]. The picture in this scenario is that the heavy composite quasiparticles that are stable in the paramagnetic phase suddenly cease to exist and break up into local moments and conduction electrons upon crossing the QCP into the ordered phase at $T = 0\text{ K}$ (Kondo breakdown). An artistic illustration of the Kondo breakdown is shown in Fig. 2.8. Also other physical properties were found to change at the T^* energy scale [46]. This is in contrast to the SDW QCP scenario, where the Kondo interaction is continuously suppressed by the RKKY interaction and the Fermi surface changes only gradually, even at $T = 0\text{ K}$.

The exact nature of the T^* scale is a highly investigated and debated issue. The sudden breakdown of the Kondo screening and its replacement by magnetic order occurs only at absolute zero. The crossover region between the small and large Fermi surface state (orange region surrounding T^* in Fig. 2.7) broadens quickly with temperature, and both large and small Fermi surface characteristics are observed in a large portion of the phase diagram [47]. The effective electron mass is enhanced on both sides of the T^* line and the material shows heavy fermion characteristics.

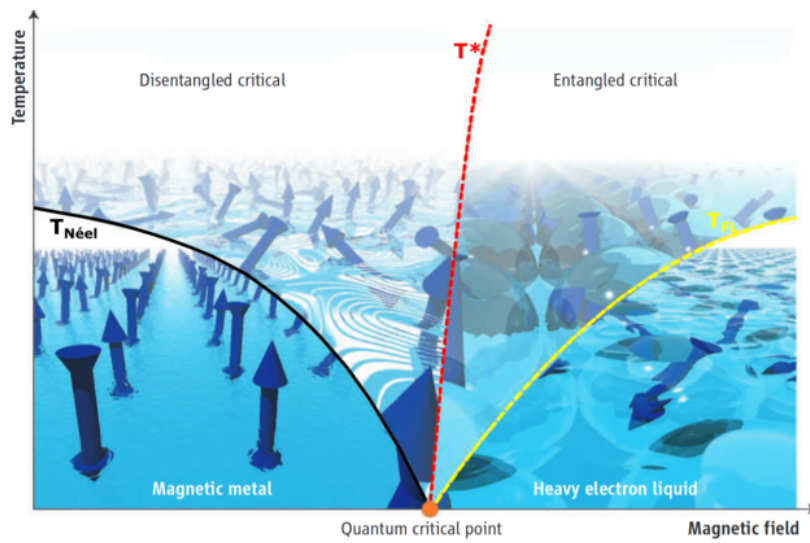


Figure 2.8: Illustration of the Kondo breakdown scenario for YbRh_2Si_2 [48]. Increasing the external magnetic field strengthens the Kondo effect, decreasing the external field drives the system towards magnetic order. The Kondo side of the T^* line is named heavy electron liquid at low temperatures and entangled critical above the crossover temperature to FL behaviour T_{FL} ; the magnetic side is called magnetic metal below the Néel temperature and disentangled critical above it [48]. It should be noted that T^* strongly broadens with temperature and that it can only be represented as a sharp line at zero temperature.

3 Experimental and technical background

3.1 Spectroscopy - ranges and techniques

In spectroscopy experiments, the energy dependence of certain physical properties is resolved by recording the interaction of matter and an energy-tunable excitation. Electromagnetic radiation is often used and can be tuned over many orders of magnitude. Whereas elastic light-matter interactions are the crucial mechanisms in various analysis

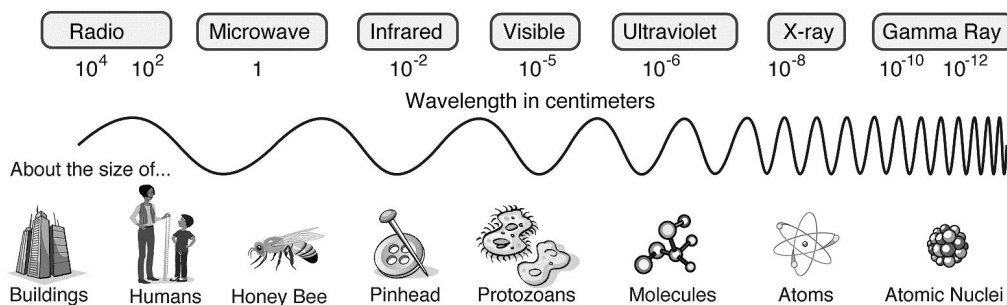


Figure 3.1: The electromagnetic spectrum spans many orders of magnitudes, in both time- and length-scales.

techniques (e.g. diffraction, transmission electron microscopy), spectroscopy can probe inelastic processes with energy transfer between the incident photons and the investigated sample. Therefore, a striking difference to other measurement techniques like quasi dc electrical transport measurements is the possibility to look at a full excitation spectrum of particles or quasiparticles. Different time and energy scales can be addressed by working in different energy regimes. By choosing the appropriate setup, the applied frequency range can vary over many orders of magnitude and therefore spectroscopy can probe a huge variety of processes, ranging from the relaxation of nuclear spins at radio frequencies to the change of energy levels of atoms in the ultraviolet or x-ray frequency ranges (as illustrated in Fig. 3.1).

Although all these interactions of electromagnetic waves and matter are described by the same principles (namely the Maxwell equations in the presence of matter) it is necessary to adapt the vocabulary and experimental techniques to the respective case. In the following subsections the wavelength of the incident wave, λ , will be compared with the length scale of the surrounding laboratory, D . Here, D stands for the order of magnitude of the dimensions of the sample and the experimental apparatus. Two limits can be distinguished in this context:

$\lambda \gg D$: If the wavelength exceeds the size of the circuit components by far, all calculations can be performed on the basis of circuit analysis. Kirchhoff's laws can be applied to a circuit with resistances, capacitances, and inductances as in a direct current scenario. Due to $\lambda \gg D$ we can assign definite phase and amplitude values of the electromagnetic field to each element at any point in time.

$\lambda \ll D$: If the wavelength is much smaller than the elements of the circuit, the situation changes completely. Instead of a constant electromagnetic field we have to take into account that the phase changes over the dimensions of the circuit elements. In this case, an approach using optical terms (lenses, beam splitters, etc.) is used to describe the physics. This holds down to frequencies in the THz range, where the term *quasi-optical* is used [49].

In the case of the frequency range used in this work, an intermediate approach has to be taken, as laboratory scales and wavelengths are of the same order of magnitude. An introduction on how the transmission of microwave signals is treated will be given in the following section.

3.2 Some microwave basics

3.2.1 A short glimpse into microwave transmission line theory

Typical microwave frequencies in the region of 1 GHz to 30 GHz fall into the intermediate region of $\lambda \approx D$. Neither of the two limits can be applied to reduce the complexity of the problem and in principle a full calculation has to be carried out. This fact makes computer-based simulations very attractive for microwave engineering because they are able to locally solve Maxwell's equations without further assumptions. An analytical approach for a more qualitative understanding is made by generalizing Kirchhoff's laws and the lumped element description to a distributed element description. It keeps the conceptual building blocks resistance, capacitance, and inductance, but they are assigned to

the circuit per unit length. The most important quantity of a circuit representation of a conduction line (consisting of inner and outer conductors) is its characteristic impedance

$$Z_0 = \sqrt{\frac{R + i\omega L}{G + i\omega C}} \quad . \quad (3.1)$$

R (in Ω/m) is the resistance, L (in H/m) the inductance, G (in $1/(\Omega\text{m})$) the shunt resistance (e.g. introduced by dielectric loss in the materials separating the conducting lines), and C (in F/m) the capacitance of the line, per unit length. A drawing of a lumped element circuit representation of a transmission line is given in Fig. 3.2.

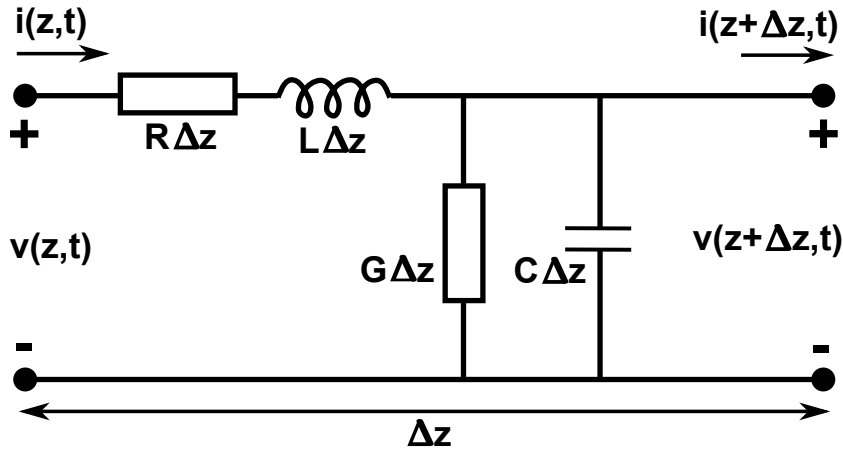


Figure 3.2: Lumped element representation of a piece of transmission line [49]. Δz refers to a small length of the transmission line, $i(z)$ refers to the current flowing through the transmission line at point z .

All quantities are defined by the field values on the transmission line, when integrated over the cross section S between the conductors, or the contours C_1 and C_2 of inner and outer conductors, respectively as

$$L = \frac{\mu}{|I|^2} \int_S \vec{H} \vec{H}^* dl \quad , \quad (3.2)$$

$$C = \frac{\epsilon}{|V|^2} \int_S \vec{E} \vec{E}^* dl \quad , \quad (3.3)$$

$$R = \frac{R_S}{|I|^2} \int_{C_1, C_2} \vec{H} \vec{H}^* dl \quad , \quad \text{and} \quad (3.4)$$

$$G = \frac{\omega \text{Im}(\epsilon_2)}{|V|^2} \int_S \vec{E} \vec{E}^* dl \quad . \quad (3.5)$$

R and G determine the losses of the transmission line. More details on how to calculate these parameters for certain geometries can be found in microwave engineering

textbooks, for instance in [49].

If at some point there is a change in the line impedance from Z_0 to Z_L , this so-called impedance mismatch leads to a partial reflection of the propagating microwave signal and the ratio of incoming and reflected wave voltages is given by

$$\Gamma = \frac{Z_L - Z_0}{Z_L + Z_0} . \quad (3.6)$$

Z_L stands for load impedance and it can be quantified by measuring the reflection coefficient Γ . Along a transmission line, ideally all impedances should match the cable standard (usually 50Ω) because every impedance mismatch at connectors, cable bends, etc. leads to reflections and, consequently, to losses along the line. This is especially important for broadband measurements, where the absorption spectrum in a broad frequency range must be known for bare cabling and sample measurement. To calibrate a broadband reflection measurement, the different standards $Z_L = 0$ (short), $Z_L = \infty$ (open), and $Z_L = 50 \Omega$ (match/load) have to be measured in order to exclude line contributions from a sample measurement. In a lossless system they yield $\Gamma = -1$, $\Gamma = 1$, and $\Gamma = 0$, respectively.

Impedance mismatches can be introduced on purpose to induce partial reflections in the transmission line. By introducing multiple reflection points into a transmission line, resonating structures can be created.

3.2.2 Coaxial lines

All the cabling inside the cryostat and from the cryostat to the vector network analyzer (VNA) is done using coaxial cables. In the microwave regime, the type of transmission line is chosen by the purpose and the requirements of the experiment. Another possible option are waveguides, which are a very efficient way to transport electromagnetic energy. For cryogenic purposes and experiments in the confined space of a cryostat these relatively massive metallic parts (with dimensions of the order of the wavelength) are hard to be implemented and the versatile coaxial transmission lines are used. They support the propagation of a transverse electromagnetic mode (TEM) wave and the upper cut-off frequency is the lowest frequency that allows parasitic transverse electric (TE) modes. Details of the characteristics of coaxial transmission lines can be found in various textbooks [50, 51, 52, 53]. A cross section of the field distribution of a coaxial cable is shown in Fig. 3.3. The applicable frequency range of a cable is determined by the dimensions of the cable; smaller cables allow higher frequencies but have higher

losses and do not support high input powers. The characteristic impedance Z_0 depends on the ratio of inner and outer conductor radii (r_{inner} and r_{outer} , respectively) as

$$Z_0 = \frac{60}{\sqrt{\epsilon_r}} \ln \frac{r_{\text{outer}}}{r_{\text{inner}}} . \quad (3.7)$$

ϵ_r is the effective dielectric constant of the wave-transmitting medium. The material of cryogenic coaxial cables is crucial for the purpose as well. Required frequency and temperature ranges, losses, thermal transport aspects, and calibration issues have to be considered.

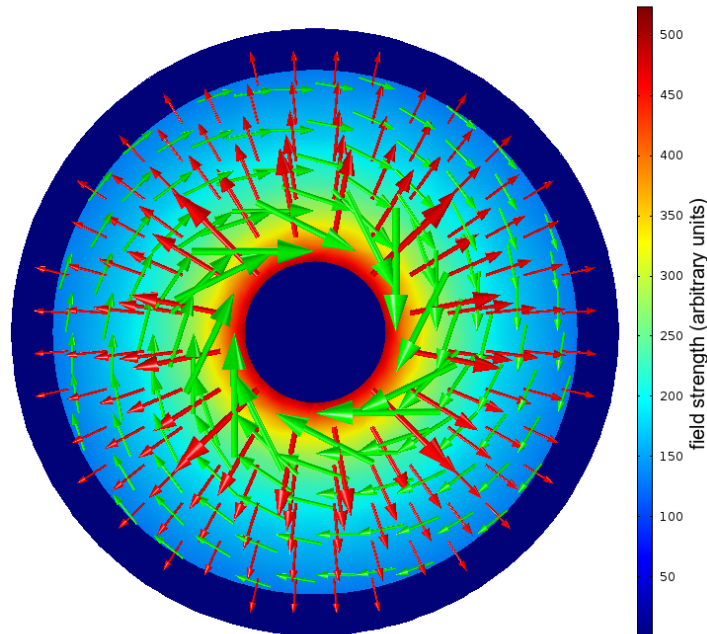


Figure 3.3: Finite element simulation of electrical (red arrows) and magnetic (green arrows) field directions and field strength (length of arrows) of a coaxial cable with the dimensions of the used UT085 cables ($r_{\text{outer}} = 2.20 \text{ mm}$ ($\approx 0.85 \text{ in}$), $r_{\text{inner}} = 0.51 \text{ mm}$) at a frequency of 2.7 GHz. The arrows correspond to the values at the position of their tails. The colour coding represents the local field strength (in arbitrary units). The metallic inner and outer conductors are field-free and therefore blue. The electric field is distributed in the dielectric in between the conductors.

3.2.3 Coplanar waveguides

The idea of coplanar transmission lines was proposed in 1969 [54]. They differ from other common transmission line geometries (like microstrip or stripline) by the fact

that all the metalization is located in a single plane. This makes the fabrication process simpler, because only one face of the substrate has to be coated and structured. Also, the substrate thickness does not affect the design properties strongly and can be chosen more freely than for other transmission line types. Two ground planes are separated by the

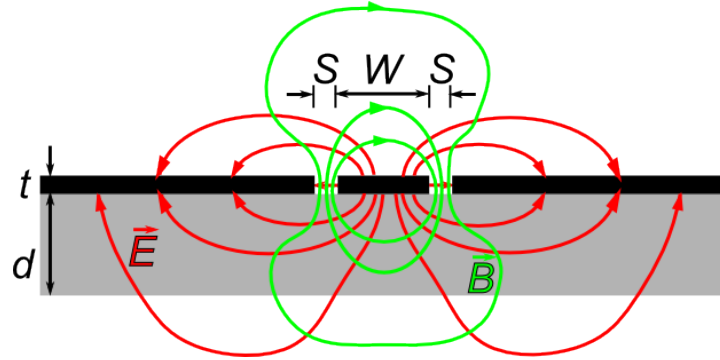


Figure 3.4: Field distribution of electric and magnetic fields (\vec{E} and \vec{B} , respectively) and relevant dimensions of a coplanar transmission line. W is the center conductor width, S the width of the two gaps between center conductor and ground planes, t is the film thickness of the metallic thin film, and d the substrate thickness.

center conductor of width W by symmetric gaps of width S . The line impedance depends on the ratio of W and S . Design parameters and characteristics can be found in textbook literature [50, 51, 52, 53]. A cross section of a coplanar transmission line is shown in Fig. 3.4. The incident wave travels perpendicular to the paper plane and is of quasi-TEM type: In contrast to a TEM wave, which does not have any field components along the propagation direction of the wave, a quasi-TEM wave has small field components. As they are considerably smaller than the perpendicular components, they can be neglected in most cases and many aspects can be approximated well with a mathematical TEM approach. Other reasonable approximations for analytical calculations are to assume infinite ground planes, an infinite substrate thickness, and a vanishing metalization thickness (see also Sect. 5.1.2). Loss channels in CPWs result from finite conductivity of the metalization, losses in the substrate (expressed in the loss tangent of a substrate $\tan \delta = \Im(\epsilon)/\Re(\epsilon)$, ϵ being the complex permittivity of the substrate, and $\Im(\epsilon)$ and $\Re(\epsilon)$ the imaginary and the real part of ϵ , respectively), and radiation losses [52].

3.2.4 Vector network analyzer

The vector network analyzer (VNA) is the main measurement device in the performed microwave experiments. An example of a Rohde&Schwarz ZVA67 is shown in Fig. 3.5. It

contains a tunable generator for microwave radiation: In the case of the Rohde&Schwarz ZVA67 (associated with the setup in the Vienna laboratory) the accessible frequency range is 10 MHz to 67 GHz, in the case of the Rohde&Schwarz ZVA24 (associated with the Garching laboratory) the accessible frequency range is 10 MHz to 24 GHz. The signal can be gripped at the VNA's ports (two or four ports are available, depending on the model) by connecting a suitable waveguide. The microwave standard for cables, connectors, adaptors, and attenuators is 1.85 mm (sometimes also called V-type) in the Vienna demagnetization refrigerator and Subminiature type A (SMA) in the Garching dilution refrigerator (see Secs. 3.3.2 and 3.3.3, respectively). Every source port also has the function of a detector, so that all S parameters S_{11} , S_{12} , ..., S_{34} , S_{44} can be measured with a four-port VNA. A VNA can measure the intensity and the phase of the incoming signal, so that the S parameter is in fact a complex entity $S_{ij} = \Re(S_{ij}) + i\Im(S_{ij})$ and represents the amplitude ratio and phase difference of the outgoing wave at port j and the incident wave at port i . Most of the time we use the terminologies S_{11} and S_{22} for reflection and S_{12} and S_{21} for transmission measurements and refer to the magnitudes of the complex observables, $\sqrt{\Re(S_{ij})^2 + \Im(S_{ij})^2}$. Referring to Eqn. 3.6, a measurement of S_{11} and S_{22} corresponds to a measurement of the reflection coefficient Γ at VNA ports 1 and 2, respectively. In the used frequency range, the reactance, i.e. the imaginary part of the impedance of the measured quantities, can sometimes not be neglected. Therefore it is crucial that a VNA can measure both real and imaginary parts of the microwave signal. The electronics needed for precise high-frequency measurements in such a broad frequency range are highly complex and will not be described here in detail. Further information on VNAs can be found in the respective specialized literature [55].

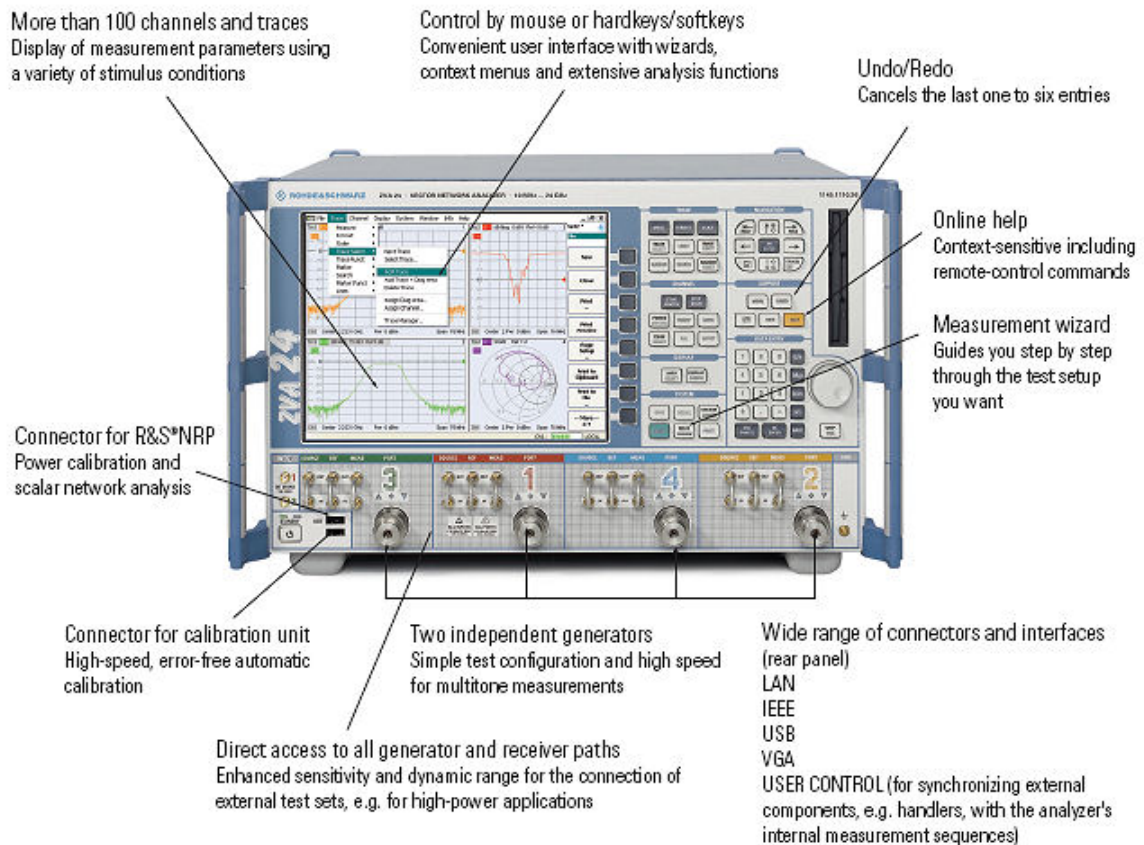


Figure 3.5: Rohde&Schwarz ZVA67 network analyzer with the most important specifications (as presented on the rohde-schwarz.us website).

3.3 Setups and techniques

One major challenge when studying low energy scales is that all parameters and external disturbances have to be very low in energy. For instance, setting the temperature of the environment to a low value also sets upper limits to all ingoing energies like read-out currents or probe beams (at least if the goal is to work under equilibrium conditions). These limitations can lead to an increased noise level and a poor signal-to-noise ratio, so that, for instance, more time has to be invested into the averaging of measurement points, or special care has to be taken when screening the feed lines etc. Also, the use of additional auxiliary instruments like cryogenic transformers or other special equipment can be helpful.

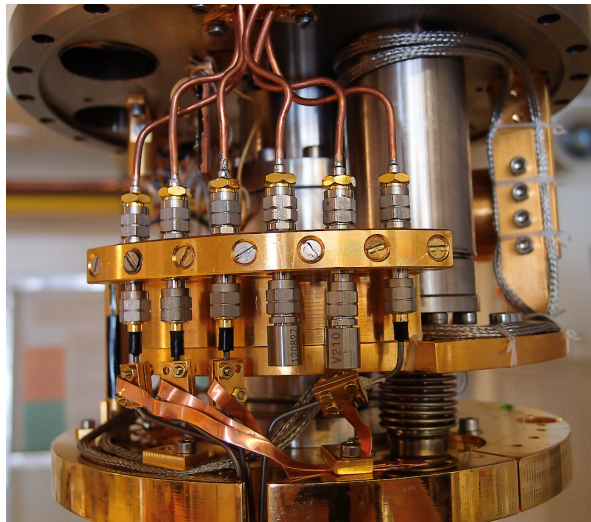


Figure 3.6: Thermal anchoring of microwave lines to the 4 K stage in the Vienna dilution refrigerator. Cu lines reach to the stage from the top; they are connected to attenuators and therefore inner and outer conductors are thermally linked and coupled to the 4 K plate. On the lower side, superconducting NbTi coaxial cables continue to the experiment. In their superconducting state, they do essentially not conduct heat and therefore they thermally decouple the lower parts of the experiment from the top.

One example of special technical solutions for experiments at low temperatures is the coupling of microwave coaxial cables to the different temperature stages of a dilution refrigerator. As the lines have to transport the signal out of the cryostat (to room temperature) eventually, there is always a thermal link to the laboratory environment. To prevent this heat load from reaching the experiment and from increasing its temperature, the cables have to be linked to the different thermal baths on the way to the experimental space inside the cryostat. This thermal anchoring of a set of microwave

attenuators can be seen in Fig. 3.6. In the following subsections, a short overview of the different low-temperature setups and of the applied measurement principles is given.

3.3.1 Oxford Kelvinox 400 dilution refrigerator

Many of the electronic transport properties that are presented in this work were measured in a commercially available dilution refrigerator, manufactured by Oxford Instruments. $^3\text{He}/^4\text{He}$ dilution refrigerators have been available since the mid-1960s [56] and their working principle can be found in textbook literature [57, 58]. The model that was used here is a Kelvinox 400, which provides a cooling power of $400\ \mu\text{W}$ at 100 mK on the mixing chamber. This cryostat typically reaches base temperatures of 20 mK to 30 mK at the mixing chamber.

It is equipped with a 15 T magnet, and several physical properties are investigated there on a regular basis: Resistivity, magnetoresistance, Hall effect, thermal conductivity, as well as Seebeck and Nernst effect. More details on the specifications of the system, such as the thermometry, accompanying devices, and measurement techniques that were not used in this work can be found elsewhere [59, 60, 61].

3.3.2 Vienna nuclear demagnetization refrigerator

As mentioned in Sect. 2.1.3, the study of FL/NFL behaviour and quantum criticality requires experiments at very low energy scales, and therefore adequate temperatures. If the goal is to excite the samples' electronic system by low-energy electromagnetic excitations, the thermal background has to be of similar or even lower energy. The lower the thermal background, the more relevant the effect of the microwave energy. From a technical point of view, a microwave signal will always introduce heat to the experimental setup, so that a cryostat has to provide the necessary cooling power. Therefore, an infrastructure consisting of microwave cables and attenuators has been installed into the powerful Vienna demagnetization refrigerator. The used coaxial lines are suited for microwave frequencies up to 65 GHz. Semi-rigid coaxial cables (SC-219/50-C-TU-L) were installed from room temperature down to the still plate. These Cu cables are thermally linked to the thermalisation stage by attenuators (see Fig. 3.6). From the still to the mixing chamber, superconducting semi-rigid NbTi coaxial lines (SC-160/50-NbTi-NbTi) were installed. In the superconducting state, they decouple the cold stages from the top of the cryostat and prevent unwanted heat input. The disadvantage of superconducting cables is that proper testing has to be performed in the superconducting state and can

thus not be done at room temperature before closing the cryostat.

The inset of the refrigerator is shown in Fig. 3.7 (further details about the cryostat are available in [62]), and a picture of the mixing chamber with the attached microwave resonators and microwave coaxial cables is shown in Fig. 3.8 (left). A closer view of a cold finger with two attached Cu boxes containing CPW microwave resonators is shown in Fig. 3.8 (right).

All microwave experiments were performed at mixing chamber temperatures. The mixing chamber plate has a diameter of 180 mm and provides enough space for several experiments. The mixing chamber can reach a base temperature of 3 mK. Despite the use of superconducting cables, attenuators, and thermal links at every cooling stage, the demagnetization stage is not used for microwave measurements because of the heat input due to the applied microwave power. Otherwise, the input power would have to be limited to very low values. In the desired type of experiment, however, a certain input power is needed in order to have a sufficient amount of microwave photons inside the resonator.

The accessed temperature range for microwave measurements is therefore higher than the temperature range for transport measurements. In the case of transport measurements not involving any electromagnetic excitation, it is possible to go to the lowest temperatures for the study of quantum criticality (see Sect. 5.2.2). The nature of quantum critical matter and the signatures of quantum criticality become more and more apparent the closer the experiment is to the QCP. Therefore, measurements at ultra-low temperatures are of great interest.

As part of this thesis, several samples were prepared for transport measurements in the Vienna nuclear demagnetization refrigerator, which is able to reach temperatures down to well below $100 \mu\text{K}$, if the demagnetization stage is used. More details on the samples and their preparation are found in Sec. 5.2.2. Apart from sample preparation, test measurements of low-temperature technology for the Vienna nuclear demagnetization cryostat were carried out, for example performance tests of various self-made noise filters (filtering high-frequency noise in the measurement lines). The frequency-dependent transmission of several of these filters is shown in Fig. 3.9. By measuring the transmission at room temperature and in liquid He it was ensured that they keep functioning at cryogenic temperatures. The two different filter materials (a commercial thermal coaxial cable and an ECCOSORB material by Emerson and Cuming MW Products) show distinct differences at room temperature, but are more similar at 4 K. The thermal coaxial cable starts at a lower transmission at the lowest frequencies, but

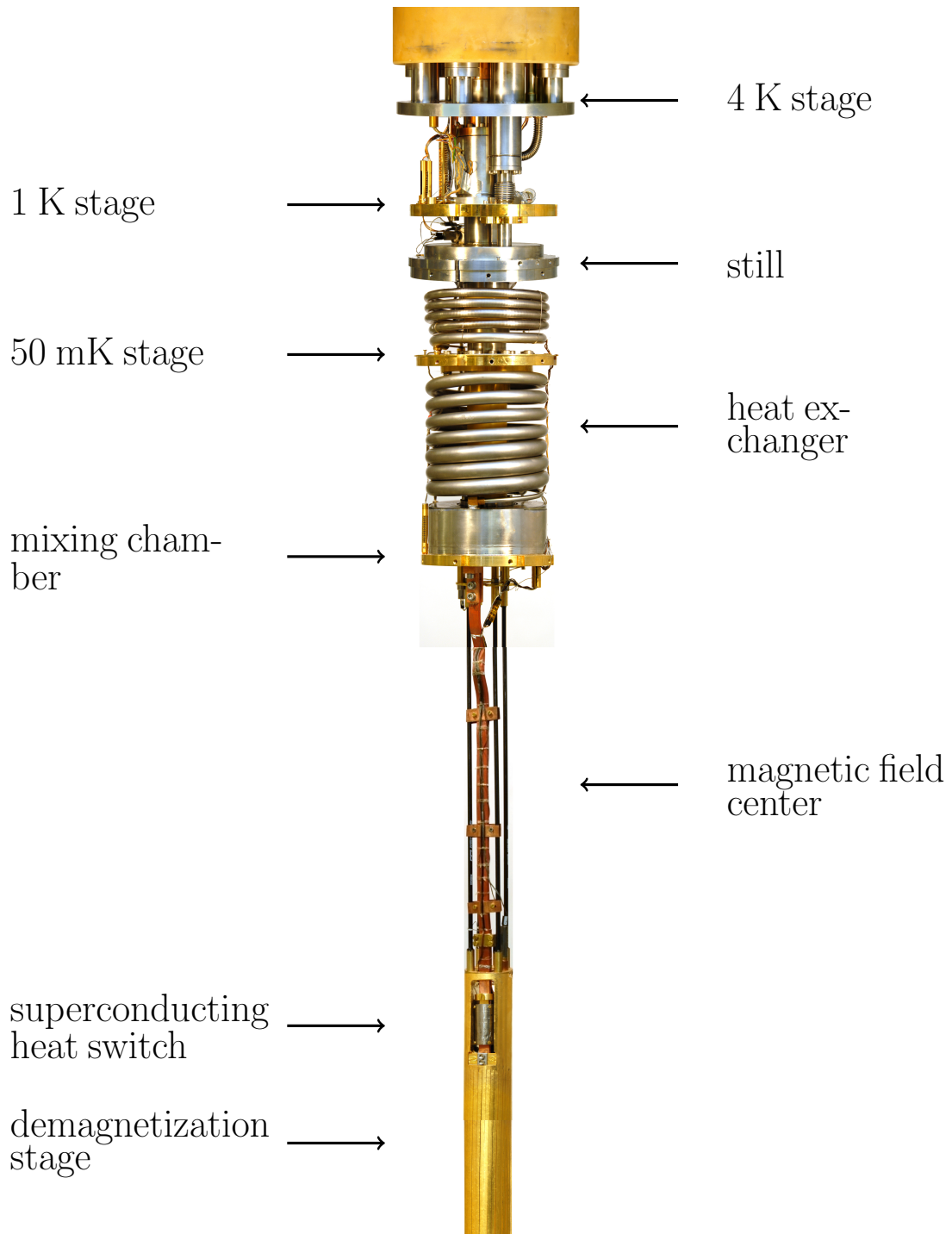


Figure 3.7: Picture of the Vienna nuclear demagnetization cryostat following the description in [62].

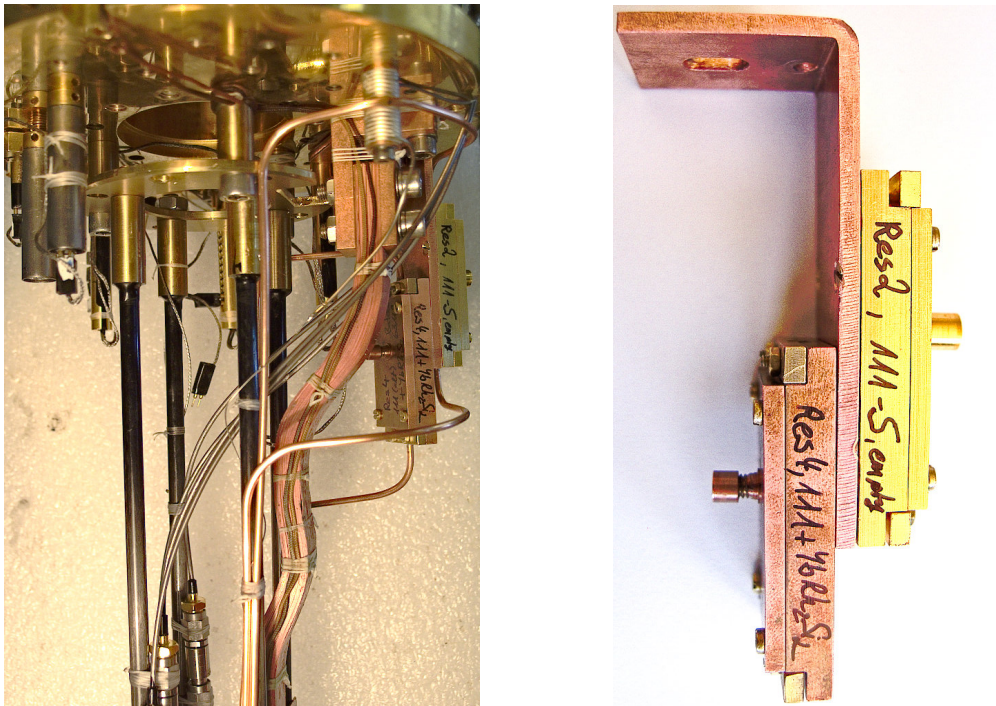


Figure 3.8: *Left:* Close-up view of the mixing chamber of the Vienna demagnetization refrigerator with two microwave resonator boxes. *Right:* Side view of resonator boxes, mounted on a cold finger for the mixing chamber of the Vienna demagnetization refrigerator.

has a flatter decrease with frequency. In both materials, the transmission through the filters is strongly reduced with increasing frequency, thereby reducing effects of the noise signal. All filters apart from the filter labeled ThCoax7 can be used for measurements. ThCoax7 seems to have a randomly different frequency dependence and it was discarded as a consequence.

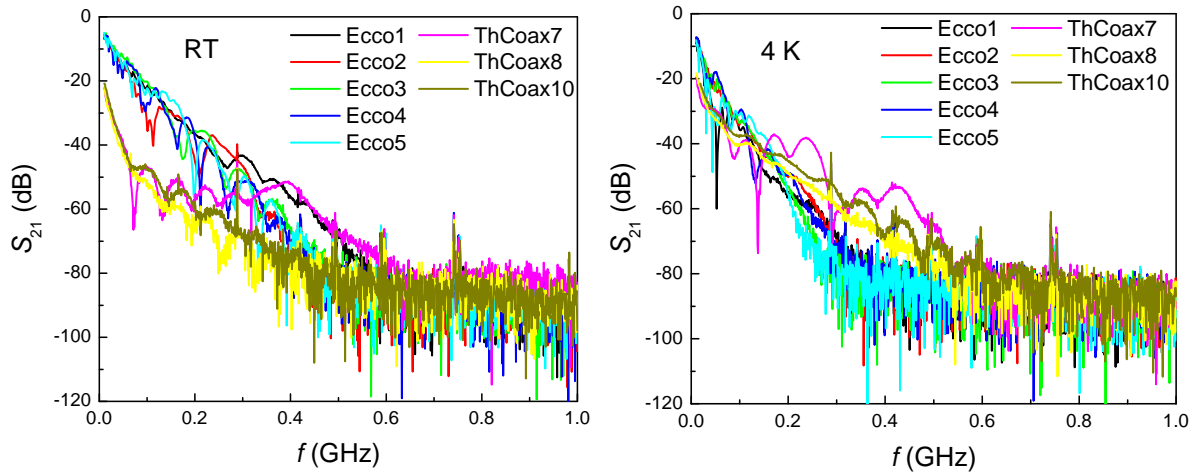


Figure 3.9: Frequency dependence of the microwave transmission of different noise filters at room temperature (*left*) and at ^4He temperature (*right*).

A 4 T to 8 T vector magnet system is part of the Vienna nuclear demagnetization cryostat and provides the required external tuning parameter to the investigated quantum critical materials. If the application of field is desired, the samples have to be placed into the central sample space with homogeneous magnetic field. The available volume roughly corresponds to a sphere of 1 to 1.5 cm radius. Experiments which are thermally coupled to the mixing chamber (like the microwave experiments) access the field center from above, whereas experiments which are coupled to the nuclear demagnetization stage (like electronic transport experiments) access the field center from below.

3.3.3 Garching microwave setup

Because of limited availability of the Vienna nuclear demagnetization refrigerator for microwave experiments, which was used during long periods for measurements at ultra-low temperatures, microwave measurements on YbRh_2Si_2 were partially performed in a setup at the Walther-Meissner-Institute in Garching, under the supervision of H. Huebl, and with measurement support by F. Wulschner. The cryostat is a self-built small dilution refrigerator of Joule-Thomson type, where the mixture is not cooled by a 1 K pot

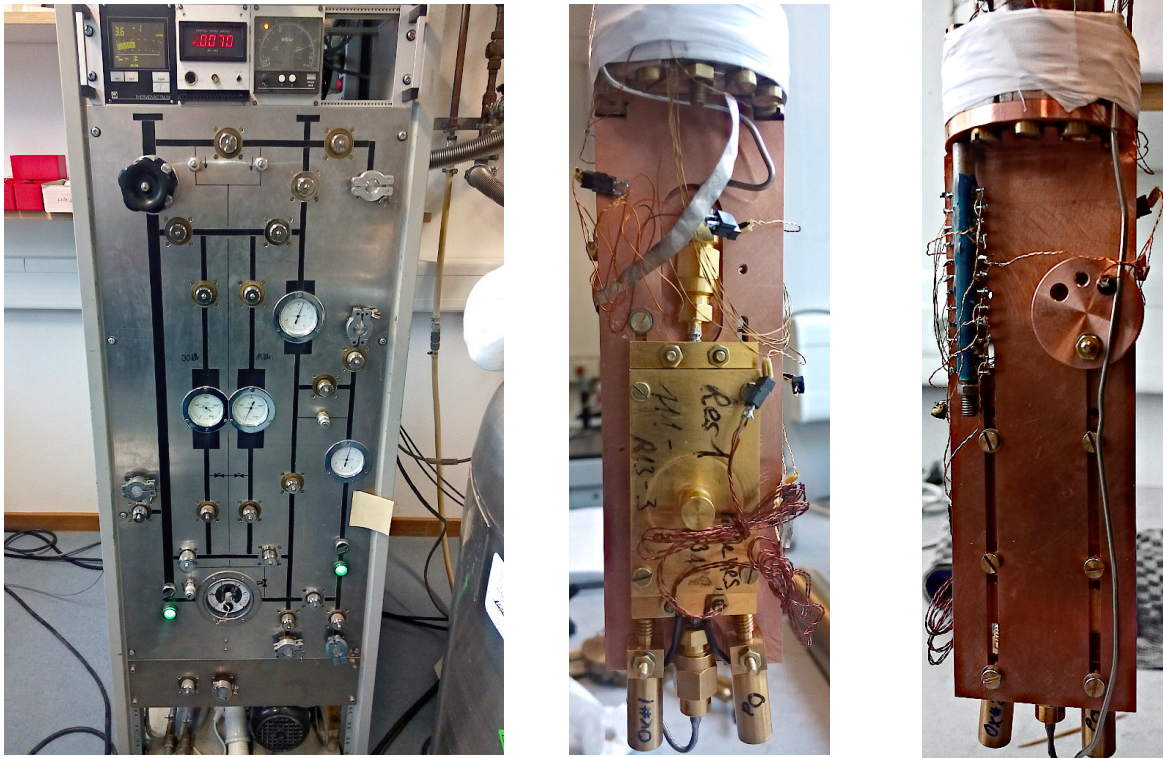


Figure 3.10: Left: Gas handling system of the dilution refrigerator in Garching, which was used for a large part of the performed microwave experiments. Center: Box with sample and resonator (inside, not visible) on the coldfinger that was designed for this cryostat. Right: Back side of the coldfinger with a temperature sensor.

(as in the Kelvinox400 of Sect. 3.3.1), but by expansion of the mixture after guiding it through an impedance with high pressure. The gas handling system is shown in Fig. 3.10 (left). The mixing chamber has a diameter of 35 mm. A cold finger was designed to fit the Cu boxes with the CPW together with sensors and wiring and optionally a cryogenic transformer. Front and backside views of the cold finger with a mounted CPW resonator box are given in Fig. 3.10 (center) and Fig. 3.10 (right). Two microwave stainless steel cables (Cu coated inner conductor, Huber+Suhner Cobra flex) are installed in the cryostat down to the 4K stage. From 4K to the mixing chamber, there are superconducting continuations (Nb inner conductor, Ti-Ni outer conductor, SC-119/50-Nb-CN, Coax Japan). There are two 3dB attenuators on the way down. The standard of all connectors and other microwave parts is SMA. The advantage of this cryostat is its short cycling time scale. Installing an experiment, cooling down, and condensing the mixture is in principle possible in one day, recovering the mixture and warming up in half a day. Also the ^4He consumption is low compared to bigger systems (especially compared to the Vienna nuclear demagnetization refrigerator). The time-efficiency of

the Garching system proved to be especially important for testing and optimizing of new measurement designs. For instance, the sample position could be optimized within a reasonable time. For this setup, a room temperature amplifier, the Agile AMT-A0019 for a frequency range of 2 GHz to 8 GHz, was available.

3.3.4 Resistance, magnetoresistance, and Hall effect measurements

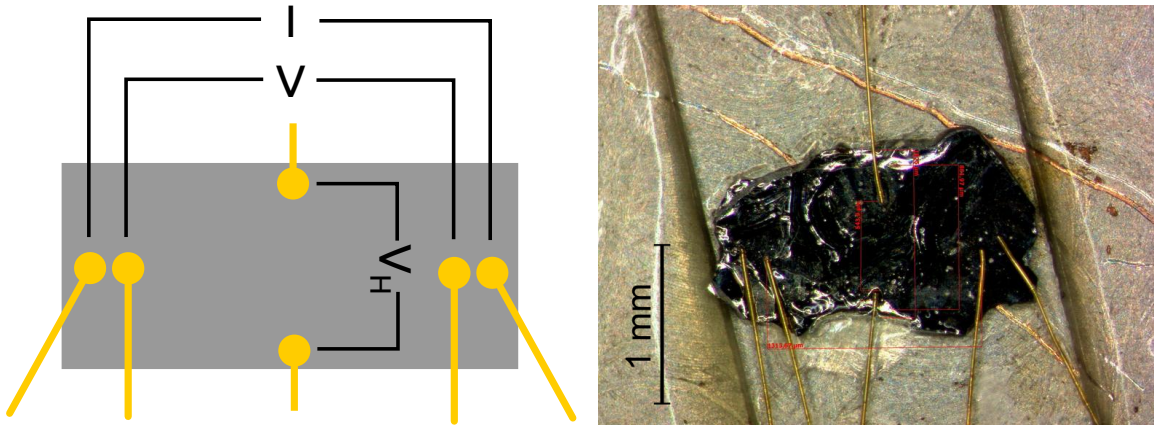


Figure 3.11: *Left:* Schematic drawing of a sample, contacted for resistivity and Hall effect measurements. *Right:* Example of a contacted YbRh_2Si_2 sample, fixed on a thin sapphire piece with grease.

Concerning electronic transport properties, mainly the resistance and for some samples the Hall resistance were measured down to low temperatures. The electrical resistivity of a material reveals information on its scattering mechanisms and their evolution with temperature. These measurements are performed using a four-point geometry with current and voltage contacts arranged as shown in Fig. 3.11 (left). Resistances of good metals at low temperatures are very low, in the $\text{m}\Omega$ or even $\mu\Omega$ range. Low contact resistances are crucial to avoid self-heating effects of the sample and noise in the measured signal. At higher temperatures and resistances, contacts with silver paste, silver epoxy, or even mechanical pressure are often sufficient. For the samples and temperatures of interest in this work, however, spot-welded contacts usually have to be applied. The material for the leads is $25\ \mu\text{m}$ or $50\ \mu\text{m}$ gold wire, depending on the size and thickness of the sample. For mechanical stability, the spot-welded contacts may be covered by a tiny drop of silver epoxy. This prevents the gold wires from moving or possibly breaking the contact, and is useful especially if the samples have to travel or move between different measurement setups. If possible, the sample surface is cleaned and polished before contacting to improve the contact quality (i.e. decrease the contact resistance).

The contact resistance usually is in the $5\text{ m}\Omega$ to $15\text{ m}\Omega$ range at room temperature and decreases with temperature. A resistivity measurement including a contact resistance of a sample is shown in Fig. 3.12 (left). In some cases, the samples can also be quite

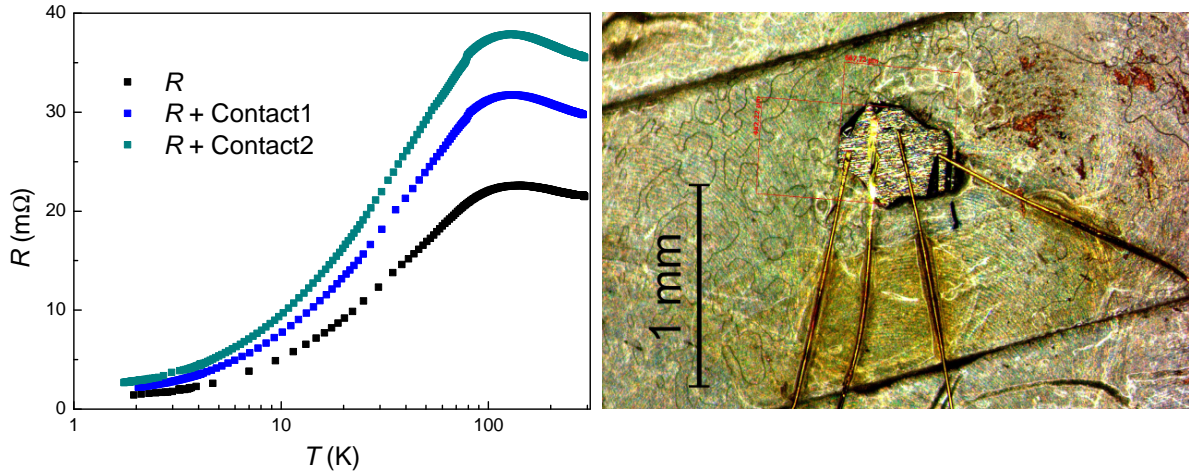


Figure 3.12: *Left:* Temperature-dependent resistance, without contact resistances and with two different contact resistances, of an YbRh_2Si_2 test sample. *Right:* Small YbRh_2Si_2 single crystal sample with dimensions below 1 mm times. 1 mm, contacted with four wires for resistivity measurements.

small (some YbRh_2Si_2 samples had a surface of less than $1\text{ mm} \times 1\text{ mm}$ for contacting), which makes contacting difficult. Then the exact location of the contacts can differ significantly from the ideal one (see comparison of Fig. 3.11 (left) and the actual contacted samples in Figs. 3.11 (right) and Fig. 3.12 (right)). On very small samples there may not be enough space for Hall contacts. An example of a small YbRh_2Si_2 sample with four contacts only is shown in Fig. 3.12 (right).

The signal is read out by a Linear Research LR700 resistance bridge using a standard four-probe ac technique (for details on the resistance bridge see [63]). The applied voltage excitation has to be chosen carefully to avoid heating of the sample due to the probing current. The voltage and/or Hall voltage signals of the measurement can be amplified using cryogenic transformers. They increase the signal considerably (by factors between 30 and 1000, depending on the sample resistance) and their use is of advantage when the measured absolute resistances is low; the applied power can be reduced and therefore the heat load on the samples is decreased, thus avoiding self heating more efficiently without losing measurement accuracy. Between the sample platform and the transformers, superconducting leads transmit the signal to avoid any heat load from the measurement lines.

3.3.5 Specific heat measurements

The specific heat capacity of a material is the ratio of a change in heat and the corresponding temperature difference, per unit mass, and reflects its ability to store thermal energy. It is the sum of different contributions from electrons, phonons, etc., and is directly connected to the internal degrees of freedom and the entropy of the system. In metals that show FL behaviour at low temperatures it includes an electronic term that is linear in temperature and a phononic term that is cubic in temperature (see Sect. 2.1.3). At the lowest temperatures the electronic part is dominant and reveals important information on the material, for instance the effective electron mass.

For some of the investigated materials, the specific heat was measured in a Physical Property Measurement System (PPMS), manufactured by Quantum Design. Details about the specific heat measurement procedure in combination with the use of the ^3He unit for temperatures down to 350 mK can be found in the manual [64].

A schematic drawing of the PPMS sample holder for specific heat measurements is shown in Fig. 3.13. Through the heater, the measurement system applies a defined amount of energy to the central platform. A thermometer on the platform monitors the temperature. The only thermal contact between the sample platform and the thermal bath is established by thin wires (which simultaneously serve as electrical leads). With this configuration the thermal relaxation to the bath temperature is sufficiently slow and reproducible. Everything has to take place in good vacuum in order to minimize the contribution of exchange gas to the thermal conduction.

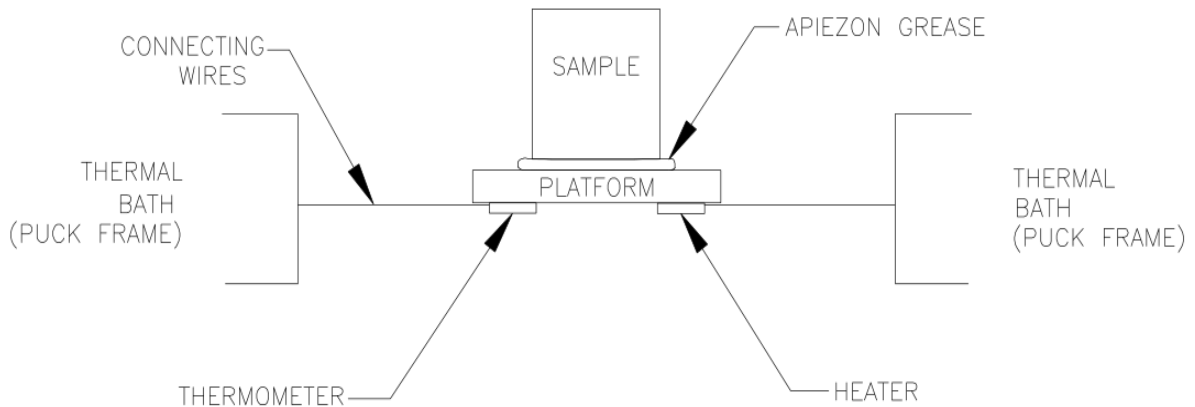


Figure 3.13: Scheme for specific heat measurements [64]

A measurement cycle consists of a heating and a thermal relaxation period, the time evolution of the system temperature is then fit by a model to obtain the value of the heat capacity at the respective temperature.

3.3.6 Possible experimental approaches for microwave measurements

Once the frequency range and the desired energy scale is set, a choice concerning the experimental technique has to be made. Thoroughly evaluating different future setups was an important process in the beginning of this work. Therefore the different options with their main advantages and disadvantages will be briefly summarized. They can be divided into three subgroups: One option is to focus on the effect of microwave radiation on the resistivity, using the microwaves as an excitation energy without evaluating the microwave signal itself. Another option is to probe the properties of the material in a broad frequency range by evaluating the microwave response after an interaction with the sample. A third possibility is to use resonant techniques, and to evaluate the microwave response at certain frequency points.

These three approaches will now be briefly discussed, followed by a more detailed description of the experiment that was set up after reviewing the different options.

Radiation induced resistivity measurement

As stated in Sect. 2.2.2, the T^* energy scale found in YbRh_2Si_2 suggests a breakdown of the Kondo effect at the QCP. According to the Kondo breakdown scenario, the quasiparticles have different natures on the two sides of the energy scale: On one side (low magnetic fields, antiferromagnetically ordered ground state), the conduction electrons are decoupled from the local moments. On the other side (high magnetic fields, paramagnetic ground state), they form composite quasiparticles with the local moments. At finite temperatures, both quasiparticles and decoupled conduction electrons and magnetic ions are present in a crossover region (see also Fig. 2.7). An interesting question is if it is possible to influence this state by providing electromagnetic energy. If the quasiparticles can be excited and broken up by microwaves, it should be possible to observe an effect in various physical properties (such as the dc resistivity). This would be a very direct proof of the nature of the T^* line. However, there are several challenges: In order to excite a relevant fraction of the available quasiparticles, the number of photons, i.e. the microwave power, should be sufficiently high. Otherwise, the measured transport property will be dominated by the not-excited majority of quasiparticles, and no change would be detected. The applicable power to the sample and thus the available number of exciting photons is, however, limited by the resulting heating effects, and if the temperature is not stable, thermal and electromagnetic effects cannot be separated

properly. Furthermore, the excitation energy is only applied to the part of a bulk sample between the surface and the skin depth. For microwave frequencies, the skin depth $\delta = \sqrt{2/(\omega\sigma\mu)}$ (ω : angular frequency, σ : conductivity, $\mu = \mu_r\mu_0$: permeability) is in the region of a few μm . It has to be taken into account that the probed physical quantity is only strongly affected by the microwave radiation within this part of the sample; if the total sample thickness is around $100\ \mu\text{m}$, the contribution of the portion within the skin depth to the total resistivity will be only 1% and may lie inside the error margin.

If the effect of a radiation-induced process should be detectable, also the relaxation time of the investigated process is crucial. The relaxation times scale with the quasiparticle mass, and for heavy fermion compounds they are shifted to the microwave region instead of the infrared region for normal metals. This is seen for instance in the slow Drude roll-off [65]. However, without additional information on time scales and relaxation processes (for instance from optical conductivity data in the microwave range with information on the scattering rate), the interpretation of experiments can be ambiguous.

Broadband measurement

In order to characterize the excitations of the investigated sample to a high extent, obtaining information on the frequency-dependent properties is desirable. At every point of the phase diagram, the complex impedance of the sample $Z = R_S + iX_S$ (R_S : surface resistance, X_S : surface reactance) can be evaluated with spectroscopic methods in the microwave range. If a broadband measurement technique can be applied, the changes of the optical properties can be quasi-continuously traced with frequency along the electromagnetic energy scale.

One suitable broadband configuration for solid state materials and cryogenic temperatures is the Corbino geometry [66, 67, 68], where the sample is used as the termination of a coaxial line. The reflection S_{11} off the sample is connected to the impedance of the sample Z_L by Eqn. 3.6,

$$S_{11} = \frac{Z_L - Z_0}{Z_L + Z_0} \quad .$$

Z_0 is the characteristic impedance of the line. In most cases a standard value of $Z_0 = 50\ \Omega$ is used. For metallic thin film samples with a thickness considerably lower than the skin depth (typically in the range of a few μm for GHz frequencies), the impedance is connected to the complex conductivity via

$$Z = \frac{\ln(b/a)}{2\pi d\sigma} \quad . \quad (3.8)$$

a and b are the diameters of the inner and outer conductor for a circular termination, σ the complex conductivity, and d the thickness of the film. The difficult part is the exact determination of the real reflection caused by the sample, because the measured reflection coefficient includes contributions from transmission lines, contact resistances, and other possible sources. This is overcome by special calibration procedures [55, 66, 69]. A measurement configuration like the Corbino one yields quantitative information, but calls for sophisticated calibration procedures and, as a consequence, cooling and cable testing conditions have to be tailored to the experiment. It was not feasible to install a setup for microwave broadband measurements in the Vienna nuclear demagnetization refrigerator during the course of this work, because the installation of ultra-low temperature experiments was also ongoing and the available time for thermal cycling and line testing was limited. Additionally, thin film samples would have been needed and were not available. The preparation of YbRh_2Si_2 thin films by molecular beam epitaxy is in progress and will provide a strong motivation for setting up a broadband microwave experiment.

One can think of less sophisticated broadband approaches that content with the determination of relative conductivity changes. The simplest configuration would be to couple a sample to a simple CPW, stripline, or microstrip through line. The different configurations and field distributions of these frequently-used types of transmission lines are shown in Fig. 3.14. However, due to the small size of a single-crystalline sample (order of mm) compared to the total length of the microwave lines (order of m, connecting from the VNA into a cryostat), the effect of the sample properties on the total transmission will be negligible.

A slightly different configuration integrates the sample into a microwave transmission line, for instance making it a bridge connecting two otherwise disconnected transmission lines. The transmission in this arrangement depends more strongly on the sample impedance than in the previous case of electromagnetic coupling between a continuous line and a sample, but to account for the feed lines, a reference bridge has to be used for calibration. This is likely to cause large uncertainties in the measurement, because exact shapes, differing contact resistances and surface characteristics of the sample and the reference have a strong influence on the result. Eventually, all broadband techniques run into the issue of calibration, even if the basic concept is less sophisticated than that of the Corbino technique.

3 Experimental and technical background

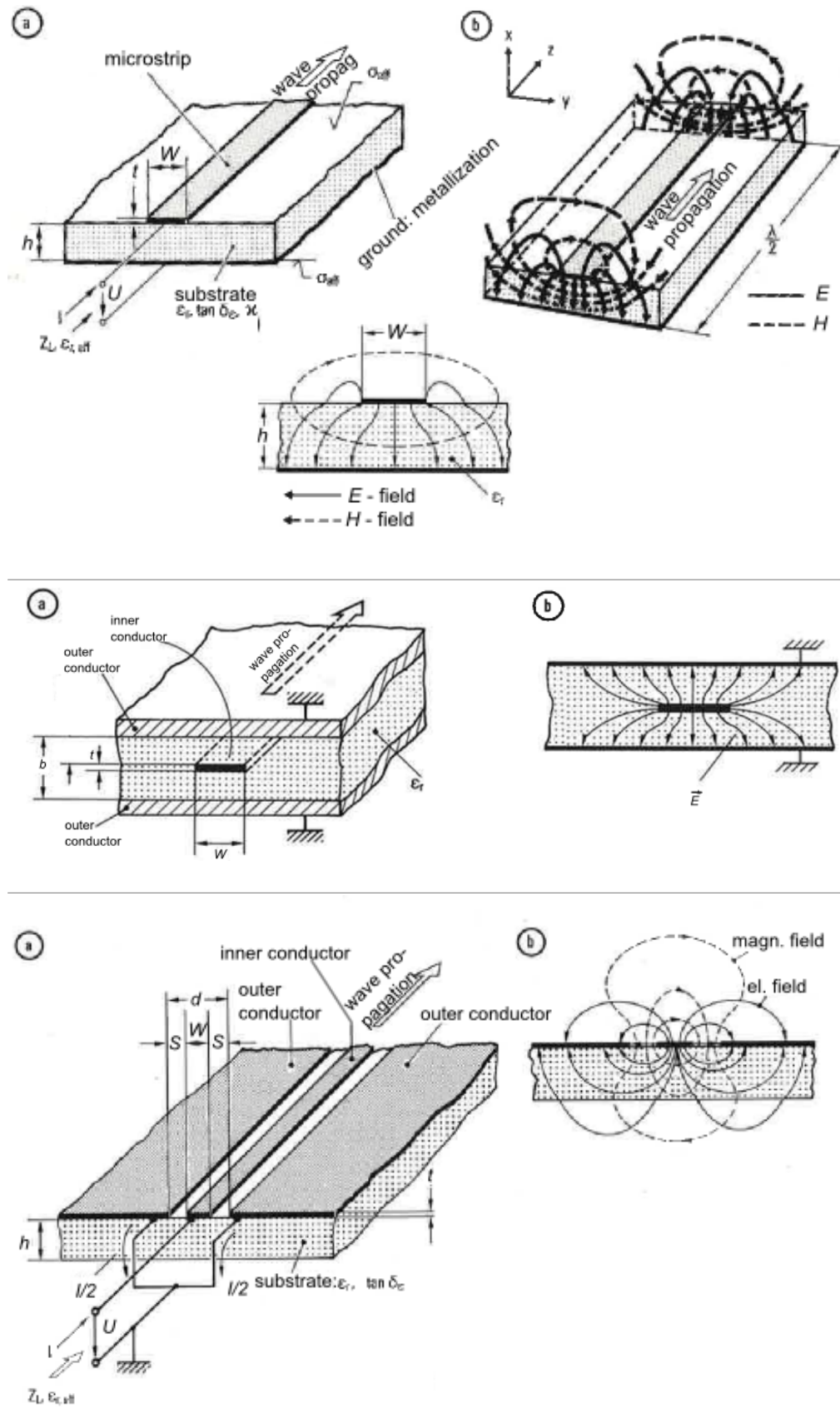


Figure 3.14: Geometries and field distributions of different microwave transmission lines [53].
 Top: Microstrip line. Center: Stripline. Bottom: CPW.

Resonant measurement

Calibration issues can be avoided if resonant methods are applied. A resonant measurement is performed in a narrow frequency band where the signal is very strong. The response at this particular point is very strong, but in order to obtain a response at another frequency, the experiment has to be changed (for instance by using a different resonator). Resonators are preferred in cases where only a specific frequency is needed, for instance as an excitation of a two-level system. For some resonator geometries, higher harmonics of the fundamental frequency are also used, and several discrete frequency points can be accessed.

One option for a resonant measurement is to use cavity resonators. They have a well-known working principle and most technical details are well established [49, 70]. Samples can be placed into a particular mode, depending on the desired coupling type (to the magnetic or the electric field components). The main disadvantage of cavity resonators is their size, which is linked to their resonance frequency due to the boundary conditions for an electromagnetic standing wave. If low frequencies should be reached, they become quite bulky metal pieces (the order of magnitude is half a wavelength, which is 5 cm in the case of 3 GHz resonance frequency). Considering the limited experimental space, a more versatile option would be desirable.

An alternative to the three-dimensional cavity approach are transmission line resonators. There, the resonance is created by feeding a microwave signal into a resonating substructure. This can be an impedance mismatch in the conduction line for capacitive coupling (usually an interruption, see also Sect. 3.2.1), or an open loop structure along the conduction line for inductive coupling. Possible transmission lines for resonating structures are microstrip, stripline, and CPW (cross sections and electromagnetic field lines given in Fig. 3.14, for CPW's see also Fig. 3.4). In the case of the microstrip line, the electric field lines mostly extend into the substrate towards the ground plane, whereas the stripline and coplanar geometries have rather symmetrical field distributions. Coplanar structures have been widely used in quantum electrodynamics in the recent years [71, 72, 73, 74]. Stripline resonators are not a standard tool, but have been recently fabricated and applied to measure the surface resistance of single-crystalline metallic samples [75, 76, 77].

In this work, a resonant approach using CPW structures was taken. Designs with high quality factors were available via a collaboration with J. Majer, TU Wien. The precision that comes with high quality factors appeared useful regarding the small relative changes that we try to detect. In the following subsections, the experimental details of this

approach will be presented.

3.3.7 Resonant measurement using a CPW resonator

CPW resonators are commonly applied in the field of circuit quantum electrodynamics [71, 72, 73, 74], where photons in the resonator couple to samples in the electromagnetic circuits, e.g. to N-vacancy centers in diamond as a realization of a qubit [78]. The used resonators consist of a superconducting Nb thin film structure on a $330\ \mu\text{m}$ sapphire substrate. The Nb film thickness is of the order of $200\ \text{nm}$ [79]. The resonating part is a section of the conduction line of a certain length with a strongly reflecting impedance mismatch at both ends. As for microstrip and stripline resonators, the mismatch is realized by interruptions of the center conductor (the coupling gaps), in the case of capacitive coupling. At the coupling gaps the signal is coupled into and out of the resonator. The ground metalization on the sides is continuous. The center conductor between the coupling gaps will also be referred to as resonating line.

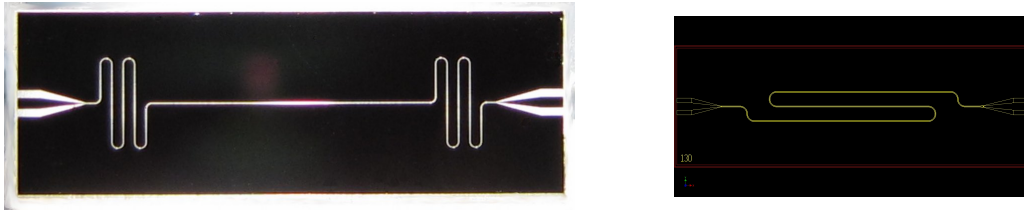


Figure 3.15: Two designs for CPW resonators, fabricated by J. Majer and collaborators, TU Wien. *Left:* Photograph of a chip with design 111 [79]. *Right:* Alternative design that would be more suitable for magnetic coupling and was used for several tests in liquid He (design plot, courtesy of C. Koller).

By calculating and simulating the properties of certain designs, resonators with different properties (e.g. different resonance frequencies, different shapes of transmission lines, capacitive or inductive coupling, and high or low quality factors) can be tailored for different purposes. The type of resonator shown in Fig. 3.15 (left) was used for most microwave measurements of this work. These $\lambda/2$ resonators were designed and fabricated by J. Majer and collaborators, TU Wien. Their quality factor is of the order of 10^5 , and their resonance frequency just below $3\ \text{GHz}$. The exact resonance frequencies and quality factors vary slightly from resonator to resonator of the same design. The center conductor width is $10\ \mu\text{m}$, the gap between center conductor and ground planes $4.15\ \mu\text{m}$, and the coupling gap is $5\ \mu\text{m}$. The coupling gaps are the same at the input and the output. This particular design was chosen to achieve good coupling of the electromagnetic microwave signal to the charge of the electrons in the sample. Conceptually,

there is no difference between $\lambda/2$ resonators with differently shaped resonating lines, and the theory behind their functionality is the same. However, it can be favourable to use certain shapes, for instance to increase the interaction between sample and resonator. At resonance, the electric field of a $\lambda/2$ resonator has antinodes at the edges of

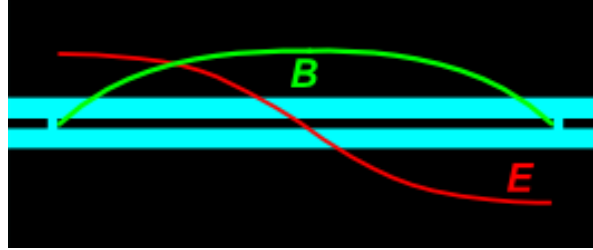


Figure 3.16: Schematic drawing of the electric and magnetic field strengths E and B of a CPW resonator at resonance.

the resonating line and a node in the center, while the magnetic field has an antinode in the center and nodes at the edges (see Fig. 3.16). Thus, a sample has to be placed at the edges to couple to the electric field and at the center to couple to the magnetic field. The design of Fig. 3.15 (left) allows a large overlap of electric field and sample if the sample is placed on top of one of the meander lines. In contrast, the resonator design in Fig. 3.15 (right) is suited to couple to the spin of the electrons rather than to the charge, because the magnetic field has an antinode in the center of the resonating line and the overlap of sample and field will be strongest there.

The resonator is integrated into a printed circuit board (PCB), which is screwed into a Cu box. Some of the Cu boxes were Au plated to avoid oxidation of the surface. A photograph of such a box is shown in Fig. 3.17. The transition from the signal-carrying coaxial cable to the resonator chip is done in two steps, matching the transmission line impedances to $50\ \Omega$ as well as possible. A mini-SMP type connector is soldered into the box, and its center conductor is soldered to the center conductor of the PCB. The pattern of vias (tiny holes with metalized surfaces) in the PCB is meant to prevent parasitic modes. The resonator chip's outer and inner conductors are connected to those of the PCB by Al wire bonds. These can be applied to well-defined spots at the edges of the Nb thin film structure. To obtain good signal quality, it is crucial to have a good electrical contact between each inner and each outer conductor of the different transmission lines, without having spurious current flows between inner and outer conductors (dirt, touching Al wires, etc.).

In contrast to experiments in the field of circuit quantum electrodynamics [78, 80], the CPW resonators were not operated in a low-power limit, but with higher inputs.

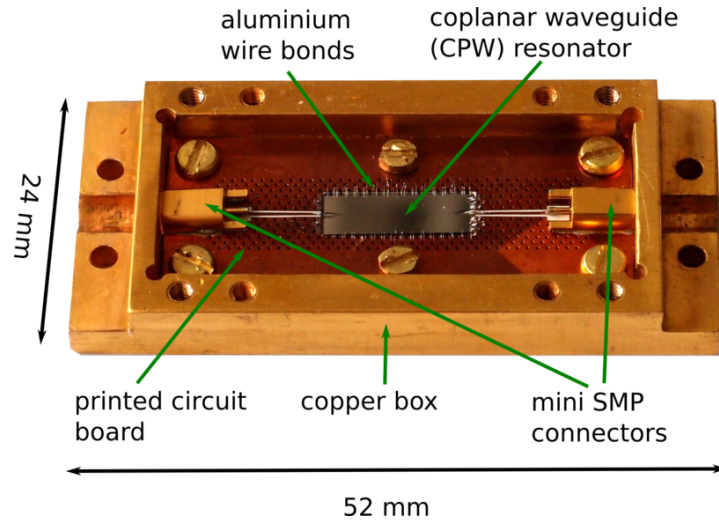


Figure 3.17: Au plated copper box with CPW resonator (designed by J. Majer and collaborators, TU Wien).

In the Garching setup, the VNA was operated with powers up to -30 dBm at the source. The damping by the coaxial lines and two -3 dBm attenuators results in about -40 dBm entering the resonator, corresponding to about 100 nW. This is orders of magnitude higher than what is applied in a low-power regime [81]. The sample has to be placed in a position where it can couple to the electromagnetic field of the resonator. Being metallic, it cannot be placed directly onto the resonating structure, because this would produce a short between the inner and outer conductors. Insulating samples like the above-mentioned diamond with N-vacancy centers can be placed directly on the surface; the microwave signal then couples to the sample's excitations that are in resonance with the applied microwave frequency, but otherwise the presence of the sample only leads to a small change of the effective relative permittivity ϵ_{eff} , which is seen by the electromagnetic field. A metallic sample, by contrast, has a continuous excitation spectrum and will thus interact much more strongly with the microwave signal. If it is placed too close to the surface, the induced currents will lead to a strong damping of the signal. If the coupling between sample and field becomes too strong, no resonance can be seen anymore in the transmitted signal. Therefore, an intermediate coupling strength has to be achieved, where the sample interacts sufficiently strongly with the electromagnetic field, but without decreasing the quality factor of the resonance too strongly. The coupling strength can be tuned by the distance between the sample and the resonator surface, as qualitatively seen in Fig. 3.18 (experimentally) and in Fig. 5.10 (simulation).

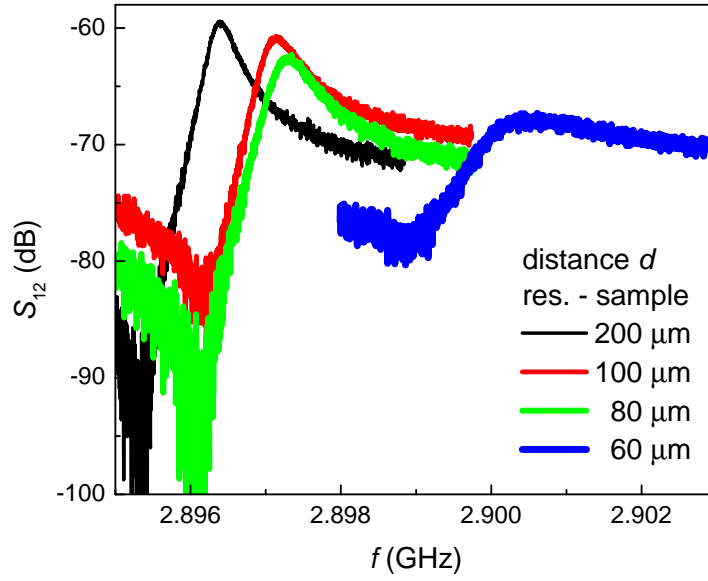


Figure 3.18: Evolution of the transmitted signal with increasing coupling strength.

A cross section of the arrangement inside the copper box is shown in Fig. 3.19. The cover was designed in such a way that a sample holding mechanism is located above one of the resonator's meanders. The distance between sample and resonator surface d defines the coupling strength and has to be adjusted. For this purpose, a sample placement stage was designed. It is shown in Fig. 3.20 and allows changing the sample distance in small steps of a few μm .

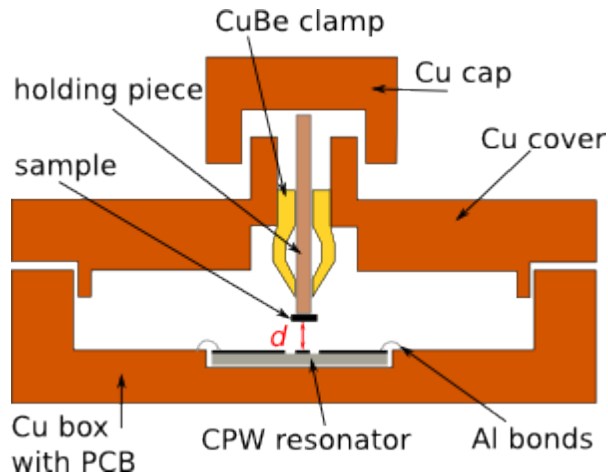


Figure 3.19: Cross section of Cu box with cover. The holding piece can slide in the clamp, until the desired distance d is reached.

The following placement procedure is applied prior to every measurement series: At first, the empty resonator's functionality is checked in liquid He. If it works well, the

Cu box is opened after the test measurement and a spacer of known thickness is placed over the surface of the resonator as a reference. The Cu box without a sample is closed and placed into the rigid frame shown in Fig. 3.20 (left). The small holding piece can be moved towards the spacer by a micrometer screw (see close view in Fig. 3.20 (right)), until it touches the spacer. The box is then taken out of the frame, opened, and the spacer is removed. Then, the sample is glued to the tip of the holding piece without moving the holding piece inside the clamp. The box, this time with the sample, is closed. Due to the spacer, the approximate distance between sample and resonator is known, and the fine tuning can start. The resonator with the coupled sample is tested in liquid He. As the distance is of the order of $200\ \mu\text{m}$, the resonance shape is most likely still similar to the shape of the empty resonator. After the measurement, the box is placed into the rigid frame again, and the holding piece with the sample is moved towards the resonator surface by a defined distance, using the micrometer screw. The last two steps are repeated until the shape of the resonance is broadened.

By determining the sample position with this method, the distance can be consecutively adjusted without taking off the cover during the procedure. The advantage is a direct feedback, because the resonator is tested in liquid He at every new position and the change of the resonance can be monitored. Figure 3.18 shows curves of such a placement procedure.

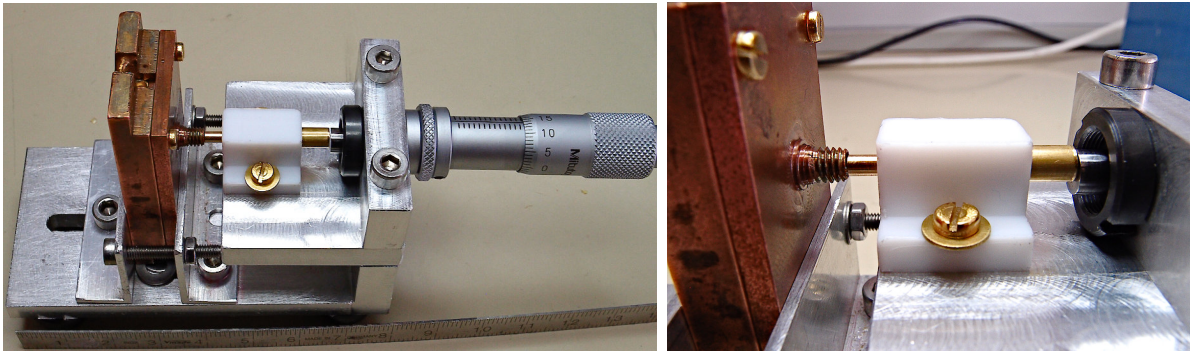


Figure 3.20: Left: Stage for sample placement, with inserted resonator box. Right: Close-up view of the sample placement stage.

At 4 K, the resonator's properties are different from the properties at 2 K, and certainly also from the properties at dilution refrigerator temperatures. Especially the quality factor Q has not reached its saturation value at 2 K, as can be seen from Fig. 3.21. For this reason, even after a successful placement procedure at 4 K, the sample can turn out to be over- or undercoupled when it is measured in a dilution refrigerator. Further details about the different achieved coupling levels will be presented in Sect. 5.2.1.

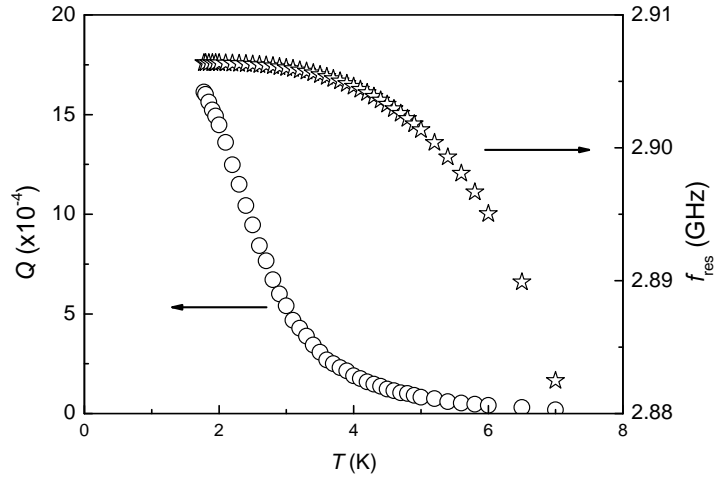


Figure 3.21: Temperature dependence of the quality factor Q and the resonance frequency f_{res} of an empty CPW resonator.

3.3.8 Resistance measurements inside the CPW resonator box

In the course of the development of the microwave measurements, an additional control parameter was introduced: The sample inside of the copper box was contacted with four wires for resistance measurements, and the signal was fed through the box using self-made round Styrcast plugs.

A schematic drawing of the measurement arrangement is shown in Fig. 3.22. A photograph of the box with integrated resistance measurement setup is shown in Fig. 3.23 (left). The required items for the resistance measurements are added to the schematic cross section in Fig. 3.19. The sample is contacted with four wires on the side which is not facing the resonator. The space for the contacts is very limited, requiring a careful placement that leaves enough space to glue the sample to its holding piece. After the contacting procedure, the sample is glued to the holding piece, with a tiny insulating piece of cigarette paper between the brass holding piece and the sample. A big sample is easier to contact and to handle until it is glued to the holder, but the wiring of a big sample is much harder to handle in the following steps: All wires inside the box have to be cautiously bent and fixed to the cover with GE varnish and thin cigarette paper between the Cu walls and the wires, as shown in Fig. 3.23 (center). There should be no large wire movements possible, no touching between the wires and no contact to ground (i.e. to the Cu box). At the same time, there has to be some flexibility, because the sample is not yet in the final position and will be moved closer to the resonator, away from the cover, and this procedure has to be possible without stressing or breaking the contacts. During the positioning of the sample, where it is moved towards the resonator step by

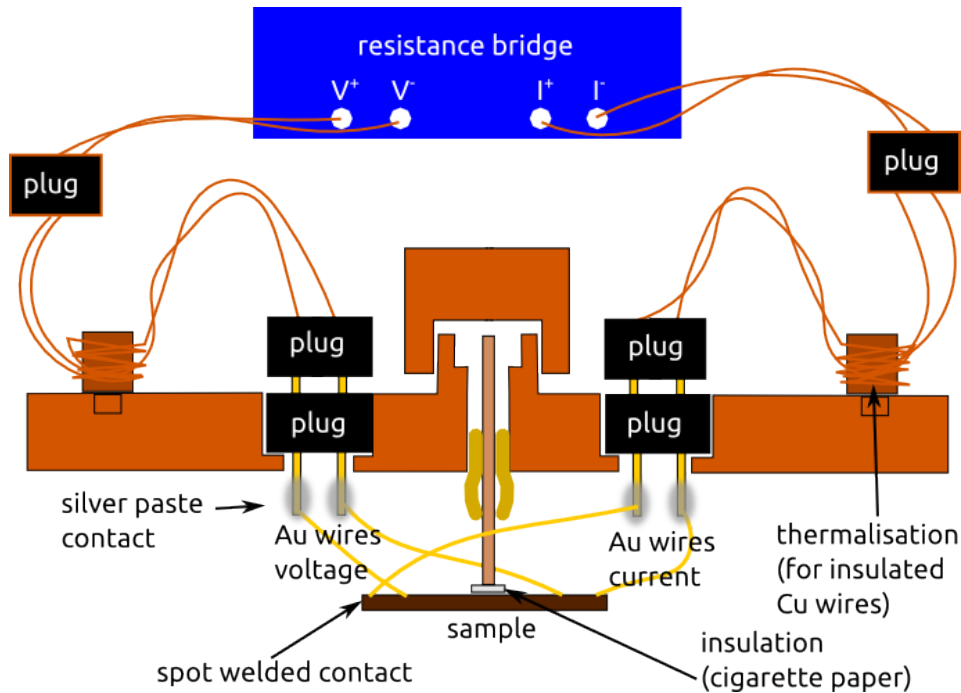


Figure 3.22: Schematic drawing of the arrangement for the in-situ resistance measurements.

step, the cabling for the resistance has to be checked at every step. The most common problem is the touching of one of the Au wires with the Cu box, the PCB, screws inside the box, or the bonding wires, which results in a contact to ground. If that happens during the placement procedure, the wires inside the box have to be rearranged until the resistance measurement can be performed correctly again. After the placement procedure has been performed successfully, and no undesired contacts to ground are found, the sample is ready for microwave and in-situ resistance measurements. A mounted and wired box is shown in Fig. 3.23 (right).

The resistance of the available YbRh_2Si_2 sample pieces is smaller than $1\text{ m}\Omega$ at dilution refrigerator temperatures. For a precise low-current resistance measurement, a cryogenic transformer was connected. It was attached to a Cu holder at the bottom of the cold finger. The measurement of the resistance was performed with a Linear Research 700 resistance bridge at a frequency of 15 Hz. The used transformation ratio was 100 and 300 (in the second and third measurement cycle, respectively (see Sect. 5.2.1)).

By the third measurement cycle, the microwave measurement setup at the Walther-Meissner-Institute had developed into the collection shown in Fig. 3.24. On the left side, there is the cryostat with filter boxes for the service lines (thermometers and heaters) on top. The blue flexible coaxial cables guide the microwave signal between the cryostat and

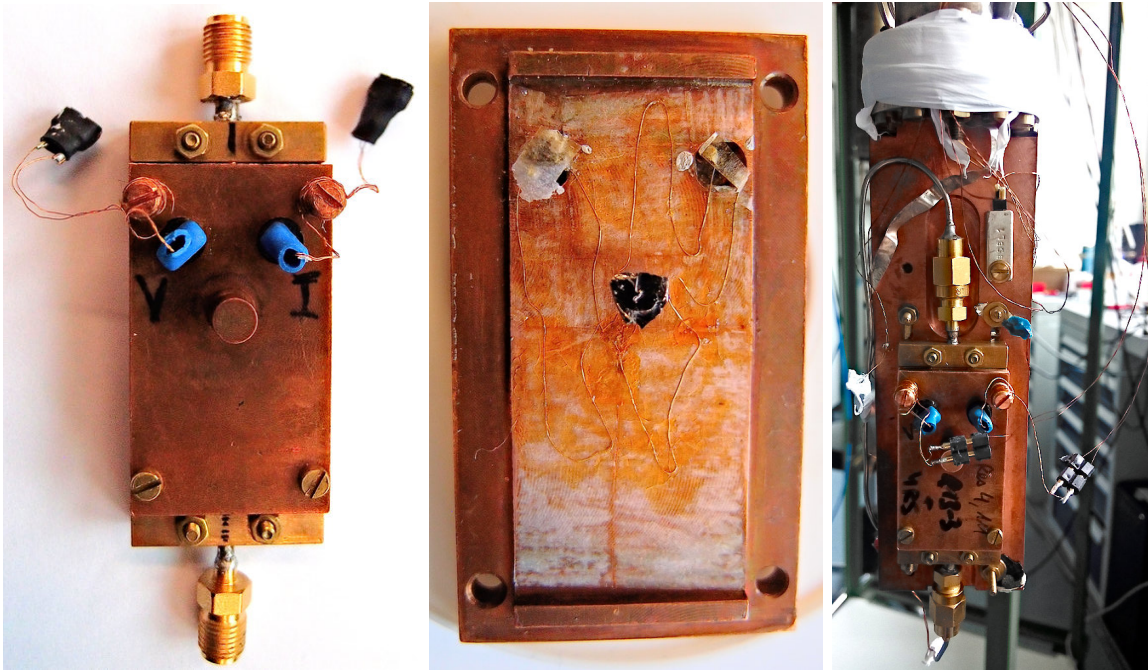


Figure 3.23: Photographs of the microwave box with the plugs for the resistance measurement (*left*), of the inner side of the box cover with the placed and contacted sample (*center*), and the closed Cu box, mounted and connected for microwave transmission measurements and simultaneous electrical resistance measurements (*right*).

the network analyzer. In between, there is a directional coupler (fixed to the cryostat; it allows connecting the coaxial line to the network analyzer and to a single frequency microwave source) and the amplifier (small Cu plate fixed to the instrument rack, blue microwave cables connected to it from both sides). The connected instruments in the rack are, from top to bottom: A microwave signal generator (used to feed in a single frequency), the Linear Research 700 resistance bridge, a VNA, a current source for the heaters inside the cryostat, a helium level meter (bottom left in the rack) and a GPIB bus isolator (bottom right in the rack), used to electrically separate the resistance bridge from the measurement PC ground to avoid errors due to ground loops. At the very bottom, partially hidden by a helium vessel, is a voltage source, which provides the appropriate voltage for the amplifier.

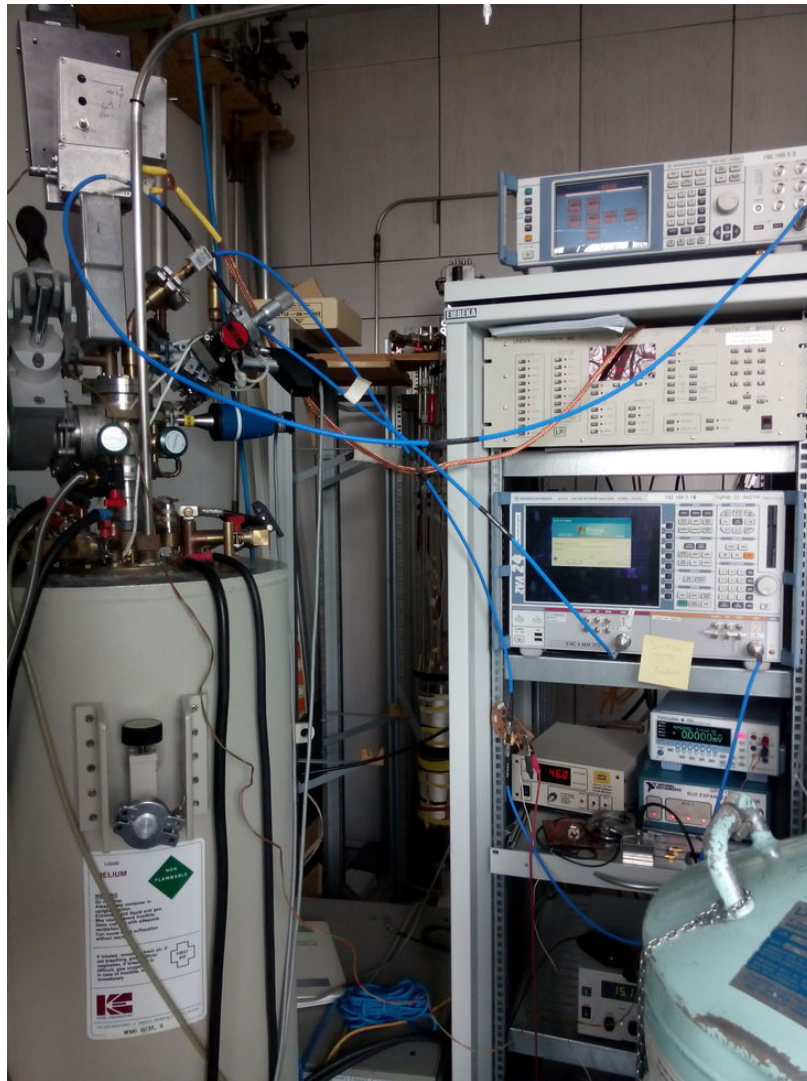


Figure 3.24: Working place at the microwave measurement setup in Garching.

4 Materials under investigation

4.1 YbRh₂Si₂

The heavy fermion compound YbRh₂Si₂ crystallizes in a tetragonal structure (space group I4/mmm) with $a = b = 4.0345 \text{ \AA}$ and $c = 9.8282 \text{ \AA}$ [82]. The Yb atoms (with the electronic configuration $[\text{Xe}]4f^{13}5d^16s^2$) form a lattice of localized magnetic moments of f -electrons. The Kondo interaction between the lattice of Yb³⁺ ions (the valence of

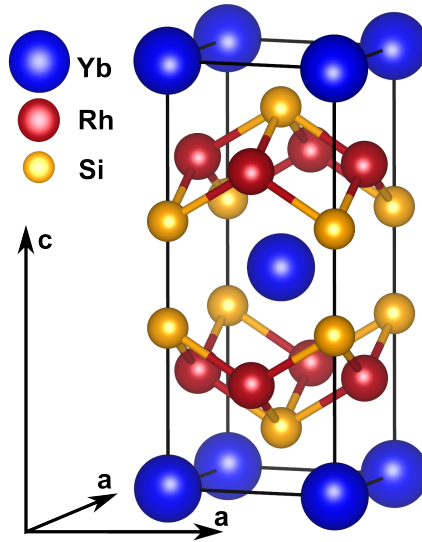


Figure 4.1: Crystal structure and crystallographic axes of heavy fermion metal YbRh₂Si₂.

the Yb ion is found to be slightly lower, but very close to the integer number of +3 [83, 84]) and the conduction electrons induces metallic heavy fermion behaviour below a temperature of approximately 100 K. At temperatures below $T_N \approx 70 \text{ mK}$ (depending on the sample quality [85, 86]), YbRh₂Si₂ orders antiferromagnetically. By applying an external magnetic field, the Néel temperature can be driven to absolute zero. The required field strengths are $B_{c\parallel} = 660 \text{ mT}$ parallel to the crystallographic c -direction [87] and $B_{c\perp} = 60 \text{ mT}$ perpendicular to c [43]. The full suppression of T_N by external magnetic fields gives rise to QCPs, from which tornado-shaped NFL regions emerge in

the temperature-magnetic field phase diagram of YbRh_2Si_2 , as shown in Fig. 4.2 (left). The properties of YbRh_2Si_2 have been thoroughly investigated at low temperatures, particularly by transport measurements [44, 43, 46, 86, 87], but also by other techniques like scanning tunneling microscopy [88], electron spin resonance [89] and infrared spectroscopy [90].

The discovery of an additional energy scale T^* , across which the Hall coefficient changes [44], has been at focus in recent years. It provides experimental evidence for local quantum criticality and the so-called Kondo destruction scenario [9] (see also introductory Sect. 2.2.2).

Spectroscopic data, probing electronic excitations in the quantum critical region of the phase diagram of YbRh_2Si_2 , would be of great interest, as well as extending the measurements of various physical properties (for instance resistivity, Hall resistivity, susceptibility) to the ultra-low temperature region.

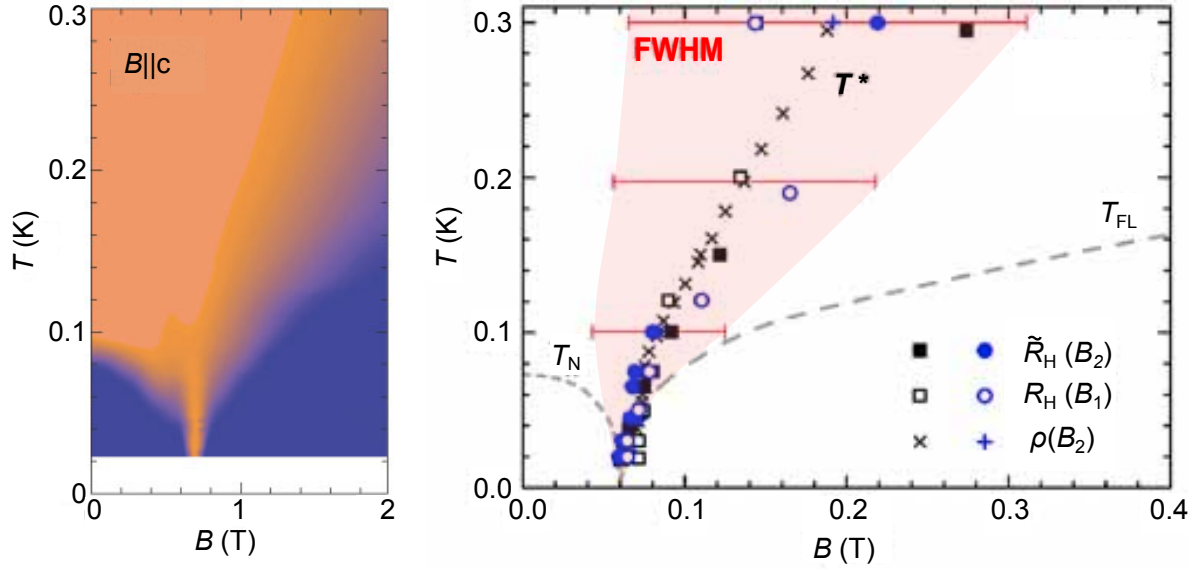


Figure 4.2: Left: Colour coded plot of temperature-magnetic field phase diagram of YbRh_2Si_2 for $B \parallel c$ [87]. Orange regions have a linear temperature dependence of the resistivity, blue regions a quadratic FL-like temperature dependence. In the experiments of this work, the external field was mostly applied perpendicular to c , $B \perp c$, where the phase diagram looks similar with respect to FL and NFL regions, but at a field scale that is lower by a factor of 11. Right: Energy scale T^* , defined by the crossover in the Hall coefficient. Hall coefficients in parallel and crossed field alignments are shown, along with the location of an inflection point in the magnetoresistance. Also the width of the crossover (FWHM) is shown; it increases rapidly with temperature [91].

4.2 $\text{CeNiAs}_{1-x}\text{P}_x\text{O}$

Iron pnictide materials were discovered a decade ago [92] and have attracted a lot of interest due to the close interplay of magnetism and unconventional superconductivity. In recent years, they have been investigated in terms of quantum criticality [11]. CeFeAsO and $\text{CeFeAs}_{1-x}\text{P}_x\text{O}$, for instance, have been studied in this context and possess rich and complex magnetic phase diagram [93, 94]. A related compound, CeNiAsO , belonging to the material class of nickel oxypnictides, has a reduced magnetic complexity because the Ni $3d$ -electrons do not order magnetically [95]. This permits a more detailed study of the antiferromagnetic order of the Ce-derived moments. The hybridization between the Ce $4f$ - and the Ni $3d$ -electrons leads to heavy fermion behaviour with a Kondo scale of $T_K \sim 15$ K. Antiferromagnetic order that sets in below $T_N = 9.3$ K can be suppressed either by applying pressure or by substitution with P, see Fig. 4.4.

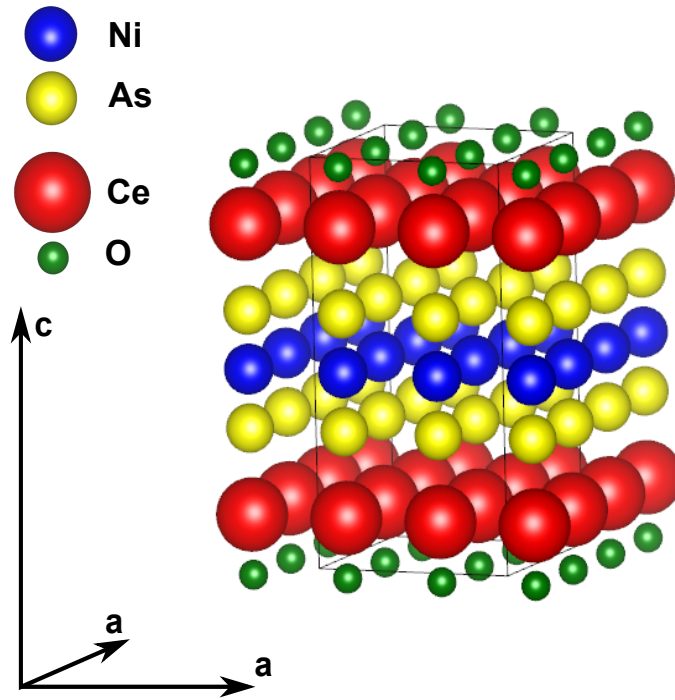


Figure 4.3: Crystal structure of the Ni oxypnictide material CeNiAsO .

The parent compound CeNiAsO ($x = 0$) crystallizes in a tetragonal structure (space group $P4/nmm$), with lattice parameters $a = b = 4.0767 \text{ \AA}$ and $c = 8.1015 \text{ \AA}$. The fully substituted compound CeNiPO ($x = 1$) has slightly smaller lattice parameters of $a = b = 3.9652 \text{ \AA}$ and $c = 7.9526 \text{ \AA}$ [96]. Polycrystalline samples of several substitution levels were available.

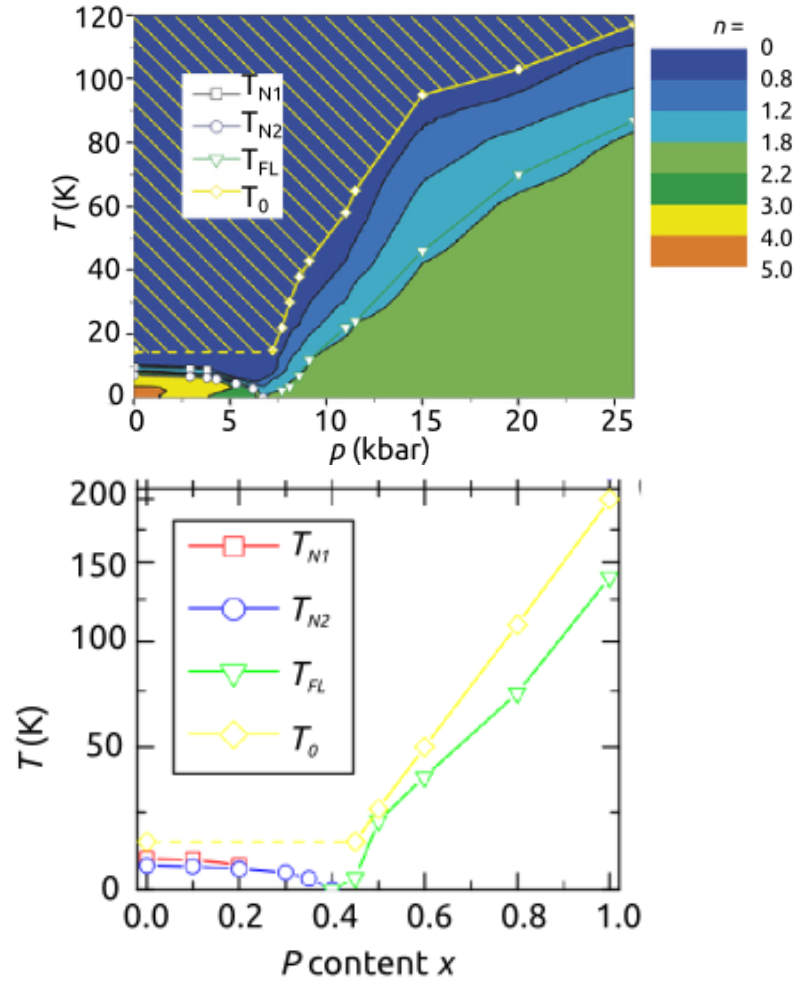


Figure 4.4: Pressure- (top) and substitution- (bottom) temperature phase diagrams of CeNiAs_{1-x}P_xO [96].

The influence of magnetic field on CeNiAs_{1-x}P_xO had not been studied previously and was investigated as part of this thesis. Also, the interplay of the different tuning parameters pressure, P substitution, and magnetic field was studied by applying pressure and external magnetic fields to doped CeNiAs_{1-x}P_xO samples.

4.3 $\text{Ti}_{1-x}\text{Sc}_x\text{Au}$

TiAu , the parent compound of $\text{Ti}_{1-x}\text{Sc}_x\text{Au}$, combines two rare properties: It is an itinerant antiferromagnet, and it does not have magnetic constituents [97]. It crystallizes in three different crystal structures, namely cubic, tetragonal, and orthorhombic. Each crystal structure shows distinct physical properties. Within this work, polycrystalline samples of the orthorhombic type (symmetry group Pmma) were studied, see Fig. 4.5. The lattice constants of the orthorhombic structure are $a = 4.632 \text{ \AA}$, $b = 2.948 \text{ \AA}$ and $c = 4.885 \text{ \AA}$. Further information regarding synthesis, crystal structure, band structure, and Fermi surface calculations, as well as evidence for the itinerant order from transport, muon spin relaxation, and neutron diffraction measurements can be found elsewhere [97]. As a rare example of an itinerant d -electron antiferromagnet, it is a good model system for fundamental investigations.

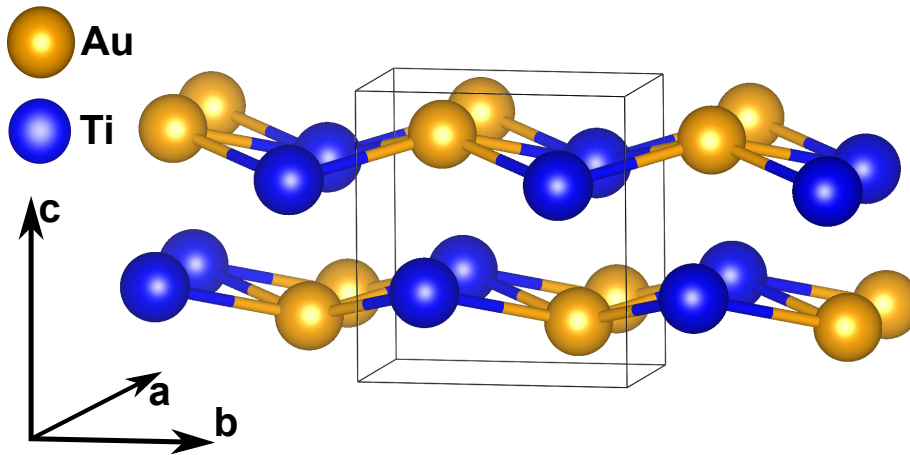


Figure 4.5: Crystal structure of orthorhombic TiAu .

The undoped TiAu has a Néel temperature of $T_N = 36 \text{ K}$. Doping with Sc to $\text{Ti}_{1-x}\text{Sc}_x\text{Au}$ induces changes in the electronic properties of the material and weakens the antiferromagnetic order. T_N is completely suppressed at a doping level around 12%.

The focus of the experimental investigations performed in this work was to extend previous measurements to lower temperatures. By these resistivity measurements, the phase diagram of this new itinerant system was explored in the vicinity of its doping-induced QCP with respect to FL and NFL behaviour.

4.4 CeB₆

CeB₆ is a cubic system (space group Pm-3m) with a lattice constant of $a = 4.141 \text{ \AA}$. Like Ce₃Pd₂₀Si₆, its phase diagram shows an AFQ and an antiferromagnetic phase. Whereas other aspects like the nature of the AFQ order have been in the focus of previous investigations, there are only few studies of quantum critical aspects [98]. CeB₆ orders antiferromagnetically below a temperature of 2.3 K. By applying an external magnetic field, this temperature can be suppressed, the exact field value being slightly different for different field alignments (along [110] or along [001]). An increase of the electronic specific heat coefficient γ and the A coefficient from electrical resistivity were reported around the critical field value, where T_N gets fully suppressed [99]. This is today interpreted as an indication of quantum critical behaviour. Furthermore, the similarities with Ce₃Pd₂₀Si₆ (which has shown unconventional quantum criticality), make it a potential candidate for the study of quantum criticality.

Single-crystalline samples were available, and a field-dependent analysis was performed down to low temperatures, with the magnetic fields applied along the different crystallographic directions. The work on this material was dedicated to approach the tentative QCPs in [110] and [001] directions in small field steps and to obtain information on the behaviour of magnetization, specific heat and resistivity in the vicinity of the critical values.

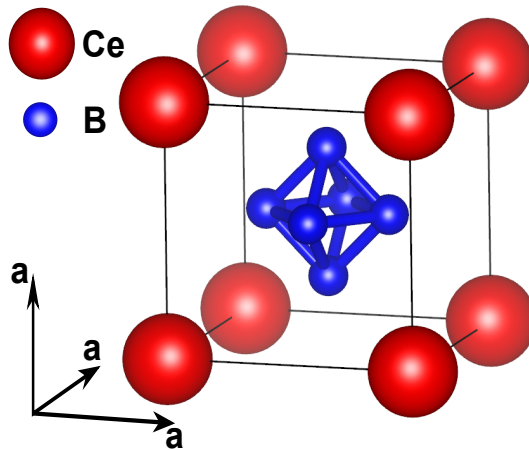


Figure 4.6: Crystal structure of heavy fermion material CeB₆.

4.5 $Ce_3Pd_{20}Si_6$

$Ce_3Pd_{20}Si_6$ is a cubic heavy fermion material (space group $Fm\bar{3}m$) with a lattice constant of $a = 12.280 \text{ \AA}$. It crystallizes in a cage structure with two inequivalent cages, as indicated in Fig. 4.7. In these two cages, the Ce^{3+} ions are situated at two different crystallographic sites, one (at position $(0,0,0)$) being surrounded by an octahedral cage of 12 Pd and 6 Si atoms, the other one (at position $(1/4, 1/4, 1/4)$) by a tetrahedral cage of 16 Pd atoms [100]. Two transitions are observed in this material, one attributed to an antiferro-quadrupolar (AFQ) transition, one to an antiferromagnetic transition [60, 101]. Additionally, an energy scale with similar properties as the T^* line of $YbRh_2Si_2$ could be identified from Hall effect measurements (Fig. 4.8). The discovery of a T^* scale in this cubic material was an important experimental contribution to the proposed global phase diagram of Fig. 4.8 (right), where quantum criticality is viewed in the context of the material's dimensionality [102].

Although the crystal structure of $Ce_3Pd_{20}Si_6$ is cubic, single crystalline samples develop anisotropies of their physical properties under external magnetic fields. Signatures of a phase transition and a tentative second QCP, which only occurs if an external magnetic field is applied along the crystallographic $[100]$ direction, has been reported [103]. To explore the vicinity of this QCP by magnetoresistivity and Hall effect measurements along the different crystallographic axes was the goal of the measurements of this work.

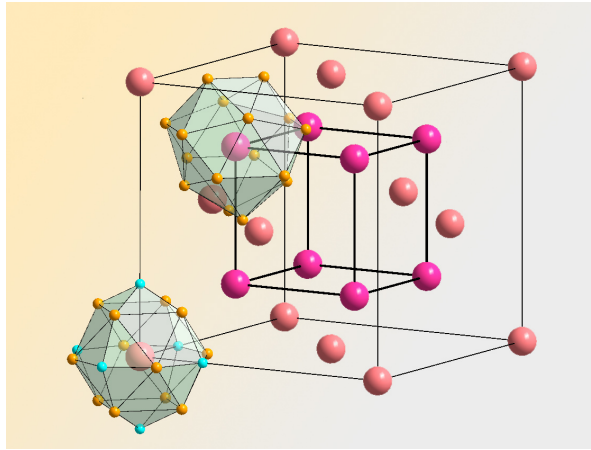


Figure 4.7: Crystal structure of cubic heavy fermion material $Ce_3Pd_{20}Si_6$ [101].

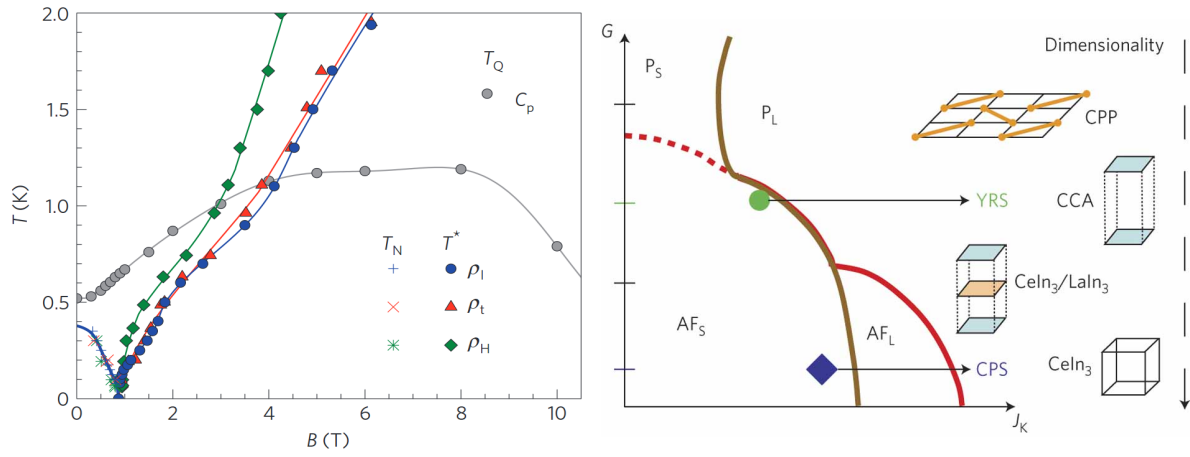


Figure 4.8: Left: Phase diagram of $\text{Ce}_3\text{Pd}_{20}\text{Si}_6$, showing the antiferromagnetic and AFQ transitions, and the signatures of the T^* crossover. Right: Suggested global phase diagram [101]. Spatial dimensionality is inversely linked to the degree of frustration G between the local moments, which is an important parameter for the relevant interactions of the investigated quantum critical materials.

5 Results and discussion

5.1 Microwave simulations

5.1.1 Finite element simulations and Comsol

Many physical properties are mathematically described by differential equations. For large and complex systems with a large number of parameters it is in many cases impossible to calculate an analytical solution. The rapid advancement of computer science and the increase of computing power and memory in the second half of the 20th century created new options for theoretical physicists: the field of numerical calculations and simulations developed, examples being density functional theory (DFT), Monte Carlo simulations, or finite element methods (FEM). The latter is often referred to as finite element analysis (FEA), if the emphasis lies on the solution of a defined problem. The basic ideas of FEM were developed in the 1940's [104, 105] and today they are a frequently used tool in applied sciences and engineering.

The respective differential equations are only solved locally for small, finite pieces of the entire system where the parameters are assumed constant and the solution is obtained comparatively easily. In the case of a metallic sample in a resonator, there is electromagnetic radiation, guided through a resonant structure; the required set of equations for the FEA are Maxwell's equations in the presence of matter,

$$\begin{aligned}\vec{\nabla} \cdot \vec{D} &= \rho \quad , & \vec{\nabla} \cdot \vec{B} &= 0 \quad , \\ \vec{\nabla} \times \vec{E} &= -\frac{\partial \vec{H}}{\partial t} \quad , & \vec{\nabla} \times \vec{H} &= \vec{j} + \frac{\partial \vec{D}}{\partial t} \quad ,\end{aligned}\tag{5.1}$$

with ρ and \vec{j} being the charge and current densities caused by free charges (polarisation charge and current flows do not contribute), $\vec{D} = \epsilon_0 \vec{E} + \vec{P}$, and $\mu_0 \vec{H} = \vec{B} - \mu_0 \vec{M}$. \vec{P} and \vec{M} are material-specific parameters, the polarization and the magnetization. If all characteristics of the systems' materials and geometry are known, Maxwell's equations can be solved locally in discrete portions of the model.

In Sect. 5.1.2 it will be shown how our system can be modeled in three dimensions, cut into a mesh of finite sections, and solved with respect to its electromagnetic properties. The program Comsol Multiphysics provides a framework of solvers and routines for all kinds of differential equations for mechanical and thermal properties, flow dynamics, etc. It is a versatile and powerful tool with a highly modular approach. Even the coupling of different sets of equations can be implemented without disproportionate effort: one typical example of coupling between modules is the increase in temperature and the temperature profile due to the interaction of electromagnetic radiation with a material. Due to a sophisticated graphic user interface it can be (and mostly is) applied by end-users like engineers and experimental scientists. However, this makes the simulations less controllable and customizable, and the results have to be reviewed carefully. Furthermore, other less modular programs might specialize in a certain group of problems and their results can be more accurate. Such alternative options of commercial FEA programs, optimized for microwave applications, are CST microwave studio or Sonnet.

5.1.2 Creating a 3D simulation of a CPW resonator - realistic and simplified models

The first step of a Comsol simulation is to create and define the physical structure. This was done in a CAD-like fashion directly within the graphical user interface. The degree of simplification will determine the complexity of the calculation and the relevance of the solution. Highly symmetrical problems can be treated much more easily and precisely. For instance, a system with perfect translation symmetry can be reduced to a two-dimensional model. In the case of our resonators, three different approaches are possible:

- **2D model:** A cross section of the resonator perpendicular to the transmission line and the current flow direction. It requires little computing power and is less prone to errors than a full 3D simulation, but by its nature it does not account for any variations along the propagation direction of the signal. Most functionalities of elements like filters and resonators originate from interruptions, couplings, or special structures of the transmission line. In a resonating structure the fields change dramatically along the line. As a consequence, the properties of these elements cannot be modeled with a 2D model alone. Nevertheless a 2D model can help to picture field distributions of different configurations qualitatively, as shown in Fig. 5.1.

- **simplified 3D model:** A realistic representation of the resonator with some geometrical simplifications. Curved or irregularly shaped transmission lines turned out to be problematic, so the geometry of the transmission line was simplified. Also the geometry of the sample, which is usually irregular, was simplified.
- **realistic 3D model:** An exact duplicate of the real resonator, only the sample was modeled with a simplified geometry because of its irregular shape.

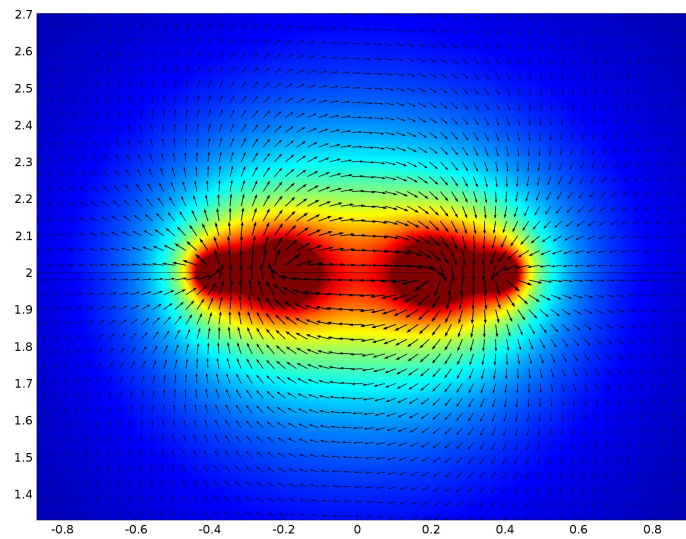


Figure 5.1: Cross sectional magnetic field distribution of a modelled coplanar transmission line, field scale and length scales in arbitrary units.



Figure 5.2: *Left:* Simulated electric field strength on a resonator surface with design 111, blue (lowest) to red (highest), arbitrary units. *Right:* Simulated magnetic flux density on a resonator surface with design 111, blue (lowest) to red (highest), field scale in arbitrary units.

The best compromise between an appropriate physical representation and a feasible computation time and model complexity turned out to be the simplified 3D model. It contains the most important elements and should be able to reveal basic trends. The realistic model contains so many details that the implementation into Comsol requires disproportionate computing power and a much more complex meshing process. An

example for a full realistic 3D model simulation result is shown in Fig. 5.2. Most results in the following subsections were calculated with a simplified 3D model. In this section

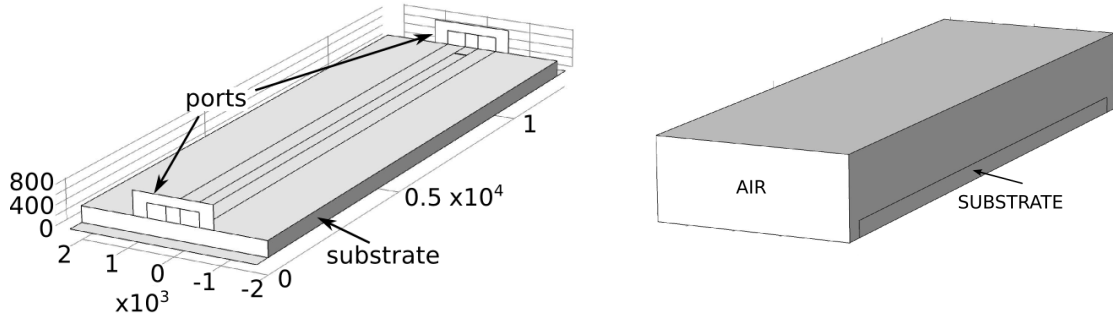


Figure 5.3: Left: Simplified CPW resonator without surrounding air box, designed in Comsol. Length units are μm . Right: The full model of the same resonator with air box. The entire structure is placed in a metallic box filled with air.

the process will be illustrated on a CPW resonator (see also Sects. 3.3.6 and 3.3.7) with the parameters $W = 0.4\text{ mm}$ (W : width of the center conductor) and $S = 0.2\text{ mm}$ (S : gap between center conductor and ground planes) and substrate thickness 2 mm . The resonator dimensions used in this work are much smaller than the substrate. This makes these models difficult to visualize because the meshing is complex due to the presence of both large (substrate width 4 mm) and very small (coupling gap $5\ \mu\text{m}$) structures. This is also the case for the simplified 3D model. Thus, the process will be visualized on a larger model structure, whereas the shown results were obtained from models with appropriate dimensions.

The principles are the same for the realistic parameters, but the meshing gets more complex due to the presence of large (substrate width 4 mm) and very small (coupling gap $5\ \mu\text{m}$) structures.

The first step is to construct the geometry of the model with a modular design principle. Figure 5.3 shows the geometry, consisting of a block of substrate in a block of air. The workplane with the metallic structure is only visible in Fig. 5.3 (left), where the air box is not shown. The surrounding air box is visible in Fig. 5.3 (right). In this representation, the metallic film is not three-dimensional, there is no film thickness associated with it. In reality, the Nb films (fabricated by the group of J. Majer) have a thickness of 200 nm [79] (see also Sect. 3.3.7). This approach is valid if we deal with a superconducting film and the London penetration depth λ (the relevant parameter in the superconducting case) is smaller than the film thickness: at 5 GHz and zero temperature the penetration depth of superconducting Nb was found to be 63.5 nm [79].

Using the temperature dependence of the penetration depth (based on the two-fluid model of superconductivity [58])

$$\lambda(T) = \frac{\lambda(0)}{\sqrt{1 - (T/T_C)^4}} \quad (5.2)$$

for for $T < T_C$, we can estimate that the penetration depth at the measured temperatures. The superconducting transition temperature of the Nb film is $T_C = 8.8 \text{ K}$ [79]. Therefore, at 1 K the penetration depth is $\lambda(1\text{K}) \approx 64 \text{ nm}$, and at 4 K it is $\lambda(4\text{K}) \approx 66 \text{ nm}$. In the case of a film thickness of 200 nm, it is of the same order of magnitude as λ and taking a finite film thickness into account would improve the accuracy of the simulation. However, the difference in scale (film thickness of 200 nm versus substrate thickness of $330 \mu\text{m}$) makes the meshing and computing of the model so much more demanding that this option will not be discussed here. It should be kept in mind that the effects of (alternating as well as static) magnetic fields on the Nb thin film is not included in the simulation and that the simplified film modeling is a possible source of error.

Another issue is to model the excitation port. There are several possibilities, one of which was adapted for the current model. The details of the port modeling are complex, but the choice of port type does not have an effect on the results of the simulation and is rather motivated by Comsol-specific considerations. Further information on port modeling will not be presented within this work, but can be found elsewhere [106]. The next step is to implement the physics into the model, again with a modular approach: As a boundary condition, the walls of the surrounding box as well as the metalization of the film are set as perfect conductors. This represents the experimental situation because the film is a superconductor and the box is a very good normal conductor. Losses due to dirt on the resonator's surface, imperfections of the film, and other possible sources are not taken into account. For our purpose we need to specify the excitation by creating a lumped port, and as exciting voltage $0.01 \text{ V} \approx -36 \text{ dBm}$ was applied.

The coupling gap plays a key role for the resonator's properties, and the coupling strength has a large impact on the quality factor. In the case of capacitive coupling, the coupling strength is determined by the width of the gap. Current densities and current and voltage variations are concentrated in the region around the gaps and along the center conductor. Having defined all physical properties of the model's constituents, the mesh is created by dividing the model into finite regions. In each of those, the local solutions will be calculated. It has to be fine enough to account for changes along

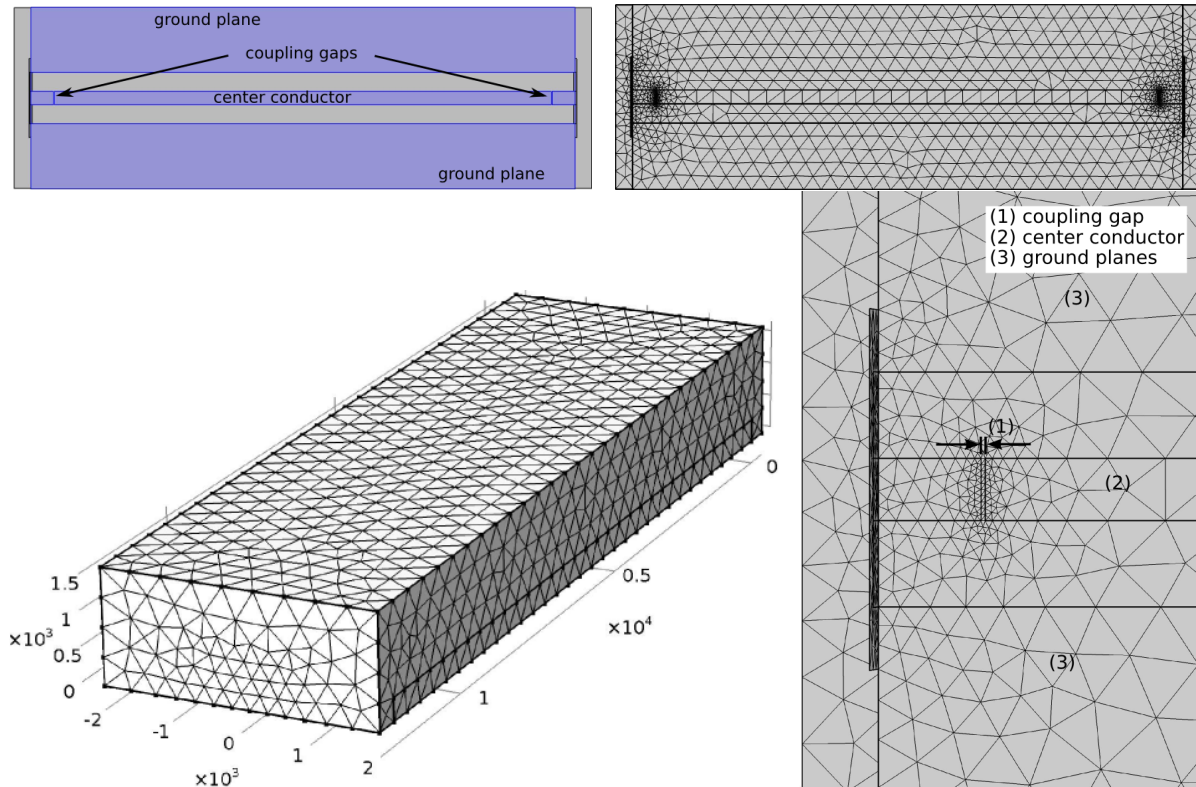


Figure 5.4: Top left: Top view on the metallic structure of the resonator, in terms of the model this corresponds to a top view on the workplane on the substrate surface. Top right: Distribution of the triangular mesh elements on the metalization. Bottom left: The mesh of the entire model with air box. Bottom right: Detail of the mesh. The coupling gaps are meshed individually in order to ensure a fine mesh and high precision in the most interesting regions.

the gaps and the center conductor, and therefore it is much denser there than in other parts of the model (see Fig. 5.4 (top right)). In order to adapt the mesh to the desired precision, the crucial elements can be meshed manually, and the final meshing of the larger parts can be left to the automated triangulation. Figure 5.5 shows how the result depends on the choice of the mesh. For large numbers of elements, the solution should converge to the real scenario. A good compromise between computing time and accuracy has to be found. In the example of Fig. 5.5, a good choice would be around 4×10^5 mesh elements, as indicated by the dashed guides to the eye.

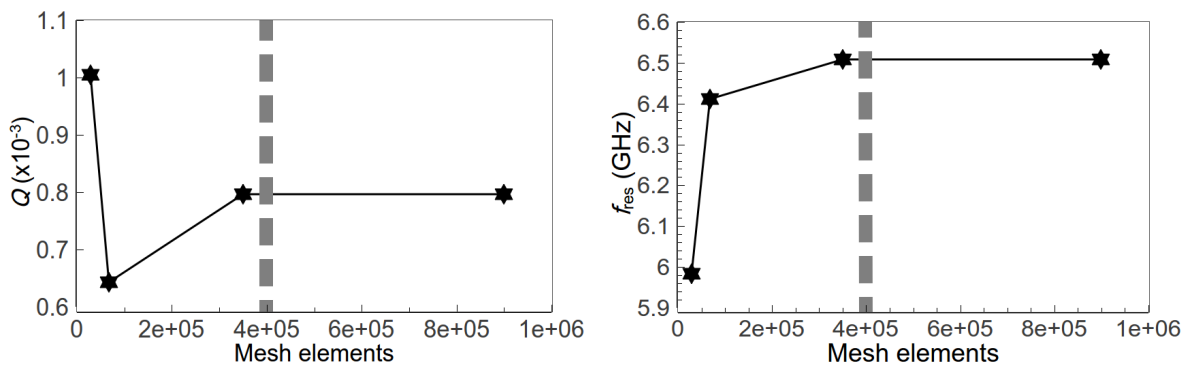


Figure 5.5: Quality factor (*left*) and resonance frequency (*right*) of a resonator (without coupled sample) of meshes with different numbers of elements. The dashed grey lines indicate a good choice for the number of mesh elements.

The final step is the calculation of the properties in every piece of the mesh by iterative solvers. Those are automatically determined by the program from the previously entered parameters and should fit the desired type of analysis. In the present model system, the complexity and therefore the computation time is determined by the number of mesh elements and the number of frequency points. From the calculated transmission, the resonance frequency f_{res} and quality factor Q can be extracted. Figure 5.6 (left) shows the result of a frequency-dependent transmission simulation through an empty CPW resonator, the fundamental resonance of the model resonator. An overview on how the extracted resonance frequency varies when various simulation parameters (mesh, rotation of a rectangular sample, and conductivity) are varied in a small range, is shown in Fig. 5.6 (right). There are no systematic changes with the mesh and the rotation. This makes sense, as the number of mesh elements exceeded the value indicated in Fig. 5.5 in both cases and the sample covers a very similar portion of transmission line in both positions. The variation of these results can therefore be interpreted as an error bar. There is a systematic change beyond the error bar level for the resistivity change, which

illustrates the fact that the sample properties are actually reflected by the transmission of the resonator.

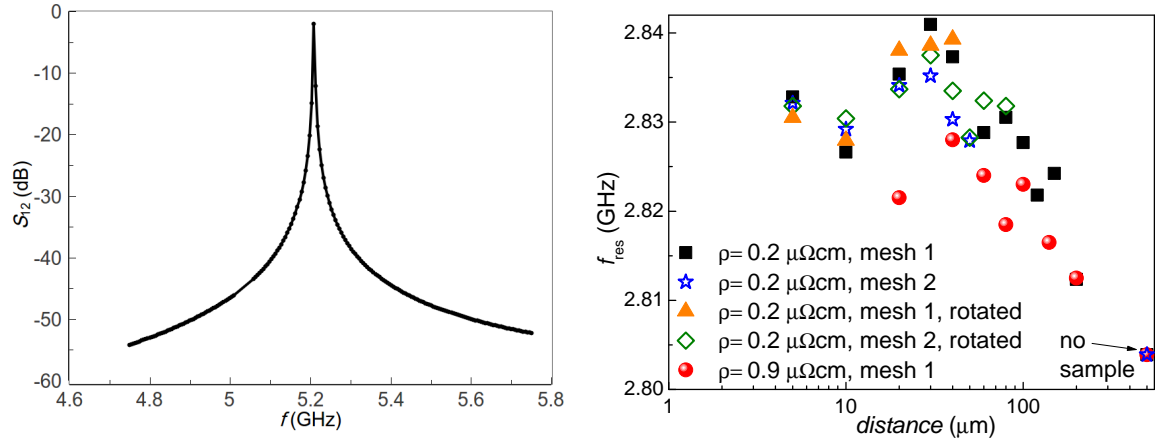


Figure 5.6: *Left:* Transmission of an empty model resonator around the resonance frequency. *Right:* Overview of different parameter changes (mesh, rotation of a rectangular sample, conductivity) and the dependence of the resonance frequency on these parameters.

5.1.3 Results of the model system

Conductivity

At a fixed distance from the metalization corresponding to the thin film surface of the real resonator, another metallic layer was placed over the model resonator as a model sample. The resistivity of this layer was varied, while the distance was kept constant at $40\ \mu\text{m}$. The model sample covers a large part of the resonator. In contrast, the real

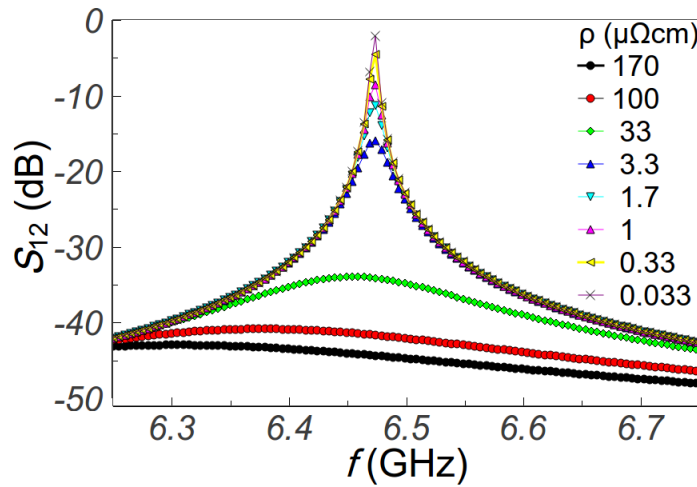


Figure 5.7: Evolution of the resonance with the sample resistivity ρ .

samples are typically irregularly shaped and cover only about a quarter. They might also have structures (holes, cracks) close to the center conductor. Finally, their thickness is thicker than the skin depth (of the order of a few μm for microwave frequencies, see Sect. 3.3.6), which is not accounted for by the infinitely thin model sample.

Figures 5.7 and 5.8 show the results of these conductivity-dependent simulations. They give a good qualitative description of the effects of a metallic sample. At very low resistivities, the quality factor Q and the resonance frequency f_{res} are independent of the sample because they are at the limit of their sensitivity. At higher resistivities, both quality factor and the resonance frequency decrease with resistivity.

It should be noted that for very high resistivities this simulation series does not describe the transition from a metallic to a dielectric sample well, because no information on e.g. the plasma frequency is involved. At some point, samples with high resistivities will become transparent to the electromagnetic radiation and their loss mechanisms and influence on the circuit have to be described differently.

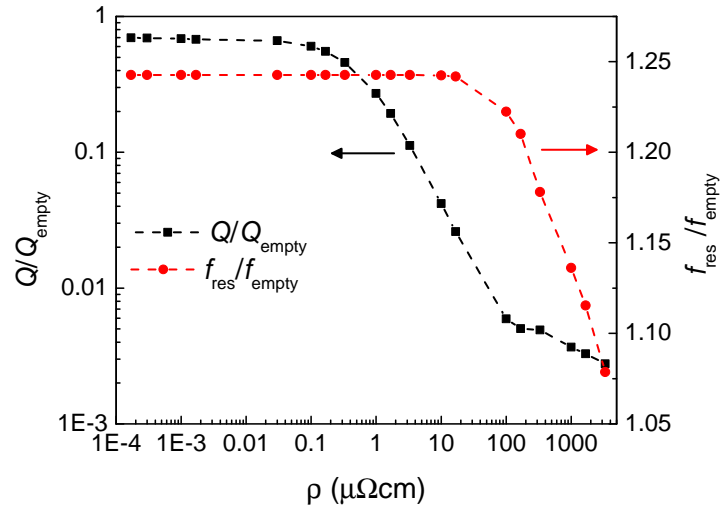


Figure 5.8: Dependence of the resonance frequency and quality factor on the sample resistivity ρ . Q_{empty} and f_{empty} are the quality factor and resonance frequency of the empty resonator (i.e. the simulation without the metallic sample layer). Q and f_{res} are the quality factor and resonance frequency of the model with metallic layer.

Sample size

The total effect of a metallic sample on the resonator properties depends on the portion of the resonator that can interact with the sample. A large sample, covering the full length of the resonator, will interact with the electromagnetic wave along the entire path and the effect on the transmission will be stronger than for a small piece of sample. Figure 5.9 illustrates this fact, showing how the resonance curves Fig. 5.9 (top) and the extracted parameters Fig. 5.9 (bottom) change with the sample dimensions. The changes due to the sample geometry are similar to those due to the sample conductivity or the distance between sample and resonator. In real experiments, a maximum effect due to changes of the sample properties was desired. For that reason, a design with meander lines at the position of the sample is advantageous.

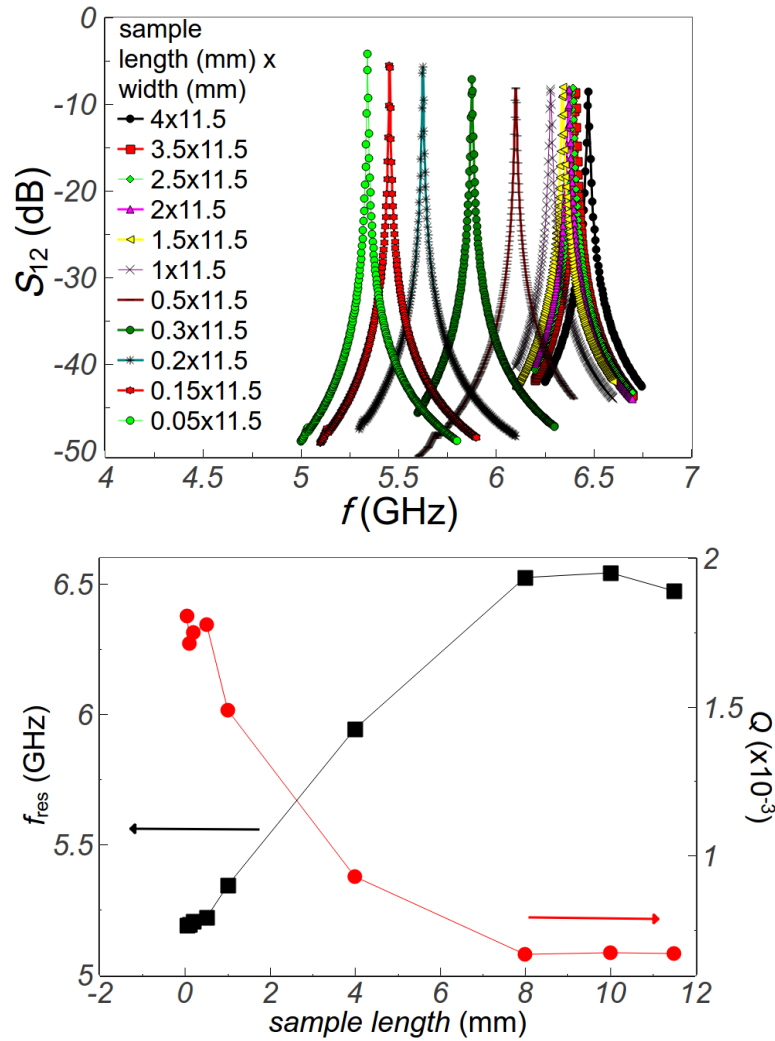


Figure 5.9: *Top*: Simulated transmission of a sample that covers nearly the entire length of the resonator $L = 12$ mm, and the width is varied. *Bottom*: Evolution of resonance frequency and quality factor when the length of the model sample is changed.

Distance

One of the main motivations to perform simulations on a model system was to obtain an idea about the influence of the distance between a metallic sample and the resonator surface. The distance is the experimental realization of the coupling strength: The closer the sample is, the stronger the interaction with the resonating microwaves and the influence on the transmission. However, strong interaction also leads to losses and dissipation currents due to the sample and to a reduced total amplitude and quality factor. In an extremely overcoupled scenario, the resonance is so strongly broadened and flattened out that it is not detectable at all. Therefore, an optimized distance has

to be found and realized experimentally, and a knowledge of the qualitative behaviour of the system is desirable. Figure 5.10 (top) shows how the transmission curves change with the distance, and Fig. 5.10 (bottom) shows how the extracted parameters Q and f_{res} are influenced by the distance between sample and resonator in the model system. If the sample is far away, the values do no longer depend on the distance; there is a saturation value for Q and f_{res} . It is not identical with the values for the empty resonator, which means that the presence of the metallic layer in the box changes the geometry and the field distribution. At distances below $200\ \mu\text{m}$, the presence of the sample starts to influence the resonator more and more, until the quality factor becomes very low and the resonance frequency shifts a lot. The best choice for a real experiment would be an intermediate distance, somewhere between $30\ \mu\text{m}$ and $100\ \mu\text{m}$.

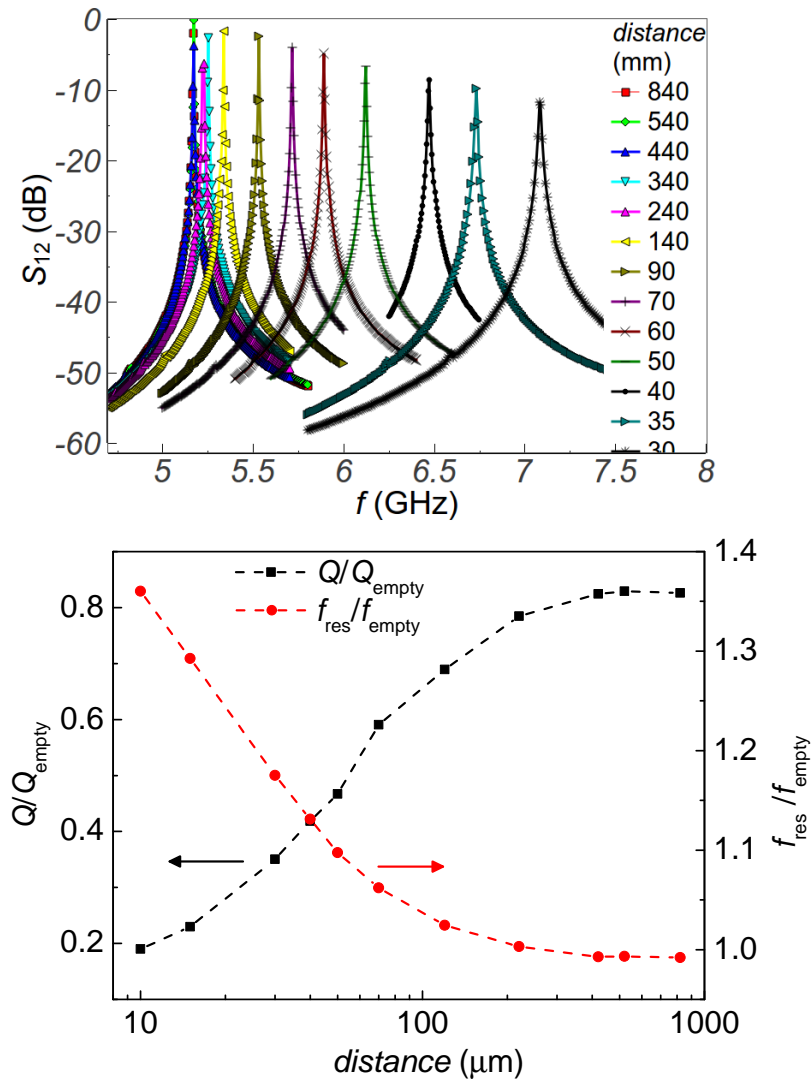


Figure 5.10: Top: Evolution of the transmission S_{12} with the distance from sample to resonator. Bottom: Dependence of the resonance frequency f_{res} and the quality factor Q on the distance between sample to resonator. The parameters Q and f_{res} of the model with sample are normalized to the parameters Q_{empty} and f_{empty} of the empty model resonator.

5.2 YbRh₂Si₂

YbRh₂Si₂ was the first compound to show clear evidence for a Kondo breakdown QCP from Hall effect measurements [44, 43], see Sect. 2.2.2. The key feature, the T^* energy scale, has been intensively investigated with electrical and magnetic transport measurements [44, 43, 46]. Within this work, it was attempted to obtain first spectroscopic information on T^* , by providing electromagnetic energy in the microwave range and observing the reaction of the electronic system of YbRh₂Si₂. As discussed in Sect. 3.3.6, there are several possible approaches to the experimental realization. The following section will present the results of the performed microwave measurements using CPW resonators (see Sect. 3.3.7).

Additionally, the electrical transport properties very close to the QCP of YbRh₂Si₂, at ultra-low temperatures, were accessed with the Vienna nuclear demagnetization refrigerator (see Sect. 3.3.2). Sample preparation and characterization preceding these measurements was part of this work and will be presented in Sect. 5.2.2. A phase diagram of YbRh₂Si₂ containing the relevant temperature and microwave energy scales of the experiments is shown in Fig. 5.11.

5.2.1 Microwave measurements

Microwave data analysis

Usually, two physically relevant quantities, the quality factor Q and the resonance frequency f_{res} , are extracted from a resonance curve by fitting an appropriate peak function to it. In theory the resonance should have a Lorentzian shape, but to account for background, noise, measurement biases, and frequency-dependent loss channels, several modifications to a Lorentzian can be made: For symmetric shapes, adding a constant and/or linear background can be sufficient. If the resonance shape is rather distorted and asymmetric, a so-called skew term (see Eqn. 5.3 below) has to be added. Bringing a highly conductive sample into the electromagnetic field distorts the resonance, similarly to the shape change in the conductivity-dependent simulation in Fig. 5.7. Following the analysis and comparison of different fitting methods by Petersan et al [107] we fit the absolute value of the transmission with an extended Lorentzian function

$$|S_{21}(f)| = A_1 + A_2 f + \frac{|S_{\text{max}}| + A_3 f}{\sqrt{1 + 4 \left(\frac{f - f_{\text{res}}}{\Delta f} \right)^2}} \quad . \quad (5.3)$$

As mentioned above, the skew term A_3f can be omitted for symmetric peaks, which are for instance observed for an empty resonator. The fitting procedure optimizes the parameters A_1 , A_2 , A_3 , S_{\max} , f_{res} , and Δf . f_{res} is the resonance frequency and

$$Q = \frac{f_{\text{res}}}{\Delta f} \quad (5.4)$$

is the quality factor of the curve.

The quality factor sums up all loss channels of the resonator as $1/Q = \sum 1/Q_i$, for instance radiation losses, dielectric losses, coupling to external structures, or coupling to the sample. If a metallic sample with the complex impedance $Z_S = R_S + iX_S$ is coupled to a resonating structure and considered as a perturbation of the electromagnetic field distribution, the losses due to the surface resistance of the sample, R_S , lead to a reduction of the quality factor. The imaginary part of the impedance, X_S , by contrast, results in a shift of the resonance frequency [27]:

$$R_S \propto \frac{1}{Q} - \frac{1}{Q_0} \quad , \quad (5.5)$$

$$X_S \propto \frac{f_{\text{res}} - f_0}{f_0} \quad . \quad (5.6)$$

The parameters Q_0 and f_0 refer to the properties of the empty resonator, where no coupling to the impedance Z_S is present. The proportionality factor depends on the geometry and other characteristics of the resonator. This simple relation is deduced for the case where the perturbation approach holds: The losses due to the sample dominate all other loss channels, but at the same time the electromagnetic field distribution is not significantly changed by the presence of the sample. When the sample is placed very close to the resonator and the shape of the resonance gets obviously distorted, the simple proportionality relation of Eqns. 5.5 and 5.6 does not necessarily hold anymore. For some resonator and sample geometries, the exact relations can be investigated, as has for instance been done for stripline resonators [77] and for various cavity geometries [108]. For our CPW resonators and irregularly shaped samples, a quantitative analysis cannot be done in a straight-forward way [76], but qualitatively R_S is still connected to $1/Q$ and X_S to f_{res} . In the above-mentioned calculation with the perturbative approach without relevant field distribution changes, the resonance frequency stays constant and $1/Q$ is proportional to the bandwidth Δf . In reality, the resonance frequency is affected by the presence of the sample and external parameters, so qualitatively it is instructive to look at the bandwidth Δf , which is a more direct measure of the resonator losses.

For this reason we mostly follow the evolution of Q , along with f_{res} and Δf with the measurement parameters.

Intrinsic resonator properties and measurement procedure

Several measurement cycles of YbRh_2Si_2 samples placed above a CPW resonators were performed. The samples were provided by C. Krellner and grown at the Max Planck Institute for Chemical Physics of Solids in Dresden, Germany (measured in the first and second measurement cycle) and at the Goethe University Frankfurt, Germany (measured in the third measurement cycle).

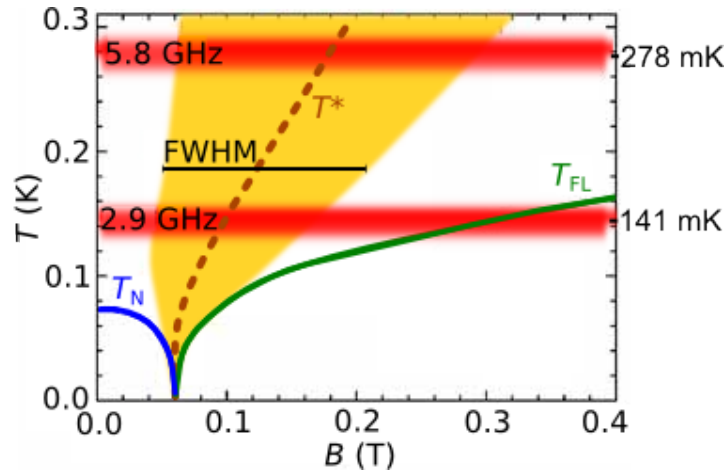


Figure 5.11: Low-temperature part of the phase diagram of YbRh_2Si_2 for fields within the tetragonal $a - a$ plane, with microwave excitation energies (adapted from [91]). The second harmonic mode at 8.7 GHz corresponds to 417 mK. T^* and the width FWHM are extracted from Hall effect and magnetoresistance measurements [43].

After a series of tests in a ^4He cryostat, the Cu box with the CPW resonator and the sample were mounted either in the Vienna demagnetization refrigerator (coupled to the mixing chamber) or to the Garching dilution refrigerator. During the tests, the position of the sample was optimized. There is a certain tentativeness to these tests, as the resonator properties still change between 4 K and 1 K (see Fig. 3.21); also the microwave lines and connections are different in each system and can have an impact on the success of a measurement. In other words, by testing everything at 4 K one cannot be sure to have the best system parameters for dilution refrigerator temperatures but it is at least likely that measurements at lower temperatures are feasible and produce quality factors in a sensible range.

Once the right configuration concerning the sample distance is set, everything is

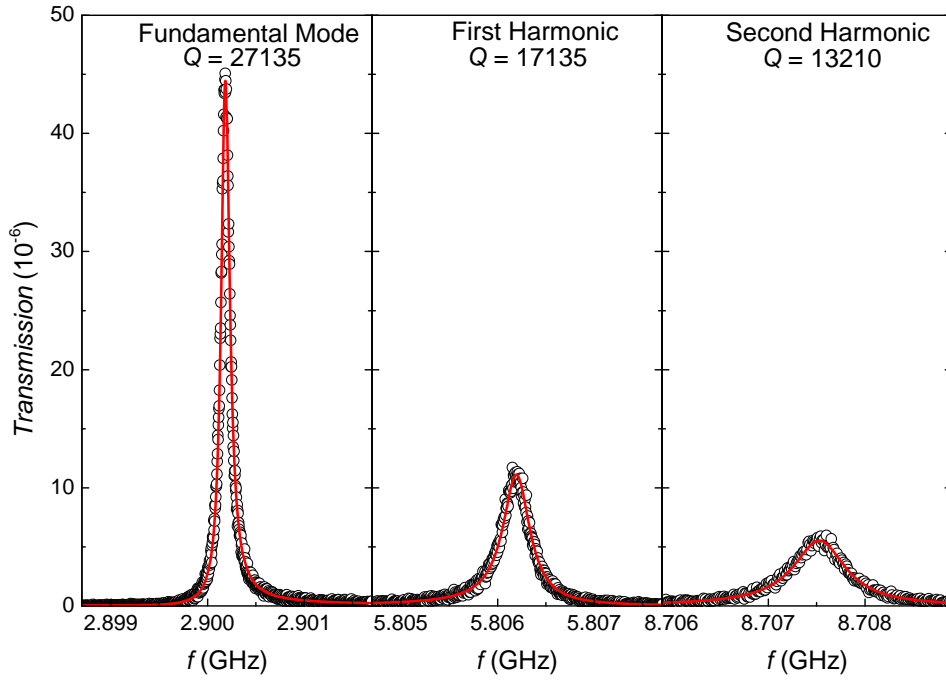


Figure 5.12: The three measured modes of the CPW resonator, coupled to an YbRh_2Si_2 sample: Raw data and Lorentzian fits after several sweeps of the field over the entire measured field range.

cooled down and the transmitted signal is analyzed. Figure 5.12 shows the three resonances which were observed and measured. The used design (fabricated by J. Majer and collaborators at TU Wien, and presented in Sect. 3.3.7) had a fundamental frequency at 2.9 GHz, the first and second harmonic are therefore found at 5.8 GHz and 8.7 GHz, respectively.

Several isotherms of the resonator and sample were recorded. A typical evolution of the resonance frequency with field can be seen in Fig. 5.13 (colour coded raw data sweeps (left), and resonance frequencies obtained from fits (right)). There is a shift in frequency as well as a strong broadening and a decrease of the quality factor Q with field. Another apparent feature in Fig. 5.13 is the strong hysteresis of the resonance frequency (black and red data points correspond to sweeping up and sweeping down the magnetic field, respectively).

In Fig. 5.14 (left), several hysteresis curves with different maximum field sweep values are shown. The hysteresis shapes scale with B_{max} . Also the quality factor Q shows a hysteresis (Fig. 5.14 (right), black and red data points correspond to sweeping up and sweeping down the magnetic field, respectively), but it is not as strong as that of the frequency. This behaviour is dominated by the characteristics of the resonator itself and

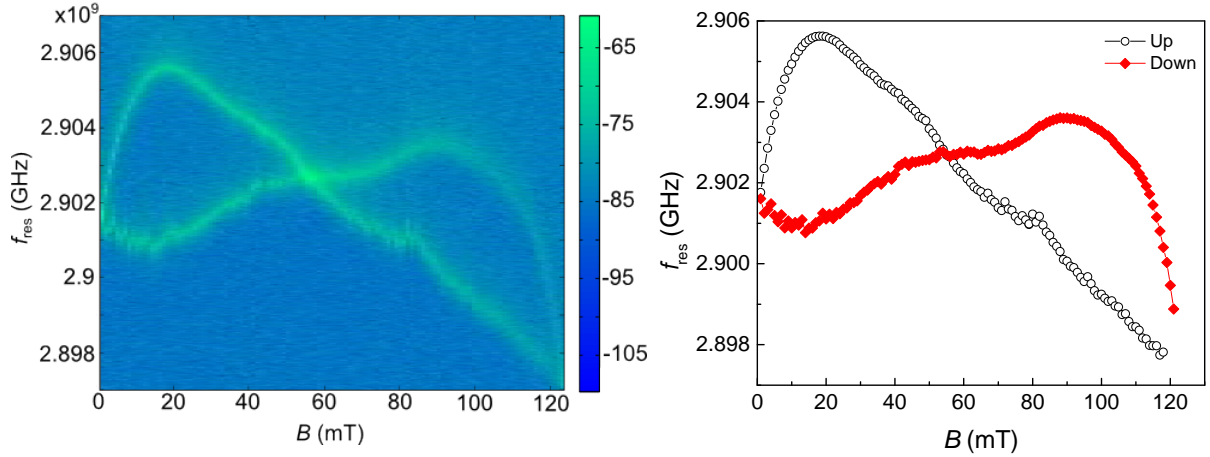


Figure 5.13: The resonance frequency f_{res} depends on the applied field B (in the plane of the resonator) and shows a strong hysteresis. *Left:* Raw data plot with colour coding of the transmission through the resonator in units of dBm over magnetic field and frequency. *Right:* Resonance frequencies obtained from the fitting procedure. Black datapoints were measured sweeping up the field, red datapoints sweeping down.

is typical for superconducting CPW resonators of Nb thin films [109]: It is basically the result of a particular redistribution of the induced currents and vortices in the superconducting film, which is not symmetric upon field direction changes. Sweeping up the field, the highest current density is built up at the edges of a superconducting conduction line, sweeping down the field the inverse effect (highest current density reduction at the current peaks at the edges) leads to a different current distribution and therefore to the observed hysteresis effect.

Although our field is meant to be applied in the plane of the Nb thin film, any unwanted misalignment will result in a field component perpendicular to the plane. A perpendicular component as low as a few mT introduces considerable losses due to trapped flux vortices. The hysteresis effects in our measurements, with 100 mT applied within the thin film plane, are of the same order of magnitude as in previous measurements, where a field of 4 mT was applied perpendicular to the thin film plane [109]. This suggests that our field misalignment is of the order of $\alpha \approx \arcsin(4/100) \approx 2.5^\circ$.

Due to the hysteretic behaviour, the measurement procedure for isothermal field sweeps was as follows: First, the field was swept up to the maximum value and back down for several times, until a reproducible hysteresis curve was reached. The sweeps become reproducible once the saturation number for trapped flux vortices is reached (for the respective maximum magnetic field). The vortices will stay trapped in the Nb

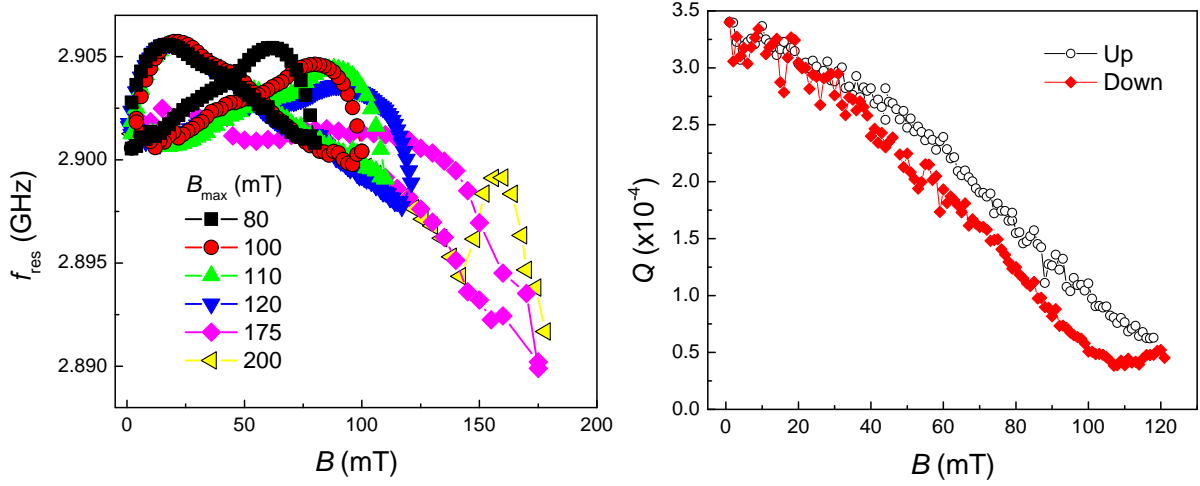


Figure 5.14: *Left:* Evolution of the hysteresis curves of the resonance frequency, if the maximum applied field is varied. *Right:* Hysteresis in the quality factor Q . Black datapoints were measured sweeping up the field, red datapoints sweeping down.

thin film until the normal state of Nb is reached again. Only when the field is further increased beyond the maximum field, additional vortices get trapped. After this initial cycling, the actual measurement was performed, sweeping the field in small steps and tracking the resonance with its parameters during the upward sweep. Figure 5.15 shows all extracted parameters of such field sweeps for the three measured modes of an empty resonator.

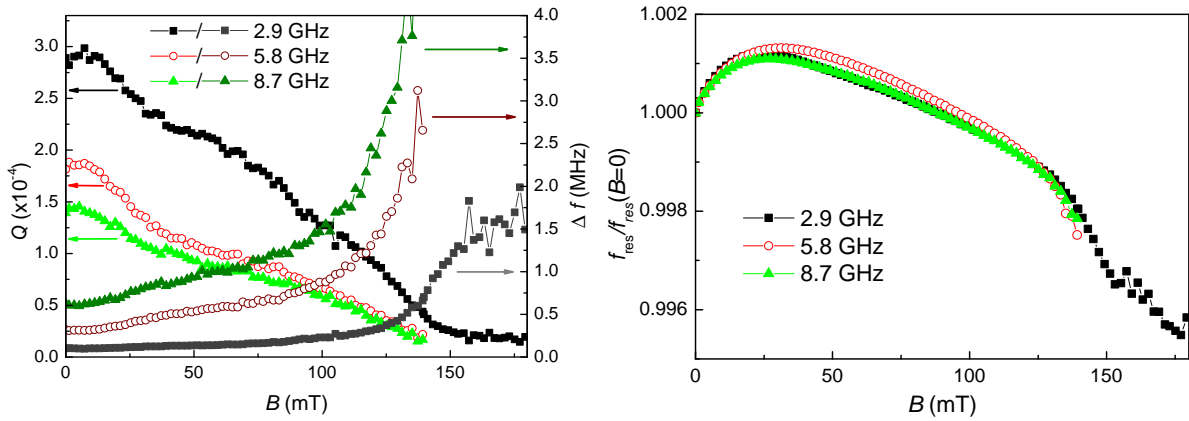


Figure 5.15: Field sweeps of the empty resonator at 45 mK. *Left:* Quality factor and bandwidth of the fundamental mode at 2.9 GHz, the first harmonic at 5.8 GHz, and the second harmonic at 8.7 GHz. *Right:* Evolution of the resonance frequency with applied field for the first three modes (scaled to their zero field value).

First measurement cycle

The first approach was to perform field sweeps, once in a configuration where the sample is placed above the resonator surface and once with the sample removed, using the same sweep parameters and the same resonator. In this approach the sample has to be positioned anew after every second cooldown. The absolute values of the parameters slightly change after every positioning, as the arrangement is sensitive to position and geometry changes.

The following data from the first measurement cycle were obtained in various cooldowns of the Garching setup. In the course of those, several experimental parameters were improved: Microwave and (quasi) dc cabling, thermometer locations and thermal anchoring of thermometers, handling and reliability of the magnetic field power supply. The setup at the Walther-Meissner-Institute for Low Temperature Research in Garching, Germany, was operated under the supervision of Hans Hübl and with support by Friedrich Wulschner, who also performed an important part of the technical improvements on the system. In the first measurement cycle, no amplifier was used, which lead to a comparatively high noise level and reduced the precision of the Lorentzian fit.

During the testing conditions in zero field, there is an obvious effect of the sample presence: The quality factor is reduced due to the losses in the sample; in absolute numbers, it is reduced from over 200,000 to 80,000, as can be seen in Fig. 5.16. This

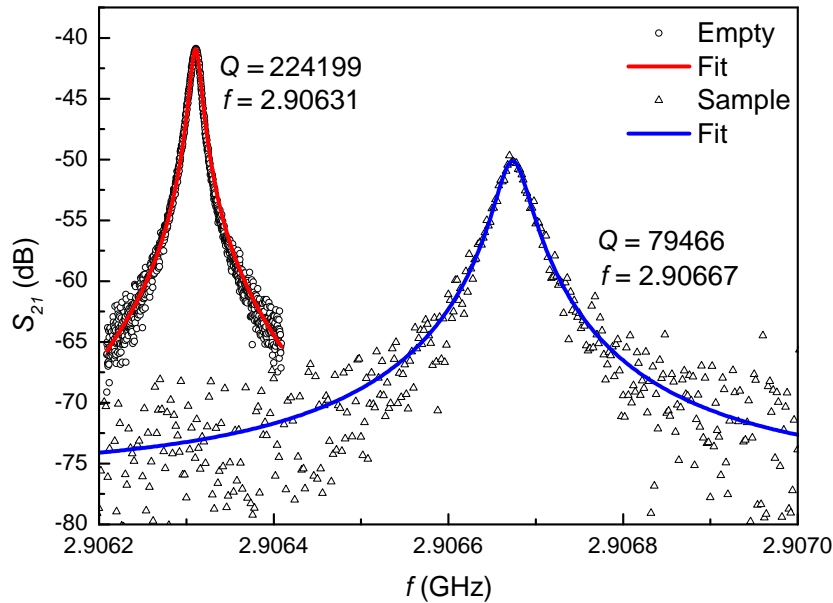


Figure 5.16: Resonance curves at 70 mK with and without the presence of an YbRh_2Si_2 sample of the fundamental mode, before any magnetic field was applied.

decrease in Q had been anticipated during tests at 4 K, and presents itself very clearly at dilution refrigerator temperatures. The curves in Fig. 5.16 were measured in the state before any magnetic field was applied, i.e. without trapped flux vortices.

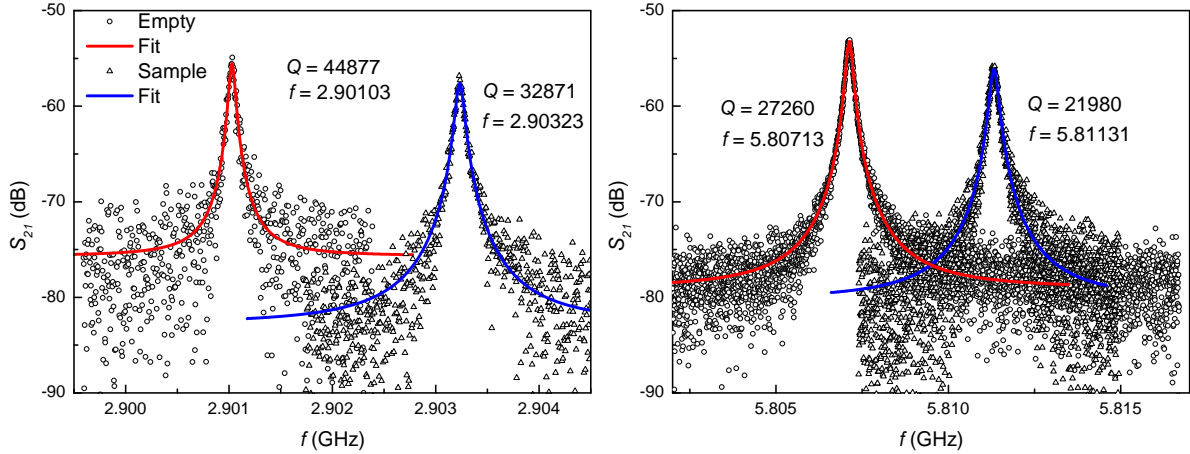


Figure 5.17: Resonance curves with and without the presence of a YbRh_2Si_2 sample at a temperature of 100 mK, after magnetic field sweeps. *Left*: 2.9 GHz. *Right*: 5.8 GHz.

After cycling the magnetic field (to obtain reproducible field sweeps, as mentioned above), the difference between the resonance curves with and without the sample is by far smaller than in the pristine state. Figure 5.17 shows the resonance curves at zero field after cycling the field for the fundamental mode Fig. 5.17 (left) and the first mode Fig. 5.17 (right). We can infer that the presence of the trapped flux vortices is a major loss channel in the resonators, and that the relative losses due to the sample are strongly reduced, yielding quality factors of similar magnitude with and without sample. When magnetic field is applied and Q is further reduced, the losses caused by the sample become irrelevant in comparison to the total losses such that Q factors with and without sample eventually converge.

Figure 5.18 (left) shows measurements with and without an YbRh_2Si_2 sample; for these cooldowns, the refrigerator operation had already been optimized to reach temperatures down to 40 mK. The effect of the sample is visible. Up to 80 mT, the quality factor with sample is reduced, above that value, the curves collapse and the field dependence of the empty resonator dominates. The frequency curve is slightly shifted in the presence of the sample, to slightly lower frequencies up to the maximum in f_{res} at about 30 mT and to slightly higher frequencies above 30 mT.

Ultimately, the focus lies on the relative changes of the sample properties with temperature, in particular on changes of features related to the T^* crossover in the temperature-

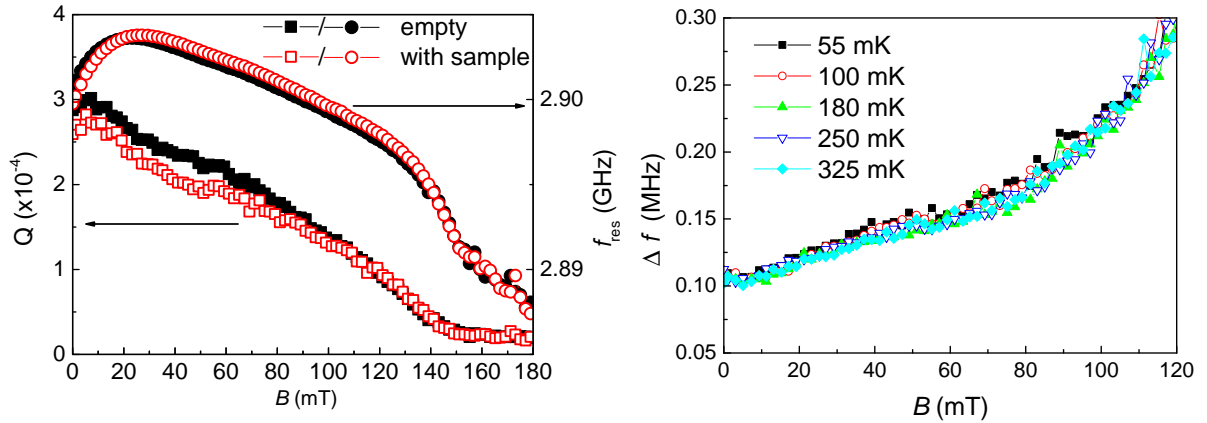


Figure 5.18: *Left:* Evolution of the quality factor and the resonance frequency with and without the YbRh_2Si_2 sample, at 55 mK. *Right:* Bandwidth of the field sweeps with sample at different temperatures.

magnetic field phase diagram. It seems that in the bandwidth at intermediate fields there is a slight difference between the curves measured at different temperatures, while at low and high fields the different curves collapse. However, the change of the quality factor difference and the change of the bandwidth (Fig. 5.18 (right)) is small and of the same order of magnitude as the measurement accuracy. The temperature evolution is too small to draw distinct conclusions from the systematic changes because of the noise level.

Apart from improved operation of the measurement setup, the conclusions of the first measurement cycle were that a stronger influence of the sample would be desirable in order to be able to unambiguously distinguish sample effects from noise. Improving the accuracy of the quality factor extraction would be useful as well. It was also concluded that a stronger focus on the temperature dependence would make sense, rather than a quantitative analysis of single curves by subtracting the background of the empty resonator, because different cooldowns are always subject to uncontrollable small offsets and changes. Furthermore, a control parameter would be desirable, that correlates possible features in the microwave measurements with sample properties and that provides feedback on the sample state (e.g. on temperature, quality); the most obvious choice seemed to be in situ dc (or low-frequency ac) resistivity measurements.

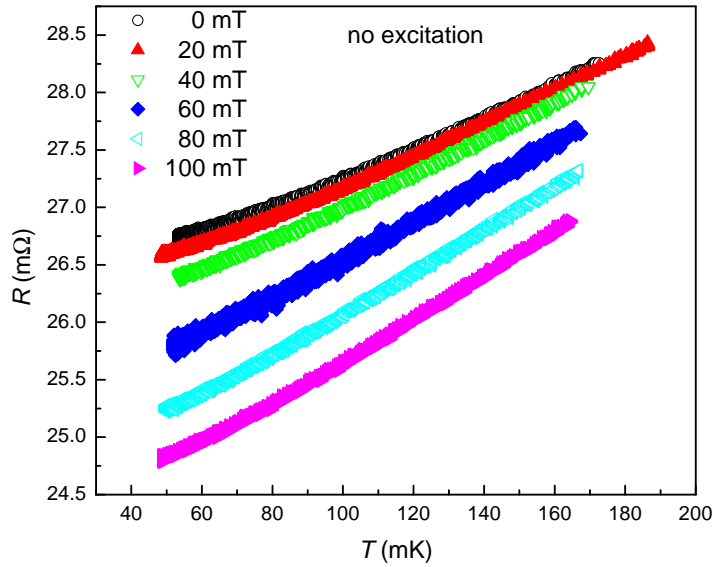


Figure 5.19: Resistance curves of YbRh_2Si_2 at different magnetic fields, measured inside the microwave box. No microwave measurement was running in parallel (therefore no excitation).

Second measurement cycle: stronger coupling to sample and in situ resistivity measurements

In the second cycle, the sample was placed much closer to the resonator surface and stayed in that position during the entire measurement cycle. A comparison to the empty resonator was only done during the placement procedure at ^4He temperatures. In contrast to the first measurement cycle, where the quality factor with sample was still of the order of 30,000, the quality factors were below 10,000 for all modes. Through the decreased distance, also the coupling to the different modes changed: In the first measurement cycle, the fundamental mode clearly had a higher quality factor than the first harmonic, and the first harmonic had a higher Q than the second (as also observed in the empty resonator, see Fig. 5.12). This order was inverted in the second measurement cycle.

During the second measurement cycle, it was possible to measure the resistance of the sample in parallel, as explained in Sect. 3.3.8. In the temperature dependence of the resistance (Fig. 5.19), the expected characteristic shoulder at the onset of antiferromagnetic order around 70 mK was not observed. This could either be a sign of poor sample quality or of a temperature offset between the sample and the thermometer. In order to exclude the latter option, the box was warmed up again after a first cooldown and a series of measurements. The contacts were reviewed and the thermal coupling between

the sample and the box was checked and improved without moving the sample.

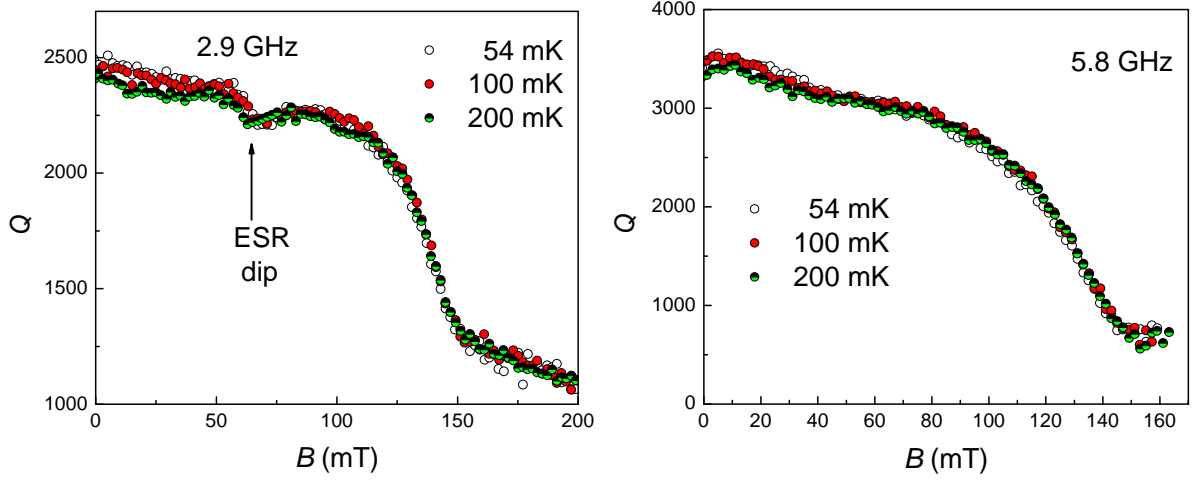


Figure 5.20: Evolution of the quality factor of a resonator with a coupled YbRh_2Si_2 sample with magnetic field, at different temperatures. *Left*: 2.9 GHz. *Right*: 5.8 GHz.

Quality factors and bandwidths of the first cooldown for the fundamental (left) and the first (right) modes are shown in Figs. 5.20 and 5.21, respectively. A new feature, a dip in the quality factor and a corresponding peak in the bandwidth, appears in the fundamental mode. It is absent in the higher modes; the first mode is shown for comparison. This feature is clearly not related to the empty resonator's properties, but

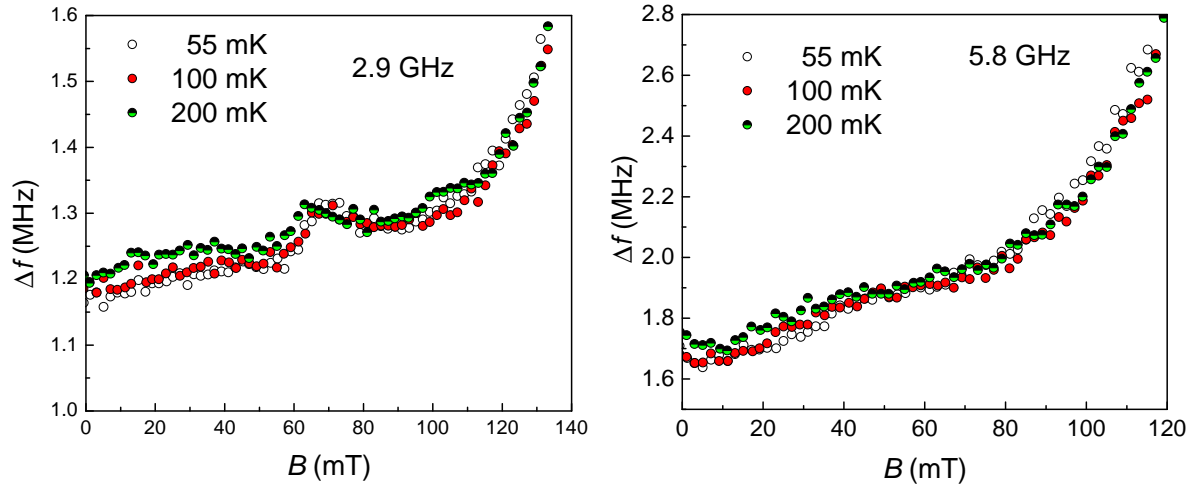


Figure 5.21: Evolution of the bandwidth with a coupled YbRh_2Si_2 sample with magnetic field, at different temperatures. *Left*: 2.9 GHz. *Right*: 5.8 GHz.

to the sample. We identify this feature as an electron spin resonance (ESR) signal. The electromagnetic energy flips the electron spins at this field. This increases the absorption

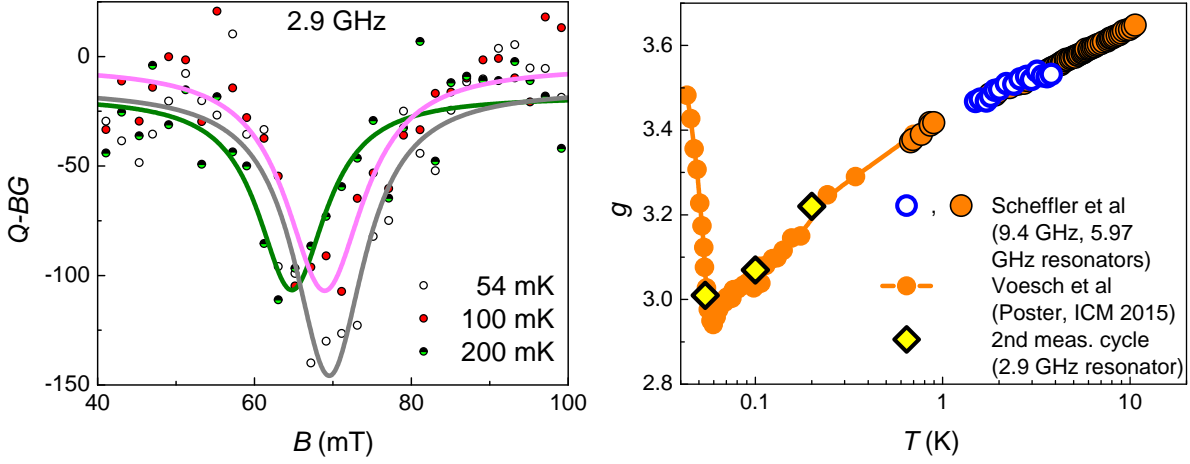


Figure 5.22: *Left*: Detail of the dip in the quality factor. A linear background has been subtracted, and the full lines correspond to Lorentzian fits to the ESR dip. *Right*: Comparison of calculated g factors with g factors from [76, 110].

and the electromagnetic losses in the sample and decreases the quality factor in a narrow field range, resulting in a dip in Q , see Fig. 5.22 (left). From Lorentzian fits to the dip we extract resonance fields of $B_{54\text{mK}} = 69.5$ mT, $B_{100\text{mK}} = 68$ mT, and $B_{200\text{mK}} = 65$ mT. The g factor can be obtained from the energy splitting of spin states due to the presence of a magnetic field,

$$g = \frac{hf_{\text{res}}}{\mu_B B} . \quad (5.7)$$

h is the Planck constant and μ_B the Bohr magneton. The calculated g factors are $g_{54\text{mK}} = 3.01$, $g_{100\text{mK}} = 3.07$, and $g_{200\text{mK}} = 3.22$. The g factor of YbRh_2Si_2 has been investigated recently at temperatures below 500 mK [76, 110]. As shown in Fig. 5.22 (right), the g factor values from the second measurement cycle are in excellent agreement with the reported values.

For the first harmonic, the resonance should be situated at approximately double the field, 2×70 mT. This is at the border of the recorded data range. In addition, the intrinsic losses of the resonator are so high in this high field range that the spin resonance curve is likely to be too broad and too flat to be observed. In contrast to the experimental approach used in [76], the experiments of this work were not primarily aimed at probing the spin properties, but rather at coupling to the charge of the conduction electrons. For this purpose, the sample was placed in a node of the magnetic field, where electron signatures of the ESR should have a minimal effect on the resonance. The fact that we still observe the corresponding dip in Q clearly shows that the spin properties are picked up strongly in the used CPW resonator approach.

As mentioned above, it was ruled out that self heating effects or bad thermal anchoring were the reason for the absence of the T_N signature before the second cooldown of the second measurement cycle. No undesired change of the sample position or loosening of surface and wire contacts could be found. The thermal coupling of the sample was nevertheless improved by adding thermal conductive Apiezon N grease and gluing a larger section of the Au wires to the Cu box. All presented data from this point on were measured in the second cooldown, with the same parameters as in the first cooldown.

The resistivity showed the same temperature dependence as before. Even though the T_N signature could not be found, the magnetoresistance corresponded to previously published data [43]: The crossover from a high-resistivity side at low fields (corresponding to the small Fermi surface state in the Kondo destruction picture) to a low-resistivity side at higher fields (corresponding to the large Fermi surface state) was observed, see Fig. 5.23.

In addition to the bare magnetoresistance data without microwave excitation, Fig. 5.23 (top) shows the magnetoresistance data at the same temperature under microwave excitation. The microwave transmission measurements in the fundamental mode at 2.9 GHz were running in parallel. During the lowest temperature runs at fields above 100 mT, temperature instabilities occurred, during which the entire system seemed to react strongly to specific magnetic field values, see Fig. 5.23 (bottom). For this reason, only the data up to a field of about 100 mT will be shown and the analysis will focus on lower fields up to approximately 80 mT, which could be measured more reliably. Despite this limitation, there seems to be a small but distinct characteristic at low fields: The magnetoresistance under microwave radiation levels off more slowly with increasing field than the magnetoresistance without radiation. This becomes most obvious at 60 mK and 100 mK, and it should be noted that at these temperatures the absolute temperature was on average slightly lower when the microwaves were applied, thus working against the observed effect. The normalized resistance curves were fit with the empirical crossover function [44, 43]

$$R(B) = R^\infty \frac{R^\infty - R^0}{1 + (B/B_0)^p} \quad . \quad (5.8)$$

R^∞ is the resistance saturation value at high fields, R^0 the zero field value (which is fixed for the normalized curves), B_0 the crossover field, and p determines the sharpness of the transition. The resulting parameters are given in Tab. 5.1.

Compared to previous measurements of the crossover in YbRh_2Si_2 , the step height is smaller. Whereas in the best samples measured in [43], the normalized resistivity

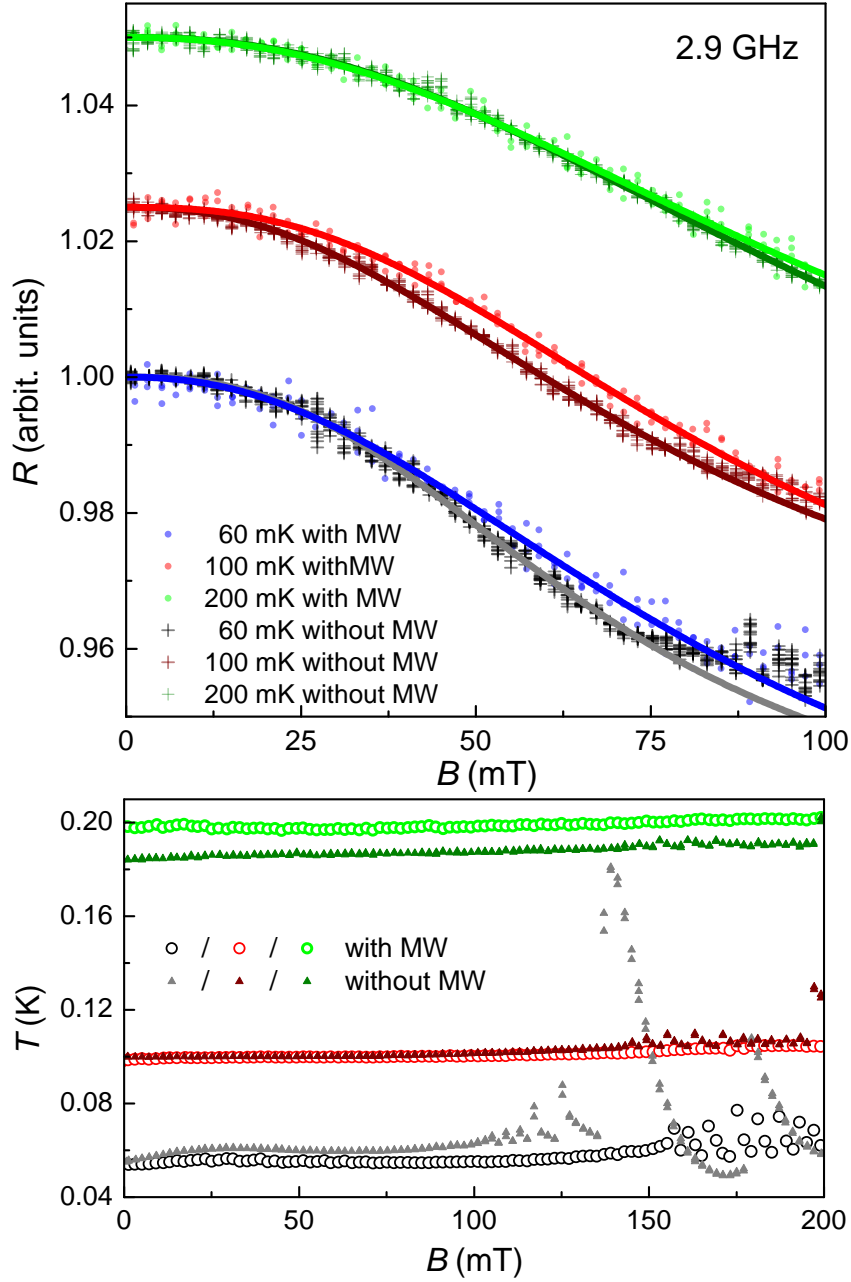


Figure 5.23: Top: Change of the resistance of YbRh_2Si_2 with field. Data points correspond to normalized raw data, lines correspond to smoothed data. An offset of 0.025 was added between the different temperatures. Some high-field portions of the data were left out due to the strong temperature oscillations in certain field ranges. The strong temperature reaction to the field change could not be removed in the second measurement cycle, so no data with higher accuracy is available for this coupling level. This issue was improved in the third cycle. Bottom: Temperature evolution during the resistance measurements.

Table 5.1: Overview of the fit parameters from fits with the empirical crossover function of Eqn. 5.8 to the magnetoresistivity data with and without applied microwave radiation. All fits were applied to the field region between 0 mT and 80 mT. To make the values of R^∞ comparable, all curves were normalized to 1 for the fitting procedures (without offset as in Fig. 5.23). The crossover field B_0 is given in units of mT.

T (mK)	R^0			R^∞			B_0			p		
	60	100	200	60	100	200	60	100	200	60	100	200
MW	1	1	1	0.92	0.93	0.92	84	86	110	2.23	2.52	2.26
no MW	1	1	1	0.94	0.93	0.92	63	80	110	2.70	2.28	2.34

decreases from $R^0 = 1$ to $R^\infty = 0.85$ at 65 mK and to $R^\infty = 0.78$ at 100 mK, the step height in our measurements is only 6% - 8% of the zero field value. This fact, and also a reduced change in the sharpness of the crossover, is possibly related to the sample quality. As also T_N of our sample could not be resolved in resistivity measurements, possibly due to its broadness, the behaviour of the crossover is also likely to be slightly different in this sample. The positions of the crossover field, however, agree rather well between the measurement without microwaves and [43]: Our values of 63 mT at 60 mK, 80 mT at 100 mK, and 110 mT at 200 mK compare to 78 mT at 60 mK, 81 mT at 100 mK, and 138 mT at 200 mK, respectively. The crossover field B_0 is the parameter that shows the most significant difference between the measurements with and without microwaves. At low temperatures, it is shifted to higher fields when microwave energies are applied. This indicates an effect of the microwaves on the electron dynamics: The magnetic field is tuned through the T^* crossover region and stabilizes the formation of heavy quasiparticles on the side of the large Fermi surface. At the same time, the microwave radiation breaks up heavy quasiparticles in a fraction of the sample and therefore prevents the resistance from reaching the same low value as without microwaves. As discussed in Sect. 3.3.6, the fractions of electrons affected by the microwaves is expected to be relatively small: For a sample thickness of 50 μm and a skin depth of 1 μm , the microwaves have access to a fraction of 2% of the electrons. If we estimate the full step height of the crossover to be about 0.08, and the visible effect due to the microwave radiation to be about 0.002 (around a field of 70 mT), we obtain a percentage of 2.5% of accessible electrons, which agrees well with the skin depth. The difference between the curves with and without microwaves decreases eventually when the temperature is increased, because the additional thermal energy also hinders the formation of the heavy quasiparticles. The microwave excitation energy gradually loses its relevance when the surrounding thermal energy becomes large in comparison, i.e. when the ratio $k_B T / \hbar f_{\text{res}}$

increases. Eventually, for $k_B T \gg hf_{\text{res}}$, the microwave excitations will not lead to any observable effect. The temperature instability at certain fields could not be improved in the second measurement cycle. Therefore, unfortunately, no in-situ resistivity data with higher accuracy are available for this coupling strength.

The evolution of Q with field for the three modes can be seen in Fig. 5.24, and the corresponding bandwidths of the resonance follow in Fig. 5.25. Small, but distinct

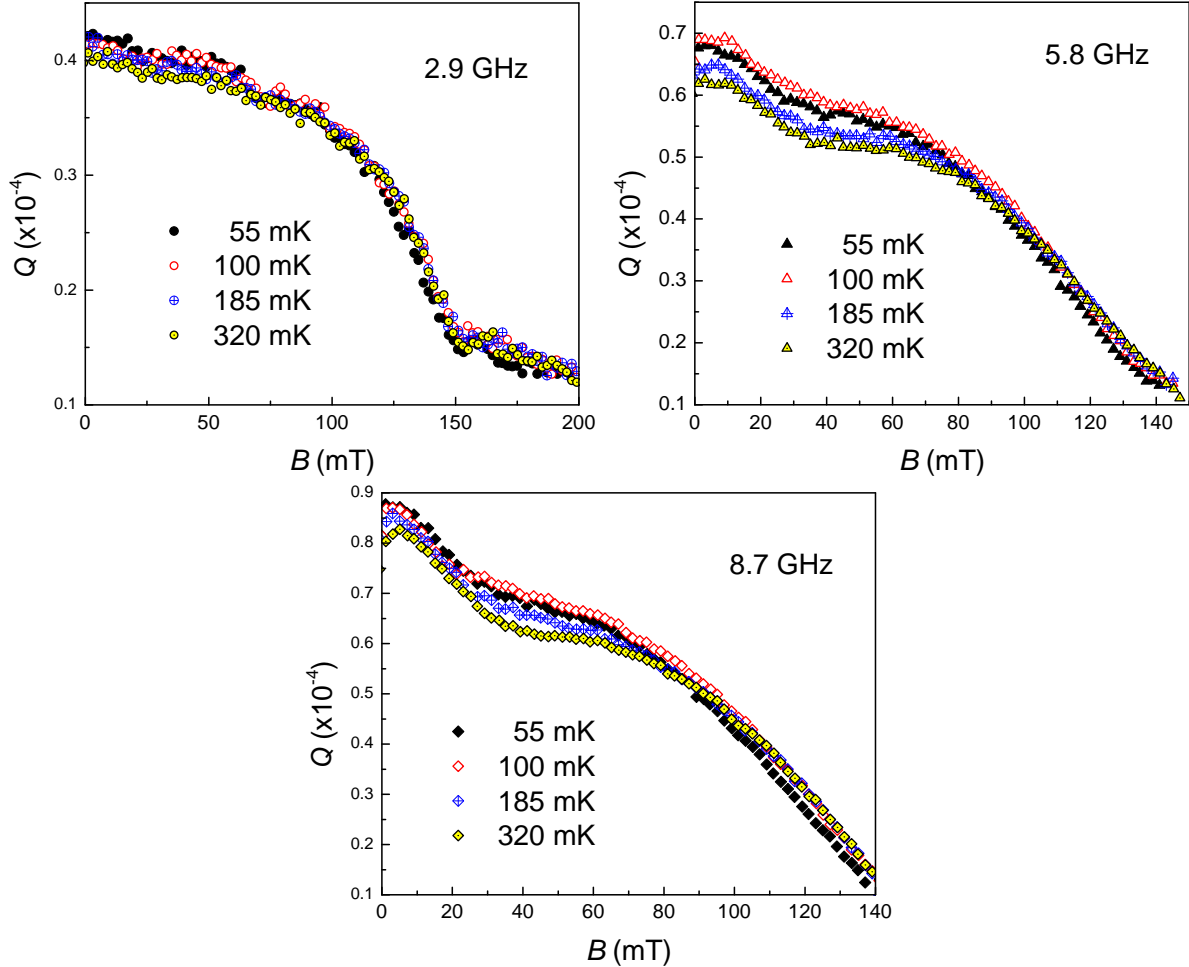


Figure 5.24: Evolution of the quality factor with magnetic field, at different temperatures. *Top left:* 2.9 GHz. *Top right:* 5.8 GHz. *Bottom:* 8.7 GHz.

differences are seen between the different isotherms. For the fundamental mode, the ESR dip at 70 mT is observed at low temperatures, but flattens out or gets covered by noise at 320 mK. The influence of temperature on the curves seems stronger in the first and second modes than in the fundamental mode. This suggests that the field distributions of the higher modes couple more strongly to the sample than the field distribution of the fundamental mode. To better quantify the temperature dependence,

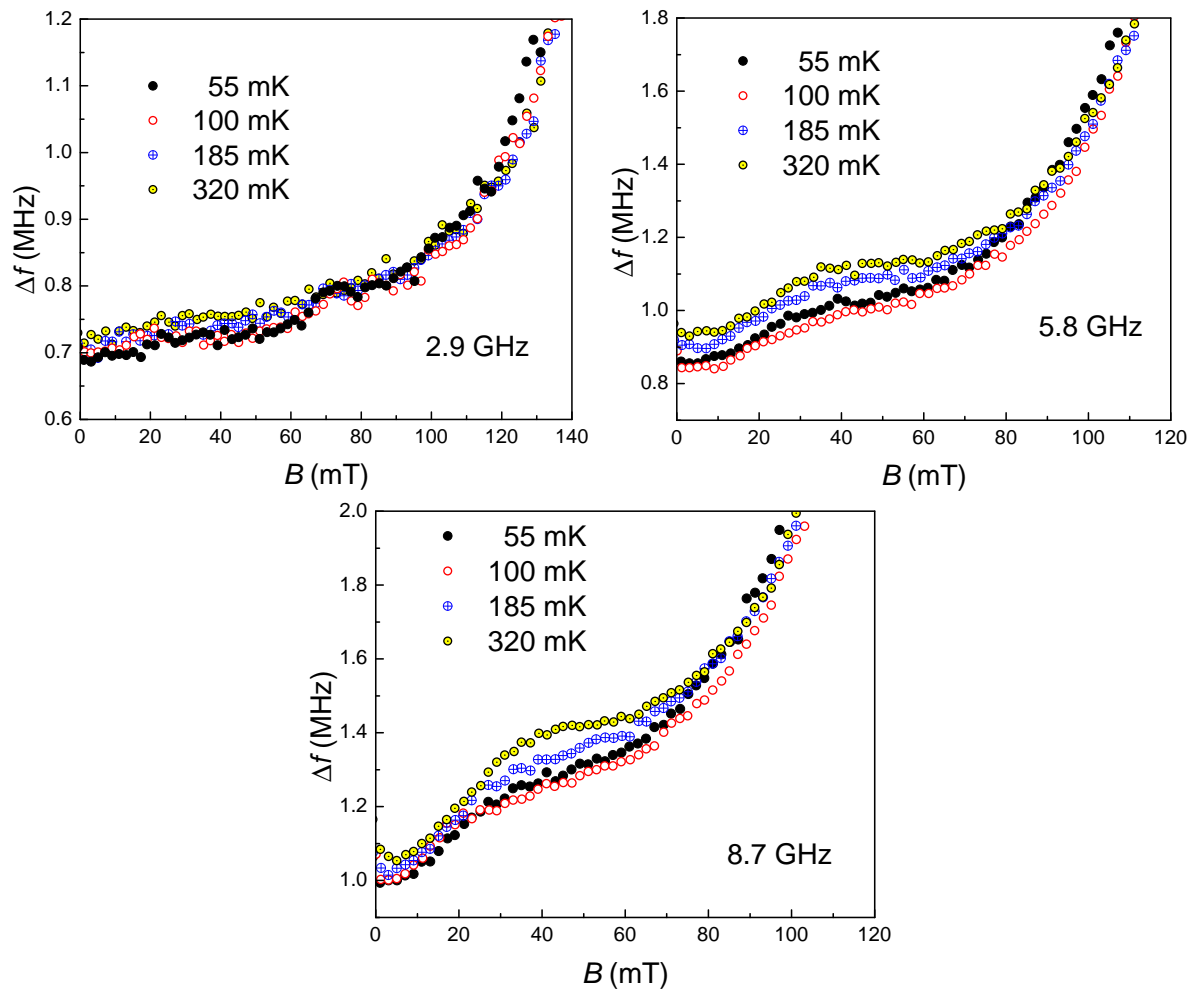


Figure 5.25: Evolution of the bandwidth with magnetic field, at different temperatures. *Top left*: 2.9 GHz. *Top right*: 5.8 GHz. *Bottom*: 8.7 GHz.

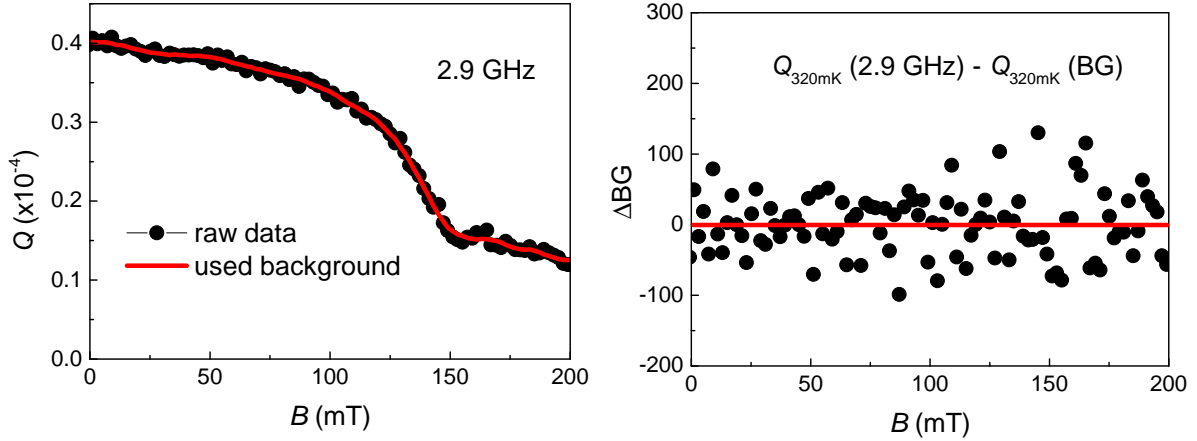


Figure 5.26: Quality factor Q at the highest measured temperature of 320 mK with corresponding background curve (left), and difference of data and background curve (right).

the curve at the highest temperature (320 mK) was subtracted from the other curves as a background. This background definition is justified in the sense that the crossover features of interest become sharper at lower temperatures (see Sect. 2.2.2). Nevertheless, as also the 320 mK data are likely to contain a broad crossover feature, the background is not perfect and may lead to some distortion of the different features. For the background subtraction, the Q curve was smoothed; as an example, raw Q data and the background curve are plotted together in Fig. 5.26 (left). In Fig. 5.26 (right), the difference between raw data and the used background curve is shown. It is smaller than a typical error bar for Q (± 200 and increasing with field) in the entire field range. Looking at the difference between the 320 mK data and the other temperatures in Fig. 5.27, a crossover between the low- and high-field Q factors is observed. The onset of the crossover in $Q - Q_{320\text{mK}}$ around 50 mT agrees well with the onset of the resistivity and Hall effect crossovers in the established phase diagram (see Fig. 5.11). As the Q factor depends inversely on the losses in the resonator, we will turn to the more instructive analysis of the bandwidths, which are proportional to the losses. A corresponding background subtraction can be done for the bandwidths (shown in Fig. 5.25). An example of such a background curve and the difference of background curve and raw data is shown in Fig. 5.28. All resulting bandwidth data are shown in Fig. 5.30. By performing this background subtraction, the large loss contribution from the resonator itself is removed, and it can be assumed that the remaining difference represents only resonator-independent loss channels. One such loss channel is the break-up of heavy quasiparticles by microwave photons. Starting at the schematic phase diagram and the resistivity crossover at low and high temperatures

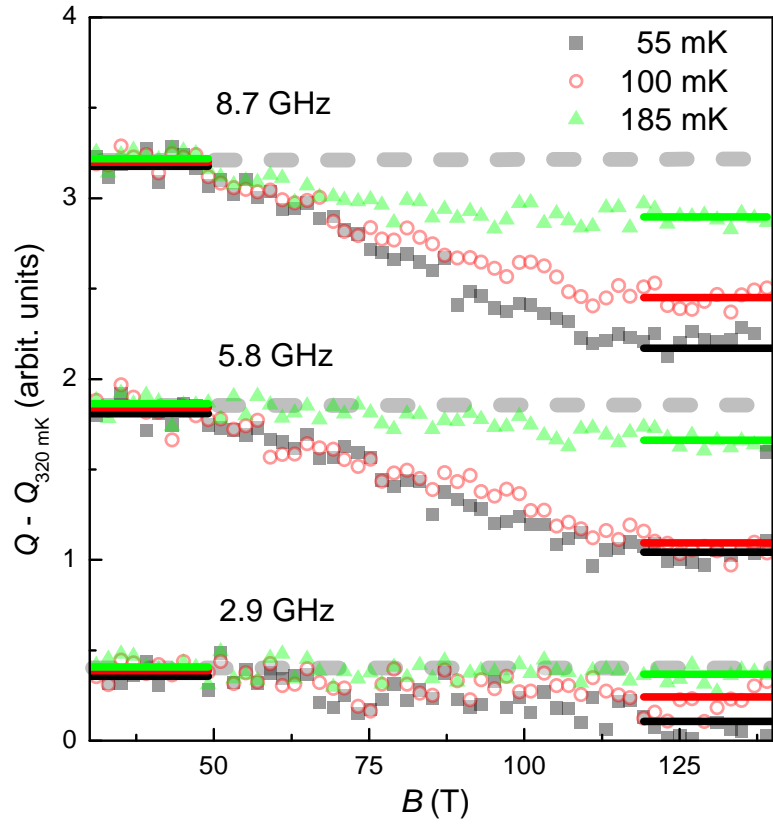


Figure 5.27: Crossover of the quality factor, with the 320 mK measurements subtracted as background. The difference is shifted by an offset of 1.5 for clarity.

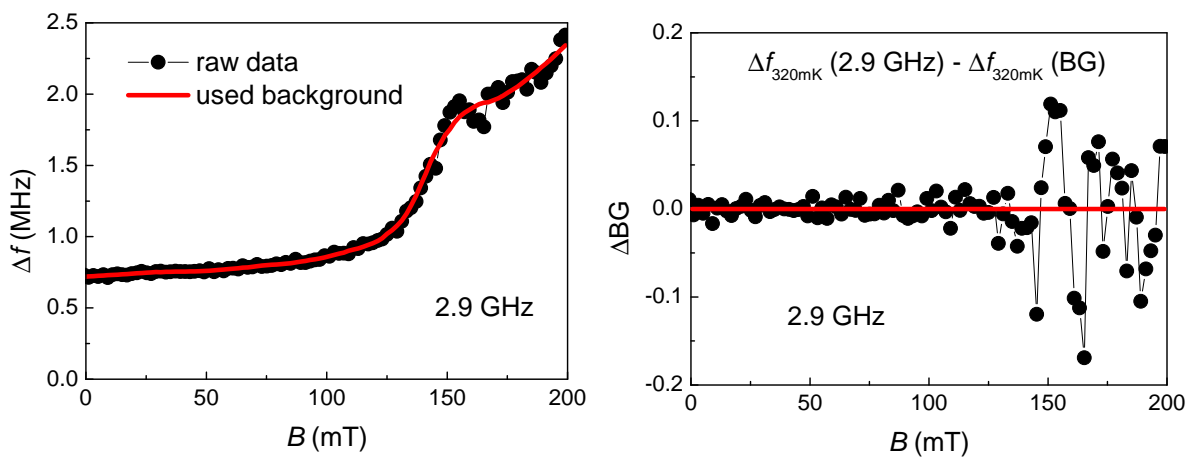


Figure 5.28: Bandwidth Δf at the highest measured temperature of 320 mK with corresponding background curve (*left*), and difference of data and background curve (*right*).

(Fig. 5.29 (top)), a comparison of the loss channels at different temperatures is shown in Fig. 5.29 (center). The difference of the loss contributions at high at low temperature is schematically shown in Fig. 5.29 (bottom). It shows a fast increase of the losses at the onset of the crossover at low magnetic fields, a maximum at intermediate fields, and a slow decrease upon further increase of the magnetic field. The performed background subtraction represents this difference.

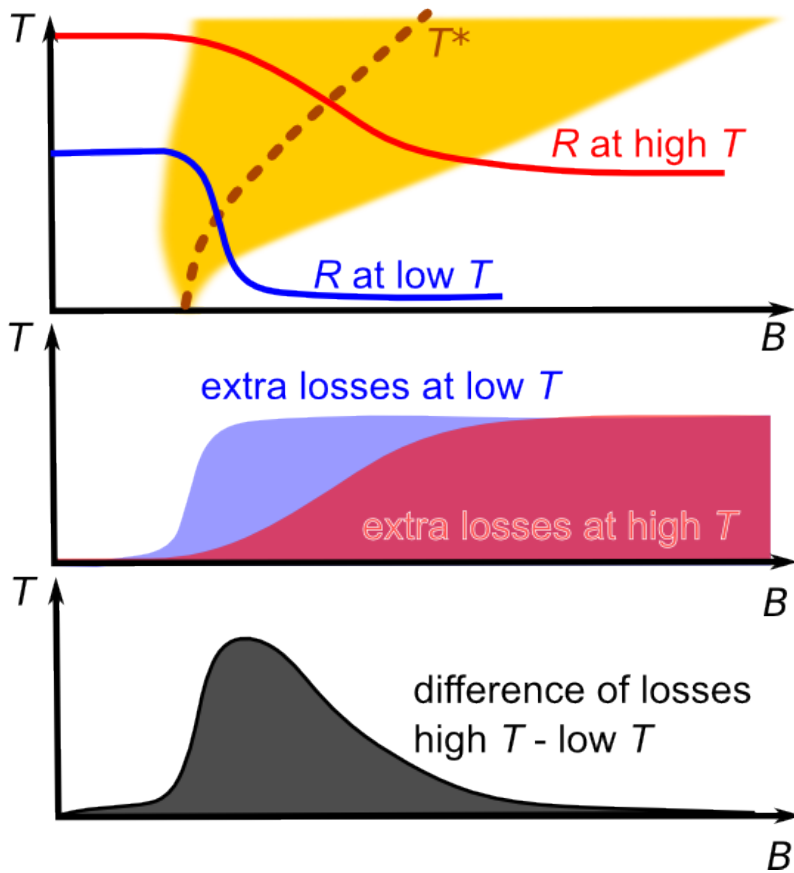


Figure 5.29: *Top:* Schematic phase diagram of YbRh_2Si_2 with the Kondo breakdown scale T^* and the corresponding crossover in the resistivity. *Center:* As the heavy quasi-particles form at a certain temperature, the microwave losses increase accordingly. The evolution of the losses at a higher temperature (in our case 320 mK) is shown in comparison to the evolution of the losses at a lower temperature (in our case 55 mK). *Bottom:* The difference of the losses at high and low temperatures, corresponding to a background subtraction.

There is only a small almost field-independent difference in the fundamental mode

(Fig. 5.30 (top left)), but in the higher modes field-dependent features appear and become stronger at lower temperatures. The observed curve shapes are very similar to Fig. 5.29 (bottom) and thus support the above interpretation of the interplay of microwave energy and T^* crossover: From fields of approximately 30 mT to 40 mT on, additional microwave absorption mechanisms set in, which are most pronounced for low temperatures and high frequencies. In terms of the Kondo breakdown scenario in YbRh_2Si_2 , these absorption mechanisms can be associated with the break-up of heavy quasiparticles by microwave radiation, which start forming in the corresponding field range and open up a loss channel for the microwave energy. The effect observed in the resistance measurements with and without microwave radiation is therefore also represented in the microwave properties.

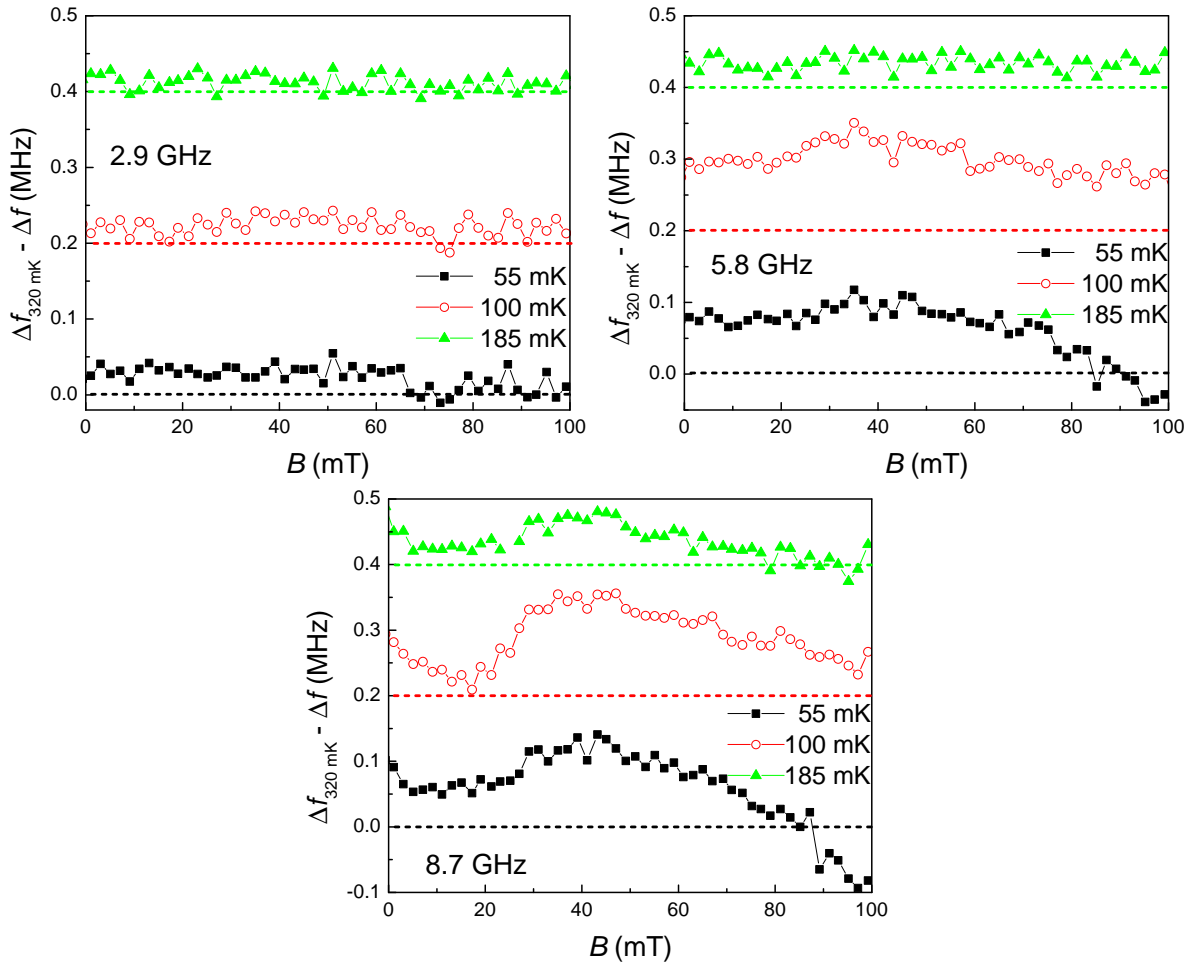


Figure 5.30: Difference of the bandwidths at different temperatures, shifted by an offset of 0.2 MHz between successive curves with increasing temperature for clarity. The respective zero lines for the different isotherms are shown as dashed lines. *Top left*: 2.9 GHz. *Top right*: 5.8 GHz. *Bottom*: 8.7 GHz.

Recently, the microwave response of the material YbRh_2Si_2 using a stripline resonator technique was investigated [111, 112], mainly focusing on qualitative changes of quality factor at specific points in the temperature-magnetic field phase diagram. In contrast to the measurements of this cycle, the temperature dependence at different fields was investigated rather than the field dependence. Figure 5.31 (left) compares normalized quality factors at 16 GHz from literature with data from this project at 8.7 GHz, both measured at an applied field of 125 mT. There is a similar change in slope, at a slightly higher or (within the error bar) similar temperature. The change in slope was interpreted as a transition between FL and NFL behaviour [111]. This signature is present in the datasets of the present work as well; it occurs at various resonance frequencies in the field region around 100 mT (Fig. 5.31 (right)) and becomes more pronounced with increasing frequency in both datasets.

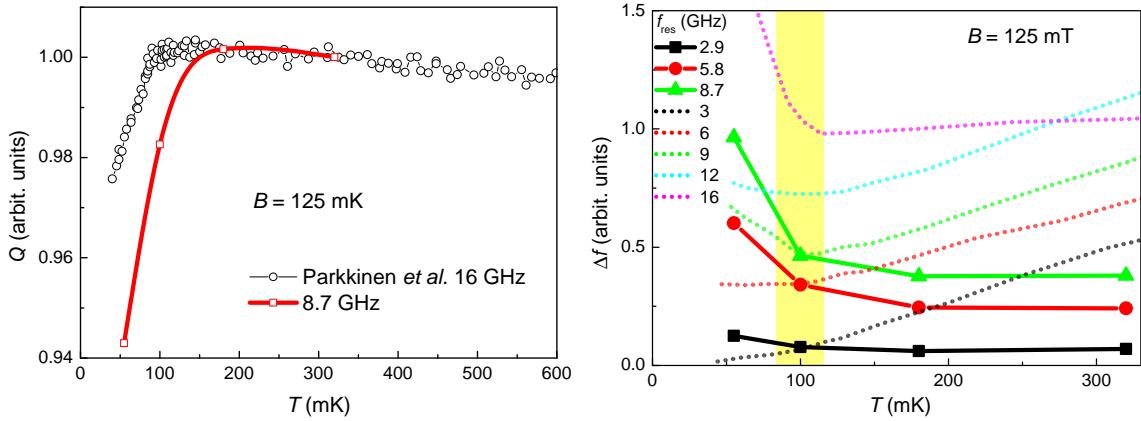


Figure 5.31: Left: Comparison of normalized quality factors at 125 mT (16 GHz [111] and 8.7 GHz). Right: Comparison of temperature dependence of bandwidths at 125 mT [111], normalized and shifted for clarity.

Third measurement cycle: sample of higher quality

Another sample was placed and positioned in the CPW resonator box, after testing the empty resonator's functionality. The sample quality is of greatest importance for ultra-low temperature measurements where a residual scattering can easily cover the relevant effects such as the intrinsic NFL power laws, but for the microwave measurements it was not considered of such great importance: Firstly, the microwave measurements are performed at temperatures above 40 mK. Secondly, higher intrinsic losses in the sample increase the effect of the sample on the resonator circuit. For these reasons, the samples of the highest quality were kept for transport measurements at ultra-low temperatures (see Sect. 5.2.2). After the second measurement cycle and the absence of the expected kink at T_N , one contacted high-quality sample was chosen to be moved from the nuclear demagnetization refrigerator (see Sect. 3.3.2) into the CPW box. Other high-quality sample pieces were too small for the microwave (plus in-situ resistance) measurements, so that the chosen piece turned out to be very large compared to the previous ones (approximately 5 mm x 3 mm instead of 2 mm x 1.5 mm). This fact led to a more challenging placement procedure, because accidental contact between the sample and other parts (e.g. bonding wires, PCB edge) is more likely to occur when a large sample is used. A similar absolute value of the quality factor as in the second measurement cycle was targeted. Field and temperature ramps were measured in the third measurement cycle.

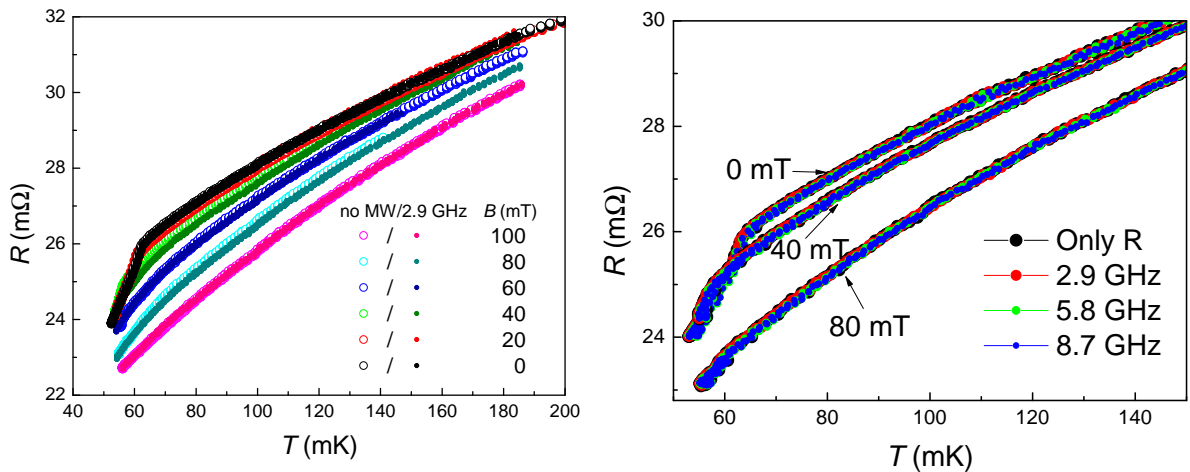


Figure 5.32: *Left*: Resistance curves with the characteristic kink at the onset of antiferromagnetic order, and suppression thereof with field. *Right*: More detailed measurement of the effect of radiation by microwaves during the resistance measurement. The datapoints for different incident frequencies show a nearly perfect overlap.

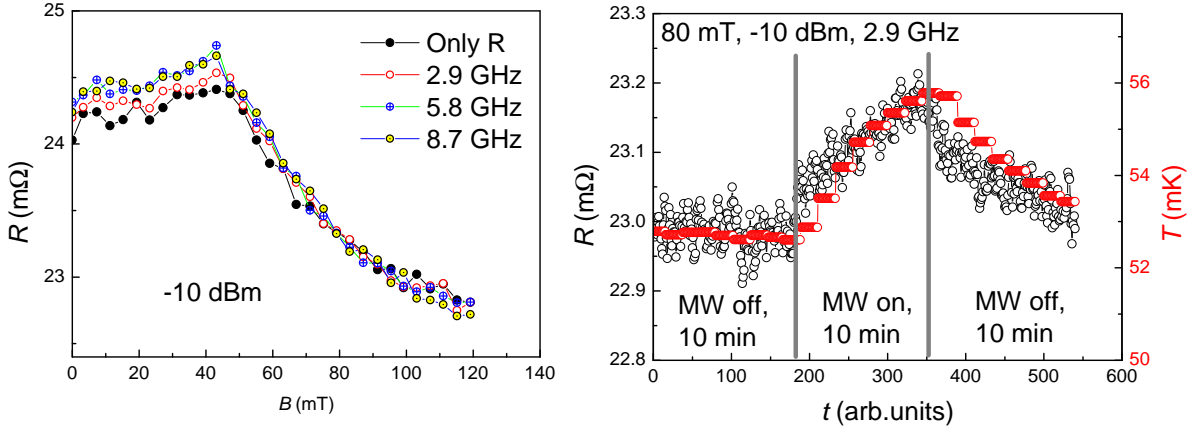


Figure 5.33: *Left*: Resistance field sweeps with different excitation modes at an increased power of -10 dBm at the microwave source. *Right*: Effect of microwave radiation on a resistance measurement.

Figure 5.32 (left) shows several temperature ramps at different magnetic fields, with and without irradiating the sample with the resonance frequency during the measurement. There is a prominent kink just above 60 mK in zero field, which shifts to lower temperatures with increasing magnetic field, the signature of T_N . The microwave radiation does not have a visible effect on the measurement, as shown in more detail for each frequency separately in Fig. 5.32 (right). This is, however, not surprising, since the effect of the microwaves on the resistance was already small in the field sweeps (see Fig. 5.27), where the crossing of the T^* region is better defined than in the temperature sweeps.

Several field sweeps were also carried out in the third measurement cycle: At each field value, the resonance frequency of the resonator was located, then this frequency was applied for a duration of 20 seconds before the resistance measurement was carried out. During the magnetoresistance measurement without microwave radiation, all microwave sources had been turned off for at least 20 seconds.

The high sample quality becomes apparent in the magnetoresistance measurements, where a typical small peak [43] around 50 mT is observed (see Fig. 5.33 (left)). However, no relevant difference between the different resistance measurements with and without microwave radiation was found. The distinct effect observed in the second measurement cycle (Fig. 5.27) could be covered by other effects in the third measurement cycle for several reasons: Due to an increased sample thickness, the contribution of the fraction within the skin depth to the resistivity is smaller. Due to the large size of the sample, the total absorption of the microwave signal can be in the same range as in the second

measurement cycle, but with a larger distance and a smaller effect of the sample's conductivity changes on the resonance. Furthermore, as also seen in the Fig. 5.34 the quality factor was of the same order of magnitude, but slightly higher than in the second measurement cycle. Thus, the coupling strength in the third measurement was lower than in the second.

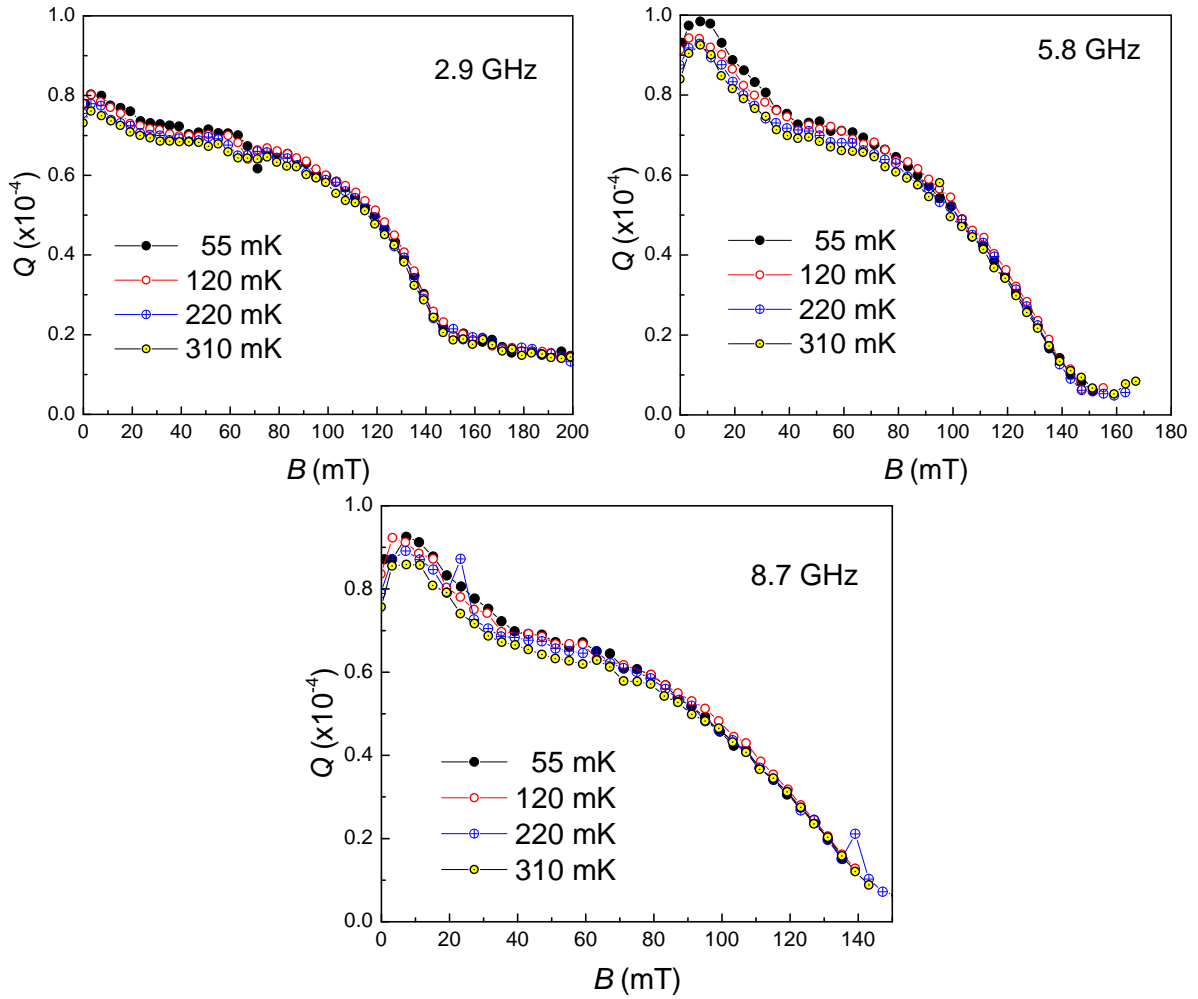


Figure 5.34: Evolution of the quality factor with magnetic field, at different temperatures. *Top left*: 2.9 GHz. *Top right*: 5.8 GHz. *Bottom*: 8.7 GHz.

In addition to the temperature and field sweeps, the effect of microwave radiation on the resistance was traced over a certain period of time: 10 minutes resistance measurements without microwave signal, then 10 minutes of measurements with incident radiation and another 10 minutes after switching the microwave source off (Fig. 5.33 (right)). In the time-dependent measurement it becomes obvious that the dominant effect, which is seen in the resistance, can be attributed to heating by the microwave ra-

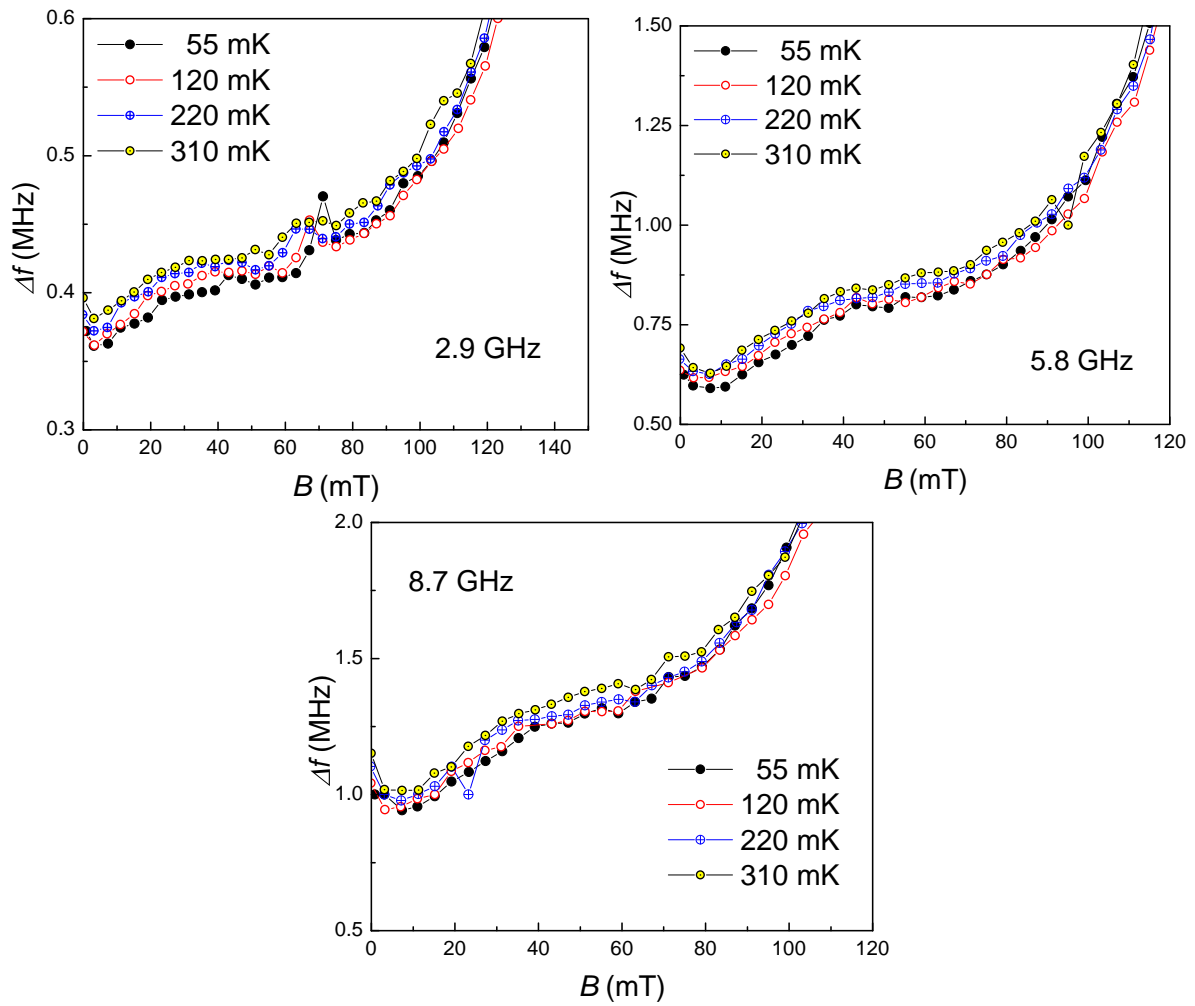


Figure 5.35: *Left:* Evolution of the quality factor with magnetic field, at different temperatures and 5.8 GHz. *Right:* Evolution of the bandwidth with magnetic field, at different temperatures and 8.7 GHz.

diation. Due to the coupling strength and size issues inferred from Fig. 5.32 and Fig. 5.33 (left), resolving the small contribution from microwaves breaking up heavy quasiparticles was beyond the measurement accuracy.

In the field sweeps (Q and Δf shown in Figs. 5.34 and 5.35), the spin resonance at the fundamental mode and 70 mK is the only obvious sample related feature. The quality factors are slightly different for different temperatures and below 100 mT, but unlike in the second measurement cycle, they evolve in parallel, with small absolute shifts. There is no evolution with temperature if the highest temperature is subtracted as a background, and everything remains equally flat. Although the quality factor is only slightly higher than for the previous sample, this seems related to weaker coupling and a weaker influence of the sample on the resonance, as mentioned above.

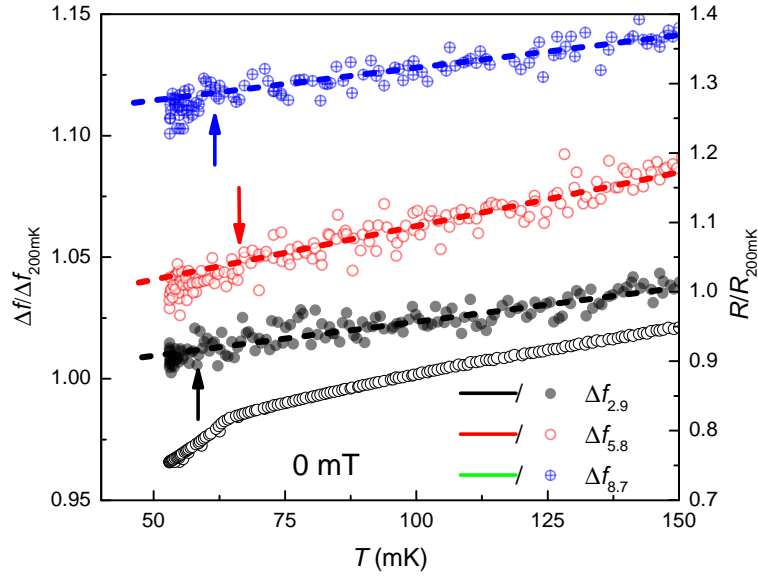


Figure 5.36: Normalized resistance curve and normalized total losses in the resonator with offsets of 0.05 (data points and guides to the eye). The low-temperature change of slope is indicated by an arrow.

Comparing the temperature dependence of the bandwidths at different resonance frequencies and the dc resistance (Fig. 5.36), it is once more pointed out that the sample resistivity is not a dominant contribution to the bandwidth. The relative resistance change is much larger than the normalized bandwidth change (for that reason, the bandwidth data are noisier than in the pure resistance data). Nevertheless, in the vicinity of the antiferromagnetic ordering temperature, a slight change of slope in the same direction is also observed in the resonance bandwidth Δf , similarly to reported measurements [111, 112].

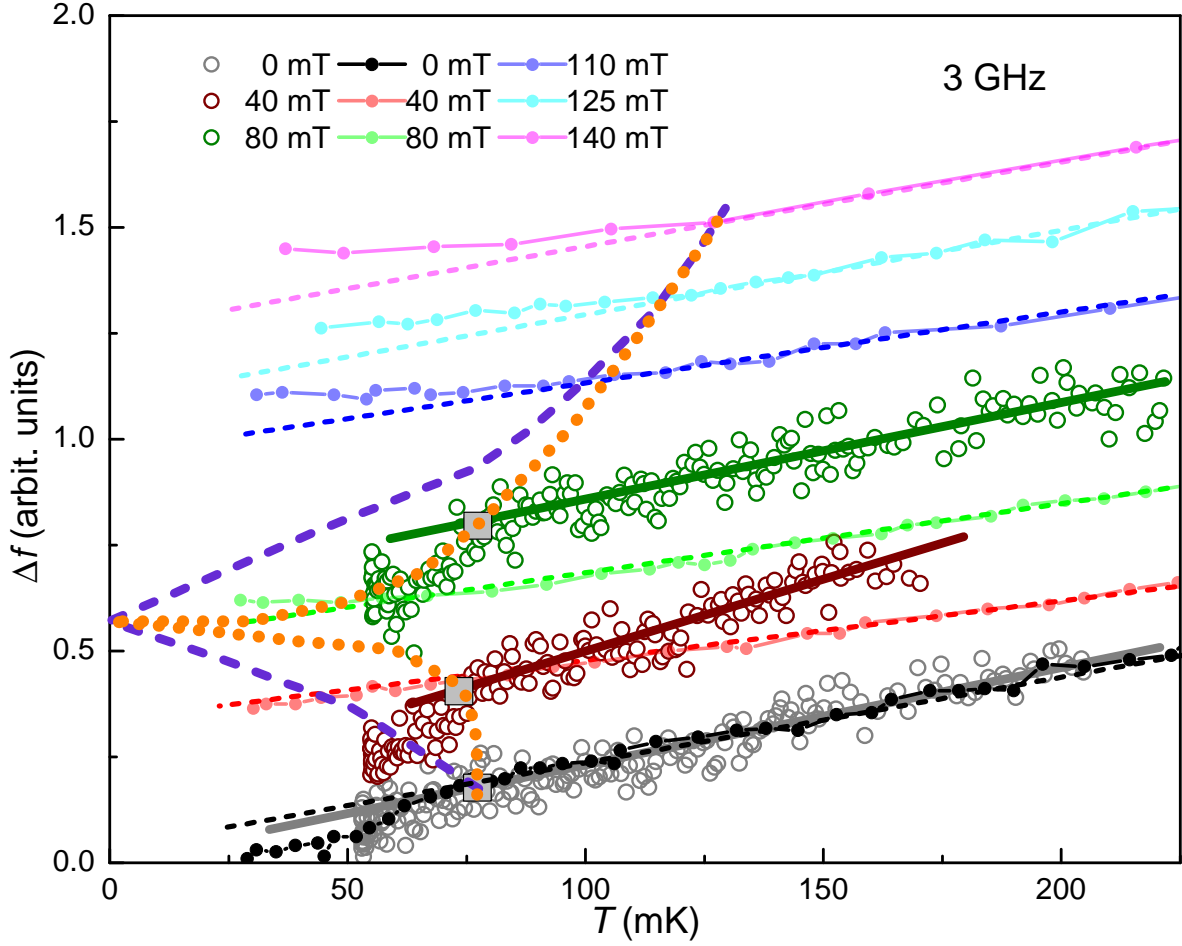


Figure 5.37: Comparison of the transition signatures in stripline resonator data at 3 GHz from [111] with the transition signatures in CPW resonator temperature sweeps at 2.9 GHz performed in the course of this work. Full dots correspond to data points extracted from [111], thin dashed lines in corresponding colours are guides to the eye indicating a linear temperature dependence. The thick dashed purple line connects the reported transition signatures [111], where the slope deviates from linear behaviour. Open circles correspond to data from the third measurement cycle, also accompanied by linear guides to the eye (full lines). The thick dotted orange line connects the transitions of CPW resonator data (indicated by the grey squares) and the transitions from stripline data at higher fields.

In Fig. 5.37 the temperature dependence of the microwave data are compared in more detail to the recent stripline measurements. Both stripline and CPW datasets refer to a resonance frequency of about 3 GHz (the exact frequency was 2.9 GHz in the CPW case). Similarly to the stripline data, slope changes are present in the CPW data. They were interpreted as signatures of a phase transition from the antiferromagnetic to the paramagnetic state (below 60 mT), and as signatures of the crossover from a NFL into a FL state (above 110 mT) [111]. When the CPW and stripline data are combined, the transition signatures are consistent with the phase diagram (Fig. 5.11). T_N decreases fast and rather linearly with increasing magnetic field in the stripline data (grey dashed line in Fig. 5.37), whereas the decrease of T_N is rather flat at low fields in the CPW data (orange dotted line in Fig. 5.37).

Summarizing the microwave measurements of the present work, the electrons in YbRh_2Si_2 were coupled to microwave radiation via their charge; this was attempted by placing the sample close to a node of the electric field in a CPW resonator. After a recursive placement procedure with consecutive tests in ^4He , the sample was kept at a fixed position. At this position, the resonance of the coupled CPW resonator was broadened, but still observable and of sufficient quality. For simultaneous resistance measurements, four Au wires were contacted to the sample via spot welding, and fed through the resonator box. The transmission through the resonator was measured with magnetic field and temperature as sweep parameters. In total, the contribution of the sample by the coupling of its complex impedance Z_S to the resonator circuit is low and difficult to resolve, especially for very good samples with absolute resistances in the $\mu\Omega$ range. It also depends strongly on the sample shape (size, thickness), resonator geometry, and the coupling strength.

In temperature sweeps, the effect of the sample is mostly covered by noise. Nevertheless, signatures of transitions are observed in the form of slope changes in the temperature dependence of the resonance bandwidth Δf . In field sweeps, which are more suitable to detect the T^* energy scale of the Kondo breakdown scenario, the contribution of the CPW resonator background is very large. The strongest effect was seen in the second measurement cycle at low temperatures, where the best coupling level to the sample was achieved. There, the resistance measurement with applied microwaves showed a crossover that was slightly shifted to higher fields compared to the measurement without applied microwaves, indicating a delay in the formation of heavy composite quasiparticles caused by the incident microwave radiation. Also the coupling to the electron spins via electron spin resonance (ESR) was observed. Measurements of

highly conductive samples in the electromagnetic field of a CPW resonator turned out to be very sensitive to many background factors, so that using non-superconducting resonators with optimized geometries (possibly for each sample size and shape) could be a promising alternative approach for bulk samples and provide more quantitative results. The thin film growth of YbRh_2Si_2 by molecular beam epitaxy is currently optimized in our group and will create possibilities for broadband spectroscopy at low frequencies.

5.2.2 Resistance measurements at ultra-low temperatures

Various YbRh_2Si_2 samples were contacted for transport measurements at ultra-low temperatures. There were pieces of different sizes (from dimensions below 1 mm x 1 mm up to nearly 5 mm x 5 mm) and thicknesses (from below 50 μm up to 300 μm). Various samples were cut from different growth batches and provided by C. Krellner (Goethe University, Frankfurt, Germany). They are poly-isotopic (including two isotopes with nuclear moments, ^{171}Yb , $I = 1/2$, natural abundance 14.3%, and ^{173}Yb , $I = 5/2$, natural abundance 16.1% [113]). In addition, mono-isotopic (^{174}Yb) samples were provided by J. Flouquet and coworkers (CEA, University of Grenoble, France).

Various surface characteristics occurred in the different samples (flat, with terraces, or porous due to the removal of In inclusions). Some examples are shown in Fig. 5.38. Most samples were contacted with six Au wires, except for the very small samples, which could only accommodate four wires. After contacting, they were mounted onto a sapphire piece and fixed with a small amount of Apiezon N cryogenic vacuum grease. In many cases, the wires were glued to the sapphire piece with a drop of GE varnish. This ensured that the wires could still be moved (e.g. for soldering to a contact pad) without applying stress to the actual spot-welded contacts.

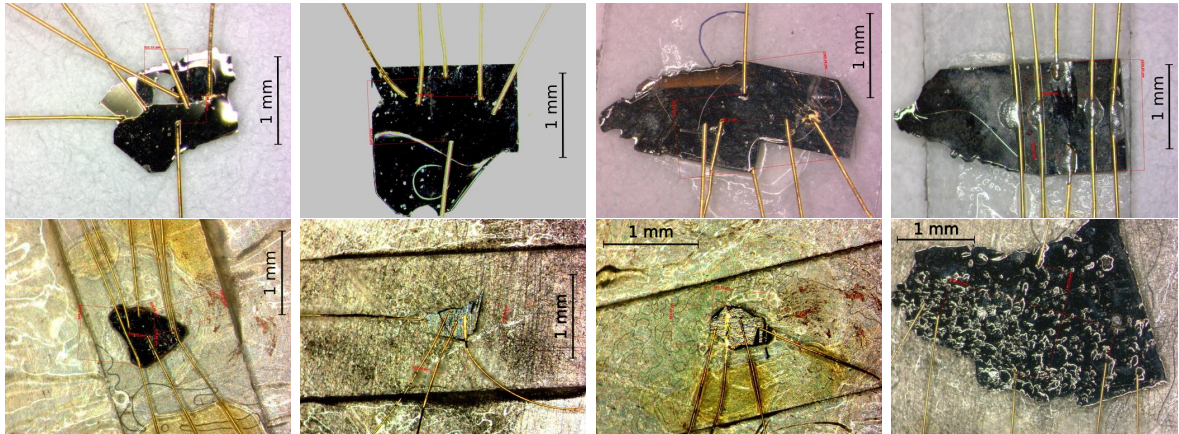


Figure 5.38: Various contacted YbRh_2Si_2 single crystal pieces.

Before mounting the sample pieces to the Vienna demagnetization refrigerator, their quality had to be tested. Even within one batch the sample quality can vary between different sample pieces, and the handling and contacting might also affect the sample's properties. The tests were carried out by measuring the electrical resistance in a pumped ^4He cryostat, and comparing the ratios between the sample resistivities at 300 K and 2 K. These ratios can be compared to literature, where the ratios at the same temperatures

are given in many cases (or alternatively the residual resistivity ratio ρ_{300}/ρ_0 with an extrapolation of ρ_0 , or the ratio ρ_{300}/ρ_4 at 4 K). In the ⁴He dewar, the samples under test were not in a vacuum pot, but immersed in a He gas atmosphere and therefore thermalization is expected to having been quick and effective.

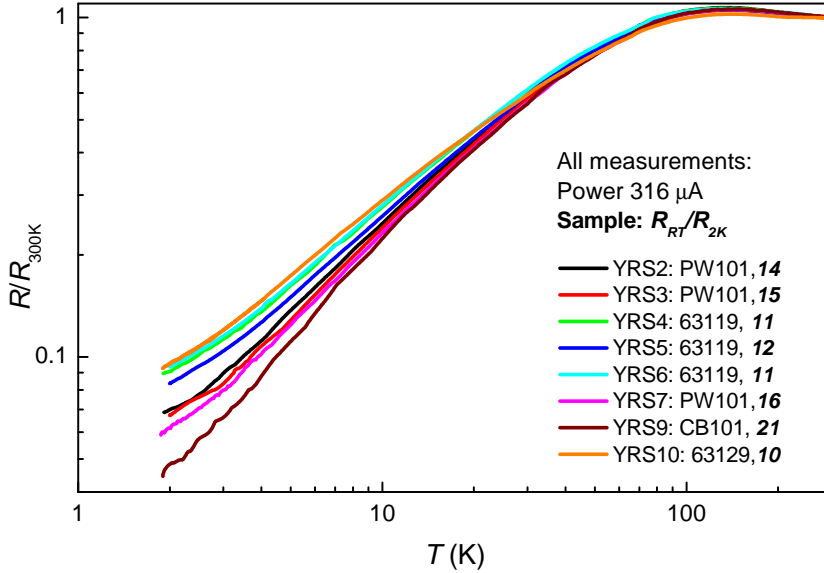


Figure 5.39: Comparison of several sample pieces with regard to their quality. Their curves have been normalized to the room temperature values, so that the quality is visually observable by comparing the low-temperature values. The sample of highest quality therefore is YRS9, with a ratio of R_{RT}/R_{2K} of 21.

An overview of the resistance curves of several tested samples is shown in Fig. 5.39. They were normalized to their room temperature resistivity value and plotted on a logarithmic scale. The ρ_{RT}/ρ_2 ratios in Fig. 5.39 vary between 10 and 21. The difference in quality is crucial, as for instance a sample with a ratio of 11 did not show a signature of antiferromagnetic order below 70 mK in our resistance measurements. A dilution refrigerator resistance measurement of two samples from the same batch (63119) with $\rho_{RT}/\rho_{2K} \approx 11$ is shown in Fig. 5.40 (left). In Fig. 5.40 (right), the resistivity of a sample with a ratio around 21 is shown for comparison: There, the kink at the position of T_N is a prominent feature.

Some of the samples (like the ones from Fig. 5.40) were installed to a dilution refrigerator before mounting them onto the nuclear demagnetization refrigerator. The ultra-low temperature measurements in the nuclear demagnetization refrigerator were carried out by A. Sidorenko and H. Nguyen: The samples were mounted to a ³He cell. The ³He cell (as for instance described in [115]) is constructed in such a way that superfluid ³He

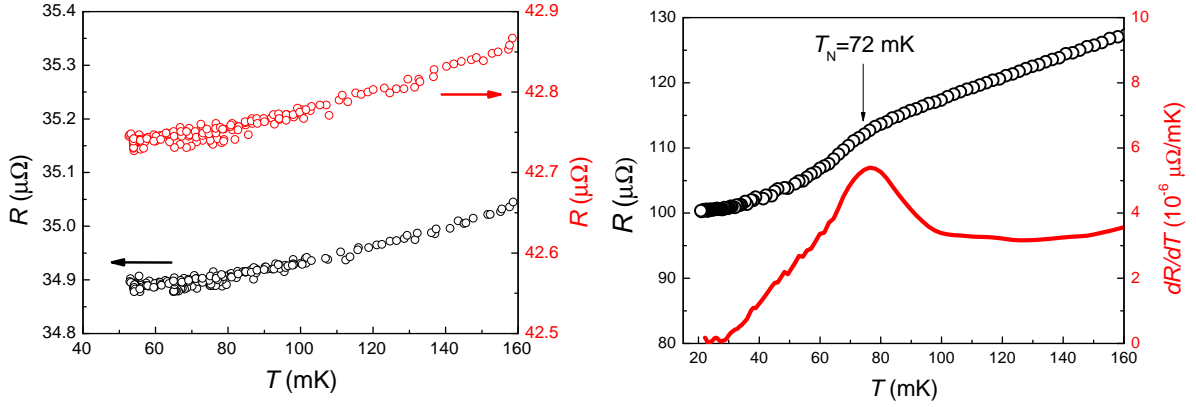


Figure 5.40: Left: Dilution refrigerator measurement of two YbRh_2Si_2 sample pieces (batch 63119), which do not show a signature of T_N . Right: Dilution refrigerator measurement and corresponding derivative of a high-quality YbRh_2Si_2 sample piece (batch PW101), revealing a clear signature at the onset of antiferromagnetic order and a transition from a linear temperature dependence above T_N to a quadratic temperature dependence below. T_N is located at the maximum of the derivative of the resistivity with respect to temperature, in this sample at $T_N = 72$ mK.

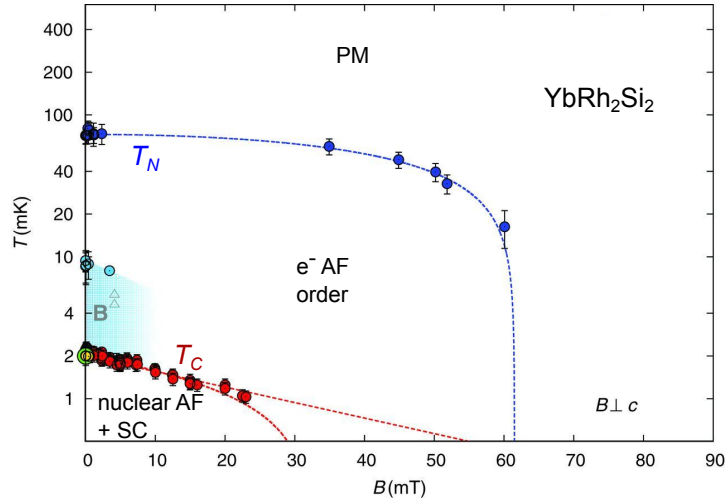


Figure 5.41: Phase diagram of YbRh_2Si_2 , obtained from magnetization and calorimetric measurements and extended to the ultra-low temperature region (adapted from [114]). The blue region indicated by the letter **B** indicates the onset of nuclear fluctuations. The dotted red lines represent possible continuations of the nuclear antiferromagnetic and superconducting phase.

thermalizes the samples effectively through its measurement wires. Additionally, the applied measurement currents have to be very small to avoid self-heating effects. In the case of very good metals with absolute resistances in the $\mu\Omega$ range, a precise resistance measurement requires the use of cryogenic transformers at a high transformation ratio of 300 or even 1000.

In view of recent reports on YbRh_2Si_2 and its phase diagram at ultra-low temperatures [114], resistivity measurements below 1 mK are desired to obtain more information on the physics of the tentative superconducting state and its connection to the QCP. Furthermore, the availability of isotope-enriched YbRh_2Si_2 samples with essentially no nuclear moments can shed some more light on the role of the nuclear spins and their interplay with the electronic properties. These investigations at ultra-low temperatures are ongoing. The material and contact quality of the prepared samples has so far been satisfying for the extreme temperature conditions: First resistance curves down to temperatures below 1 mK have been obtained for different applied magnetic fields and are shown in Figs. 5.42 (absolute resistivity) and 5.43 (normalized resistivity). At these ultra-low temperatures, a new feature was detected. It is indicated by upwards pointing arrows in Fig. 5.43 (left). The downward pointing set of arrows at higher temperatures indicates the onset of antiferromagnetic ordering, which is suppressed with field. The new low-temperature feature only occurs when fields between 50 mT and 90 mT are applied. The position of the feature delineates a dome-like phase above the QCP, a phase diagram region which is superconducting in various other heavy fermion materials (but there at higher temperatures) [36].

Further refinements on technical details concerning shielding, stray field effects, and measurement precision will be applied in the near future. These first findings will then be verified and complemented in order to obtain information on the nature of the newly found features and the interplay of superconductivity, antiferromagnetism, and nuclear moments in the vicinity of the QCP.

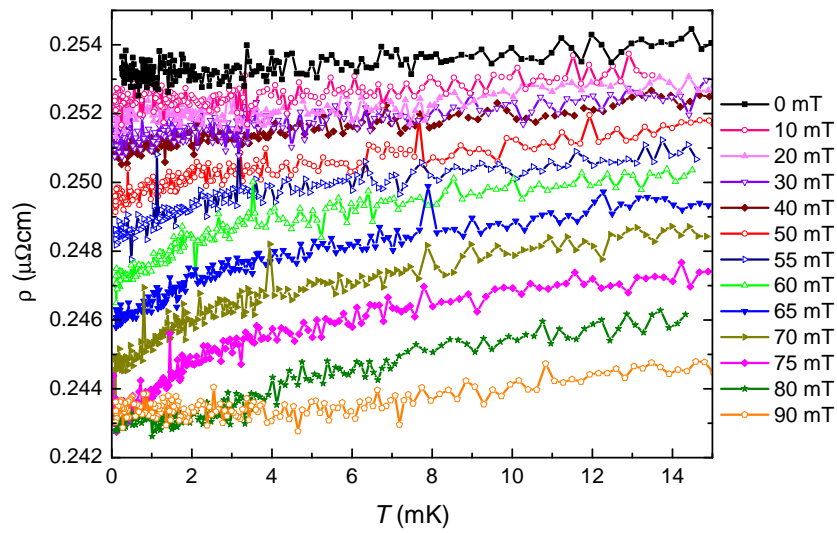


Figure 5.42: Resistivity measurements at ultra-low temperatures and various applied fields along the crystallographic c direction of one contacted sample (measurements performed by A. Sidorenko and H. Nguyen).

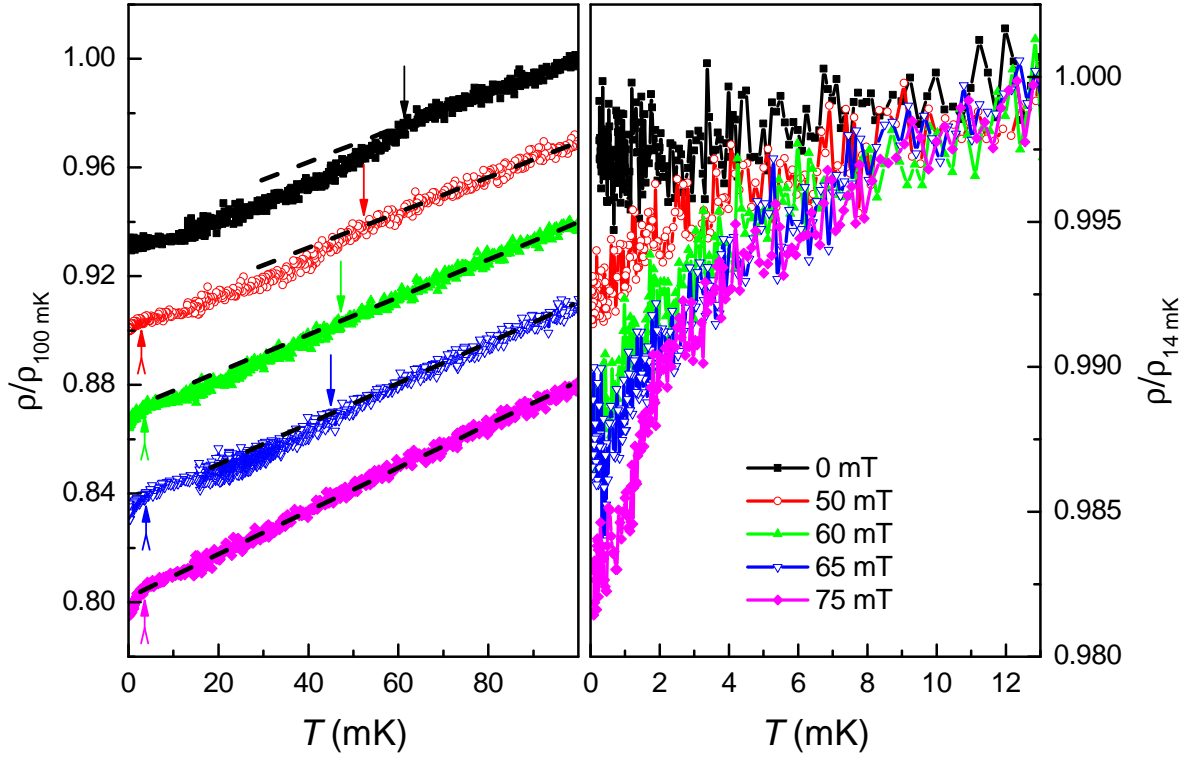


Figure 5.43: Left: Normalized resistivity curves, offset by 0.04 between adjacent curves for better visibility, at ultra-low temperatures and various applied fields along the crystallographic c direction of YbRh_2Si_2 (batch CB101). The arrows indicate the transition temperatures, where a slope change in the temperature-dependence of the resistivity occurs. Arrows with a single tail are directed at the antiferromagnetic transition, arrows with split tails at the new transition. *Right:* Detailed view of the low-temperature region at selected fields (measurements performed by A. Sidorenko and H. Nguyen).

5.3 CeNiAs_{1-x}P_xO

Iron-pnictide materials have attracted a lot of interest due to their intriguing properties such as the coexistence of superconductivity and magnetism [92]. A few years ago, researchers have started studying this material class in the context of quantum critical phenomena [11], joining material classes like heavy fermion materials [33, 91] and high-temperature superconductors [12].

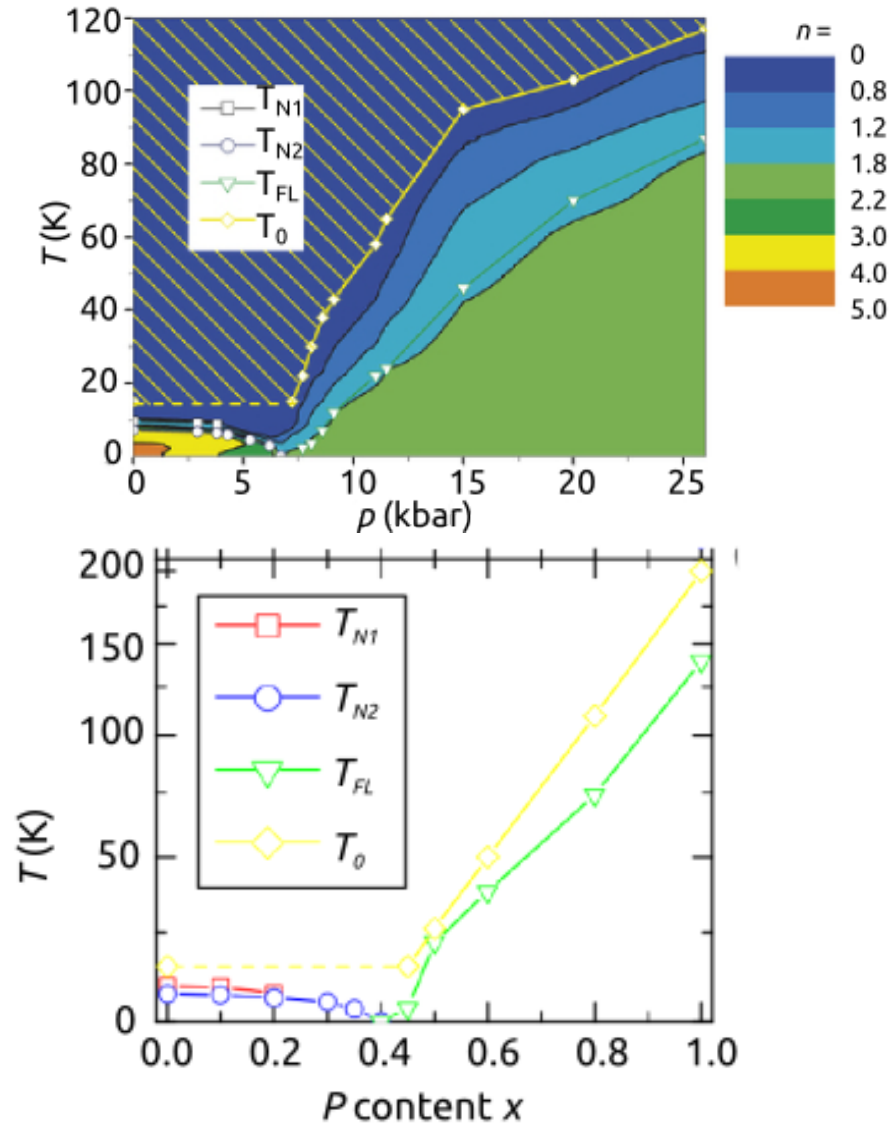


Figure 5.44: Top: Temperature-pressure phase diagram of the oxpnictide CeNiAsO [96]. Bottom: Temperature-P content phase diagram of the oxpnictide substitution series CeNiAs_{1-x}P_xO [96].

Investigations of quantum criticality in CeFeAsO and CeFeAs_{1-x}P_xO were reported previously [93, 94]. They revealed rich and complex magnetic phase diagrams. Following up on these results, the related compound CeNiAsO, where Fe is exchanged by Ni (making it a member of the nickel oxypnictides), has attracted attention. Unlike in CeFeAsO, where the 3*d*-electrons order antiferromagnetically, no magnetic order of the 3*d*-electrons is observed in CeNiAsO [95]. This leads to a reduced magnetic complexity and an easier access to the other electronic correlations. In particular, it permits to focus on the antiferromagnetic order of the Ce moments and its consequences. The hybridization between the Ce 4*f*- and the Ni 3*d*-electrons leads to heavy fermion behaviour with a Kondo scale of $T_K \sim 15$ K. The antiferromagnetic order can be suppressed either by applying pressure or by substitution with P [96]. In addition to pressure and substitution of As by P, magnetic field is also a tuning parameter that could affect the physical properties at low temperatures. During the course of this study, the main interest was the interplay of the different tuning parameters and their influence on the phase diagrams of CeNiAs_{1-x}P_xO (Fig. 5.44). The polycrystalline samples were provided by Zhu'an Xu and collaborators, Zhejiang University, Hangzhou, China. The preparation of the samples, the measurement stages, and the cabling was carried out together with J. Larrea. The dilution refrigerator measurements were supported by J. Larrea, G. Pristas, P. Popcevic, and K. Velebit.

Mainly the two substitution levels with P concentration $x = 35\%$ and $x = 40\%$ were investigated by resistivity measurements under different conditions. As part of the sample preparation, the sample surfaces were polished and Au wires were spot welded on the polished faces. The measurements were performed with a standard four-probe ac resistivity arrangement (see also Sect. 3.3.4). These preparation steps had to be carried out under Ar atmosphere to avoid oxidation of the samples and exposure of the experimentalists to hazardous powder residues. This was achieved by performing the sample preparation in commercially available inflatable glove chambers (fabricated by Glas-Col), which could be disposed after the process.

The resistivity of one sample of each substitution level was measured in a pumped ⁴He cryostat down to 2 K before mounting the samples to the dilution refrigerator sample stages, see Fig. 5.45 (left). The previously reported temperature dependence [96] was reproduced, and the test ensured that the quality had not been affected by the preparation.

In order to investigate the effect of hydrostatic pressure on the antiferromagnetic order of CeNiAs_{0.65}P_{0.35}O, a sample piece was installed in a CuBe pressure cell of self-

clamped piston-cylinder type. Kerosene was used as the pressure transmitting medium. The pressure was estimated according to the relative piston displacement, which was measured during the initial application of pressure. The relation between the piston displacement and the hydrostatic pressure inside the cell was established in several previous experiments, using the superconducting transition of lead as manometer. A comparison of the electrical resistivity of our CeNiAsO sample with published data [96] proved our pressure estimate to be consistent. Pressures up to 3.5 kbar and magnetic fields up to 10 T were applied. Additionally, a second 35% and a 40% piece were mounted on a Cu cold finger for measurements at ambient pressure.

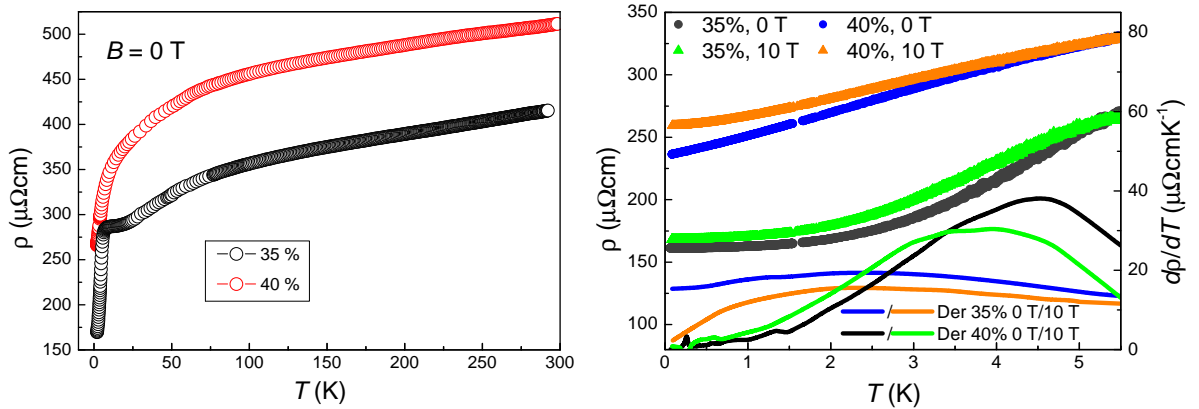


Figure 5.45: Left: Temperature-dependent electrical resistivities of CeFeAs_{1-x}P_xO for $x = 35\%$ and $x = 40\%$ at ambient pressure. Right: Temperature-dependent electrical resistivities at 0 T and 10 T for the sample with $x = 35\%$ around the antiferromagnetic transition and corresponding derivatives.

According to the phase diagram (Fig. 5.44) both substitution levels are very close to the critical point. Extending the temperature range to 50 mK confirmed the previous placement of the samples in the phase diagram: The antiferromagnetic transition is visible in the resistivity curve of the sample with $x = 35\%$; for the sample with $x = 40\%$, no ordering transition is observed down to lowest temperatures. This can be observed in Fig. 5.45 (right), where the temperature-dependent resistivity is shown together with its derivative with respect to temperature. CeNiAs_{0.65}P_{0.35}O shows a clear maximum is seen at T_N for both fields 0 T and 10 T . The derivatives CeNiAs_{0.6}P_{0.4}O only show flat and broad features, which is a typical behaviour of CeNiAs_xP_xO when T_N is fully suppressed and no antiferromagnetic order develops [96].

Resistivity of CeNiAs_{0.65}P_{0.35}O at ambient pressure

As can be seen in Fig. 5.46 (left), the temperature dependence of the resistivity is rather weak in the case of CeNiAs_{0.65}P_{0.35}O, and there is only a small change with field at fields below 5 T. From the raw data it becomes apparent that applying an external magnetic field does not trigger a strong reaction (for instance a dramatic change in slope). From the comparison of the data at the highest measured field, 10 T, with the zero field data in Fig. 5.45 (right), a shift of the inflection point (maximum in $d\rho/dT$) and thus of the ordering temperature to lower temperatures is seen.

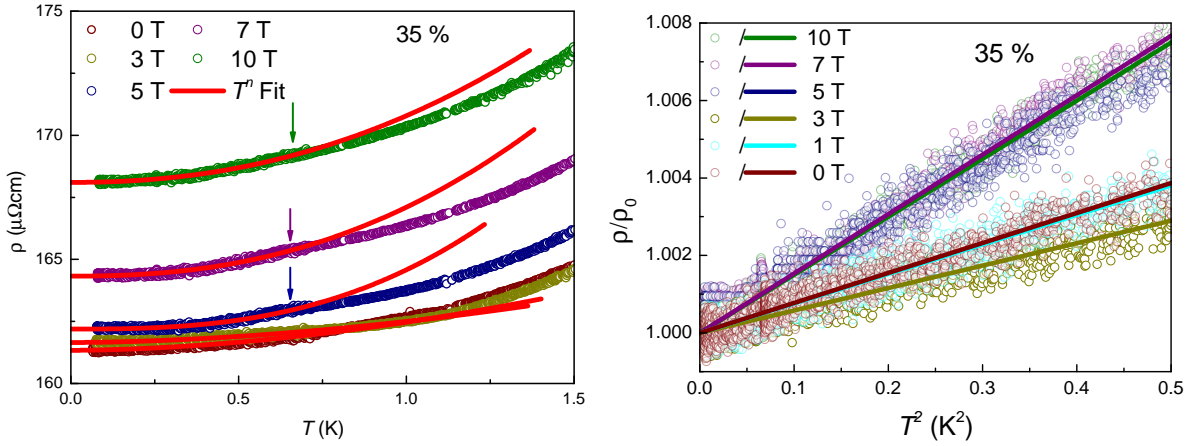


Figure 5.46: *Left*: Temperature-dependent resistivity of CeNiAs_{0.65}P_{0.35}O at different magnetic fields (linear scale). The red lines are power law fits (Eqn. 5.9) in the temperature range up to 700 mK. *Right*: Normalized resistivity data ρ/ρ_0 of CeNiAs_{0.65}P_{0.35}O, plotted vs T^2 . The full lines correspond to fits with Eqn. 5.10 up to 600 mK at the same magnetic fields.

In Fig. 5.46, resistivity data for CeNiAs_{0.75}P_{0.35}O are shown in zero field and at various magnetic fields up to 10 T. Power law fits

$$\rho(T) = \rho_0 + A'T^n \quad , \quad (5.9)$$

with fit parameters ρ_0 , A' and n , as well as a quadratic FL fits

$$\rho(T) = \rho_0 + AT^2 \quad , \quad (5.10)$$

with fit parameters ρ_0 and A , were applied to the data. The power law fits of Eqn. 5.9 were applied to the temperature range up to 700 mK and are shown in Fig. 5.46 (left). As the fit parameter n takes values around 2, the FL fit of Eqn. 5.10 can be applied in a rather large temperature range up to 600 mK. Normalized resistivity data at different

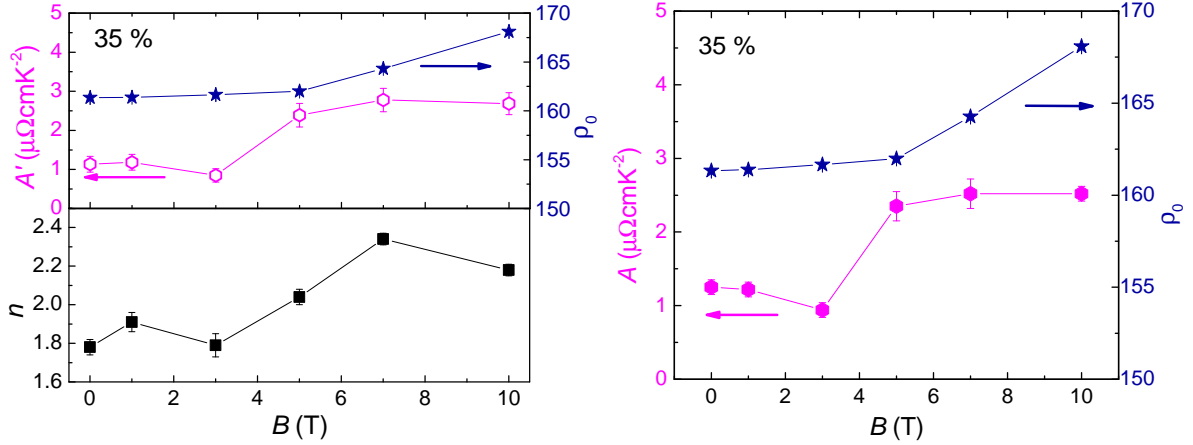


Figure 5.47: Left: Evolution of the fit parameters A' , n , and ρ_0 from fits to CeNiAs_{0.65}P_{0.35}O resistivity data according to Eqn. 5.9. Right: Evolution of the fit parameters A and ρ_0 from fits to CeNiAs_{0.65}P_{0.35}O resistivity data according to Eqn. 5.10.

fields, together with FL fits, is shown in Fig. 5.46 (right). The resulting fit parameters of the fits from Eqn. 5.9 and Eqn. 5.10 are shown in Fig. 5.47 (left) and Fig. 5.47 (right), respectively. There is a small but distinct change of all parameters with magnetic field: A' , A , and n show a step-like increase above 4 T, and ρ_0 starts increasing from 5 T on. For the parameter A , this fact is also seen in Fig. 5.46 (right), where the slopes can be assigned to two groups: One with slightly steeper slopes at high fields and one with slightly flatter slopes at low fields. n is close to the FL value of 2, but slightly lower at fields below 4 T and slightly higher at fields above 4 T. Upon increasing the temperature, a cubic power law with $n = 3$ is reached (see Fig. 5.48).

The magnetoresistivity is positive for all applied fields. Above the field value of approximately 4 T, the magnetoresistivity (Fig. 5.49) follows a quadratic field dependence, as illustrated by linear fits to the data above 7 T in Fig. 5.49. This is often found to be the leading temperature-dependent contribution in non-magnetic metals [116]; in the case of CeNiAs_{0.65}P_{0.35}O, however, the B^2 dependence is located within the anti-ferromagnetic phase. The slopes slightly increase with temperature. At low fields, the isotherms are rather flat with a linear temperature dependence, which can be observed in the linear plot in the inset of Fig. 5.49.

For the substitution level of 35%, the external magnetic field has a very weak influence up to 4 T. At higher fields, changes of the temperature dependence of the resistivity and of the magnetoresistivity are observed; scattering processes are enhanced, as can be seen in the increase of the absolute resistance and the change from a linear to a quadratic dependence in the magnetoresistivity. Concerning the temperature dependence of the

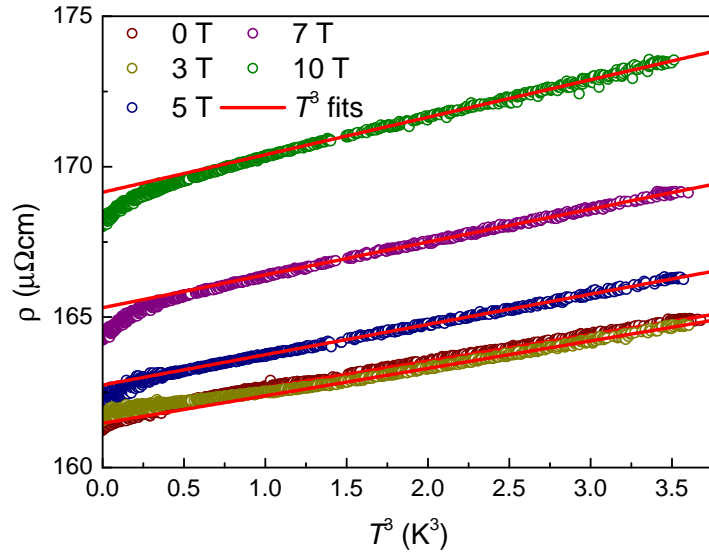


Figure 5.48: Resistivity data of CeNiAs_{0.65}P_{0.35}O, plotted vs T^3 . The full lines correspond to fits according to $\rho(T) = \rho_0 + A''T^3$ in the temperature range 1.1 K to 1.6 K.

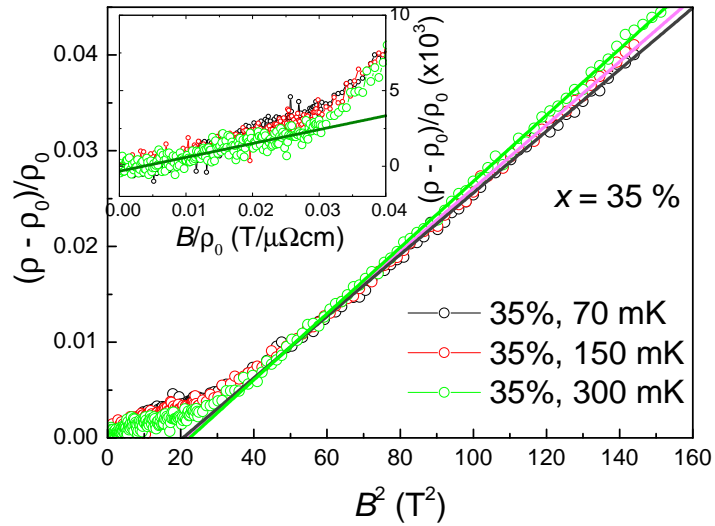


Figure 5.49: Magnetoresistivity of CeNiAs_{0.65}P_{0.35}O plotted over B^2 , with a linear fit to the high-field region. *Inset*: Linear plot of the resistivity of CeNiAs_{0.65}P_{0.35}O at low fields with a linear fit to low magnetic fields up to 4 T.

resistivity, no pronounced NFL behaviour is observed at the lowest temperatures. n increases from 1.8 to 2.2. The temperature dependence of the resistivity is therefore nearly quadratic at low temperatures and cubic at higher temperatures. This behaviour is also found in CeNiAsO under a pressure around 5 kbar, which is still in the antiferromagnetic phase, but close to the QCP at 6.7 kbar [96]. The antiferromagnetic transition is only slightly shifted to lower temperatures at the highest measured field of 10 T. Magnetic field as a tuning parameter obviously suppresses the antiferromagnetic order, but the energy scales are quite high in CeNiAs_{0.65}P_{0.35}O, and the sample properties and the interplay of magnetic moments and conduction electrons seem robust upon the application of low and moderate magnetic fields below 4 T.

Resistivity of CeNiAs_{0.6}P_{0.4}O at ambient pressure

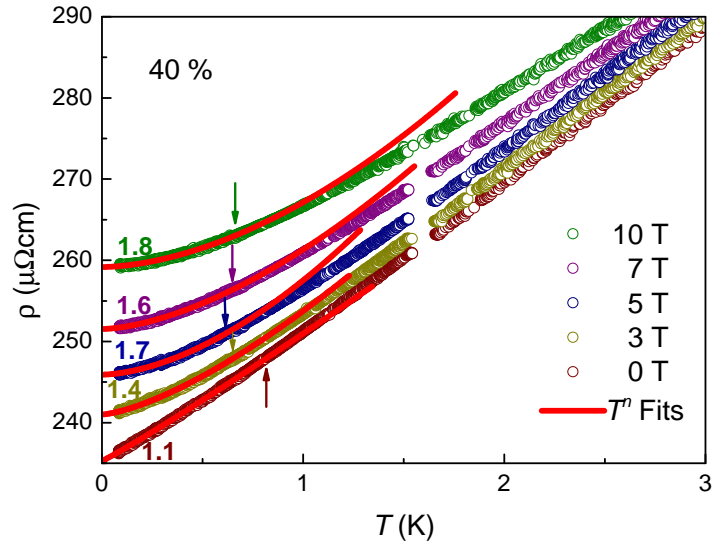


Figure 5.50: Temperature-dependent resistivity of CeNiAs_{0.6}P_{0.4}O with power law fits (see Eqn. 5.9) at selected magnetic fields. The values of the parameter n are shown next to each fit curve, and the crossover temperatures T_{FL} are indicated by the arrows.

Figure 5.50 shows the electrical resistivity of CeNiAs_{0.6}P_{0.4}O as a function of temperature in different magnetic fields. The applied fields have a much stronger effect on both the absolute value and the temperature dependence than for CeNiAs_{0.65}P_{0.35}O. Fits with Eqn. 5.10 to the low-temperature resistivity data are shown as red full lines. As discussed in more detail below, a power n close to 1 is found for low magnetic fields.

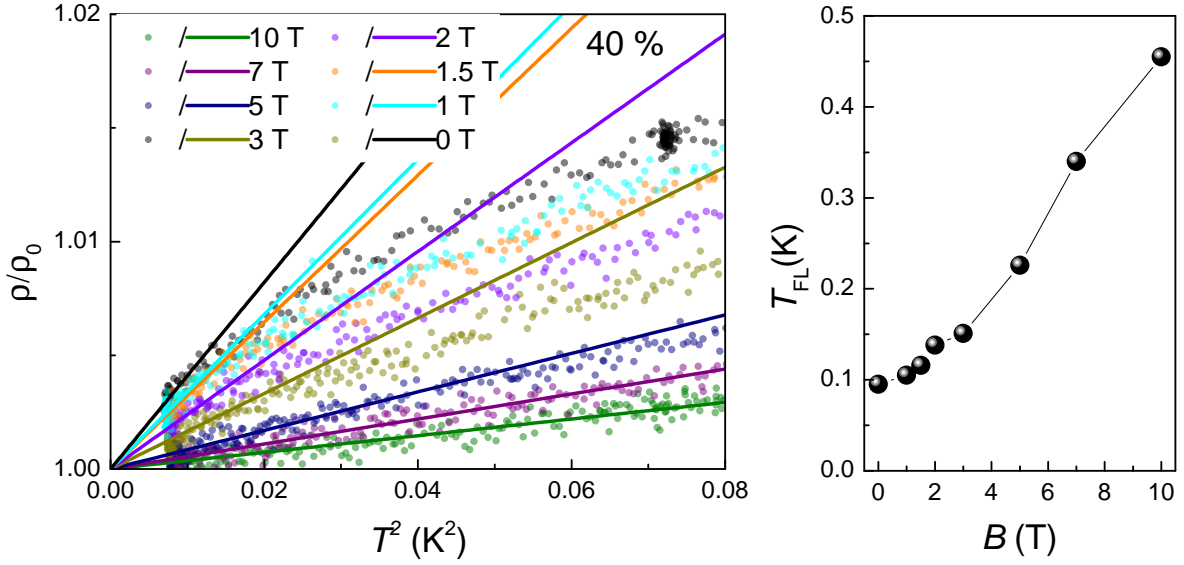


Figure 5.51: Left: Normalized ρ/ρ_0 resistivity data of CeNiAs_{0.6}P_{0.4}O, plotted vs T^2 . FL fits according to Eqn. 5.10 were applied to the data in the $T \rightarrow 0$ limit and are also shown in the corresponding colours. Their slopes determine the value of the A coefficient, which gets strongly suppressed by the magnetic field. Right: Crossover temperature T_{FL} , defined by $(\rho - \rho_{fit})/\rho_{fit} > 1\%$, vs magnetic field.

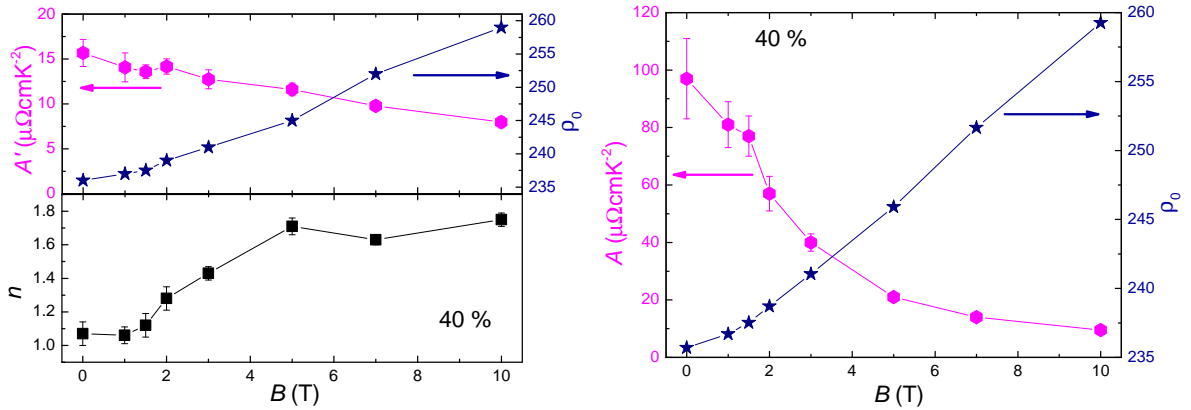


Figure 5.52: Left: Evolution of the fit parameters A' , n and ρ_0 from fits to CeNiAs_{0.6}P_{0.4}O resistivity data according to Eqn. 5.9. Right: Evolution of the fit parameters A and ρ_0 from fits to CeNiAs_{0.6}P_{0.4}O resistivity data according to Eqn. 5.10.

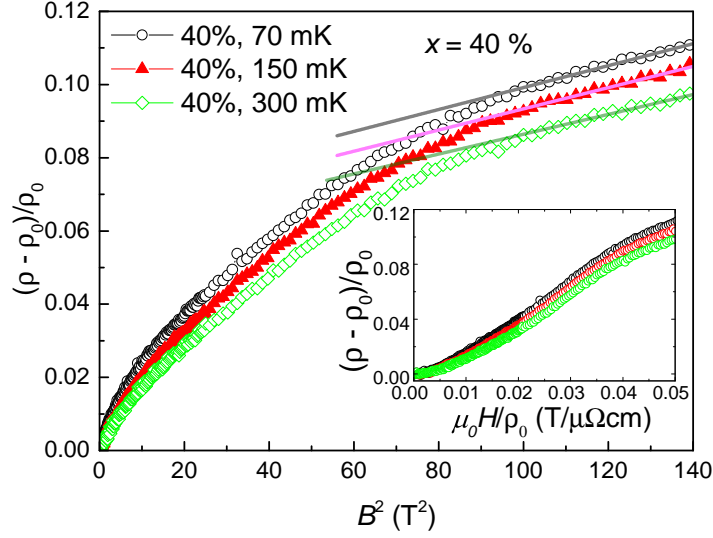


Figure 5.53: Magnetoconductivity of $\text{CeNiAs}_{0.6}\text{P}_{0.4}\text{O}$ plotted over B^2 , with linear fits to the high-field region above 10 T. *Inset*: Linear plot of the resistivity of $\text{CeNiAs}_{0.6}\text{P}_{0.4}\text{O}$ at low fields.

Figure 5.51 (left) shows the normalized resistivity ρ/ρ_0 of $\text{CeNiAs}_{0.6}\text{P}_{0.4}\text{O}$, plotted vs T^2 . In the $T \rightarrow 0$ limit, the data were fit by a quadratic temperature dependence (Eqn. 5.10) up to a crossover temperature T_{FL} , where $(\rho - \rho_{fit})/\rho_{fit} > 1\%$ is reached. All fits in Figs. 5.50 and 5.51 (right) are plotted beyond the crossover temperature to illustrate the deviations. For the quadratic fits of Eqn. 5.10, T_{FL} vs field is shown in Fig. 5.51 (right). It increases with magnetic field, and the applicable fit range for the FL fit of Eqn. 5.10 grows from 60 mK - 95 mK at $B = 0$ T to 60 mK - 450 mK at 10 T. The resulting fit parameters from both fitting procedures, shown in Figs. 5.50 and 5.51, are summarized in Fig. 5.52. There is a clear field dependence for all fit parameters. ρ_0 and n increase with field, A and A' decrease. n is nearly linear at low fields and low temperatures, indicating clear NFL behaviour. At high fields, n approaches the FL value of 2, but saturates at a slightly lower value around 1.8. The A coefficient is very high at low fields (approximately two orders of magnitude higher than $\text{CeNiAs}_{0.65}\text{P}_{0.35}\text{O}$), and is strongly and continuously suppressed by the applied magnetic field until it reaches a value of 9.5 at 10 T.

The magnetoconductivity of $\text{CeNiAs}_{0.6}\text{P}_{0.4}\text{O}$ (shown in Fig. 5.53) does not follow a quadratic behaviour at low fields. However, at fields above 10 T, B^2 behaviour is clearly observed, as indicated by the linear fits in Fig. 5.53, which is consistent with a FL state above 10 T.

In the raw resistivity data of $\text{CeNiAs}_{0.6}\text{P}_{0.4}\text{O}$ in Fig. 5.50, a change of the power-law

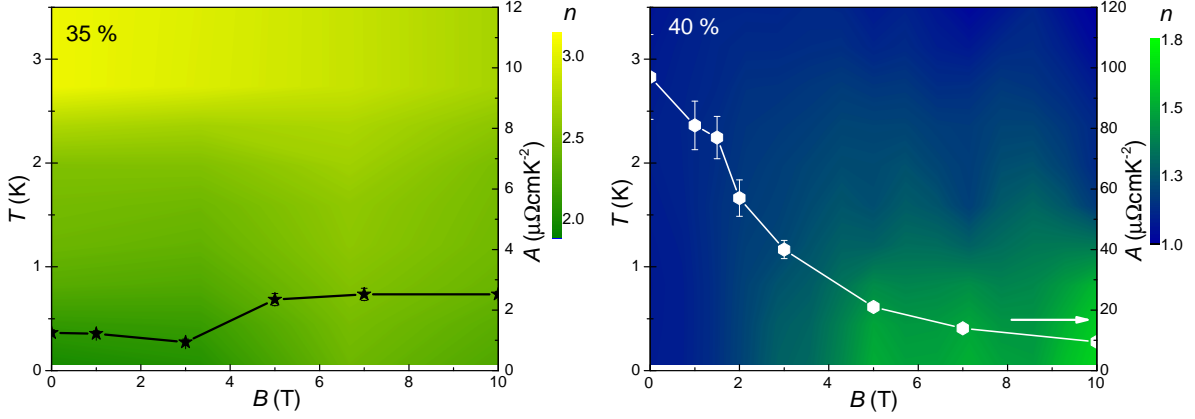


Figure 5.54: Colour-coded phase diagrams of $\text{CeNiAs}_{0.65}\text{P}_{0.35}\text{O}$ left and $\text{CeNiAs}_{0.6}\text{P}_{0.4}\text{O}$ right. The values of the parameter n from fits with Eqn. 5.9 are represented by different colours and plotted vs magnetic field and temperature. Additionally, the A coefficients from fits with Eqn. 5.10 in the $T \rightarrow 0$ limit are shown (right scale).

temperature dependence can be seen. The curves seem to evolve into a linear temperature dependence above the crossover temperature. This behaviour was accessed by fitting Eqn. 5.9 to different temperature regions and summarizing the obtained values of n in a colour-coded phase diagram. Such diagrams are shown for both $\text{CeNiAs}_{0.65}\text{P}_{0.35}\text{O}$ and $\text{CeNiAs}_{0.6}\text{P}_{0.4}\text{O}$ in Fig. 5.54 (left) and Fig. 5.54 (right), respectively. The A coefficients, obtained from FL fits (Eqn. 5.10) are also shown. In the case of $x = 35\%$, magnetic fields above 4 T induce small but significant changes to the physical properties within the antiferromagnetic phase, increasing both n and A . Upon approaching the antiferromagnetic transition at 3.5 K, a T^3 temperature dependence is recovered at all fields. The effects of the magnetic field are stronger in the case of the sample with $x = 40\%$. At lowest temperatures it is driven from a NFL state towards a FL state by the magnetic field. In the NFL region with $n \approx 1$ at low fields, the A coefficient is strongly enhanced. Upon increasing the temperature, the NFL behaviour is recovered also at high fields and extends in the entire measured field range. Thus, there are clear indications for quantum criticality in the temperature-dependent resistivity of $\text{CeNiAs}_{0.6}\text{P}_{0.4}\text{O}$: The temperature-magnetic field phase diagram shows the typical characteristics of a QCP at zero or low fields, with a tornado-shaped NFL region extending from the QCP to higher temperatures, and a FL state, which is recovered when the system is tuned away from the QCP.

Resistivity under pressure

In addition to applying the previously not explored tuning parameter magnetic field, we also studied the interplay of hydrostatic and chemical pressure in $\text{CeNiAs}_{1-x}\text{P}_x\text{O}$: How do the phase diagrams for these different types of pressure compare? As mentioned above, here the effect of hydrostatic pressures up to 3.5 kbar on a sample with a substitution level of $x = 35\%$ was investigated.

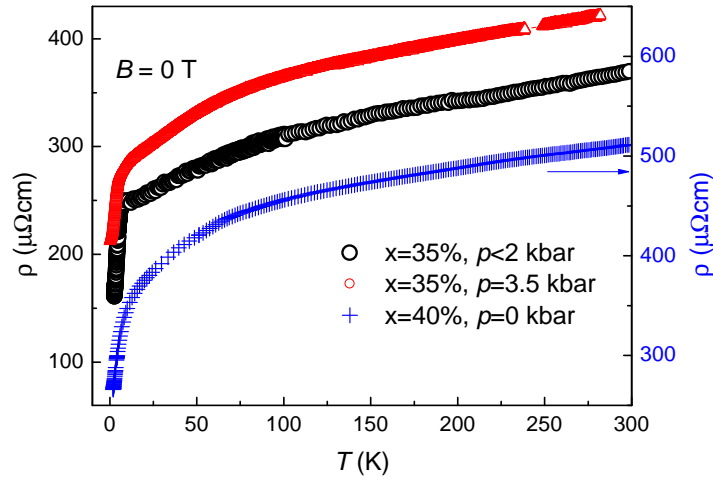


Figure 5.55: Temperature-dependent resistivity of $\text{CeNiAs}_{0.65}\text{P}_{0.35}\text{O}$ in a temperature range from 60 mK to room temperature; the curve for $\text{CeNiAs}_{0.6}\text{P}_{0.4}\text{O}$ at ambient pressure is shown for comparison. The measurements with pressures of $p < 2$ kbar were performed by G. Pristas, the measurement at $p = 3.5$ kbar was performed by P. Popcevic.

The phase diagram of CeNiAsO exhibits a QCP at a critical pressure of 6.7 kbar (Fig. 5.44 (top)). For $\text{CeNiAs}_{1-x}\text{P}_x\text{O}$ with $0 < x < 0.4$, for which T_N is reduced compared to the parent compound, the critical pressure is expected to be smaller as well. The effect at the investigated pressures below 3.5 kbar (which were $p_1 = 1.3$ kbar and $p_2 = 1.8$ kbar) is small, and the resistivity curves are very similar to the ones at ambient pressure. Therefore we will mainly focus on the properties at 3.5 kbar.

As seen from the temperature dependence of the electrical resistivity of the sample with $x = 35\%$ (Fig. 5.55), the application of a hydrostatic pressure alters the behaviour in several ways: The characteristic step-like feature close to the ordering temperature becomes less pronounced and smoother under pressure, and the overall shape of the curve of $\text{CeNiAs}_{0.65}\text{P}_{0.35}\text{O}$ evolves towards the shape of the curve of $\text{CeNiAs}_{0.6}\text{P}_{0.4}\text{O}$ at ambient pressure. At high temperatures, a resistivity offset between measurements at different pressures is observed in $\text{CeNiAs}_{0.65}\text{P}_{0.35}\text{O}$. This pressure-dependent change in

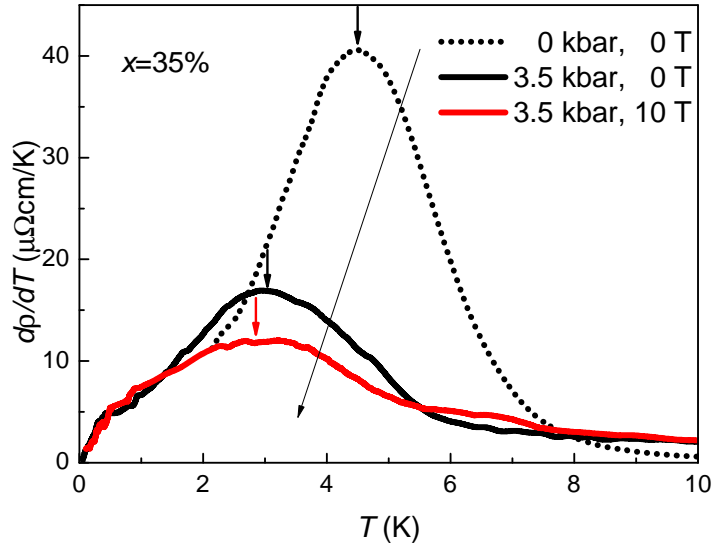


Figure 5.56: Temperature derivatives of the resistivity of CeNiAs_{0.65}P_{0.35}O, emphasizing the shift of the magnetic ordering temperature T_N induced by pressure and magnetic field. The field at the peaks of the derivatives with respect to temperature and thus the location of T_N are marked with vertical arrows.

absolute value is similar to the previously reported change for the parent compound CeNiAsO.

Turning to the derivatives with respect to temperature in Fig. 5.56 it can be seen that T_N is shifted by The applied field drives the system towards the QCP by lowering the temperature T_N . T_N was defined as the inflection point in the resistance curves, i.e. the maximum in the derivative (a detailed analysis of the general curve shapes on both sides of the QCP can be found in [96]). The derivatives are given in Fig. 5.55. The maximum at 3.5 kbar is clearly shifted to lower temperatures and is less pronounced. It is, however, still a well-defined maximum, which means that CeNiAs_{0.65}P_{0.35}O still orders antiferromagnetically at low temperatures and that the critical pressure for CeNiAs_{0.65}P_{0.35}O is higher than 3.5 kbar. Figure 5.57 shows the resistivity at 3.5 kbar and zero field. There is a kink around 0.5 K, which separates two temperature dependencies. A T^n fit (Eqn. 5.9) to the low-temperature part yields a value for n slightly above 2, a fit to the higher-temperature part gives a value slightly below 2. In both temperature regions, the sample is thus in or close to a FL phase, with a crossover between the two regimes at 0.5 K. This feature is not present in the ambient pressure measurements and is triggered by the application of pressure. It persisted in all measurements in the pressure cell, independently of other measurement parameters, so that a simple measurement artifact (for instance due to change in heating rates) can be ruled out. No linear temperature

dependence is observed in the resistivity, indicating that pressure has not yet driven $\text{CeNiAs}_{0.65}\text{P}_{0.35}\text{O}$ close enough to a QCP.

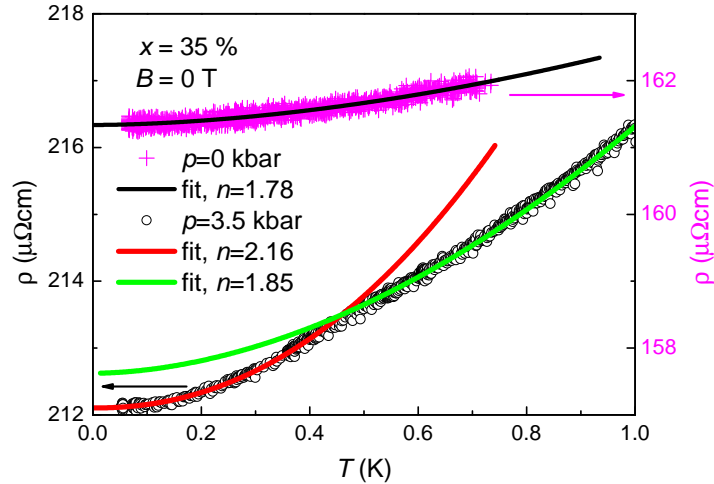


Figure 5.57: Temperature-dependent resistivity of $\text{CeNiAs}_{0.65}\text{P}_{0.35}\text{O}$ at ambient pressure, at $p = 3.5$ kbar, and in zero field. Power-law fits using Eqn. 5.9 are shown (low-temperature fit, 3.5 kbar (red): $n = 2.16$; high-temperature fit, 3.5 kbar (green): $n = 1.85$; fit at 0 kbar, $n = 1.78$).

Apart from the kink at 0.5 K, pressure induces a change to the slope of the resistivity at low temperatures, see Fig. 5.57. Whereas the temperature dependence is weak at ambient pressure, it depends stronger on the temperature at $p = 3.5$ kbar. The powerlaw dependence, however, remains close to the FL value of 2, as at ambient pressure. The A coefficient is slightly enhanced (from $A = 1.75$ at zero field and ambient pressure to $A = 3.39$ at zero field and $p = 3.5$ kbar), but remains of the same low order of magnitude. The influence of the applied pressure on the sample with a P substitution of $x = 35\%$ is summarized in Fig. 5.58, an extended phase diagram including measurements from [96] and the contributions from the measurements of this work. A tentative critical pressure value for $\text{CeNiAs}_{0.65}\text{P}_{0.35}\text{O}$ of just below 5 kbar was added to the extended phase diagram.

Magnetic field was applied to the pressurized $\text{CeNiAs}_{0.65}\text{P}_{0.35}\text{O}$ sample to study the interplay of pressure and field close to the QCP. The resistivity was measured at a field of 10 T and is compared to the zero-field data in Fig. 5.59. The step-like transition feature at the Néel temperature is smoothed out by the field, suggesting that the process of the antiferromagnetic ordering is influenced. In the derivative of the electrical resistivity with respect to temperature, the maximum associated with the transition shifts to lower temperatures (see Fig. 5.56). This indicates that the magnetic field weakens

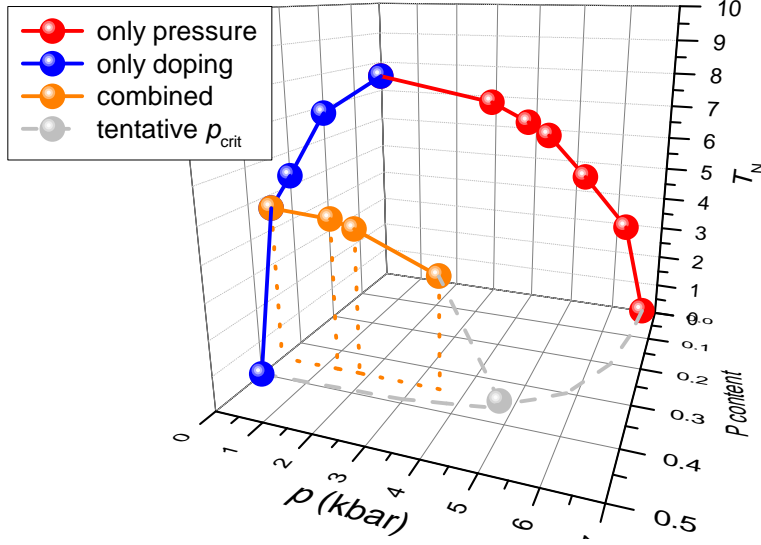


Figure 5.58: Extended pressure-substitution-temperature phase diagram. The orange points are results of this study and complement the blue and red points from [96]. The critical pressure was estimated from scaling the T_N -pressure curves of CeNiAsO and CeNiAs_{0.65}P_{0.35}O and yields a value of $p_{\text{crit}} \lesssim 5$ kbar. This is indicated by the tentative critical point (gray).

Table 5.2: Overview of the low-temperature fit parameters from Eqns. 5.9 and 2.1.3 at different pressures and magnetic fields.

doping	pressure [kbar]	field [T]	A [$\mu\Omega\text{cm}/\text{K}$]	ρ_0	n	ρ_0	A'
35%	ambient	0	1.25	162	1.78	163	1.1
35%	3.5	0	4.9	212	2.03	212	4.95
35%	3.5	10	4.8	202	1.90	202	4.80
40%	ambient	0	98	236	1.1	237	16

the antiferromagnetic order. The subtle kink around 0.5 K is hardly observable on the logarithmic scale, but is indicated by the arrows in the inset of Fig. 5.59.

The characteristics at the lowest temperatures, deep within the antiferromagnetic state, are only weakly affected by magnetic field. The low-temperature data in zero field and at 10 T are shown in Fig. 5.60, together with the corresponding power law fits according to Eqn. 5.9. The kink around 0.5 K (Fig. 5.57) persists at 10 T and is shifted to a slightly higher temperature of 0.6 K. All low-temperature fit parameters are summarized in Tab. 5.2. The quadratic behaviour in the lowest accessed temperature range, as well as the A coefficient, are only weakly influenced by the magnetic field.

Summarizing, we have investigated polycrystalline samples at two substitution levels

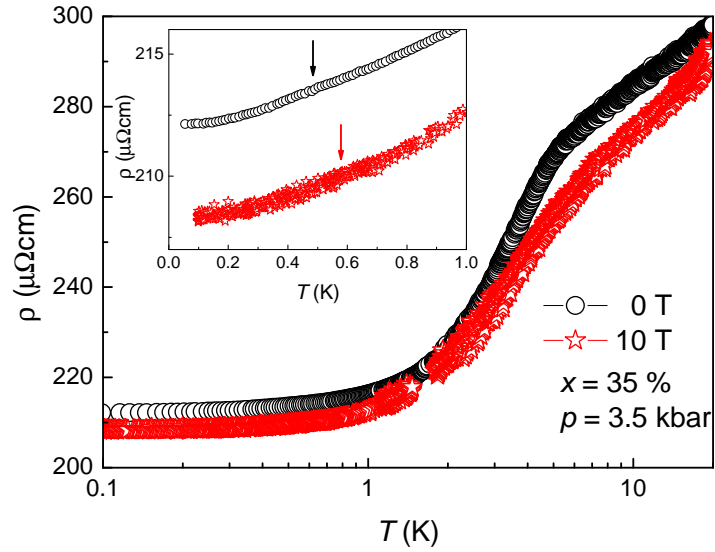


Figure 5.59: Comparison of the temperature-dependent resistivity of $\text{CeNiAs}_{0.65}\text{P}_{0.35}\text{O}$ at $p = 3.5$ kbar in zero field and at 10 T. *Inset*: Zoom into the low-temperature region (on a linear scale). The arrows indicate the temperatures separating two FL-like temperature dependencies. The measurements were performed by P. Popcevic.

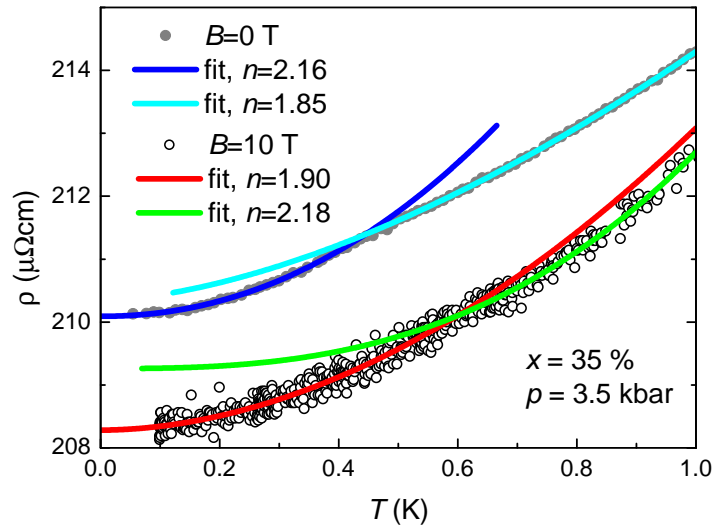


Figure 5.60: Temperature-dependent resistivity of $\text{CeNiAs}_{0.65}\text{P}_{0.35}\text{O}$ at $p = 3.5$ kbar, in zero field and at 10 T. The curve at 0 T was shifted by $2 \mu\Omega\text{cm}$ for clarity.

of the oxypnictide series CeNiAs_{1-x}P_xO, $x = 35\%$ and $x = 40\%$. Resistivity measurements were performed at ambient and under hydrostatic pressure up to 3.5 kbar, and with an applied static magnetic field up to 10 T. The influence of magnetic field on NFL and FL behaviour was studied in the vicinity of the QCPs in these materials. Previous investigations [96] have reported a QCP at a critical P substitution level of approximately $x = 40\%$ in zero pressure and at a critical pressure of $p_c = 6.7$ kbar for the parent compound CeNiAsO.

On CeNiAs_{0.65}P_{0.35}O, which orders antiferromagnetically at low temperatures in all performed measurements, hydrostatic pressure and magnetic field show a similar effect: The ordering temperature T_N is slightly reduced, and the typical step-like feature at the antiferromagnetic transition is smoothed out. Pressure and field therefore tune CeNiAs_{0.65}P_{0.35}O towards the QCP, but the applied parameter values (up to $p = 3.5$ kbar and 10 T) do not induce quantum critical behaviour. No NFL behaviour is found, and at low temperatures the observed properties are FL-like.

In the case of On CeNiAs_{0.6}P_{0.4}O, an applied magnetic field has a strong influence on the temperature dependence of the resistivity at temperatures below 1 K and drives the material from a NFL state with nearly linear temperature dependence towards a FL state. Clear NFL behaviour with nearly linear temperature dependence of the resistivity is observed in a large temperature range, indicating quantum criticality in CeNiAs_{0.6}P_{0.4}O, emerging from a QCP at zero or low magnetic fields. This is supported by large values of the A coefficient at low magnetic fields.

5.4 $\text{Ti}_{1-x}\text{Sc}_x\text{Au}$

In the doping series $\text{Ti}_{1-x}\text{Sc}_x\text{Au}$, the antiferromagnetic order of the parent compound TiAu can be suppressed by Sc doping. The undoped TiAu had been previously synthesized and analyzed [97], the main interest being the study of magnetism in metals with itinerant moments.

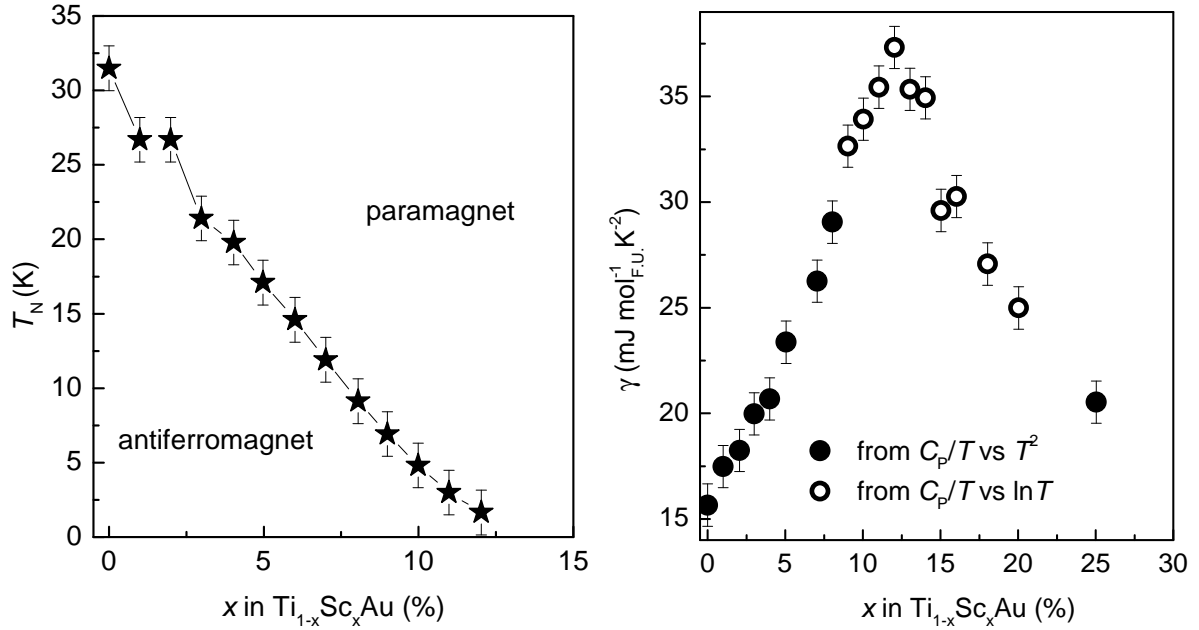


Figure 5.61: Left: Suppression of the antiferromagnetic order in $\text{Ti}_{1-x}\text{Sc}_x\text{Au}$. Right: Evolution of the electronic specific heat with Sc doping (measured by E. Svanidze) [97, 117].

TiAu combines several rare characteristics: It is an itinerant transition metal magnet without magnetic constituents. The only other known examples sharing those characteristics are the ferromagnets ZrZn_2 [118] and $\text{Sc}_{3.1}\text{In}$ [119]). TiAu is the only known antiferromagnetic compound of this type. Regarding its electronic structure, it is different from the other compounds studied in this work, because itinerant d -electrons (instead of f -electrons in the other compounds) provide the magnetic moments and are the basis for the studied correlation effects. The above mentioned properties make TiAu a model system for the study of weak itinerant antiferromagnetism in transition metal magnets and for the analysis of effects of spin fluctuations to such systems.

The study of the pure parent materials' magnetic properties is an interesting field of research by itself, but will not be discussed here. Instead, the effect of doping with Sc will be investigated, as already proposed in [97]. The suppression of the weak itinerant antiferromagnetic order of TiAu by Sc is shown in Fig. 5.61 (left). From resistivity

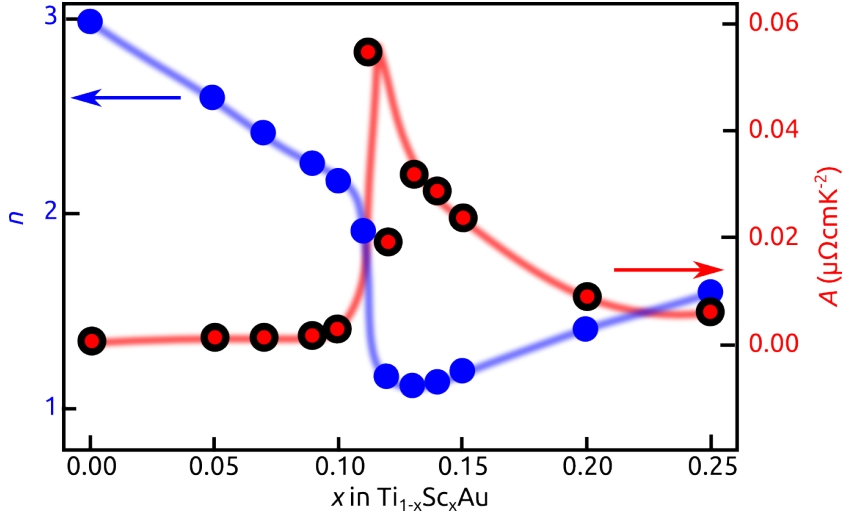


Figure 5.62: Evolution of the power law of the resistivity-temperature dependence and A coefficient from quadratic fits to the lowest temperature region (measured by E. Svanidze) [117].

and specific heat measurements down to 400 mK (performed by E. Svanidze at Rice University, Houston, USA), a change of the physical properties in the vicinity of the critical doping level was observed. The Sommerfeld coefficient γ was extracted from specific heat measurements by fitting

$$C_p/T = \gamma - \tilde{\beta} \ln T \quad (5.11)$$

to the specific heat of samples with doping levels close to critical doping, and by fitting the FL expectation

$$C_p/T = \gamma + \beta T^2 \quad (5.12)$$

to the specific heat of samples with doping levels away from critical doping. γ clearly shows a peak around 12%-13% of Sc doping, as shown in Fig. 5.61 (right).

The resistivity data of samples with different doping levels were generally fit with the NFL expression

$$\rho(T) = \rho_0 + \tilde{A}T^n \quad (5.13)$$

for the extraction of n , and with the FL expression

$$\rho(T) = \rho_0 + AT^2 \quad (5.14)$$

at the lowest temperatures to extract A . The results are shown in Fig. 5.62. There is

a minimum in n around $x = 13\%$, where the temperature dependence of the resistivity is close to linear, $n \approx 1$, indicating a NFL region in the temperature-doping phase diagram. Around this doping level, the A coefficient also experiences a change and is enhanced. The enhancements of A and γ in combination with the NFL behaviour are

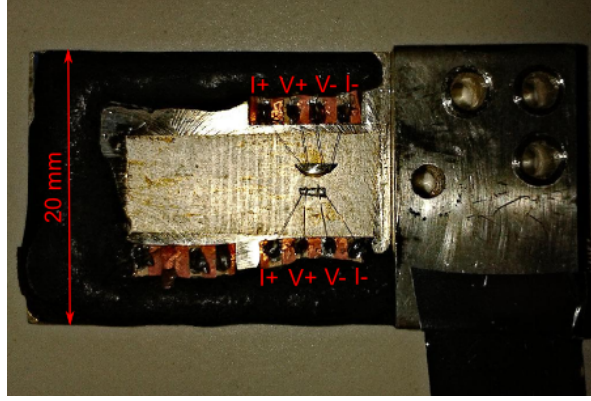


Figure 5.63: Two of the three measured $\text{Ti}_{1-x}\text{Sc}_x\text{Au}$ samples, contacted and mounted on a holder for dilution refrigerator resistivity measurements.

strong indications for a QCP. In the course of this work, additional low-temperature resistivity data below 400 mK were measured to verify this interpretation.

The measurements were performed on polycrystalline $\text{Ti}_{1-x}\text{Sc}_x\text{Au}$ samples (grown by E. Svanidze) of three doping levels: The parent compound ($x = 0$), a sample close to the critical doping level $x = 13\%$, and one with $x = 25\%$ Sc doping. Two of the three samples are shown in Fig. 5.63, mounted onto a silver measurement platform. They were electrically insulated from the silver platform by cigarette paper and glued to the platform with GE varnish. The samples were contacted in a standard four-point geometry, by spot welding four $50 \mu\text{m}$ gold wires to their polished top surfaces. The silver plate with the mounted samples was tightly screwed to a silver cold finger. The samples had a room temperature resistance of a few $\mu\Omega$. For the low-temperature resistivity measurements in the $\text{m}\Omega$ or sub- $\text{m}\Omega$ range, two cryogenic transformers were available for voltage signal amplification. The transformers were connected to the $x = 0\%$ and $x = 13\%$ samples. The measured resistances of all three samples at dilution refrigerator temperatures are shown in Fig. 5.64, together with previous measurements at higher temperatures. Being measured without transformer, the $x = 25\%$ sample presents a higher noise level. For all samples, different maximum excitation voltages were compared: 5 (lowest possible), 10, 20, and 50% of $20 \mu\text{V}$. No difference in the temperature dependence was found. All data presented in the figures were recorded with a maximum excitation value of 20% of $20 \mu\text{V}$.

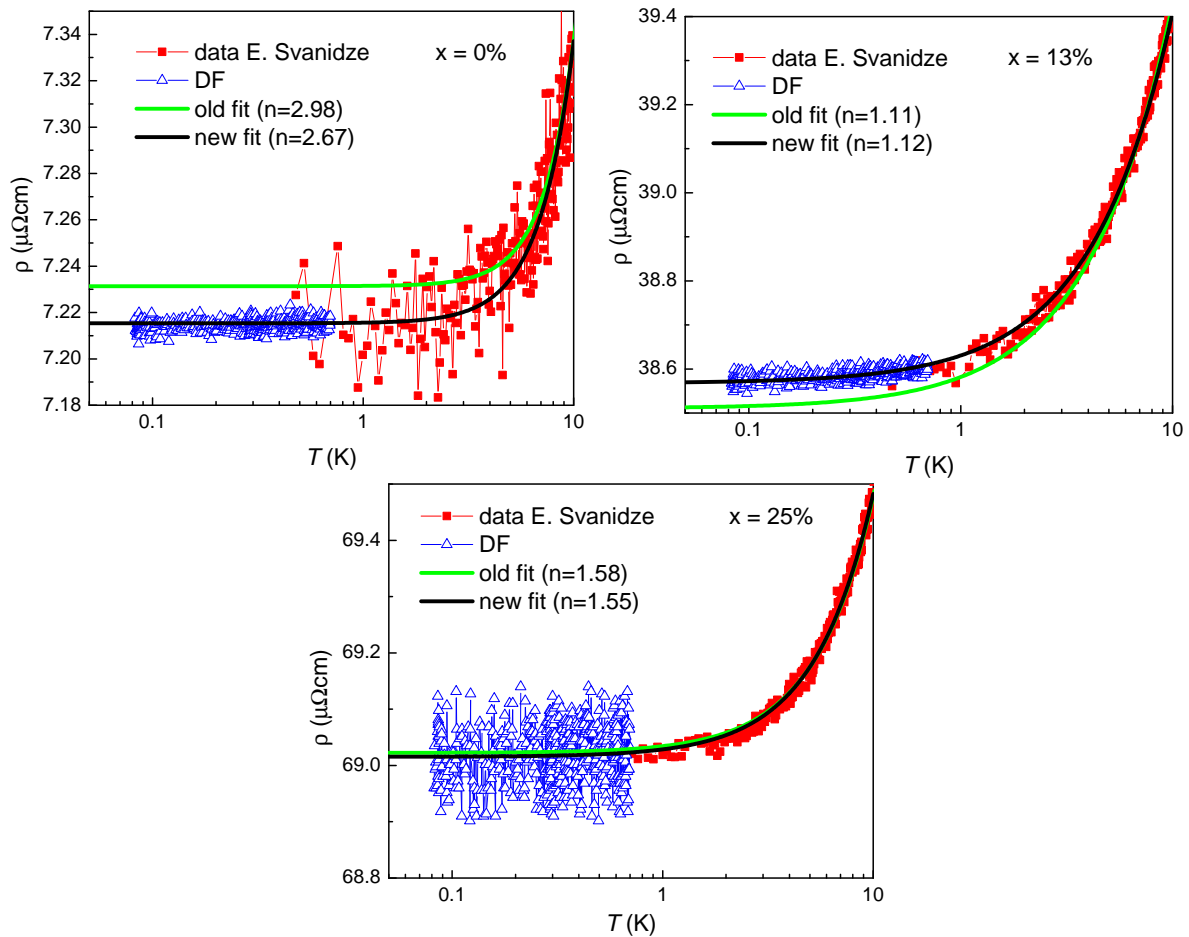


Figure 5.64: Previously measured data (red) and dilution refrigerator data (blue). The dilution refrigerator data were scaled to the high-temperature data by matching the averaged values. Full green lines are fits to the high-temperature data, full black lines are the updated fits including both dilution refrigerator data and previously measured data up to 15 K.

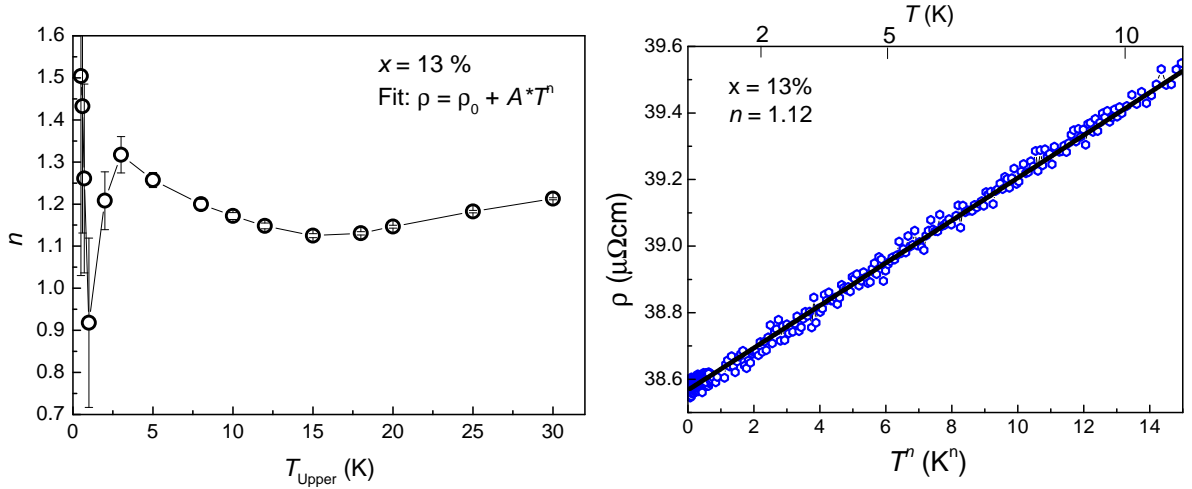


Figure 5.65: Left: Evolution of the power of the resistivity-temperature dependence, n , with the fit range (starting at the lowest measured temperatures, up to T_{Upper}). Right: Resistivity data over $T^{1.12}$.

The dilution refrigerator data were scaled to the high-temperature data. In addition to the previously and newly measured datasets, Fig. 5.64 shows different fit curves: The data range of the old high-temperature fits was extended, and the fits were updated (black) to fit also the low-temperature data. Minor changes to the fit parameters are sufficient to reproduce the new low-temperature data well. An overview of all fit parameters for different fit ranges is given in Tab. 5.3.

The resistivity of the critical concentration was investigated in more detail. The exponent of the temperature dependence, n , is shown in Fig. 5.65 (left) for different temperature ranges of the applied fit. Clearly, the temperature dependence is of non-NFL type and close to 1 (except for very small fit ranges, where the error bar is large and n tends to increase towards 1.5). Plotting the resistivity data vs $T^{1.12}$, as shown in Fig. 5.65 (right), emphasizes the quasi-linear NFL character.

The data obtained at dilution refrigerator temperatures only require small changes of the calculated parameters, and are clearly consistent with the high-temperature data. Therefore, the new measurements support the conclusion that the $\text{Ti}_{1-x}\text{Sc}_x\text{Au}$ doping series reveals the first antiferromagnetic QCP in an itinerant d -electron system.

A colour-coded phase diagram summarizing the experimental results is shown in Fig. 5.66. At low doping levels, but temperatures above the Néel temperature, the system behaves like a FL with a quadratic temperature dependence of the resistivity. C_p/T also exhibits a T^2 temperature dependence [117], indicating a leading phononic contribution to the specific heat and conventional metallic behaviour. The resistivity evolves into a

Table 5.3: Collection of resulting parameters from quadratic and power law fits to the measured resistivity data. Old fits refer to the high-temperature data above 400 mK. Temperatures refer to the upper limit of the fit range, the starting point is always the lowest measured temperature. The last column refers to a FL fit, applied to the lowest temperatures, up to 1 K.

	old	fits	to	15 K	to	20 K	to	30 K	T^2 to 1 K
	n	\tilde{A}	n	\tilde{A}	n	\tilde{A}	n	\tilde{A}	A
0 %	2.98	0.001	2.67	0.001	2.93	$1.3e^{-4}$	2.83	$1.8e^{-4}$	0.0007
13 %	1.11	0.052	1.12	0.063	1.15	0.060	1.21	0.050	0.0563
25 %	1.58	0.013	1.55	0.013	1.56	0.013	1.55	0.013	0.0075

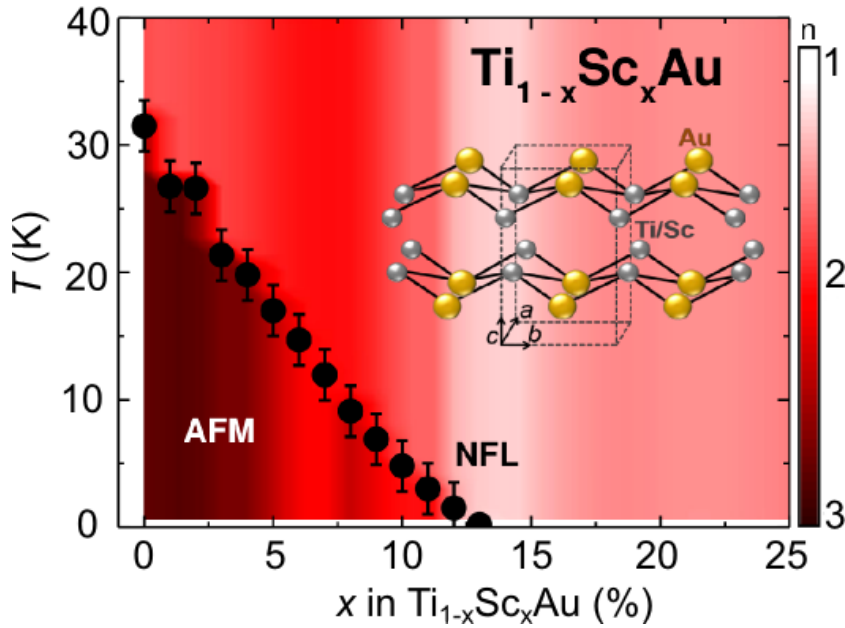


Figure 5.66: Colour coded phase diagram of the quantum critical doping series $Ti_{1-x}Sc_xAu$ [117], showing the temperature dependence of the resistivity, along with the Néel temperature T_N at different doping levels, and the crystal structure.

cubic temperature dependence in the antiferromagnetic phase, as also found in other materials (see for instance Sect. 5.3). Approaching the critical doping level, the transport properties become NFL-like, with a nearly linear temperature dependence of the resistivity and a $C_p/T \propto -\ln T$ dependence of the specific heat (specific heat data not shown, see [117]). Upon further increasing the Sc doping, the resistivity exponent increases to 1.5, and the specific heat returns to a $C_p/T \propto T^2$ temperature dependence. The phase diagram shows some differences to typical phase diagrams of other quantum critical materials with f -electrons (for instance the CeNiAs $_{1-x}$ P $_x$ O oxypnictide series of Sect. 5.3 or YbRh $_2$ Si $_2$ [87]). Unlike typical phase diagrams of the mentioned established f -electron systems, the NFL region does not extend into a tornado-shaped region of the phase diagram, but rather remains limited to a narrow band of doping levels. Also, no robust FL phase is established at low temperatures on the paramagnetic side of the QCP. The investigation of the A coefficient at the lowest temperatures shows that there is a strong increase of A around the critical value. The resistivity exponent n is predicted to be $n = 1.5$ for a 3D antiferromagnetic QCP, and $n = 1$ for the 2D case by self-consistent renormalization theory [120, 41, 121] (see also Sect. 2.2.1). Even though the orthorhombic crystal structure would rather point to a 3D system, the transport properties thus suggest 2D fluctuations.

Deviations from FL behaviour have also been discussed in the context of disorder effects in the case of itinerant antiferromagnets, $n = 1$ and $n = 1.5$ representing the clean and disordered limits, respectively [122, 123, 124]. However, in this case there are strong indications that the NFL behaviour is not related to disorder effects, but to quantum criticality: The comparison of Ti $_{1-x}$ Sc $_x$ Au with itinerant ferromagnets suggests that disorder effects are not relevant in the case of Ti $_{1-x}$ Sc $_x$ Au: The residual resistivity ratio of $\rho(200\text{ K})/\rho_0 \approx 2$ was compared to similar systems and falls into a range where disorder effects do not influence the physical properties strongly [117]. Also the ratio of the resistivity change in the quasi-linear range, $\Delta\rho$, and the residual resistivity ρ_0 should relate as $\Delta\rho \ll \rho_0$ in the case of strong disorder effects, but in all Ti $_{1-x}$ Sc $_x$ Au samples they are of the same order of magnitude [117].

Assuming only a marginal contribution of disorder effects, Ti $_{1-x}$ Sc $_x$ Au is the first example of an itinerant antiferromagnetic QCP in a d -electron material. The experimental data in the vicinity of the QCP suggest that 2D quantum critical fluctuations are associated with the QCP.

5.5 CeB₆

Introduction

The phase diagram of CeB₆ has been studied for several decades, but so far quantum critical aspects have not been in the focus of these studies. CeB₆ shares several characteristics with Ce₃Pd₂₀Si₆ (cubic structure, antiferromagnetic and AFQ phases, see Sect. 5.6). As the suppression of T_N in Ce₃Pd₂₀Si₆ has been shown to lead to quantum critical behaviour and even a breakdown of the Kondo effect [101], it would be of great interest to know if CeB₆ shares these properties as well.

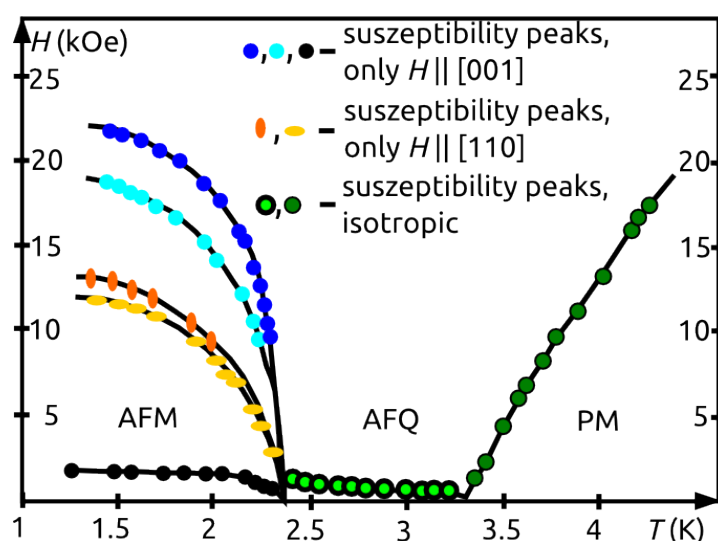


Figure 5.67: Phase diagram of CeB₆ from magnetic susceptibility measurements [125].

Previously, cusp-like enhancements of the Sommerfeld coefficient γ_0 from specific heat measurements and the A coefficient from resistivity measurements were reported [99]. These enhancements are today considered as strong indications for quantum criticality and provide a strong motivation to investigate CeB₆ in greater detail in this context. As in the case of Ce₃Pd₂₀Si₆, the measured properties are discriminated between the crystallographic directions along which the magnetic field is oriented.

As mentioned in Sect. 4.4, CeB₆ is a cubic system, which exhibits different types of ordered states in its phase diagram, antiferromagnetic and AFQ order [126, 127]. A phase diagram from literature, mainly obtained from magnetic susceptibility measurements, is shown in Fig. 5.67. In zero field, it shows a transition from an antiferromagnetic into a AFQ phase around 2.3 K, and upon further increasing the temperature, to a paramagnetic state at 3.3 K. Application of an external magnetic field weakens the

antiferromagnetic order, but stabilizes the AFQ phase.

External magnetic fields suppress T_N faster if they are applied along $[110]$ than if they are applied along $[001]$. Also, T_N (for both field directions) is split into two branches upon decreasing the temperature. The susceptibility features at low fields in Fig. 5.67 are not attributed to phase transitions, but to a change in the structure of the magnetic domains [125].

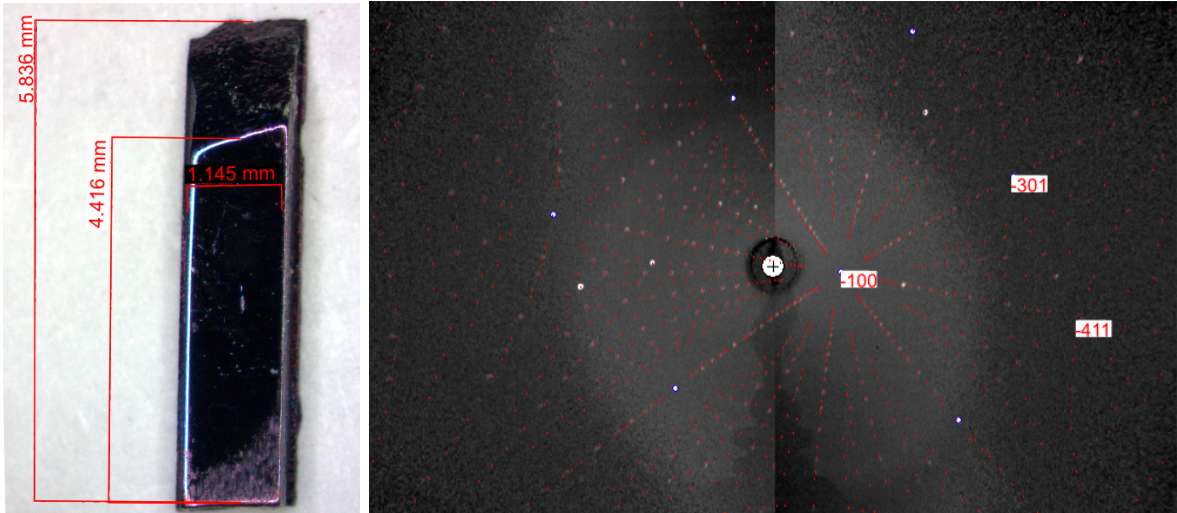


Figure 5.68: CeB₆ sample with polished $[001]$ face (left) and corresponding Laue diffraction pattern (right). The simulated $[001]$ diffraction pattern (red dots) is in excellent agreement with the diffraction pattern (black and white).

Specific heat, electrical resistivity, and magnetization were investigated in the vicinities of putative QCPs, that may result if the phase transitions of Fig. 5.67 are continuous down to $T = 0$ K, by applying magnetic field as an external parameter along the two mentioned directions. The studied single crystals were grown and oriented by Y. Onuki (Osaka University, Japan). After polishing their surfaces, the orientation of the different single crystal pieces was verified by Laue diffraction (together with J. Larrea). One example of a sample with a polished top surface along with the corresponding Laue pattern is shown in Fig. 5.68. It illustrates the correct assignment of the orientations of the surface and the crystallographic axes as well as the good quality of the orientation. Three sample pieces were used for the measurements: The one from Fig. 5.68 for resistivity and specific heat measurements with field along $[001]$, another piece for measurements of the same properties with field along $[110]$, and a third sample piece for magnetization measurements.

Magnetization

The magnetization was measured (by A. Sidorenko) down to 300 mK with magnetic fields from 50 mT to 1.5 T, applied along [110]. In the field dependence of the magnetization (Fig. 5.69 (left)), two step-like features can be identified, indicated as B_1 and B_2 for the lowest-temperature curve. These are associated with two antiferromagnetic transitions

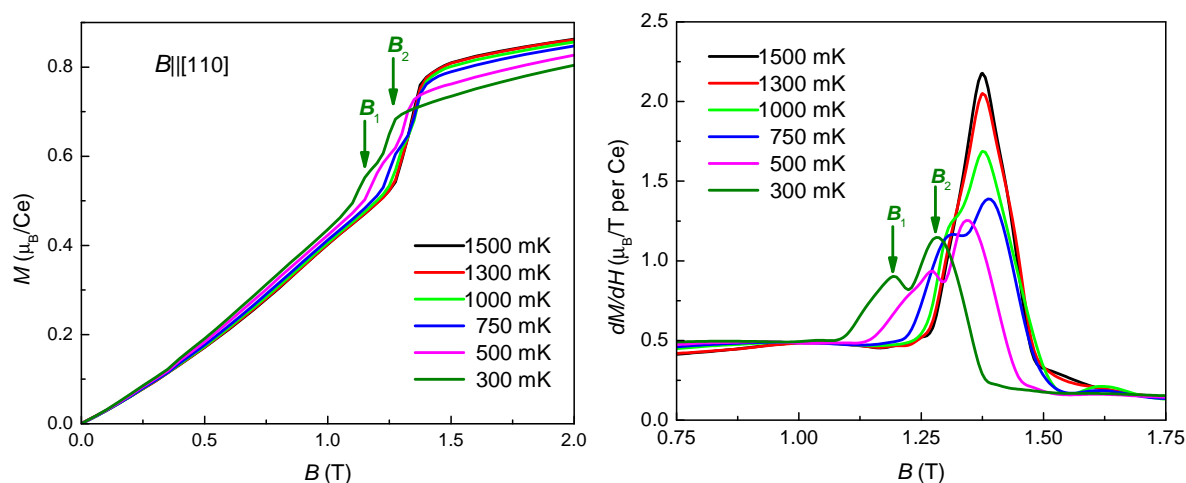


Figure 5.69: *Left:* Magnetization vs magnetic field (measurements carried out by A. Sidorenko). *Right:* Derivative of the magnetization with respect to magnetic field vs magnetic field.

(corresponding to the branch with orange and yellow ovals in Fig. 5.68). In the derivative of the magnetization with respect to magnetic field (Fig. 5.69 (right)), these features have the form of two maxima. Upon increasing the temperature, the two distinct transitions of one branch approach each other and collapse into one, which is consistent with the literature phase diagram in Fig. 5.67.

Turning to the temperature dependence of the magnetic susceptibility in Fig. 5.70, the two antiferromagnetic transitions are seen as a shoulder and a maximum, marked with T_1 and T_2 , respectively, for the curve at 1.2 T. They are shifted to lower temperatures and broaden when the magnetic field is increased. The features originating from the antiferromagnetic transitions are summarized in the temperature-magnetic field phase diagram (for field applied along [110]) in Fig. 5.71 (left). The transition fields were determined as the fields where the dM/dH isotherms show maxima, as shown in Fig. 5.69 (right). Extrapolating the phase transition linearly to $T = 0$ K yields the critical field $B_c = 1.34$ T. The transition feature of the second branch at T_2 does not shift to such low temperatures as T_1 and is fully suppressed once a field of 1.4 T is reached. The following analysis will be focused on the T_1 branch. The magnetization was not measured for

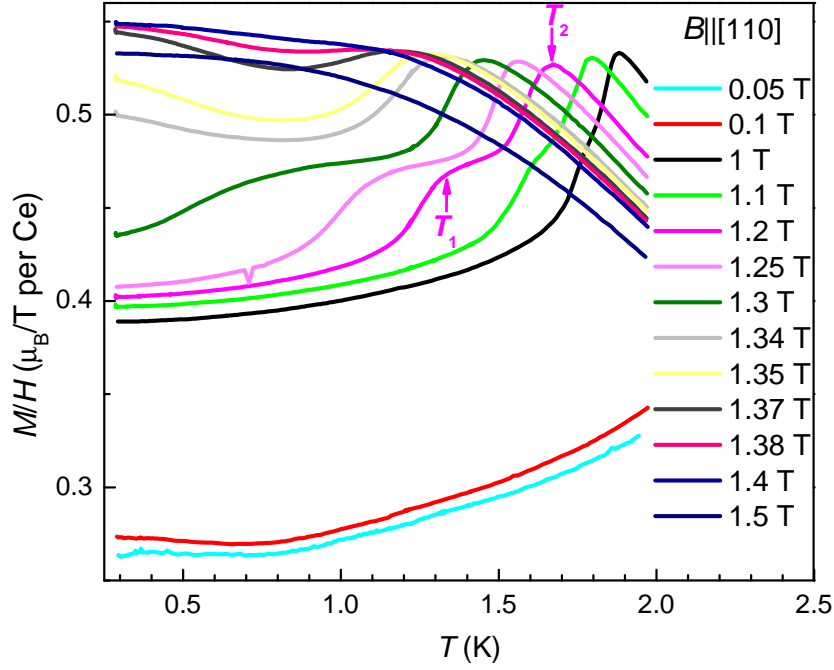


Figure 5.70: Magnetic susceptibility (defined as M/H) vs temperature, transition temperatures are indicated by T_1 and T_2 (measurements carried out by A. Sidorenko).

$B||[001]$, therefore the respective critical field will be determined solely from specific heat and electrical resistivity measurements.

At high fields, the antiferromagnetic transition is completely suppressed and the magnetic susceptibility saturates at low temperatures, so that M/H becomes constant (Fig. 5.71 (right)), as indicated by the dotted line in Fig. 5.71 (right).

In the $H \rightarrow 0$ limit of the isothermal data, the Pauli susceptibility $\chi(T)$ is determined. $\chi(T)$ in the $T \rightarrow 0$ is χ_0 . To estimate χ_0 , a linear extrapolation from the lowest temperature points was taken. The χ_0 data is plotted vs magnetic field $B - B_C$ and a

$$\chi_0 = P_0 |B - B_C|^{-\delta} \quad (5.15)$$

fit (P_0 : amplitude, δ : critical exponent) is applied on both sides of the critical field. This is shown in Fig. 5.72 for $B||[110]$. The value of the critical exponent in CeB_6 , extracted from susceptibility data, is $\delta = 0.66 \pm 0.13$. χ_0 diverges at a similar rate as reported for other quantum critical materials, for instance $\text{YbRh}_2(\text{Si}_{0.95}\text{Ge}_{0.05})_2$ with $\delta_{\text{YRSG}} = 0.6$ and $B_C = 0.027\text{T}$, and faster than the logarithmic SDW QCP expectation [128].

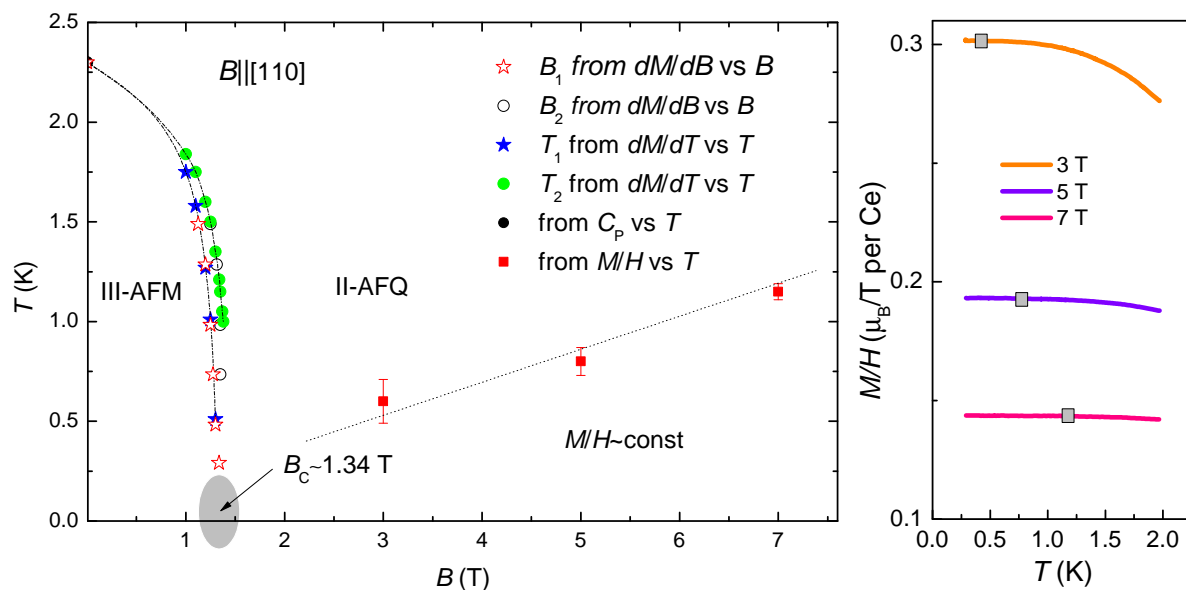


Figure 5.71: Left: Temperature-magnetic field phase diagram of CeB₆ for $B \parallel [110]$, mainly extracted from magnetization measurements. The dotted line marks the onset of $M/H \sim \text{constant}$, corresponding to FL behaviour. Right: M/H at high magnetic fields, used for the determination of the FL region. The squares indicate the temperature below which M/H is constant.

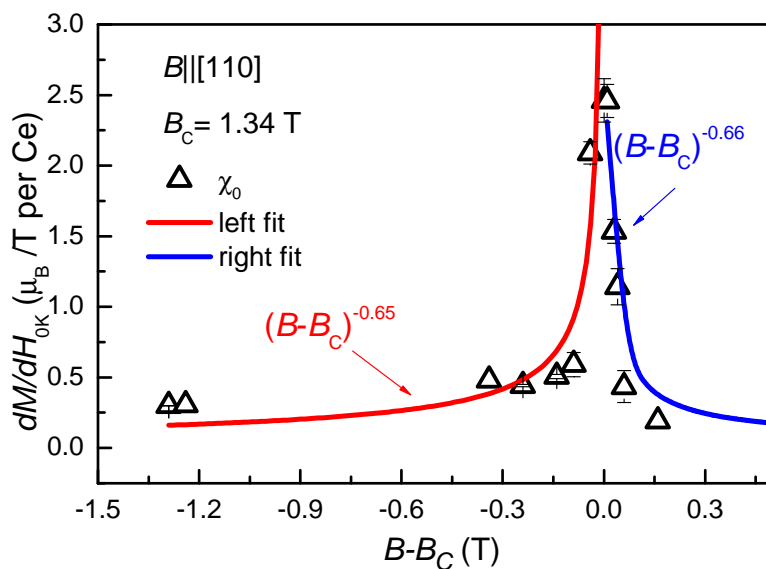


Figure 5.72: Extraction of critical exponents from fits to χ_0 with magnetic field applied along the $[110]$ direction. $B_c = 1.34$ T, $P_0 = 0.096$.

Specific heat

The specific heat was measured with magnetic field applied along both directions in collaboration with J. Larrea. Fields between 0 T and 3 T (1.75 T) were applied along [001] ([110]) and the specific heat was measured in the temperature range between 0.4 K and 4.5 K, for selected fields up to about 6 K. C_p vs T data are shown in Fig. 5.73. Due to temperature stabilization issues, especially in the temperature region around 2 K, the number of data points around T_N is limited. We will therefore concentrate at the low-temperature region of the measured data.

As also mentioned in Sect. 2.2.1, C_P/T vs T has shown $-\sqrt{T}$, or $-\ln T$ temperature dependences in the quantum critical regime. Logarithmic behaviour, associated with underlying 2D quantum fluctuations of a SDW QCP, was, for instance, reported in $\text{Ti}_{1-x}\text{Sc}_x\text{Au}$ around the critical doping level (see Sects. 4.3 and 5.4) and in the cubic quantum critical material $\text{Ce}_3\text{Pd}_{20}\text{Si}_6$ close to its QCP at 0.9 T, inside its AFQ phase [129] (see also Sects. 4.5 and 5.6). A striking difference to $\text{Ce}_3\text{Pd}_{20}\text{Si}_6$ is the evolution of the antiferromagnetic transition signature in the specific heat with field. Whereas it is strongly shifted and broadened in the case of $\text{Ce}_3\text{Pd}_{20}\text{Si}_6$, its position remains nearly constant in the case of CeB_6 , and it is not broadened to such a high extent. Upon approaching the critical field, the specific heat curves resemble the shape of itinerant systems rather than localized ones (antiferromagnetic TiAu , or, at higher energy scales, ferromagnetic Cr [97, 130]). In the low-temperature region, C_P/T is mostly linear in T^2 (Fig. 5.74), i.e. there is no appreciable increase of C_P/T with decreasing temperature at any field. Thus, if there is an underlying quantum critical contribution, it does not dominate the behaviour of the specific heat. No crossover to NFL behaviour is observed in the critical region, and as a consequence all specific heat data were analyzed within the FL framework. From the data in Fig. 5.74, the γ_0 values are extracted.

A linear fit

$$C_P/T = \gamma_0 + \beta T^2 \quad (5.16)$$

was applied to the C_P/T vs T^2 curves. β is a parameter quantifying the phonon contribution to the specific heat, and γ_0 is the Sommerfeld coefficient of the electronic contribution. γ_0 is proportional to the effective electron mass.

The critical exponents were evaluated by plotting γ_0 of the two field directions along [001] and [110] over $(B - B_c)$ and fitting this by a power law function

$$\gamma_0 = P_1 |B - B_c|^{-\delta} \quad (5.17)$$

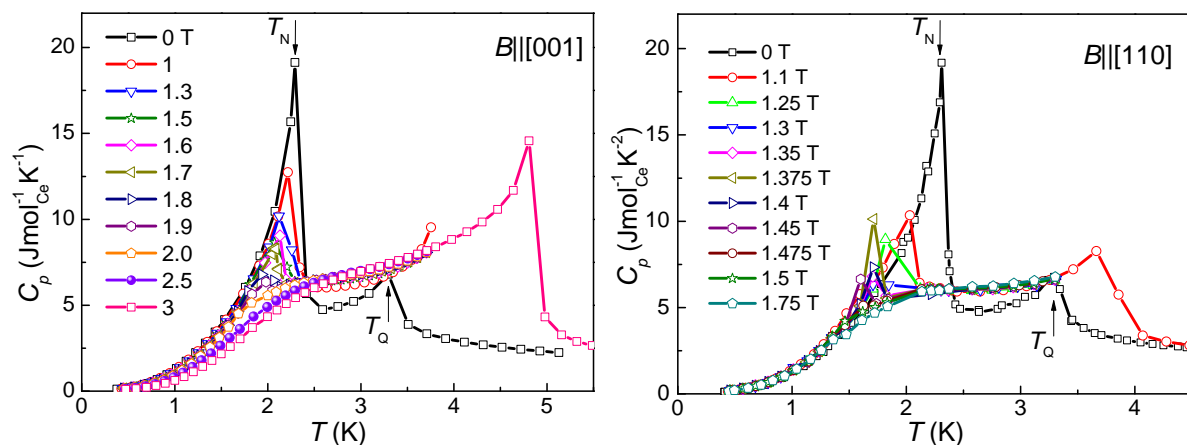


Figure 5.73: Specific heat measurements of CeB₆ with magnetic field applied along the [001] (left) and [110] (right) directions. The transitions to the antiferromagnetic and the AFQ phase are indicated on the 0 T curve as T_N and T_Q , respectively.

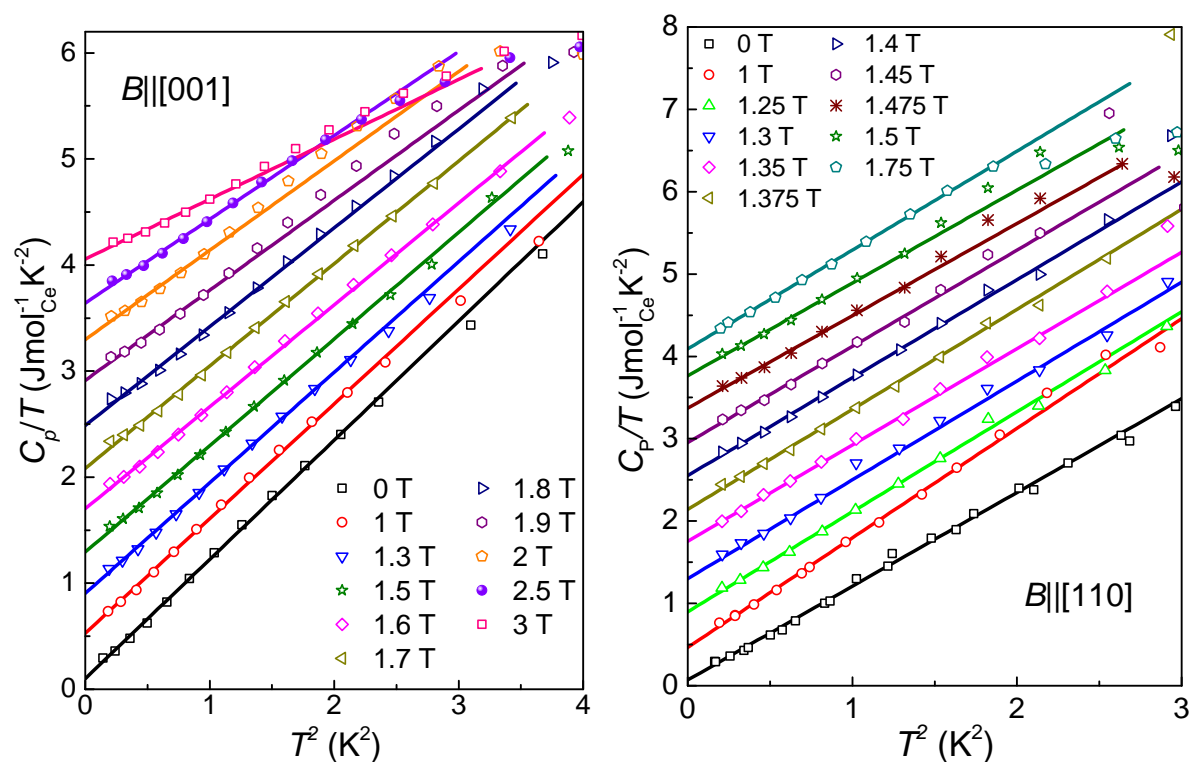


Figure 5.74: C_p/T vs T^2 of CeB₆ with magnetic field applied along the [001] (left) and [110] (right) directions. Each curve has been shifted by $0.4 \text{ Jmol}^{-1}\text{K}^{-2}$ for clarity. The dashed lines are the linear fits to the low-temperature region, γ_0 is the intersection of a fit with the $T = 0$ axis.

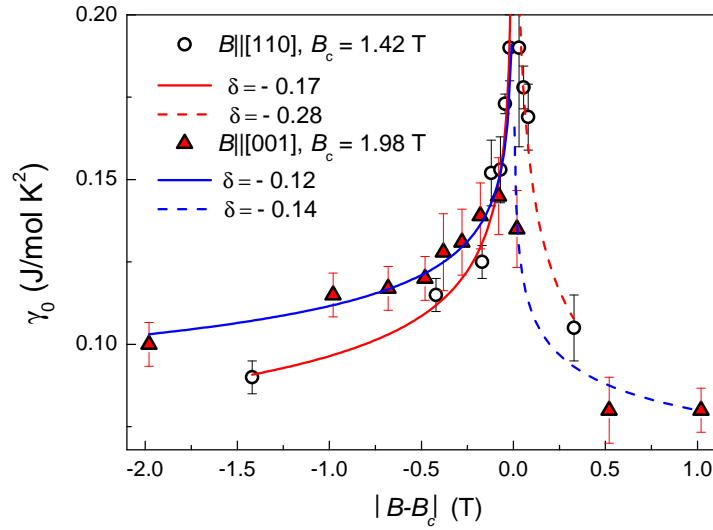


Figure 5.75: γ_0 vs $|B - B_c|$ for both field directions, along with fits corresponding to Eqn. 5.17.

P_1 is a parameter, B_c the critical field, and δ the critical exponent. This is shown in Fig. 5.75. γ_0 is enhanced around the critical field, a behaviour which was reported previously on CeB₆ [99]: The literature data has only a handful of data points up to 1 T and one around 2.5 T, so that the present data provides additional information about the divergence at closer proximity of the QCP. The cusp in γ_0 had also not been investigated with the magnetic field applied along defined crystallographic directions. The relative enhancement between the lowest and highest measured points is similar (about 100%) in both literature and our measurements.

For both field directions, the exponents are slightly different on the two sides of the respective critical field, the $B > B_c$ side diverging a bit faster with a higher exponent (Tab. 5.4). Compared to the divergence of χ_0 , which is nearly symmetrical around the critical value and around $\delta_\chi = -2/3$, there is a larger discrepancy between δ at $B < B_c$ and $B > B_c$ with field along [110], and overall the exponent δ indicating the divergence of γ_0 is lower (see Fig. 5.75). Compared to other quantum critical materials, the divergence is slower. For instance, Ce₃Pd₂₀Si₆ shows a nearly symmetrical divergence of the Sommerfeld coefficient towards to QCP with $\delta \sim 0.4$.

Another discrepancy to magnetization and resistivity measurements (analysis see below) is the critical field value for applied field along [110]. The value derived from specific heat is by 80 mT higher than the value derived from the other measured properties. This is likely due to a misalignment of the sample on the sample holder (as the sample is only fixed with a small amount of grease, and does not have a perfectly rectangular shape). A misalignment of a few degrees is therefore a possible measurement error. If a para-

sitic field component along [001] is assumed, a misalignment of approximately 7° would enhance the critical field by the observed value via $(B_{c[001]} - B_{c[110]}) \sin(7^\circ) \approx 78 \text{ mT}$.

Electrical resistivity

The resistivity was investigated in a dilution refrigerator and is shown for both field directions in Fig. 5.76. In analogy to the A coefficient analysis in Sect. 5.3, the resistivity was plotted vs T^2 , and the slope in the lowest temperature region, the A coefficient, was determined from fits to the data with

$$\rho(T) = \rho_0 + AT^2 \quad . \quad (5.18)$$

$\rho(T) - \rho_0$ data plotted vs T^2 , together with the low-temperature fits, are shown in Fig. 5.77. For field along [001], the temperature dependence can be described by T^2

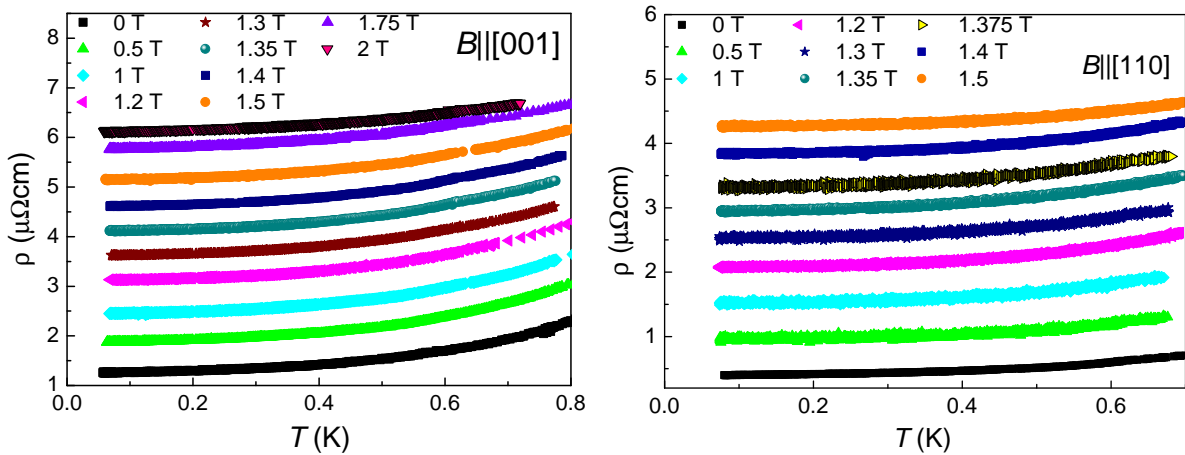


Figure 5.76: Resistivity data, for magnetic field applied along [001] (left) and [110] (right). An offset of $0.5 \mu\Omega\text{cm}$ was added to each curve with $B > 0$ for clarity.

behaviour at least up to 300 mK for all fields, as indicated by the arrows in Fig. 5.77. The T^2 range is larger in zero field and for the high fields 1.75 T and 2 T. For field along [110], a T^2 behaviour can describe the data at least up to 300 mK. From Fig. 5.76, it can also be seen that there is no clear linear temperature dependence, as for instance observed in $\text{CeNiAs}_{1-x}\text{P}_x\text{O}$ in Fig. 5.50 of Sect. 5.3. In CeB_6 , at the lowest temperatures, FL behaviour is observed, which crosses over into a T^3 dependence with increasing temperature. These temperature dependencies are more obvious for $B||[001]$. For $B||[110]$, the difference between T^2 and T^3 fits is small in the low-temperature range, because the curves are flatter and show a higher noise level. Only in the zero field curve, a downturn

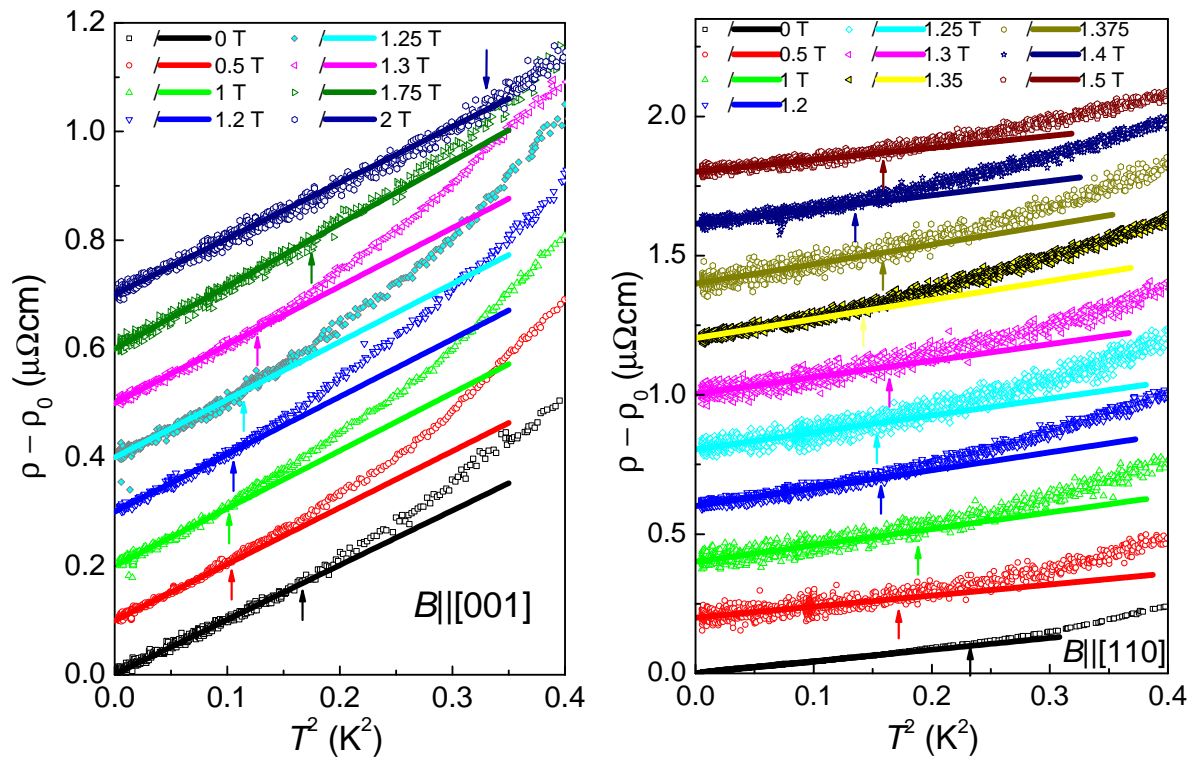


Figure 5.77: Resistivity vs T^2 for selected magnetic fields applied along [001] (left) and [110] (right). Offsets of $1 \mu\Omega\text{cm}$ (left) and $1 \mu\Omega\text{cm}$ (right) have been added for clarity. The arrows indicate the temperature, where the difference of raw data and fit exceeds 2% (left) and 4% (right).

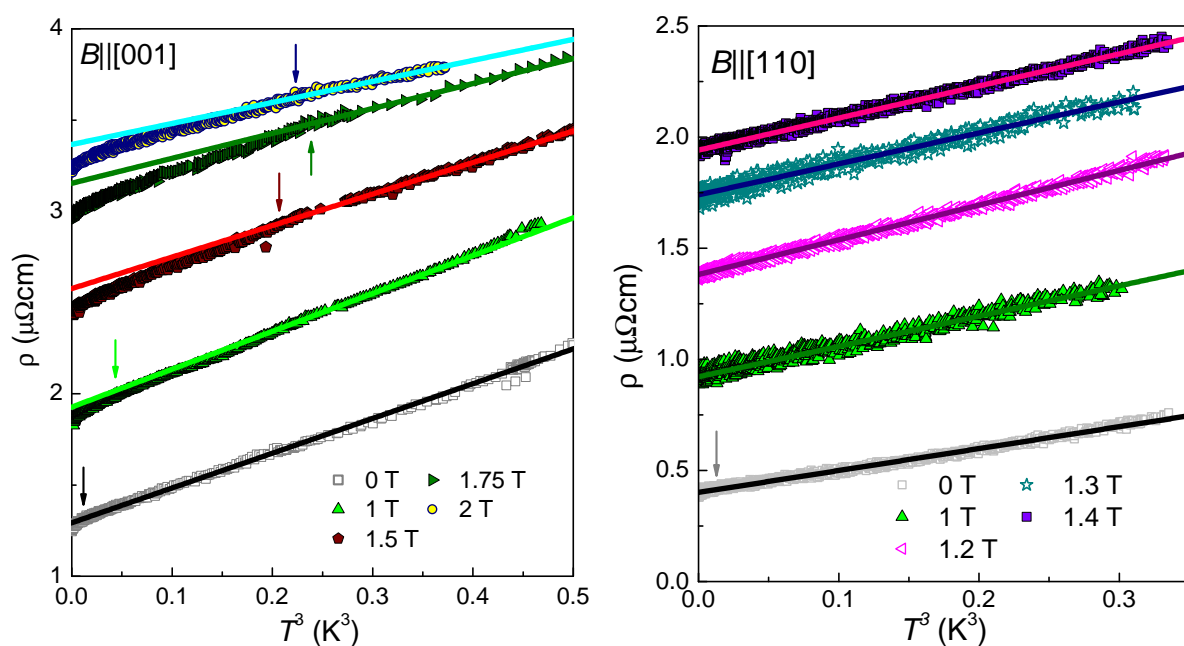


Figure 5.78: Resistivity vs T^3 for selected magnetic fields applied along [001] (left) and [110] (right). Offsets of $0.1 \mu\Omega\text{cm}$ (left) and $0.4 \mu\Omega\text{cm}$ (right) have been added for clarity. The full lines are linear fits to the data, the arrows (left) indicate the lowest temperature, where the fit is within 2% of the data. The gray arrow (right) is a guide to the eye.

at the lowest temperatures can be observed (indicated by the arrow in Fig. 5.78 (right)). The data are plotted vs T^3 in Fig. 5.78. This power law dependence (T^2 at lowest, T^3 at higher temperatures), does not change when the critical field is crossed.

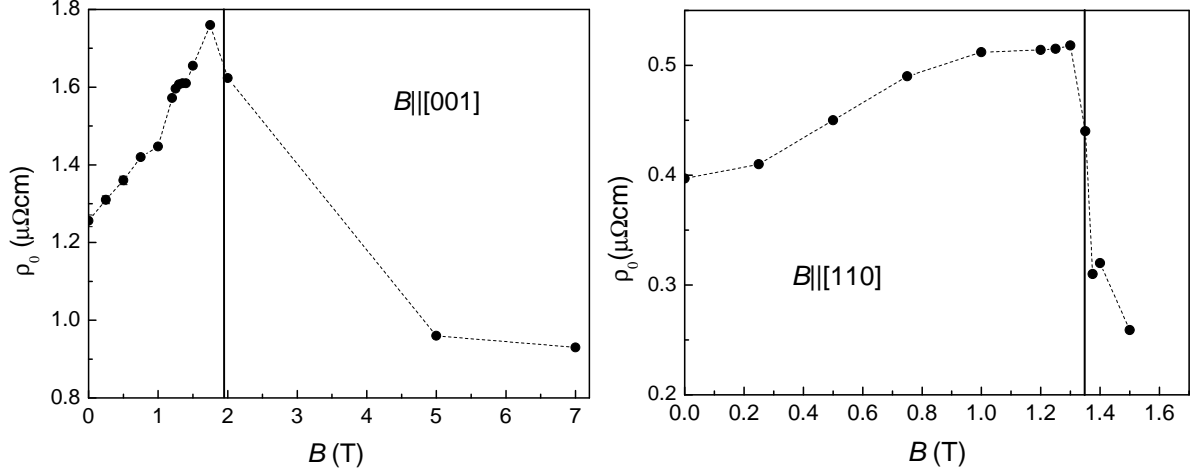


Figure 5.79: Evolution of ρ_0 , obtained from quadratic fits to the low-temperature resistivity, for magnetic field applied along [001] (left) and [110] (right).

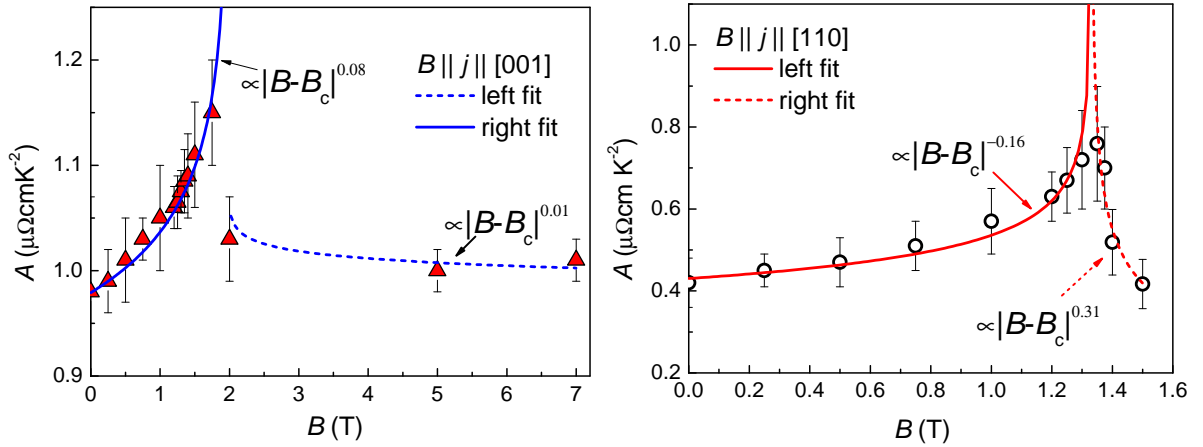


Figure 5.80: Evolution of the A coefficient, obtained from quadratic fits to the low-temperature resistivity, for magnetic field applied along [001] (left) and [110] (right), and fits to $A = P_2|B - B_c|^\delta$ (P_2 : Amplitude).

The evolutions of ρ_0 and the A coefficient with field are shown in Figs. 5.79 and 5.80, respectively. Both show a change around the critical fields. In the resistivity data, the A coefficient was fit to a power law analogous to Eqns. 5.9 and 5.17 on both sides of the critical field (Fig. 5.80). As in the cases of γ_0 and χ_0 , there is an enhancement of the A coefficient around $B_c = 1.98$ T ($B||[001]$) and $B_c = 1.34$ T ($B||[110]$). However, the

divergence of the A coefficient is weak compared to materials like YbRh₂Si₂ ($\delta_{YbRh_2Si_2} \sim 1$) or Ce₃Pd₂₀Si₆ ($\delta_{Ce_3Pd_{20}Si_6} \sim 0.4$).

Table 5.4: Comparison of the fit parameter δ as defined in Eqns. 5.15 and 5.17, and in Fig. 5.80.

$B \parallel$		χ_0	γ_0	A
[001]	left	-	0.12	0.08
[001]	right	-	0.14	0.01
[110]	left	0.65	0.17	0.16
[110]	right	0.66	0.28	0.31

Discussion

The KWR (A/γ_0^2 , see also Sect. 2.1.3) for the two different field directions is plotted in Fig. 5.81 as function of the applied field. In the two CeB₆ samples we observe a similar value of this ratio as reported in literature (shown for various heavy fermion compounds, including CeB₆, in Fig. 2.4 in Sect. 2.1.3): $10 \mu\Omega\text{cm mol}^2\text{K}^4\text{J}^{-2}$ for the sample used for the measurements along [001], and a slightly lower value of $5 \mu\Omega\text{cm mol}^2\text{K}^4\text{J}^{-2}$ for the sample used for the measurements along [110]. The values in zero field should be the same, and the difference has to be regarded as a systematic offset error, which could for instance be caused by the misalignment of the sample in the specific heat measurements (as discussed above). Regarding the field dependence of the KWR, it has been reported to change in the quantum critical region and even diverge when the QCP is approached [26]. There is no strong increase in the KWR of the measured CeB₆ data, but in Fig. 5.81, a step is seen at the critical field. This is especially supported by the many available data points for the [110] direction. For field alignment along [001], the data is consistent with a step at the critical field of $B_c = 1.98 \text{ T}$. Additional data points in the close vicinity of the critical field could substantiate this. Clearly, there is no step at $B_c = 1.34 \text{ T}$, when the field is applied along the other direction, [001], so that the feature seems correlated with the anisotropic suppression of T_N .

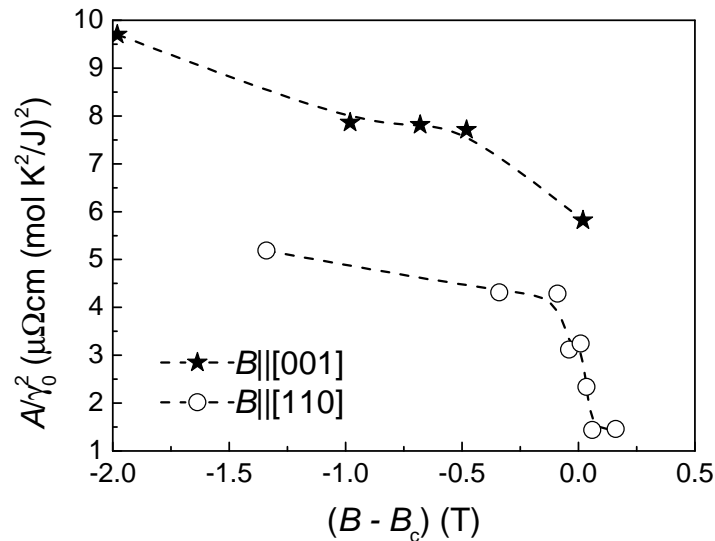


Figure 5.81: KWR vs $(B - B_c)$ for magnetic field applied along the two crystallographic directions of CeB₆.

Summarizing the quantum critical aspects of the measurements on CeB₆: On the one hand, several indications of quantum critical behaviour were confirmed, namely

the enhancements of χ , γ_0 , and A from magnetization, specific heat, and resistivity (Figs. 5.72, 5.75, 5.80), respectively. The divergences of γ_0 and A , however, are slower than in other materials with confirmed quantum critical behaviour. Furthermore, a change of the residual resistivity value ρ_0 and a change of the KWR at the critical field (Fig. 5.81) were observed. On the other hand, no typical temperature dependences are found. From theory, quantum critical contributions corresponding to $C_p/T \propto -\sqrt{T}$ ($C_p/T \propto -\ln T$), $\chi \propto T^{-3/2}$ ($\chi \propto -(\ln T)/T$), and $\rho \propto T^{3/2}$ ($\rho \propto T$) are expected for a 3D (2D) antiferromagnetic QCP [6, 8, 39] (see also Sect. 2.2.1). Whereas this is observed in various materials (see for instance Tab. 2.2 in Sect. 2.2.1), no such contribution could be found in the temperature dependences of CeB₆. One could argue that the situation is more complex than in many other materials, because of the presence of AFQ order. However, Ce₃Pd₂₀Si₆, a cubic material that also shows AFQ order and therefore shares many characteristics with CeB₆, has obvious $C_p/T \propto -\ln T$ and $\rho \propto T$ contributions near its critical field [60].

No NFL behaviour is found at lowest temperatures and close to the critical fields in resistivity and specific heat. The temperature dependence of the resistivity at lowest temperatures is FL-like, crossing over to a T^3 dependence at higher temperatures, clearly no T^η with $\eta < 2$ is observed. This persists when the critical value is exceeded and CeB₆ has evolved from antiferromagnetic to AFQ order. Also from specific heat, no typical quantum critical signatures are visible (as found in the other materials within this work, CeNiAs_{1-x}P_xO, Ti_{1-x}Sc_xAu, and Ce₃Pd₂₀Si₆).

It seems that in CeB₆, several effects are related to the suppression of a transition temperature, but not to quantum criticality. The key to understanding this situation might be to look at the defining differences between quantum critical Ce₃Pd₂₀Si₆ and CeB₆. As mentioned above, these two cubic materials share several characteristics, but one remarkable difference is the anisotropy of CeB₆ with respect to field, starting from the lowest fields. In the case of Ce₃Pd₂₀Si₆, up to fields above the confirmed QCP at 0.9 T, no difference was found for different field alignments. While antiferromagnetic order has been confirmed in zero field by neutron diffraction experiments, the application of field leads to complex magnetic ordering phenomena of both local and itinerant type [131, 132]. This evolution of the magnetic order itself could be the reason why a QCP is not observed, similarly to CeCoGe_{3-x}Si_x, where the suppression of T_N is intertwined with the evolution of a spin-wave gap; this leads to an electrical resistivity which is dominated by magnetic excitations at low energies [133]. Recent results from inelastic neutron scattering experiments have emphasized the importance of ferromagnetic fluctuations

in CeB_6 , together with the proximity of CeB_6 to a ferromagnetic instability [134]. If the application of magnetic field stabilizes ferromagnetic order, the quantum phase transition will turn into a first order transition, and no QCP will occur [135]. This is consistent with the fact that small signatures of the transition (cusps in A , χ , γ_0 , steps in ρ_0 , KWR) are seen in the physical properties, but no comprehensive quantum critical behaviour is observed.

5.6 $Ce_3Pd_{20}Si_6$

In this cubic material, the suppression of antiferromagnetic order at around 0.9 T gives rise to a QCP. At fields above the critical field, another type of order is established, which is most likely of AFQ type [60]. Previous measurements of the Hall coefficient and the magnetoresistivity [60, 101] revealed a crossover with decreasing width as temperature decreases, which extrapolates to an abrupt change at $T = 0$ K. This behaviour suggests that a Kondo breakdown occurs at this QCP in $Ce_3Pd_{20}Si_6$. Before, similar indications for the Kondo destruction scenario had only been observed in $YbRh_2Si_2$ [44]. In contrast to $Ce_3Pd_{20}Si_6$, $YbRh_2Si_2$ has a tetragonal crystal structure with $c > 2a$ (a, c crystallographic directions, see Sect. 4.1), which effectively results in a reduced dimensionality. As low-dimensional spin fluctuations were essential for the modeling of the Kondo destruction scenario, it was believed that a Kondo destruction could not occur in cubic systems [9]. $Ce_3Pd_{20}Si_6$ seems perfectly three-dimensional from its crystallographic point of view (details on the material parameters see Sect. 4.5), and the observation of a Kondo destruction is therefore of great interest. Thus, results from this material were a valuable addition to the suggested global phase diagram for quantum critical systems [102] (see Sect. 4.5). The work on $Ce_3Pd_{20}Si_6$ within this thesis was dedicated to exploring its phase diagram beyond the abovementioned QCP, and was carried out in collaboration with V. Martelli, and with support of J. Hänel for the dilution refrigerator measurements.

Previous results were obtained on polycrystalline samples and included data from neutron scattering experiments, magnetic property measurements, low-temperature resistivity measurements, magnetoresistivity measurements, and Hall effect measurements [60]. They were focused on the QCP at 0.9 K and the properties of the putative AFQ phase.

Going one step further, to the investigation of oriented singly-crystalline samples, strong anisotropies with respect to the direction along which a magnetic field is applied were reported; depending on the orientation of the applied field (along [100], [110], or [111] directions), specific heat, magnetoresistivity, and Hall effect measurements showed anisotropic behaviour at magnetic fields above 1 T [136, 137, 138]. Up to 1 T, no differences between the field orientations are found, including the suppression of T_N at the first QCP at 0.9 T, which takes fully place in the isotropic part of the phase diagram. The transition from the putative AFQ phase to the paramagnetic phase, however, is anisotropic with respect to the field direction: Whereas the AFQ ordering temperature

T_Q is fully suppressed at 4 T for fields along [100], T_Q is only fully suppressed at 10 T for fields along [110], and T_Q is fully suppressed at even higher fields above 14 T along [111] [137]. There seems to be a striking difference when magnetic field is applied along [100]: Only in this direction, an anomaly in the specific heat within the AFQ phase was observed [138], and interpreted as the signature of a phase transition (the exact nature of the involved phases, named II and II' , remaining unclear).

To study the possible suppression of the AFQ phase in field and thus, possibly, expose a quadrupolar QCP, magnetoresistivity measurements were performed with fields along [100] and [110] by V. Martelli et al [103]. For $B||[100]$, a kink in the transverse magnetoresistivity was observed at the position of the tentative new transition between phase II and II' , $T_k(B)$, identified by specific heat measurements [138] (Fig. 5.82). For fields applied along [110] no signature could be identified in the magnetoresistivity across $T_k(B)$.

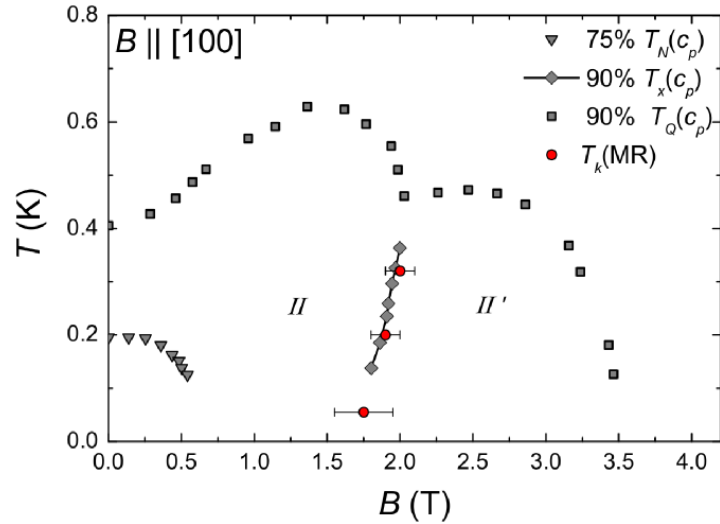


Figure 5.82: Temperature - magnetic field phase diagram of $Ce_3Pd_{20}Si_6$ with magnetic field applied along [100], as presented in Ref. [103]. The red data points at T_k are extracted from magnetoresistance data. $T_x(B)$ and $T_k(B)$ separate two phase diagram regions, named.

In order to single out the unique features of the $B||[100]$ phase diagram across $T_k(B)$, measurements with magnetic field along [110] or [111] can be used as a background because no features are observed at $T_k(B)$ for these directions. For this purpose, a set of magnetoresistance and Hall effect measurements was performed on the two samples shown in Fig. 5.83. The magnetic field was applied perpendicular to the current flow and along the [100] crystallographic direction of the sample in Fig. 5.83 (left), and along

the [111] crystallographic direction of the sample in Fig. 5.83 (right).

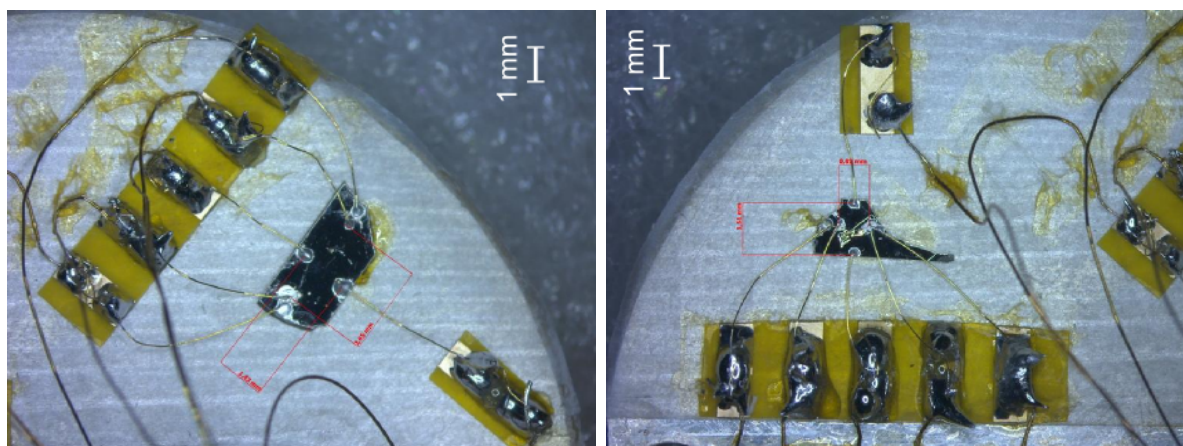


Figure 5.83: The two differently oriented $Ce_3Pd_{20}Si_6$ samples (grown by A. Prokofiev, batch number SC5t, samples a and c), which were investigated in the course of this work: The contacted faces were perpendicular to [100] (*left*) and [111] (*right*) crystallographic directions.

Each of the two samples was contacted by spot welding six $50\ \mu\text{m}$ Au wires onto its polished surface. The arrangement of the wires is described in Sect. 3.3.4. The contacts were covered with a tiny drop of silver glue for mechanical stability. The two samples were then mounted onto a silver platform with contact pads and leads for the electrical lines. Everything was electrically insulated from the electrical ground by cigarette paper and a thin layer of GE varnish. The contacted sample pieces, with their Au wires soldered to the contact pads, are shown in Fig. 5.83.

The voltage and Hall voltage signals of both samples were amplified by cryogenic transformers. Two measurement runs were carried out; the presented data will mostly originate from the second run, where the transformer ratios and the field ramping/waiting times were optimized. Figure 5.84 shows magnetoresistivity curves for the lowest measured temperatures from both measurement runs. Due to the considerable reduction of the noise level in the second run the features of interest (indicated by B_k in Fig. 5.84) can be clearly observed. At these low temperatures, the shoulders just below 2 T are prominent characteristics of the isothermal curves. Also the hump somewhat above 4 T, indicating the suppression of the AFQ phase at B_Q , is visible.

A measurement artifact in the form of a very narrow peak close to zero field was observed in several measurements. The origin of this peak is unclear, but seems to be due to the measurement setup rather than to intrinsic sample properties (for instance an electronic effect caused by the starting magnetic field ramp). As the focus of the

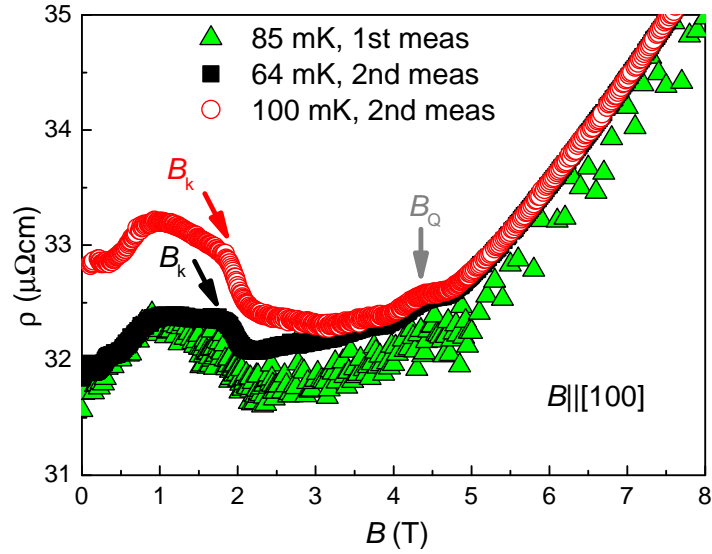


Figure 5.84: Exemplary magnetoresistance curves at low temperatures (with precision improvement of the measured data in the second measurement run).

present study is the field region above 1 T, where anisotropic effects start to set in, the narrow zero-field peak is not shown and will not be discussed further.

Figure 5.85 shows the isothermal magnetoresistance data for several temperatures for both $B||[100]$ and $B||[111]$. Most isotherms were measured up to a maximum field of 10 T, a few to 14 T, and at the lowest temperature of 64 mK measurements were performed up to 8 T. At high temperatures, the curves with field alignment along [100] (Fig. 5.85 (left)) and along [111] (Fig. 5.85 (right)) have a similar shape. Upon decreasing the temperature, the aforementioned shoulder at B_k develops in the curves of Fig. 5.85 (left), whereas the shoulder is absent in the curves of Fig. 5.85 (right). The shoulder's width increases strongly with temperature and is hardly observable in the raw data at the highest measured temperature of 1150 mK.

Figure 5.86 shows the resulting curves after the background subtraction: Each curve was normalized to its zero field value ρ_0 , and the normalized background curve with $B||[111]$ was subtracted from the curve with $B||[100]$ for every temperature. The resulting curves take the form of a peak-like anomaly below about 5 T. At the lowest temperatures, the shape of this anomaly seems to be rather a hat than a peak, with a relatively flat portion at intermediate fields, but a pronounced increase at small fields and a pronounced decrease near 2 T. The maximum of the overall feature, B_{max} , shifts to higher fields, and the anomaly broadens with increasing temperature.

For an analysis of this situation with respect to the Kondo breakdown scenario for

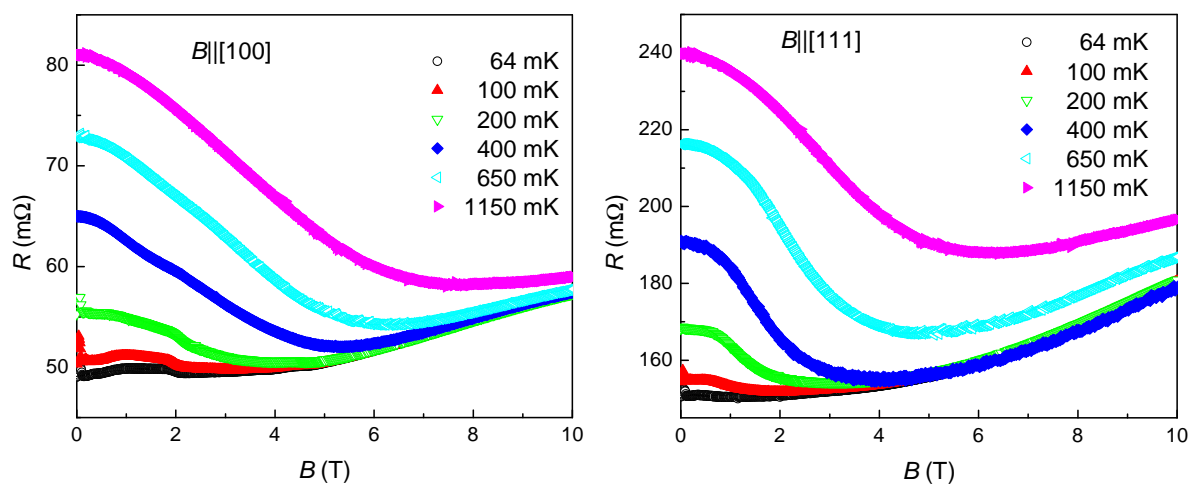


Figure 5.85: Different isotherms of magnetoresistance data for field aligned along [100] (*left*) and [111] (*right*). The absolute values are enhanced by a factor of 100 due to the amplification of the cryogenic transformers.

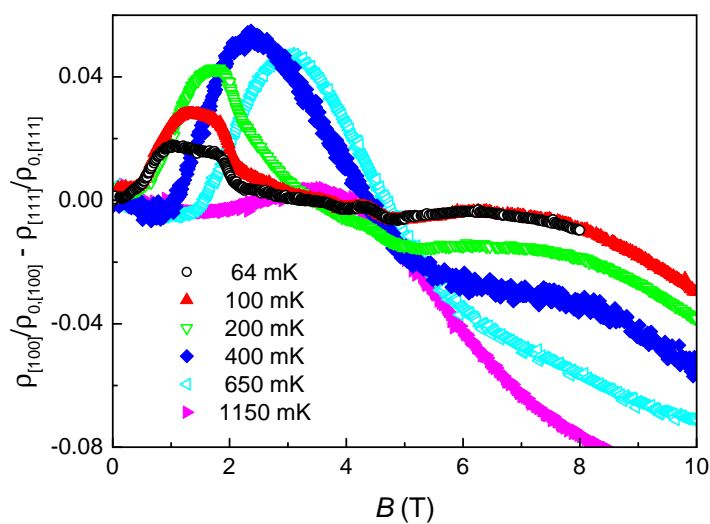


Figure 5.86: Difference of the isothermal resistivity curves: The data measured with field along [111] were subtracted from the data measured with field along [100]. The arrows are guides to the eye and trace the approximate position of the resulting peak.

the second QCP at 1.8 T, the peak structure has to be understood in detail. For a single peak, the position and width has to be determined at every temperature and extrapolated to absolute zero, as was done for the QCP at 0.9 T in the polycrystalline samples [60]. A collapse of the peak width at the tentative QCP would be a strong indication for a Kondo breakdown. The optimization of the analysis procedure for the observed hat-like feature, as well as additional measurements, are ongoing.

For a thorough analysis of a tentative Kondo breakdown, a very promising option is to turn to Hall measurements, where signatures of a Kondo breakdown have been most clearly observed (see Sect. 2.2.2). Analyses of both Hall and magnetoresistivity crossovers have been performed for YbRh_2Si_2 and polycrystalline $\text{Ce}_3\text{Pd}_{20}\text{Si}_6$ [44, 43, 101].

The Hall resistivity data of the two measured single-crystalline $\text{Ce}_3\text{Pd}_{20}\text{Si}_6$ samples are shown in Fig. 5.87. Compared to the magnetoresistivity data, the Hall resistivity becomes increasingly noisy when the magnetic field increases. This is surprising, since higher fields tend to increase and stabilize the Hall signal and therefore reduce the noise. The reason for the high-field noise is unclear; adjusting the measurement parameters in the second cooldown could not improve the Hall measurement to the desired precision. As no such noise increase was reported for polycrystalline samples, the underlying reason is likely to be related to instabilities in the measurement system (stray fields, electronic fluctuations, grounding issues). Various irregularities connected with the use of the magnet (unusually high He consumption rates, crashes of the source, etc.) were possibly related to a leak in the cold trap and could have introduced high noise to the measurements in magnetic field. Another possible explanation would be an insufficient quality of the Hall contacts of the sample. However, this is unlikely to show the same effect in both samples. Furthermore, the magnetoresistance measurements were not affected by increasing noise at high fields, even though the contacts were applied in the same way.

Nevertheless, an evolution can be seen in the different Hall isotherms, and the two directions are clearly different in their overall behaviour. For $B||[111]$ (Fig. 5.87 (right)), the Hall resistivity is constantly decreasing with field, with a gradual change of slope. The crossover between a steeper and a flatter slope broadens with temperature and shifts to higher fields. In contrast to that, for $B||[100]$ (Fig. 5.87 (left)), the Hall resistivity shows a broad minimum. The minimum broadens even more with increasing temperature and shifts to higher fields. Following the arguments for the magnetoresistivity, the Hall data with field along [111] can be used as background for the curves with field along

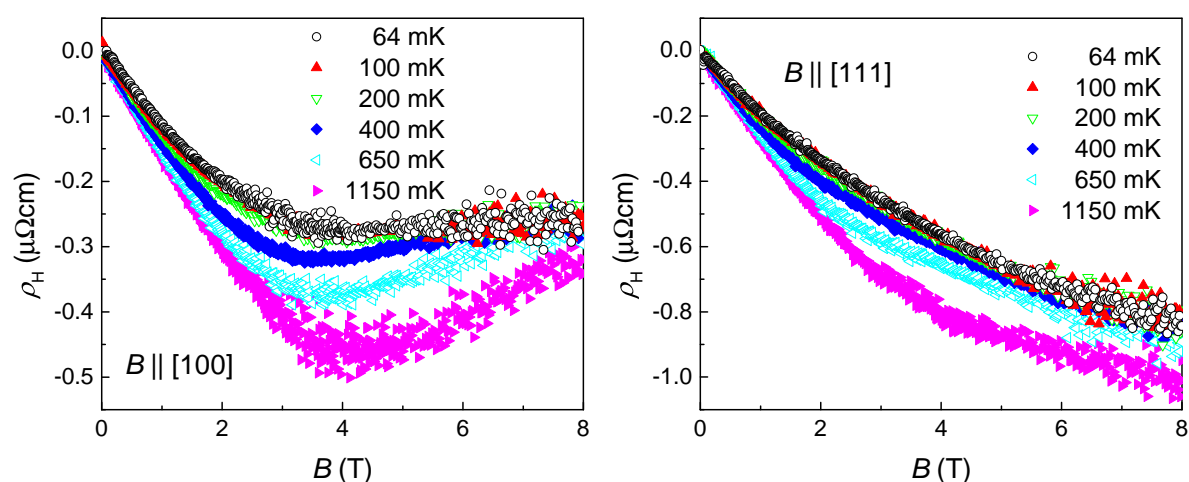


Figure 5.87: Isothermal Hall resistivity data, with magnetic field applied along [100] (*right*) and [111] (*left*). Every data point is obtained by averaging the Hall resistivity values at the respective positive and negative field. The amplification ratio of the cryogenic transformer was 100, as for the data in Fig. 5.85.

[100]. If the noise can be successfully decreased in future Hall measurements, the width of the Hall crossover can be determined and extrapolated to 0 K. These investigations are ongoing, and after several of the above-mentioned technical issues of the dilution refrigerator measurements have been solved, it should be possible to decrease the noise level considerably, or at least to pin down the underlying source.

6 Summary and outlook

In the course of this thesis, several materials were investigated in the context of quantum criticality at low energies. Various transport measurements were performed at low temperatures, and in the case of YbRh_2Si_2 , a low-temperature microwave experiment was set up.

YbRh_2Si_2 was the first material to show clear indications of a Kondo breakdown and a corresponding $k_B T^*$ energy scale emerging from the QCP. The exact nature of this energy scale is currently under debate, and experimental data on the electronic excitations across this energy scale are of great interest. To access these electronic excitations, YbRh_2Si_2 single crystals were coupled to the electric field of a microwave resonator. Prior to performing the microwave measurements, finite element simulations were performed to obtain information on the qualitative behaviour of coplanar waveguide resonators in the presence of metallic samples. The quality factor and resonance frequency of the resonator are affected by the conductivity (lower conductivity, lower quality factor), size (larger sample, lower quality factor), and distance (smaller distance, lower quality factor) of the sample, and these parameters had to be considered in the experimental setup. A coplanar waveguide resonator design with quality factors of the order 10^5 was adapted for this purpose. The sample was placed into an electric field antinode at the resonance. By an iterative placement procedure using the cover of the resonator box with a designed sample holding mechanism, the sample was positioned very close to the resonator surface and thus coupled to the electromagnetic field. While being installed in the microwave resonator box, the sample resistance could be measured with a four-probe standard technique. Several measurement cycles were performed with this arrangement at dilution refrigerator temperatures, sweeping through the temperature - magnetic field phase diagram of YbRh_2Si_2 . The main goal was to retrieve information on the crossover between large and small Fermi surface states by analyzing electronic excitations in the low-energy microwave range. It was seen that the application of microwave energy slows down the process of formation of heavy composite quasiparticles, and that the crossover in the magnetoresistance is slightly shifted to higher magnetic fields in the presence of

microwaves. However, it also became clear through the performed measurements that, in the present arrangement of sample characteristics and resonator design, the contribution of the sample properties to the transmission of the resonator is small in comparison to background effects and noise. Also, achieving the right coupling between sample and resonator turned out to be difficult, as well as reproducing the same coupling level with a different sample piece. Alternative resonator designs, optimized for sample sizes and shapes, and for the specific measurement type (temperature or field sweep), could be of advantage, even if the achieved (unloaded) quality factors would be lower.

In addition to electronic excitations, access to the physical properties in the very vicinity of the QCP are of great interest. As all energy scales are very low, ultra-low temperature measurements can reveal fundamentally important information (e.g. if a superconducting dome occurs in YbRh_2Si_2). A series of samples was prepared and characterized by resistance measurements for this purpose, and first successful measurements down to the μK range were obtained.

In the nickel oxyphosphide substitution series $\text{CeNiAs}_{1-x}\text{P}_x\text{O}$, quantum critical points occur when the Néel temperature is suppressed to zero, either by pressure ($p_{\text{crit}} \sim 6.7 \text{ kbar}$ for $x = 0$) or substitution with P ($x_{\text{crit}} \sim 40\%$). Resistivity measurements at dilution refrigerator temperatures down to 50 mK were performed on polycrystals close to the critical doping level. The influence of an external magnetic field up to 10 T was investigated for the P substitution levels $x = 35\%$ and $x = 40\%$. Additionally, the influence of pressure up to $p = 3.5 \text{ kbar}$ and magnetic field up to 10 T was investigated for $\text{CeNiAs}_{0.65}\text{P}_{0.35}\text{O}$. Magnetic field does not have a strong effect on $\text{CeNiAs}_{0.65}\text{P}_{0.35}\text{O}$. At the lowest temperatures its resistivity behaves like a Fermi liquid, towards higher temperatures a T^3 temperature dependence develops. The antiferromagnetic transition is slightly shifted by the application of high magnetic fields, but at lowest temperatures, antiferromagnetic order is always present.

For $\text{CeNiAs}_{0.6}\text{P}_{0.4}\text{O}$, by contrast, the applied magnetic field strongly affects the physical properties at low temperatures: At zero and low fields, the resistivity is nearly linear in temperature and thus shows clear non-Fermi liquid behaviour in the entire measured temperature range. Upon increasing the field, Fermi liquid behaviour is established at the lowest temperatures, but it evolves into a linear-in-temperature dependence at higher temperatures. This establishes magnetic field as a useful tuning parameter for the study of quantum criticality in $\text{CeNiAs}_{1-x}\text{P}_x\text{O}$. It tunes $\text{CeNiAs}_{1-x}\text{P}_x\text{O}$ into the same direction as pressure and P substitution, away from magnetic order: $\text{CeNiAs}_{0.65}\text{P}_{0.35}\text{O}$ is therefore shifted towards the quantum critical point, $\text{CeNiAs}_{0.6}\text{P}_{0.4}\text{O}$ away from it,

deeper into the paramagnetic phase.

Pressure shifts the antiferromagnetic transition in $\text{CeNiAs}_{0.65}\text{P}_{0.35}\text{O}$ to lower temperatures, adding a high magnetic field of 10 T suppresses it further. The highest applied pressure of $p = 3.5$ kbar was still below the critical value for this substitution level: Down to the lowest temperatures, Fermi liquid behaviour is found for all fields. Estimating the critical pressure from the performed measurements, it is expected to be around 5 kbar. Future investigations could include measurements at higher pressures for $\text{CeNiAs}_{0.65}\text{P}_{0.35}\text{O}$ to approach the quantum critical point even more closely and eventually cross it. Knowing the critical pressure, this could be compared to the unsubstituted parent compound CeNiAsO . Similarly, magnetic field could be applied to the parent compound at different pressures, and higher magnetic fields could be applied to the samples with $x = 35\%$ and $x = 40\%$. Eventually, the complex interplay of pressure, doping, and magnetic field could be analyzed in detail. Furthermore, the Hall resistivity could be added and would provide information on the type of quantum critical point, and whether/how it evolves when the tuning parameter is changed.

In $\text{Ti}_{1-x}\text{Sc}_x\text{Au}$, previous measurements had suggested a quantum critical point at a doping level around $x = 12\%$. In this thesis, these findings could be corroborated by extending the temperature range to lower values. For three selected doping levels ($x = 0\%$, $x = 13\%$, and $x = 25\%$), the resistivity measurements were expanded to lower temperatures by installing them into a dilution refrigerator. The low-temperature results were consistent with the interpretation of the high-temperature data, but the power laws of the quantum critical behaviour could be pinned down with higher accuracy. $\text{Ti}_{1-x}\text{Sc}_x\text{Au}$ has thus turned out to be a rare example of a material showing an itinerant antiferromagnetic quantum critical point, which shows non-Fermi liquid behaviour consistent with a two-dimensional spin-density-wave scenario.

CeB_6 is of interest as one of only few cubic materials displaying a readily accessible putative quantum critical point in its temperature - magnetic field phase diagram. Furthermore, it shares many characteristics with $\text{Ce}_3\text{Pd}_{20}\text{Si}_6$, which shows unconventional quantum criticality and indications for a Kondo breakdown. In CeB_6 , magnetization, specific heat, and resistivity were measured and analyzed with respect to quantum criticality. Antiferromagnetic order is suppressed by magnetic field, with different critical values for fields applied along different crystallographic axes. Whereas some properties point towards quantum critical behaviour (enhancement of the A coefficient, γ_0 , and χ_0 at the critical value, and changes of the residual resistivity ρ_0 and of the Kadowaki-Woods ratio at the critical value), no clear signatures of non-Fermi liquid behaviour

were found at low temperatures. Unlike in other cubic compounds such as $\text{Ce}_3\text{Pd}_{20}\text{Si}_6$ or CeIn_3 , where clear non-Fermi liquid behaviour was reported, it seems that the enhancement of the Fermi liquid parameters is not induced by quantum criticality. The anisotropy with magnetic field, starting from the lowest field values, distinguishes CeB_6 from the otherwise similar $\text{Ce}_3\text{Pd}_{20}\text{Si}_6$; also the process of suppressing T_N presents itself differently in the specific heat measurements. The physical properties of CeB_6 seem to be governed by complex magnetic ordering mechanisms (possibly an interplay of anti-ferromagnetic and ferromagnetic channels of localized and itinerant type) at non-zero fields rather than quantum critical effects. The importance of ferromagnetic fluctuations have also been reported and could turn the suppression of T_N into a first order quantum phase transition, thereby avoiding a quantum critical point.

In $\text{Ce}_3\text{Pd}_{20}\text{Si}_6$, resistivity and Hall resistivity measurements on single crystals were needed to investigate a new putative quantum critical point that only occurs when the magnetic field is applied along the crystallographic [100] direction. In order to single out its features, the same set of measurements was performed with the magnetic field applied along [111] and [110], to use these latter as background for the [100] data. Indeed, a careful subtraction leads to well-defined anomalies. Their position clearly relates them to the putative quantum critical point. For a quantitative analysis with respect to a Kondo breakdown scenario, however, further data of even higher resolution, in particular for the Hall effect data, are needed.

Within the above-mentioned investigations, several experimental aspects in the field of quantum criticality could be addressed: On the one hand, properties of materials which have only been recently investigated in this context could be described in more detail and their quantum critical behaviour could be pinned down experimentally ($\text{CeNiAs}_{1-x}\text{P}_x\text{O}$, $\text{Ti}_{1-x}\text{Sc}_x\text{Au}$, CeB_6). On the other hand, very advanced and subtle questions were addressed in well-established and highly investigated quantum critical materials ($\text{Ce}_3\text{Pd}_{20}\text{Si}_6$ and YbRh_2Si_2). Especially in the case of YbRh_2Si_2 , new experimental routes (microwave experiments, ultra-low temperature investigations) could be explored and refined. The insights that could be gained will provide an important basis for the further development of these new experimental techniques.

7 Bibliography

- [1] J. Kondo. *Prog. Theor. Phys.* **32**, 37 (1964). doi:10.1143/PTP.32.37.
- [2] K. Andres, J. E. Graebner, H. R. Ott. *Phys. Rev. Lett.* **35**, 1779 (1975). doi:10.1103/PhysRevLett.35.1779.
- [3] M. A. Ruderman, C. Kittel. *Phys. Rev.* **96**, 99 (1954). doi:10.1103/PhysRev.96.99.
- [4] T. Kasuya. *Prog. Theor. Phys.* **16**, 45 (1956). doi:10.1143/PTP.16.45.
- [5] K. Yosida. *Phys. Rev.* **106**, 893 (1957). doi:10.1103/PhysRev.106.893.
- [6] J. A. Hertz. *Phys. Rev. B* **14**, 1165 (1976). doi:10.1103/PhysRevB.14.1165.
- [7] T. Moriya. *Spin fluctuations in itinerant electron magnetism* (Springer 1985).
- [8] A. J. Millis. *Phys. Rev. B* **48**, 7183 (1993). doi:10.1103/PhysRevB.48.7183.
- [9] Q. Si, S. Rabello, K. Ingersent, J. L. Smith. *Nature* **413**, 804 (2001). doi:10.1038/35101507.
- [10] L. D. Landau. *JETP Lett.* **3**, 920 (1957).
- [11] J. Dai, Q. Si, J.-X. Zhu, E. Abrahams. *PNAS* **106**, 4118 (2009). doi:10.1073/pnas.0900886106.
- [12] D. v. d. Marel, H. J. A. Molegraaf, J. Zaanen, Z. Nussinov, F. Carbone, A. Damascelli, H. Eisaki, M. Greven, P. H. Kes, M. Li. *Nature* **425**, 271 (2003). doi:10.1038/nature01978.
- [13] W. Meissner, B. Voigt. *Ann. Phys.* **399**, 892 (1930). doi:10.1002/andp.19303990803.
- [14] C. Zener. *Phys. Rev.* **81**, 440 (1951). doi:10.1103/PhysRev.81.440.

- [15] A. C. Hewson. *The Kondo Problem to Heavy Fermions* (Cambridge University Press 1993).
- [16] P. W. Anderson. *Phys. Rev.* **124**, 41 (1961). doi:10.1103/PhysRev.124.41.
- [17] B. Coqblin, J. R. Schrieffer. *Phys. Rev.* **185**, 847 (1969). doi:10.1103/PhysRev.185.847.
- [18] A. A. Abrikosov. *JETP Lett.* **21**, 660 (1965).
- [19] H. Suhl. *Phys. Rev.* **138**, A515 (1965). doi:10.1103/PhysRev.138.A515.
- [20] Y. Nagaoka. *Phys. Rev.* **138**, 1112 (1965). doi:10.1103/PhysRev.138.A1112.
- [21] N. Andrei, K. Furuya, J. H. Lowenstein. *Rev. Mod. Phys.* **55**, 331 (1983). doi:10.1103/RevModPhys.55.331.
- [22] E. Bauer, S. Paschen. *Lecture Notes: Strongly Correlated Electron Systems* (2012).
- [23] P. Coleman. *Handbook of Magnetism - Heavy Fermions: Electrons at the Edge of Magnetism* (Wiley 2007).
- [24] C. Kittel. *Introduction to Solid State Physics* (Wiley 2005).
- [25] K. Kadowaki, S. Woods. *Solid State Commun.* **58**, 507 (1986). doi:10.1016/0038-1098(86)90785-4.
- [26] J. Custers. *Quantum-critical behaviour in HF compounds YbRh₂Si₂ and CeIn_{3-x}Sn_x*. Ph.D. thesis, TU Dresden (2003).
- [27] M. Dressel, G. Grüner. *Electrodynamics of Solids* (Cambridge University Press).
- [28] R. Gurzhi. *JETP Lett.* **8**, 673 (1959).
- [29] L. Degiorgi. *Rev. Mod. Phys.* **71**, 687 (1999). doi:10.1103/RevModPhys.71.687.
- [30] A. Rosch, P. C. Howell. *Phys. Rev. B* **72**, 104510 (2005). doi:10.1103/PhysRevB.72.104510.
- [31] S. Doniach. *Physica B+C* **91**, 231 (1977). doi:10.1016/0378-4363(77)90190-5.
- [32] W. Li, C. L. Vicente, J. S. Xia, W. Pan, D. C. Tsui, L. N. Pfeiffer, K. W. West. *Phys. Rev. Lett.* **102**, 216801 (2009). doi:10.1103/PhysRevLett.102.216801.

-
- [33] P. Gegenwart, Q. Si, F. Steglich. *Nat. Phys.* **4**, 186 (2008). doi:10.1038/nphys892.
- [34] T. Vojta. *Ann. Phys.* **9**, 403 (2000). doi:10.1002/1521-3889(200006).
- [35] S. Sachdev. *Quantum Phase Transitions* (Cambridge University Press 2008).
- [36] D. M. Broun. *Nat. Phys.* **4**, 170 (2008). doi:10.1038/nphys909.
- [37] S. Sachdev. *Nat. Phys.* **4**, 173 (2008). doi:10.1038/nphys894.
- [38] S. Sachdev, B. Keimer. *Phys. Today* **64**, 29 (2011). doi:10.1063/1.3554314.
- [39] G. R. Stewart. *Rev. Mod. Phys.* **73**, 797 (2001). doi:10.1103/RevModPhys.73.797.
- [40] H. v. Löhneysen, A. Rosch, M. Vojta, P. Wölfle. *Rev. Mod. Phys.* **79**, 1015 (2007). doi:10.1103/RevModPhys.79.1015.
- [41] T. Moriya, T. Takimoto. *J. Phys. Soc. Jpn.* **64**, 960 (1995). doi:10.1143/JPSJ.64.960.
- [42] G. Lonzarich. *Electron* (Cambridge Univ. Press 1997).
- [43] S. Friedemann, N. Oeschler, S. Wirth, C. Krellner, C. Geibel, F. Steglich, S. Paschen, S. Kirchner, Q. Si. *PNAS* **107**, 14547 (2010). doi:10.1073/pnas.1009202107.
- [44] S. Paschen, T. Lühmann, S. Wirth, P. Gegenwart, O. Trovarelli, C. Geibel, F. Steglich, P. Coleman, Q. Si. *Nature* **432**, 881 (2004). doi:10.1038/nature03129.
- [45] P. Coleman, C. Pépin, Q. Si, R. Ramazashvili. *J. Phys.: Condens. Matter* **13**, R723 (2001). doi:10.1088/0953-8984/13/35/202.
- [46] P. Gegenwart, T. Westerkamp, C. Krellner, Y. Tokiwa, S. Paschen, C. Geibel, F. Steglich, E. Abrahams, Q. Si. *Science* **315**, 969 (2007). doi:10.1126/science.1136020.
- [47] S. Paschen, S. Friedemann, S. Wirth, F. Steglich, S. Kirchner, Q. Si. *J. Magn. Magn. Mater.* **400**, 17 (2016). doi:10.1016/j.jmmm.2015.09.008.
- [48] A. J. Schofield. *Science* **315**, 945 (2007). doi:10.1126/science.1139335.
- [49] D. M. Pozar. *Microwave Engineering* (Wiley 2005).

- [50] M. B. S. T. C. Edwards. *Foundations of Interconnect and Microstrip Design, 3rd Edition* (Wiley 2000).
- [51] R. N. Simons. *Coplanar Waveguide Circuits, Components, and Systems* (Wiley 2001).
- [52] P. B. I. Bahl. *Microwave Solid State Circuit Design, 2nd Edition* (Wiley 2003).
- [53] R. K. Hoffmann. *Integrierte Mikrowellenschaltungen* (Springer 1983).
- [54] C. P. Wen. *IEEE Trans. Microwave Theory Tech.* **17**, 1087 (1969). doi:10.1109/TMTT.1969.1127105.
- [55] M. Hiebel. *Fundamentals of Vector Network Analysis* (Rohde & Schwarz 2007).
- [56] P. Das, R. B. Ouboter, K. W. Taconis. *Low Temp. Phys.* (1965). doi:10.1007/978-1-4899-6443-4_133.
- [57] F. Pobell. *Matter and methods at low temperatures* (Springer 2007).
- [58] S. Hunklinger. *Festkörperphysik* (Oldenbourg 2011 (3rd)).
- [59] O. Instruments. *Operation of $^3\text{He}/^4\text{He}$ dilution refrigerator manual*.
- [60] K.-A. Lorenzer. *Quantum critical behaviour in cubic heavy-fermion compounds*. Ph.D. thesis, TU Wien (2012).
- [61] J. Haenel. *to be published*. Ph.D. thesis, TU Wien (2016).
- [62] D. H. Nguyen, A. Sidorenko, M. Müller, S. Paschen, A. Waard, G. Frossati. *J. Phys. Conf. Ser.* **400**, 052024 (2012).
- [63] Linear Research INC. *LR-700 AC resistance bridge user's manual* (1995).
- [64] Quantum Design. *PPMS Manual*.
- [65] M. Scheffler, M. Dressel, M. Jourdan, H. Adrian. *Nature* **438**, 1135 (2005). doi:10.1038/nature04232.
- [66] M. Scheffler, M. Dressel. *Rev. Sci. Instrum.* **76**, 074702 (2005). doi:10.1063/1.1947881.

-
- [67] H. Kitano, T. Ohashi, A. Maeda. *Rev. Sci. Instrum.* **79**, 074701 (2008). doi:10.1063/1.2954957.
- [68] K. Steinberg, M. Scheffler, M. Dressel. *Rev. Sci. Instrum.* **83**, 024704 (2012). doi:10.1063/1.3680576.
- [69] D. Geiger. *Electrodynamics at Quantum Phase Transitions - High Frequency Spectroscopy on Ferromagnetic Materials*. Master's thesis, University of Stuttgart (2011).
- [70] R. E. Collin. *Foundations Of Microwave Engineering (2nd edition)* (Wiley-IEEE Press 2011).
- [71] L. Frunzio, A. Wallraff, D. Schuster, J. Majer, R. Schoelkopf. *IEEE Trans. Appl. Supercond.* **15**, 860 (2005). doi:10.1109/TASC.2005.850084.
- [72] D. I. Schuster, A. A. Houck, J. A. Schreier, A. Wallraff, J. M. Gambetta, A. Blais, L. Frunzio, J. Majer, B. Johnson, M. H. Devoret, S. M. Girvin, R. J. Schoelkopf. *Nature* **445**, 515 (2007). doi:10.1038/nature05461.
- [73] M. Goppl, A. Fragner, M. Baur, R. Bianchetti, S. Filipp, J. M. Fink, P. J. Leek, G. Puebla, L. Steffen, A. Wallraff. *J. Appl. Phys.* **104**, 113904 (2008). doi:10.1063/1.3010859.
- [74] R. J. Schoelkopf, S. M. Girvin. *Nature* **451**, 664 (2008). doi:10.1038/451664a.
- [75] M. Scheffler, C. Fella, M. Dressel. *J. Phys.: Conf. Ser.* **400**, 052031 (2012). doi:10.1088/1742-6596/400/5/052031.
- [76] M. Scheffler, K. Schlegel, C. Clauss, D. Hafner, C. Fella, M. Dressel, M. Jourdan, J. Sichelschmidt, C. Krellner, C. Geibel, F. Steglich. *Phys. Status Solidi B* **250**, 439 (2013). doi:10.1002/pssb.201200925.
- [77] D. Hafner, M. Dressel, M. Scheffler. *Rev. Sci. Instrum.* **85**, 014702 (2014). doi:10.1063/1.4856475.
- [78] R. Amsüss, C. Koller, T. Nöbauer, S. Putz, S. Rotter, K. Sandner, S. Schneider, M. Schramböck, G. Steinhauser, H. Ritsch, J. Schmiedmayer, J. Majer. *Phys. Rev. Lett.* **107**, 060502 (2011). doi:10.1103/PhysRevLett.107.060502.

- [79] C. Koller. *Towards the experimental realization of Hybrid Quantum Systems*. Ph.D. thesis, TU Wien (2012).
- [80] S. Putz, D. Krimer, R. Amsüss, A. Valookaran, T. Nöbauer, J. Schmiedmayer, S. Rotter, J. Majer. *Nat. Phys.* (2014). doi:10.1038/nphys3050.
- [81] R. Voglauer. *Optical Response of Superconducting Transmission Line Resonators*. Master's thesis, TU Wien (2013).
- [82] C. Krellner, S. Taube, T. Westerkamp, Z. Hossain, C. Geibel. *Philos. Mag.* **92**, 2508 (2012). doi:10.1080/14786435.2012.669066.
- [83] R. Hu, J. Hudis, C. Stock, C. L. Broholm, C. Petrovic. *J. Cryst. Growth* **304**, 114 (2007). doi:10.1016/j.jcrysgro.2007.02.022.
- [84] H. Nakai, T. Ebihara, S. Tsutsui, M. Mizumaki, N. Kawamura, S. Michimura, T. Inami, T. Nakamura, A. Kondo, K. Kindo, Y. H. Matsuda. *J. Phys. Soc. Jpn.* **82**, 124712 (2013). doi:10.7566/JPSJ.82.124712.
- [85] C. Krellner. *Ferromagnetische Korrelationen in Kondo-Gittern: YbT_2Si_2 und CeTPO ($T = \text{Übergangsmetall}$)*. Ph.D. thesis, TU Dresden (2009).
- [86] O. Trovarelli, C. Geibel, S. Mederle, C. Langhammer, F. M. Grosche, P. Gegenwart, M. Lang, G. Sparn, F. Steglich. *Phys. Rev. Lett.* **85**, 626 (2000). doi:10.1103/PhysRevLett.85.626.
- [87] J. Custers, P. Gegenwart, H. Wilhelm, K. Neumaier, Y. Tokiwa, O. Trovarelli, C. Geibel, F. Steglich, C. Ppin, P. Coleman. *Nature* **424**, 524 (2003). doi:10.1038/nature01774.
- [88] S. Ernst, S. Kirchner, C. Krellner, C. Geibel, G. Zwicknagl, F. Steglich, S. Wirth. *Nature* **474**, 362 (2011). doi:10.1038/nature10148.
- [89] U. Schaufuß, V. Kataev, A. A. Zvyagin, B. Büchner, J. Sichelschmidt, J. Wykhoff, C. Krellner, C. Geibel, F. Steglich. *Phys. Rev. Lett.* **102**, 076405 (2009). doi:10.1103/PhysRevLett.102.076405.
- [90] S. Kimura, J. Sichelschmidt, J. Ferstl, C. Krellner, C. Geibel, F. Steglich. *Phys. Rev. B* **74**, 132408 (2006). doi:10.1103/PhysRevB.74.132408.

-
- [91] Q. Si, S. Paschen. *Phys. Status Solidi B* **250**, 425 (2013). doi:10.1002/pssb.201300005.
- [92] Y. Kamihara, H. Hiramatsu, M. Hirano, R. Kawamura, H. Yanagi, T. Kamiya, H. Hosono. *J. Am. Chem. Soc.* **128**, 10012 (2006). doi:10.1021/ja063355c.
- [93] S. Kitagawa, K. Ishida, T. Nakamura, M. Matoba, Y. Kamihara. *Phys. Rev. Lett.* **109**, 227004 (2012). doi:10.1103/PhysRevLett.109.227004.
- [94] Y. Luo, Y. Li, S. Jiang, J. Dai, G. Cao, Z. Xu. *Phys. Rev. B* **81**, 134422 (2010). doi:10.1103/PhysRevB.81.134422.
- [95] Y. Luo, H. Han, H. Tan, X. Lin, Y. Li, S. Jiang, C., J. Dai, G. Cao, Z. Xu, S. Li. *J. Phys.: Condens. Matter* **23**, 175701 (2011).
- [96] Y. K. Luo, L. Pourovskii, S. E. Rowley, Y. K. Li, C. M. Feng, A. Georges, J. H. Dai, G. Cao, Z. Xu, Q. Si, N. P. Ong. *Nat. Mater.* (2014). doi:10.1038/nmat3991.
- [97] E. Svanidze, J. K. Wang, T. Besara, L. Liu, Q. Huang, T. Siegrist, B. Frandsen, J. Lynn, A. H. Nevidomskyy, M. B. Gamza, M. Aronson, Y. Uemura, E. Morosan. *Nat. Commun.* **6** (2015). doi:10.1038/ncomms8701.
- [98] S. Paschen, J. J. Larrea. *J. Phys. Soc. Jpn.* **83**, 061004 (2014). doi:10.7566/JPSJ.83.061004.
- [99] C. Marcenat, R. Fisher, N. Phillips, J. Flouquet. *J. Magn. Magn. Mater.* **76**, 115 (1988). doi:10.1016/0304-8853(88)90332-0.
- [100] A. V. Gribanov, Y. D. Seropegin, O. I. Bodak. *J. Alloy. Compd.* **204** (1994).
- [101] J. Custers, K.-A. Lorenzer, M. Müller, A. Prokofiev, A. Sidorenko, H. Winkler, A. M. Strydom, Y. Shimura, T. Sakakibara, R. Yu, Q. Si, S. Paschen. *Nat. Mater.* **11**, 189 (2012). doi:10.1038/nmat3214.
- [102] Q. Si. *Physica B* **378**, 23 (2006). doi:10.1016/j.physb.2006.01.156.
- [103] V. Martelli, J. J. Larrea, K.-A. Lorenzer, J. Hänel, A. Prokofiev, S. Paschen. *J. Phys. Conf. Ser.* **592**, 012080 (2015). doi:10.1088/1742-6596/592/1/012080.
- [104] A. Hrennikoff. *J. Appl. Mech.* **8**, 619 (1941).

- [105] R. L. Courant. *Bull. Amer. Math. Soc.* **49**, 1 (1943). doi:10.1090/S0002-9904-1943-07818-4.
- [106] 'Modeling of Coplanar Waveguides' from <http://www.comsol.com/blogs/modeling-coplanar-waveguides/>.
- [107] P. J. Petersan, S. M. Anlage. *J. Appl. Phys.* **84**, 3392 (1998). doi:10.1063/1.368498.
- [108] O. Klein, S. Donovan, M. Dressel, G. Grüner. *Int. J. Infrared Millimeter Waves* **14**, 2423 (1993). doi:10.1007/BF02086216.
- [109] D. Bothner, T. Gaber, M. Kemmler, D. Koelle, R. Kleiner, S. Wünsch, M. Siegel. *Phys. Rev. B* **86**, 014517 (2012). doi:10.1103/PhysRevB.86.014517.
- [110] W. Voesch, C. Clauss, M. Javaheri, M. Dressel, K. Kliemt, C. Krellner, J. Sichelschmidt, C. Geibel, M. Scheffler. In *Poster, ICM 2015*.
- [111] K. Parkkinen. *Microwave Spectroscopy on the Skin Effect of Heavy Fermion Metals using Stripline Resonators*. Master's thesis, University of Helsinki/University of Stuttgart (2015).
- [112] K. Parkkinen, M. Dressel, K. Kliemt, C. Krellner, C. Geibel, F. Steglich, M. Scheffler. *Physics Procedia* **75**, 340 (2015). doi:10.1016/j.phpro.2015.12.040.
- [113] G. Knebel, R. Boursier, E. Hassinger, G. Lapertot, P. G. Niklowitz, A. Pourret, B. Salce, J. P. Sanchez, I. Sheikin, P. Bonville, H. Harima. *J. Phys. Soc. Jpn.* **75**, 114709 (2006). doi:10.1143/JPSJ.75.114709.
- [114] E. Schuberth, M. Tippmann, L. Steinke, S. Lausberg, A. Steppke, M. Brando, C. Krellner, C. Geibel, R. Yu, Q. Si, F. Steglich. *Science* **351**, 485 (2016). doi:10.1126/science.aaa9733.
- [115] S. Rogge, D. Natelson, D. D. Osheroff. *Rev. Sci. Instrum.* **68**, 1831 (1997). doi:10.1063/1.1148055.
- [116] A. B. Pippard. *Magnetoresistance in metals*, (Cambridge University Press 2009).
- [117] E. Svanidze, T. Besara, J. K. Wang, D. Geiger, L. Prochaska, J. Santiago, J. W. Lynn, S. Paschen, T. Siegrist, E. Morosan. *in preparation* (2016).
- [118] B. T. Matthias, R. M. Bozorth. *Phys. Rev.* **109**, 604 (1958). doi:10.1103/PhysRev.109.604.

-
- [119] B. T. Matthias, A. M. Clogston, H. J. Williams, E. Corenzwit, R. C. Sherwood. *Phys. Rev. Lett.* **7**, 7 (1961). doi:10.1103/PhysRevLett.7.7.
- [120] N. D. Mathur, F. M. Grosche, S. R. Julian, I. R. Walker, D. M. Freye, R. K. W. Haselwimmer, G. G. Lonzarich. *Nature* **394** (1998). doi:10.1038/27838.
- [121] P. Coleman, A. S. Schofield. *Nature* (2005). doi:10.1038/nature03279.
- [122] A. Rosch. *Phys. Rev. Lett.* **82**, 4280 (1999). doi:10.1103/PhysRevLett.82.4280.
- [123] C. Pfleiderer, A. Fain, H. von Löhneysen, S. Hayden, G. Lonzarich. *J. Magn. Magn. Mater.* **226**, 258 (2001). doi:10.1016/S0304-8853(00)00655-7.
- [124] M. Nicklas, M. Brando, G. Knebel, F. Mayr, W. Trinkl, A. Loidl. *Phys. Rev. Lett.* **82**, 4268 (1999). doi:10.1103/PhysRevLett.82.4268.
- [125] N. Brandt, V. Moshchalkov, S. Pashkevich, M. Vybornov, M. Semenov, T. Kolobyanina, E. Konovalova, Y. Paderno. *Solid State Commun.* **56**, 937 (1985). doi:10.1016/S0038-1098(85)80029-6.
- [126] J. Effantin, J. Rossat-Mignod, P. Burlet, H. Bartholin, S. Kunii, T. Kasuya. *J. Magn. Magn. Mater.* **47**, 145 (1985). doi:10.1016/0304-8853(85)90382-8.
- [127] H. Nakao, K. Magishi, Y. Wakabayashi, Y. Murakami, K. Koyama, K. Hirota, Y. Endoh, S. Kunii. *J. Phys. Soc. Jpn.* **70**, 1857 (2001). doi:10.1143/JPSJ.70.1857.
- [128] P. Gegenwart, J. Custers, Y. Tokiwa, C. Geibel, F. Steglich. *Phys. Rev. Lett.* **94** (2005). doi:10.1038/nphys892.
- [129] A. M. Strydom, A. Pikul, F. Steglich, S. Paschen. *J. Phys. Conf. Ser.* **51**, 239 (2006). doi:10.1103/PhysRevLett.114.037202.
- [130] E. Fawcett. *Rev. Mod. Phys.* (1988). doi:10.1103/RevModPhys.60.209.
- [131] P. Burlet, J. Rossat-Mignod, J. M. Effantin, T. T. Kasuya, S. Kunii, T. Komatsubara. *J. Appl. Phys.* (1982). doi:10.1063/1.330762.
- [132] A. S. Cameron, G. Friemel, D. S. Inosov. *Rep. Prog. Phys.* **79**, 066502 (2016). doi:10.1088/0034-4885/79/6/066502.

- [133] M. A. Continentino, S. N. de Medeiros, M. T. D. Orlando, M. B. Fontes, E. M. Baggio-Saitovich. *Phys. Rev. B* **64**, 012404 (2001). doi: 10.1103/PhysRevB.64.012404.
- [134] H. Jang, G. Friemel, J. Ollivier, A. V. Dukhnenko, N. Y. Shitsevalova, V. B. Filipov, B. Keimer, D. S. Inosov. *Nat. Mater.* **13**, 682 (2014). doi:10.1038/nmat3976.
- [135] D. Belitz, T. R. Kirkpatrick, T. Vojta. *Phys. Rev. Lett.* **82**, 4707 (1999). doi: 10.1103/PhysRevLett.82.4707.
- [136] T. Goto, T. Watanabe, S. Tsuduku, H. Kobayashi, Y. Nemoto, T. Yanagisawa, M. Akatsu, G. Ano, O. Suzuki, N. Takeda, A. Dönni, H. Kitazawa. *J. Phys. Soc. Jpn.* **78**, 024716 (2009). doi:10.1143/JPSJ.78.024716.
- [137] H. Mitamura, T. Sakuraba, T. Tayama, T. Sakakibara, S. Tsuduku, G. Ano, I. Ishii, M. Akatsu, Y. Nemoto, T. Goto, A. Kikkawa, H. Kitazawa. *J. Phys. Conf. Ser.* **200**, 012118 (2010). doi:10.1088/1742-6596/200/1/012118.
- [138] H. Ono, T. Nakano, N. Takeda, G. Ano, M. Akatsu, Y. Nemoto, T. Goto, A. Dönni, H. Kitazawa. *J. Phys.: Condens. Matter* **25**, 126003 (2013).

Acknowledgements

I would like to thank everyone who contributed to the success of this thesis:

- My PhD supervisor **Silke Bühler-Paschen** for the opportunity to work in her group and her support throughout the duration of my thesis.
- The reviewer of my thesis, **Steffen Wirth**. Thank you for finding the time to review this thesis and for joining the thesis committee.
- My second supervisor within the Solids 4 Fun doctoral school, **Johannes Majer**. Together with his former PhD students **Christian Koller** and **Stefan Putz**, he provided me with various resonators, boxes and PCBs within our collaboration on the microwave experiments. Thank you as well for letting me use the Atominstitut laboratory equipment on several occasions.
- **Ha Nguyen** and **Andrey Sidorenko**. Without their efforts, the microwave setup in the Vienna demagnetization refrigerator would not have been set up and used. They played a crucial role in the choice and development of the microwave measurement procedure, and especially Andrey in the reviewing and analysis of the obtained data.
- **Hans Hübl** and **Rudolf Gross** from Walther-Meissner-Institut in Garching, for the opportunity to use their facilities and for the various discussions and ideas. Also part of the Walther-Meissner-Institut team, my special thanks go to **Friedrich Wulschner** for all his efforts at the Garching setup. Without his preparation of additional measurement infrastructure and his support during the experimental phases, my experiments would not have reached the same level.
- **Julio Larrea** and **Valentina Martelli**, who collaborated with me on several investigations ($\text{Ce}_3\text{Pd}_{20}\text{Si}_6$, $\text{CeNiAs}_x\text{P}_{1-x}\text{O}$, CeB_6). Julio was the one to introduce me to the operation of the dilution refrigerator, the PPMS, and the Laue diffractometer. Many thanks to both Julio and Valentina for being available for

questions and discussions in the last two years despite the long distance and the time difference.

- **Eteri Svanidze** and **Emilia Morosan**, for the opportunity to take part in their study of $\text{TiSc}_{1-x}\text{Au}_x$.
- **Gabriel Pristas**, **Petar Popcevic**, **Neven Barišić**, and **Kristija Velebit**, who contributed to measurements and/or discussion on the oxypnictide samples.
- **Petr Tomeš**, for being a great office mate during the first two years and who also introduced me to spot welding and my first PPMS measurements.
- **Günther Lientschnig** for giving me access to the bonder at the clean room, **Martin Müller** and **Herbert Müller** for technical support at the dilution refrigerator.
- **Friedrich Kneidinger**, **Karina Bulgakova**, **Patrick Heinrich**, **Leonid Salamakha**, for measurement support and a friendly atmosphere in the transport laboratory.
- **Lukas Prochaska** and **Jonathan Hänel**. We shared many hours of work, responsibilities, trouble-shooting discussions at the dilution refrigerator, some great conferences, summer schools, and ultimate frisbee sessions.
- **Matthias Ikeda** for fruitful discussions about fundamental physics questions and many other things.
- **Vanda Peter** for her kind introduction to sample preparation in general and in particular for providing me with some motivation when it was desperately needed. Also I would like to thank **Peter Hundegger**, for introducing me to the diamond wire saw, and for being a helpful and friendly person to talk to at any time.
- The other people at our office, who contributed to creating a good atmosphere: **Szami Dzaber**, **Mathieu Taupin**, **Gaku Eguchi**.
- **André Vogel**, for making so many administrative things so easy, and being incredibly understanding and helpful.
- **Graeme Johnstone** for all the tea breaks (especially for the really comfortable ones in the cellar next to the dilution refrigerator...) and for listening to all my tea-break-stories.

-
- Very importantly, my flatmates; without them, everything would have been so much more difficult: **Stefan Laumann** and **Nicholas Shore**.
 - My parents, who have always supported me along the way.

I acknowledge financial support by the Doctoral College Solids for Function W1243, funded by the Austrian science fund FWF, and by the European Research Council/ERC Advanced Grant No 227378.

Declaration

Versicherung

Hiermit versichere ich, dass ich die vorliegende Arbeit ohne unzulässige Hilfe Dritter und ohne Benutzung anderer als der angegebenen Hilfsmittel angefertigt habe. Die aus fremden Quellen direkt oder indirekt übernommenen Gedanken sind als solche kenntlich gemacht. Die Arbeit wurde bisher weder im Inland noch im Ausland in gleicher oder ähnlicher Form einer anderen Prüfungsbehörde vorgelegt. Die vorliegende Dissertation wurde am Institut für Festkörperphysik der Technischen Universität Wien unter der wissenschaftlichen Betreuung von Univ. Prof. Dr.rer.nat. Silke Bühler-Paschen angefertigt. Ich erkenne die Promotionsordnung der Technischen Universität Wien an.

Wien, 27. Juli 2016

Lebenslauf

Persönliche Daten

Diana Geiger
Favoritenstrasse 174/9a
1100 Wien

Tel.: 0677 61404467
E-Mail: diana.geiger@gmx.de

Geb. am 09. 11 1985, Kronstadt (Rumänien)
Staatsangehörigkeit: deutsch

Ausbildung und Arbeitserfahrung

- seit 10/2011 Doktoratsstudium der Physik (Projektassistentin), TU Wien:
Stark korrelierte Elektronensysteme, Quantenkritikalität, Experimente bei tiefen Temperaturen und niedrigen Frequenzen
- 03/2011–09/2011 Wissenschaftliche Hilfskraft, Universität Stuttgart:
Praktikumsbetreuung, Labview Programmierung, THz-Spektroskopie
- 03/2010–03/2011 Diplomarbeit, 1. Physikalisches Institut, Universität Stuttgart:
Mikrowellen- und THz-Spektroskopie, Quantenphasenübergänge
- 08/2009–01/2010 Wissenschaftliche Hilfskraft, Universität Stuttgart: Entwurf, Planung, Aufbau eines Gehäuses für einen Durchflusskryostaten
- 10/2005–03/2011 Studium der Physik, Universität Stuttgart, Abschlussnote 1,0
- 09/2008–05/2009 Studienjahr im Ausland, University of Toronto/Kanada
- 04/2008–05/2008 Werkstudentin bei Siemens Healthcare Computed Tomography:
Algorithmen zur Rauschreduktion mit MATLAB
- 09/1996–07/2005 Uhland-Gymnasium Tübingen, Abiturnote 1,0

Sonstige Kenntnisse

Sprachen Deutsch (Muttersprache), Englisch, Französisch, Rumänisch, Latein
Computer Latex, Autodesk Inventor, Ubuntu Linux, Origin, Python

Stipendien

- 08/2007–04/2011 Stipendiatin der Studienstiftung des Deutschen Volkes
- 01/2007–04/2011 YOLANTE (Young Ladies Network of Technology, Siemens Förderkreis)
- 08/2008–05/2009 DAAD Jahresstipendium Nordamerika (Kanada)
- 07/2005 Scheffelpreis (Deutsche Literarische Gesellschaft, für Abituraufsatz)

Scientific output

- planned Interplay of localized and itinerant magnetism in CeB₆ close to a field-induced magnetic instability; J. Larrea, D. Geiger, A. Sidorenko, V. Martelli, Y. Onuki and S. Paschen
- planned Accessing the Kondo breakdown scale in YbRh₂Si₂ with microwave excitations; D. Geiger, A. Sidorenko, H. Nguyen, S. Putz, J. Majer, F. Wulschner, H. Huebl, R. Gross, C. Krellner, S. Paschen
- planned Transport properties of quantum critical YbRh₂Si₂ at ultra-low temperatures; H. Nguyen, A. Sidorenko, D. Geiger, S. Paschen et al.
- planned Kondo breakdown in a heavy fermion system with quadrupolar order; V. Martelli, D. Geiger, J. Hänel, J. Larrea, A. Prokofiev, Q. Si, and S. Paschen
- planned Magnetic field as a tuning parameter of the quantum-critical oxypnictide series CeNiAs_{1-x}P_xO; D. Geiger, P. Popcevic, K. Velebit, N. Barišić, G. Pristas, J. Larrea, Y. Luo, Z. Xu, S. Paschen.
- under review Doping-induced Quantum Critical Point in the Itinerant Antiferromagnetic Metal TiAu; *Phys. Rev. Lett.*, E. Svanidze, T. Besara, J. K. Wang, D. Geiger, L. Prochaska, J. Santiago, J. W. Lynn, S. Paschen, T. Siegrist, and E. Morosan
- 04/2016 THz conductivity of Sr_{1-x}Ca_xRuO₃; *Phys. Rev. B* **93**, D. Geiger, U. S. Pracht, M. Dressel, J. Mravlje, M. Schneider, P. Gegenwart, and M. Scheffler
- 07/2015 Probing quantum critical materials with microwaves; *ICM 2015, Barcelona*, poster
- 01/2015 Exploring low-energy phase diagrams of quantum critical materials: a microwave approach; *Walther-Meissner-Institut, Garching*, invited talk
- 09/2014 Applying microwave resonators to measure the dynamical response in the vicinity of a quantum critical point; *QCM 2014, Obergurgl*, poster
- 06/2014 Measuring the microwave response close to a quantum critical point; *NGSCES 2014, Nice*, contributed talk
- 05/2013 Low-energy electronic properties of clean CaRuO₃: elusive Landau quasiparticles; *Phys. Rev. Lett.* **112**, M. Schneider, D. Geiger, S. Esser, U. S. Pracht, C. Stingl, Y. Tokiwa, V. Moshnyaga, I. Sheikin, J. Mravlje, M. Scheffler, and P. Gegenwart
- 09/2013 Electrical coupling of quantum critical materials to a microwave coplanar waveguide resonator at milli-Kelvin temperatures; *OEPG/SPS Annual Meeting 2013, Linz*, contributed talk

- 08/2013 Measuring quantum-critical materials with microwaves at low temperatures via electrical coupling to coplanar waveguide resonators; *SCES 2013, Tokyo*, poster
- 12/2012 Broadband microwave study of SrRuO₃ and CaRuO₃ thin films; *J. Phys. Conf. Ser.*, **273**, D. Geiger, M. Scheffler, M. Dressel, M. Schneider, and P. Gegenwart
- 03/2011 Low-frequency optics of Sr_{1-x}Ca_xRuO₃; *SCES 2011, Cambridge*, poster
- 03/2011 Ferromagnetic resonance in Heusler thin films using microwave broadband spectroscopy; *DPG Spring Meeting 2011, Dresden*, poster